



**On the Interaction between vortex-induced vibrations and galloping
in rectangular cylinders of low side ratio**

Dissertation

submitted to and approved by the

Department of Architecture, Civil Engineering and Environmental Sciences
University of Braunschweig – Institute of Technology

and the

Department of Civil and Environmental Engineering
University of Florence

in candidacy for the degree of a

Doktor-Ingenieur (Dr.-Ing.) /

**Dottore di Ricerca in Processes, Materials and Constructions in Civil and
Environmental Engineering and for the Protection of the Historic-
Monumental Heritage^{*)}**

by

Tommaso Massai

born 08/11/1983

from Bagno a Ripoli (FI), Italy

Submitted on	16/03/2015
Oral examination on	11/05/2015
Professorial advisors	Prof. Gianni Bartoli Prof. Klaus Thiele

2016

^{*)} Either the German or the Italian form of the title may be used.

Statement of Originality

I, Tommaso MASSAI, the undersigned, declare that this thesis and the material presented in it are, to the best of my knowledge and belief, original and my own work and contains no material previously published or written by another person, except where due reference is made in the text of the thesis. I confirm that:

- The work was done during candidature for the research degree at the International PhD between the University of Florence and the Technische Universität Carolo-Wilhelmina zu Braunschweig.
- Where I have consulted the published work of others, it is clearly attributed.
- Where I have quoted from the work of others, the source is always given.
- I have mainly used Open-Source Software and they are cited within the dissertation; where I have used proprietary software they are declared and covered by license under my Institutions.
- I have acknowledged all sources of help.
- Where the thesis is based on work done by myself jointly with others, the contributions by each party are attributed.

Signed: _____

Date: _____

Abstract

On the Interaction between vortex-induced vibrations and galloping in rectangular cylinders of low side ratio

by Tommaso MASSAI

The present work deals with the interaction between vortex-induced vibrations (VIV) and galloping for rectangular cylinders of low side ratio, which is defined as the body width on the body depth facing the fluid flow ($SR = B/D$). In particular, the interaction mechanism has been characterized for a wide range of Reynolds numbers (Re) and mass ratios (m^*), aiming to provide a complete description of the response in several flow situations (smooth and turbulent, air and water) for bodies which exhibited, or were known to have, a pronounced proneness to this type of instability.

This type of flow-induced vibrations (FIV) phenomenon occurs for particular combinations of both aerodynamic and dynamic characteristics of a system. The present study consists in two main parts, both of them aimed at proposing a complete framework for scientific and designing purposes. The first one investigates the phenomenon occurring in sectional models purposely designed and experimentally tested. Therefore, the experimental activity has been dichotomously carried out in air- and water flow to characterize two different ranges of m^* and Re for smooth flow, while turbulent measures were performed in wind tunnel only. It is worth noting that for $SR = 1.5$ and 0.67 such a low m^* range has never been investigated. Then, the second part is devoted to the implementation of a predictive model for the interaction, implying also further experimental measures to assess the model key-parameter.

Despite extensive works have been already undertaken in the study of the interaction mechanism, there are still many issues to fully comprehend the variety of responses exhibited by different low SR cross-sections, in turns characterized by different properties related to flow regimes and system dynamics. Several sectional models of a $SR = 1.5$ have been tested given that this section demonstrated to be particularly prone to the interaction between VIV and galloping. Nevertheless, the majority of former literature investigations were performed on the square section. The response features of such a phenomenon are still not fully understood. In order to have a deeper insight and to give a comprehensive description of the interaction, the present investigation was conducted focusing particularly on the $SR = 1.5$ rectangular section: this is a soft oscillator respect to the incipient instability, while the same rotated section with an angle of attack $\alpha = 90^\circ$, that is $SR = 0.67$, is generally referred to as a hard-type one. Results in air flow showed peculiar amplitude response curves differently shaped depending on Re , m^* and corners sharpness accuracy; in some cases the arise of a super-harmonic resonance at one third of Kármán-resonance velocity has been observed, in agreement with literature. Turbulent flow measurements showed a delayed onset for galloping instability, either interacting with vortex-shedding or not, suppressing the response for high turbulence intensity and integral length scale. Results in water flow showed the response in amplitude and frequency to be strongly influenced by the abrupt change of m^* , recalling the different responses in air- and water flow regime reported in literature for a circular cylinder, though related to VIV only.

The afterbody has a remarkable effect too, as $SR = 0.67$ shows a completely different response, although remaining, differently from air flow measurements, a soft oscillator. Further tests on m^* variation constituted an integration for the data so far available in literature about these sections.

Finally, although big efforts have been done in assessing the sensitive parameter of the chosen model for the interaction, numerical results have been not satisfying, showing a good capability for the model to predict the instability onset, though exhibiting also a poor accordance between modelled stable amplitudes and experimental values in the post-critical branch.

Sommario

La tesi tratta dell'interazione fra vibrazioni indotte da distacco di vortici (VIV) e galoppo in corpi a sezione rettangolare con basso il rapporto fra i lati ($SR = B/D$). In particolare il fenomeno dell'interazione è stato caratterizzato in un vasto range relativo al numero di Reynolds (Re) e fattore di massa (m^*), con lo scopo di fornire una descrizione completa della risposta in qualsiasi condizione di flusso (laminare e turbolento, aria ed acqua), per quei corpi caratterizzati da una spiccata tendenza a questo tipo di instabilità. Tale fenomeno si manifesta per particolari combinazioni di caratteristiche dinamiche ed aerodinamiche del sistema. Il lavoro consta di due parti, entrambe concorrenti nella formulazione di un quadro utile per scopi sia scientifici sia progettuali. La prima relativa alla sperimentazione su modelli sezionali, appositamente progettati e testati in laboratorio: l'attività sperimentale è stata suddivisa in prove in aria ed acqua, per così caratterizzare due distinti intervalli di fattori di massa e Re , aventi ordini di grandezza diversi, in flusso laminare, mentre misure in flusso turbolento sono state eseguite solo in galleria del vento. In seguito, una seconda parte descrive l'implementazione di un modello predittivo per l'interazione, che ha comportato la necessità di effettuare ulteriori test di laboratorio per determinare il parametro fondamentale del modello.

Nonostante la vasta letteratura al riguardo, ci sono ancora molte questioni aperte nel tentativo di chiarire completamente la varietà di tipi di risposta, osservata per differenti sezioni rettangolari, caratterizzata a sua volta da diverse proprietà dinamiche e tipologie di flusso. Data la straordinaria predisposizione all'interazione tra distacco di vortici e galoppo per il rettangolo con $SR = 1.5$, sono stati testati diversi modelli sezionali del medesimo per cercare di descrivere al meglio il fenomeno, considerando anche i molti studi sperimentali, numerici e teorici già pubblicati sulla sezione quadrata; tale sezione è ben nota per essere un oscillatore *soft* rispetto all'incipiente instabilità, mentre la stessa sezione ruotata per un angolo di attacco pari a $\alpha = 90^\circ$, cioè $SR = 0.67$, è generalmente considerato un oscillatore *hard*. I risultati ottenuti in galleria del vento hanno mostrato diversi tipi di curve di risposta che cambiano dipendentemente dal modello sezionale utilizzato; talvolta è stato osservato il manifestarsi di una risonanza super-armonica ad un terzo della velocità critica di risonanza. Misure in flusso turbolento hanno messo in luce un ritardo nella velocità di innesco dell'instabilità, sia in regime di interazione con VIV sia di galoppo, sopprimendo le vibrazioni per alti valori di intensità di turbolenza e scala integrale.

Negli esperimenti in canaletta si è registrata una risposta in ampiezza e frequenza molto influenzata dal valore completamente differente di m^* , ricordando una simile differenza riportata per il cilindro circolare nel passaggio fra test in aria e acqua, sebbene per questo solo la risposta in distacco di vortici sia possibile. Anche l'effetto del retrocorpo è risultato molto marcato, dal momento che il rettangolo con $SR = 0.67$ risponde in maniera completamente diversa, tuttavia rimanendo un oscillatore *soft*, diversamente da quanto accade in flusso d'aria. Ulteriori test sulla variazione del fattore di massa hanno colmato vuoti di letteratura per queste sezioni rettangolari, a valori molto bassi di quest'ultimo, fin'ora mai sperimentati.

Infine, nonostante sia stata dedicata una notevole cura nella determinazione sperimentale dei parametri cui il modello è sensibile, i risultati finali non sono soddisfacenti, mostrando una buona capacità del modello per l'interazione nel predire la velocità di innesco, risultando d'altra parte scarsa l'accuratezza nel riprodurre la risposta sperimentale in ampiezza nel tratto post-critico.

Zusammenfassung

Die vorliegende Dissertation beschäftigt sich mit der Interaktion zwischen wirbelerregten Querschwingungen und der Galloping Instabilität von rechteckigen Körpern mit geringem Streckungsverhältnis SR (Verhältnis von Breite zur Höhe). Der Interaktionsmechanismus beider Phänomene wurde für einen breiten Bereich von Reynoldszahlen (Re) und Massenverhältnissen (m^*) untersucht. Damit wurden laminare und turbulente Strömungszustände sowie Fluide, wie zum Beispiel Luft und Wasser, abgedeckt. Diese Art von strömungsinduzierten Schwingungen entsteht für bestimmte Kombinationen aus aerodynamischen und strukturendynamischen Zuständen.

Die Dissertation gliedert sich dabei in zwei Teile, die sich mit wissenschaftlichen Erkenntnissen und Bemessungsvorschlägen beschäftigen. Im ersten Teil werden Untersuchungen am rechteckigen Körper vorgestellt. Diese Experimente wurden sowohl im Wind- als auch im Wellenkanal durchgeführt, um das Massenverhältnis m^* und die Reynoldszahl Re der Strömung zu berücksichtigen. Im zweiten Teil wurde ein Modell vorgeschlagen, um die Interaktion zwischen wirbelerregten Querschwingungen und Galloping zu prognostizieren. Trotz der großen Anzahl an Untersuchungen blieben dennoch Fragen offen, um das komplette Spektrum an beobachteten Antworten des Systems abdecken zu können. Im Gegensatz zu bestehenden Studien aus der Literatur an quadratischen Körpern ($SR = 1$), hat die vorliegende Arbeit Untersuchungen an rechteckigen Körpern mit $SR = 3/2$ (beschrieben als weiche Schwinger) und $SR = 2/3$ (harte Schwinger) zum Gegenstand.

Die Ergebnisse unter Luftströmung zeigen variierende Amplitudenverläufe in Abhängigkeit des Modellquerschnitts. Außerdem werden superharmonische Resonanzen bei einem Drittel der karmanschen Resonanzgeschwindigkeit beobachtet, die mit Ergebnissen aus der Literatur übereinstimmen. Die Experimente unter turbulenter Strömung zeigen eine Verschiebung der Einsatzgeschwindigkeit hin zu höheren Werten, mit oder ohne Interaktion mit den wirbelerregten Querschwingungen. Amplituden unterhalb eines höheren Turbulenzgrades und Integrallängenmaßes werden abgemindert.

Versuche im Wellenkanal zeigen, dass die Antwort hinsichtlich der Amplitude und der Frequenz stark vom Massenverhältnis m^* abhängig ist. Dieser Effekt wurde mehrmals in der Literatur für zylindrische Körper beschrieben. Auch das Heckteil zeigt einen großen Einfluss, denn für den Fall $SR = 2/3$ wirkt das Verhältnis im Gegensatz zum Windkanal als weicher Schwinger.

Experimente mit variierenden Massenverhältnissen m^* liefern wertvolle Information. Dies gilt insbesondere für die Streckungsverhältnisse $SR = 3/2$ und $2/3$, da für diese Fälle keine Studien mit niedrigen Werten von m^* in der Literatur vorhanden sind. Schließlich wurden numerische Simulationen durchgeführt, um die experimentellen Untersuchungen zu verifizieren. Trotz der großen Anzahl an untersuchten Parametern im Wind- und Wellenkanal erweist sich das numerische Modell lediglich als geeignet, die Einsatzgeschwindigkeit zu prognostizieren, wohingegen das Modell ungeeignet ist, die Schwingungsamplitude im überkritischen Bereich zu prognostizieren.

Acknowledgements

It seems impossible to hold in once the whole amount of people which supported me, and to thank them all in writing. But that's the life, it's made of choices and these are mine; however, I'll begin by thanking my parents, for the unshakable support they always gave me.

I want to thank my Italian advisor, Prof. Gianni Bartoli, for the scientific and, when needed, financial support he provided during the last five years, and for his valuable suggestions during the course of the thesis, but even before, as a student who decided to apply for a Ph.D. position. He taught me to look at the problems from different perspectives always widening the sight to have a comprehensive view.

I thank as well my German advisor Prof. Klaus Thiele for the availability always showed me during the last three years. He's always been ready to let me see how to solve problems by decomposing them in simple pieces. Thanks also to Mathias Clobes, for his help and enthusiasm in wind kanal testing at Stahlbau, and my friend Hodei for the pleasant time we had in the department and laboratory; he always showed me consideration and respect, which are of course reciprocal.

I wish also to extend my thanks and gratitude to Prof. John Sheridan who gave me the opportunity to have one the most valuable experience I ever had, hoping it won't be the best I'll ever have, and to Prof. David Lo Jacono as well: they were always available to help and support me in so many ways. Thanks also to the workshop guys, to Nat in particular, but also Andrew and Hugh, for being so meticulous in constructing my models and appendices. A heartfelt thanks goes especially to András, Lawrence and Jisheng which became friends to me, besides having supported me during my stay at *WCLab*.

It goes without saying that I have to thank my colleagues in *CRIACIV* which are friends to me. So thank you Andrea, Luca, Davide for the happy days we had and for your companionship, both in- and outside the laboratory during the last five years. A special thanks goes to Ninni for the passionate discussion about job and not only, for the extremely frank opinions and nice 'prophecies', and, last but not least to Claudio, who has been simply an example for me, in work as well as in life. I'm sure he won't like the feeling these words of mine will give him, he's too modest. That's way I thank him twice.

I would like also to thank Cambridge University Press and ELSEVIER for the permissions of reproduce data coming from Journal of Fluid Mechanics and Journal of Wind Engineering and Industrial Aerodynamics; a special thank goes to Jisheng Zhao for his courtesy in sharing even unpublished data.

Contents

Abstract	i
Sommario	iii
Zusammenfassung	iv
Acknowledgements	v
List of Figures	xi
List of Tables	xxi
Abbreviations	xxiii
Physical Constants	xxv
Symbols	xxvii
1 Introduction	1
1.1 FIV of low side ratio rectangular cylinders	1
1.2 Motivations	2
1.3 Structure of the Thesis	3
2 Interaction VIV-galloping: a selective review	5
2.1 Introduction	5
2.2 Vortex-induced vibrations and lock-in	6
2.2.1 Flow past a stationary circular cylinder	6
2.2.2 Vortex-induced vibrations	9
2.2.2.1 Synchronization	11
2.3 Galloping	14
2.3.1 Nonlinear Quasi-Steady model for galloping	15
2.4 Afterbody effects and formation mechanism in rectangles of low side ratios .	20
2.5 Turbulence effect	24
2.6 Interaction VIV-galloping	24
2.6.1 Velocity and side ratio role on interaction	26
2.6.2 Quenching-effect	29

2.7	Chapter summary	30
3	Experimental methodology	
	Part. 1 - Wind tunnels testing	31
3.1	Introduction	31
3.2	Stahlbau <i>WK</i> experimental campaign	32
3.2.1	Static tests	33
	Static rig (B_s)	33
3.3	CRIACIV <i>WT</i> experimental campaign	36
3.3.1	Flow system and sectional models	36
3.3.2	Static tests	38
	Static rig 1 (F_{s1})	38
	Static rig 2 (F_{s2})	40
3.3.3	Aeroelastic tests	44
	Springs rig (F_{d1})	44
	Blades rig (F_{d2})	45
	3.3.3.1 Free-decay test	46
	3.3.3.2 Smooth flow	48
	3.3.3.3 Turbulent flow	59
3.4	Chapter summary	61
4	Experimental methodology	
	Part. 2 - Water channel testing	65
4.1	Introduction	65
4.2	FLAIR <i>WC</i> experimental campaign	65
4.2.1	Flow system and sectional models	65
4.2.2	Rigs and instrumentation	68
4.2.3	Static tests	70
	Static rig 1 (M_{s1})	71
	Static rig 2 (M_{s2})	71
4.2.4	Hydroelastic tests	76
	4.2.4.1 Free-decay test	78
	4.2.4.2 Angle of attack study (α -study)	83
	4.2.4.3 Mass ratio variation study (m^* -study)	88
4.3	Chapter summary	91
5	Modelling of the VIV-galloping interaction	93
5.1	Introduction	93
5.2	VIV and galloping modelling in literature	93
5.3	Brief review on interaction VIV-galloping models in literature	102
	5.3.1 Tamura & Shimada's model (1987) - <i>TS</i>	106
5.4	Implementing <i>TS</i> model for $SR = 1$	107
5.5	Rotational rig testing	109
5.6	Implementing <i>TS</i> model for $SR = 1.5$	114
5.7	Chapter summary	117
6	Discussion	123
6.1	Introduction	123
6.2	Comparing experimental data in air & water flow	123

6.2.1	Results for each SR	125
6.2.2	Comprehensive results	130
6.3	Framework for low side ratio rectangular cylinder	131
6.4	Chapter summary	132
7	Conclusions	135
7.1	Main contributions of the present work	135
7.2	Recommendations for future work and outlooks	137
A	Aerodynamics characteristics for rectangular sharp edged cross-sections of low side ratio	139
B	Instrumentation technical characteristics	143
C	Hydroelastic tests' extensive results	147
	Bibliography	181

List of Figures

2.1	Bluff-Body Aerodynamics. [reproduced from Matsumoto (1996)]	6
2.2	Sharp edged bluff-bodies aerodynamics characteristics. [from Takeuchi and Matsumoto (1992)]	6
2.3	Re -dependent regimes of flow around a smooth, circular cylinder in steady flow. [from Sumer and Fredsøe (1997)].	7
2.4	Picture and interpretation of the flow in the near wake of a stationary cylinder in a flow starting from rest. Sequence of events begins at (a) and continues to (f). [from Perry <i>et al.</i> (1982)].	8
2.5	Definition sketch for cross-flow VIV of a circular cylinder. The cylinder undergoes free vibrations constrained in the transverse y direction to the free-stream U in x direction.	10
2.6	Schematic illustrations of frequency response in air and water with regard to cross-flow vibrations. [from Sumer and Fredsøe (1997)]	12
2.7	Amplitude and frequency responses of VIV of a circular cylinder. \circ indicate $m^* = 248$ and $\zeta = 0.00103$ ($m^*\zeta = 0.255$) by Feng (1968) while \bullet represent $m^* = 2.4$ and $\zeta = 0.0045$ ($m^*\zeta = 0.011$). [reproduced from Khalak and Williamson (1997)]	12
2.8	Model stack nondimensional amplitude response of a circular cross-section for different values of structural damping ($Re < Re_{cr}$). (Wooton, 1969).	13
2.9	Definition sketch for cross-flow galloping of a square cylinder moving in y direction with velocity \dot{y} , hence subject to the relative, or apparent, velocity U_{rel}	16
2.10	Lateral force coefficient vs. apparent angle of attack for a square sectional model. \circ : experiment (Parkinson and Smith, 1964), $Re = 22300$, —: 7 th order polynomial approximation using original paper coefficients ($A_1 = 2.69$, $A_3 = 168$, $A_5 = 6270$, $A_7 = 59900$).	18
2.11	Amplitude response of a square cylinder experiencing galloping ($f_n = 6.01$ Hz, $n = 4.3 \cdot 10^{-4}$, $\zeta = 0.00196$, $Re = 4000 \div 20000$) calculated with quasi-steady Parkinson's nonlinear model. —: QS -model stable amplitudes (Y_S) increasing flow velocity ($Y_0 = 0.05$); \cdots : decreasing flow velocity ($Y_0 = 2$); \bullet : unstable limit cycle; \blacksquare : resonance velocity ($U_r^* \approx 0.35$); - - -: Parkinson and Smith's rule of thumb from experimental results ($Y_S = 0.3 \cdot U$).	19
2.12	Unified results for drag and base pressure coefficients. C_D (only markers): \triangle Nakaguchi <i>et al.</i> (1968), \times Bearman and Trueman (1972), \blacksquare Fage and Johansen (1927) on a flat plate, \circ Courchesne and Laneville (1982). C_{pb} (markers & coloured lines): $-\triangle-$ Nakaguchi <i>et al.</i> (1968), $-\times-$ Bearman and Trueman (1972). - - - reference line for the critical section $\bar{S}R = 0.62$	21
2.13	Mean oil flow patterns around rectangular models of SR equal to 0.25 (<i>left</i>), 0.64 (<i>center</i>) and 1.75 (<i>right</i>). [partially reported from Laneville and Yong (1983)]	22

2.14	Near wake vortex formation region as a filament line representation for a two-dimensional low side ratio rectangular cylinder; the upper (adjacent) vortex is on the verge to be shed while the lower one (opposite) has still to start growing up. [reproduced and revisited from Laneville and Yong (1983)]	23
2.15	Interaction sketch: — separated phenomena, - - - interaction VIV-galloping.	25
2.16	response curves of a square section differently damped (<i>left</i>) and for a $SR = 1.50$ section (<i>right</i>). - - -: resonance velocity, big empty markers: correspondent theoretical U_g^* derived from Smith (1962) and Parkinson and Wawzonek (1981), big filled markers: theoretical U_g^* proposed with the value of A_1 derived from present static tests (see Ch. 3).	27
3.1	View of the <i>Stahlbau</i> Boundary Layer Wind Tunnel (Windkanal) in Braunschweig. [by courtesy of Dr.-Ing. Hodei Aizpurua Aldasoro]	32
3.2	Schematic lateral view of the windkanal; note that the test section utilized during measurements is the number one. [by courtesy of Dr.-Ing. Hodei Aizpurua Aldasoro]	33
3.3	Side view of the B_s static test rig composed by the three force sensors linked to the light and rigid aluminium arm sustaining the model.	34
3.4	View from the inside of the WK on a model end anchor point in which is visible the elliptical carbon fibre end plate.	34
3.5	Results of drag (<i>left</i>) and lift (<i>right</i>) coefficients for H53 tested with B_s rig, $Re = 10.68 \cdot 10^5$.	35
3.6	Re -dependency for the lateral force coefficient C_{F_y} , for H53 tested with B_s rig.	35
3.7	Evaluation of A_1 parameter from the lateral force coefficient C_{F_y} , for a $Re = 10.68 \cdot 10^5$.	35
3.8	View of the <i>CRIACIV-DICeA</i> Boundary Layer Wind Tunnel in Prato.	36
3.9	Schematic view of the wind tunnel after the last survey conducted by the author (without office rooms and workshop); position 4 indicate the static and aeroelastic test section, while the symbol placed in the up-right position indicates the snapshot point of Fig. 3.8	37
3.10	Turbulence intensity variation by increasing flow velocity determined through hot-wire anemometry. [data recorded on December 2014]	37
3.11	(<i>left</i>) F_{s1} static test rig render view, with the position of the load cells with a generic cross-sectional bridge model suspended; (<i>right</i>) render view of the F_{s2} rig with the force balances connected to the rigid frames, without any sectional model suspended.	38
3.12	(<i>top</i>) Results in terms of drag (<i>left</i>) and lift (<i>right</i>) coefficients for D77; the dashed line represents the linear regression of the lift around $\alpha = 0^\circ$, while the A_1 term is obtained from Eq. 2.21. (<i>bottom</i>).	39
3.13	(<i>top</i>) D77 sectional model's power spectral density of lift coefficient (S_{LL}) and (<i>bottom</i>) pressure coefficient at the midpoint of the lower side (S_{pp}), for four wind speeds; dominant peaks represent the St chosen value for $SR = 1.5$.	40
3.14	Front view and zooming on one side of the D30 model in correspondence of the junction with the balance.	41
3.15	(<i>left</i>) D77, (<i>center</i>) D30 and (<i>right</i>) D45: hot-wire anemometry results performed in different velocity ranges; the dashed line is placed in correspondence of the mean values in the range of velocity giving reliable values though the chosen values derive from spectral analysis.	41
3.16	Results of drag (<i>left</i>) and lift (<i>right</i>) coefficients for D77 tested with F_{s2} rig, $Re = 147095$.	42

3.17	<i>Re</i> -dependency for the lateral force coefficient C_{F_y} , for D77 tested with F_{s2} rig.	42
3.18	Evaluation of A_1 parameter from the lateral force coefficient C_{F_y} , for a $Re = 14.71 \cdot 10^4$	42
3.19	Results of drag (<i>left</i>) and lift (<i>right</i>) coefficients for D30 tested with F_{s2} rig, $Re = 57455$	42
3.20	<i>Re</i> -dependency for the lateral force coefficient C_{F_y} , for D30 tested with F_{s2} rig.	43
3.21	Evaluation of A_1 parameter from the lateral force coefficient C_{F_y} , for a $Re = 57.45 \cdot 10^3$	43
3.22	Results drag (<i>left</i>) and lift (<i>right</i>) coefficients for D45 tested with F_{s2} rig, $Re = 85722$	43
3.23	<i>Re</i> -dependency for the lateral force coefficient C_{F_y} , for D45 tested with F_{s2} rig.	43
3.24	Evaluation of A_1 parameter from the lateral force coefficient C_{F_y} , for a $Re = 85.72 \cdot 10^3$	43
3.25	(<i>left</i>) View of the <i>springs rig</i> F_{d1} from the mounted D77 model rear towards the tunnel inlet; (<i>right</i>) close-up view on one side of the rig showing the suspension arm and the springs mounting system.	44
3.26	(<i>left</i>) View of the <i>blades rig</i> F_{d2} from the mounted D77 model rear towards the tunnel inlet; (<i>right</i>) render view of the test rig without any model mounted.	45
3.27	(<i>left</i>) plunging window on which the MULS analysis has been applied; (<i>right</i>) MULS reconstructed signal superimposed to the windowed plunging signal.	46
3.28	F_{d1} aeroelastic response curves in terms of nondimensional amplitude <i>rms</i> D77 cases A1÷A7: light blue coloured markers, namely A6 and A7 ones, are related to the test cases not experiencing the interaction, but just a resonance.	52
3.29	Close-up window on the critical velocity range. [data already published in Mannini <i>et al.</i> (2013)].	52
3.30	Reference curves and velocity points for which nondimensional displacements are proposed for D77-A.	53
3.31	D77-A1 [■] (<i>left</i>): $U/U_r = 0.98$: modulations around U_r . (<i>center</i>): $U/U_r = 1.11$: higher reduced velocity. (<i>right</i>): $U/U_r = 1.2$: change in time trace's profile.	53
3.32	D77-A4 [●] (<i>left</i>): $U/U_r = 1.37$: velocity in the mid-unstable branch. (<i>center</i>): $U/U_r = 1.53$: change of time trace's profile. (<i>right</i>): $U/U_r = 1.69$: point in the kink.	53
3.33	D77-A5 [◆] (<i>left</i>): $U/U_r = 1.22$: point after U_r . (<i>center</i>): $U/U_r = 1.35$: higher reduced velocity but different time trace's profile. (<i>right</i>): $U/U_r = 1.67$: point in the kink.	53
3.34	F_{d1} aeroelastic response curves in terms of nondimensional amplitude <i>rms</i> D77 cases B1÷B7.	54
3.35	Close-up window on the secondary resonance, where coloured markers (B1÷B4) are related to the test cases experiencing it.	54
3.36	Reference curves and velocity points for which nondimensional displacements are proposed for D77-B.	55
3.37	D77-B1 [●] (<i>left</i>): $U/U_r = 0.46$, peak of the secondary resonance. (<i>center</i>): $U/U_r = 1.04$: instability onset. (<i>right</i>): $U/U_r = 1.49$: mid-branch of the instability.	55

3.38	D77-B6 [■] (<i>left</i>): $U/U_r = 1$: instability onset. (<i>center</i>): $U/U_r = 1.27$: mid-branch of the instability. (<i>right</i>): $U/U_r = 1.49$: highest reduced velocity.	55
3.39	F_{d1} aeroelastic response curves in terms of nondimensional amplitude <i>rms</i> D30 cases B1÷B7.	56
3.40	Close-up window on the resonance region: red × and + markers (D30-B6 and B7) are related to test cases in which interaction occurs.	56
3.41	Reference curves and velocity points for which nondimensional displacements are proposed for D30-B.	57
3.42	D30-B1 [●] (<i>left</i>): $U/U_r = 0.99$: galloping-type instability onset. (<i>center</i>): $U/U_r = 1.27$: higher reduced velocity. (<i>right</i>): $U/U_r = 2.32$: mid-branch of the instability.	57
3.43	D30-B4 [◆] (<i>left</i>): $U/U_r = 1.33$: beginning of stable zone. (<i>center</i>): $U/U_r = 4.78$: point before U_g^* (note that $\Lambda = 7.4$). (<i>right</i>): $U/U_r = 9.93$: mid-branch of galloping.	57
3.44	D30-B6 [▲] (<i>left</i>): $U/U_r = 1.00$: phenomenon onset. (<i>center</i>): $U/U_r = 1.47$: mid-linear trend. (<i>right</i>): $U/U_r = 3.12$: second steeper branch of the instability.	57
3.45	D30-B7 [■] (<i>left</i>): $U/U_r = 1.56$: peak of the first increasing branch. (<i>center</i>): $U/U_r = 2.86$: end of the <i>plateau</i> . (<i>right</i>): $U/U_r = 4.87$: highest velocity point.	58
3.46	F_{d1} aeroelastic response curves in terms of nondimensional amplitude <i>rms</i> D45 cases B1 and B2.	58
3.47	(<i>left</i>) View from the rear towards the tunnel inlet of the <i>blades rig</i> F_{d2} , with mounted D30 aluminium model and the turbulence grid type G1; (<i>right</i>) closer view of the G2 grid type.	59
3.48	F_{d2} aeroelastic turbulent flow response curves in terms of nondimensional amplitude <i>rms</i> D77 cases T1÷T8 (Tab. 3.7).	62
3.49	Close-up window on the secondary resonances range; T1÷T3 and T7 show the secondary resonance starting at $U_r/3$. Superimposed empty markers (○, △, □ respectively for T1, T2, T3) denote the response by decreasing wind speed.	62
3.50	F_{d2} aeroelastic turbulent flow response curves in terms of nondimensional amplitude <i>rms</i> D30 cases T1÷T8 (Tab. 3.8).	63
3.51	Close-up window on the T1 and T2 instability onset velocity. Filled smaller markers denote the response by decreasing wind speed while the dashed line is placed in correspondence of the <i>QS</i> -galloping velocity.	63
4.1	View of the <i>FLAIR</i> Water Channel Laboratory. [by courtesy of Dr. Jisheng Zhao]	66
4.2	Schematic view of the water channel . [from Zhao (2012)]	66
4.3	(<i>left</i>) D25 and D24/D37 models; (<i>right</i>) view of a model mounted on the rig suspended above the perspex platform.	67
4.4	Air-bearings system view.	69
4.5	Circuit scheme of the LVDT transducer.	70
4.6	(<i>left</i>) static rig in M_{s1} configuration obtained by clamping the <i>AB</i> system; (<i>right</i>) view of submerged rectangular aluminium model attached to the force balance.	71
4.7	M_{s1} results in terms of C_{F_y} for the entire range of imposed α	72
4.8	View from below <i>AB</i> system towards the rotor rig.	72
4.9	Results in terms of C_{F_y} for the entire range of α imposed with M_{s2}	73
4.10	<i>Re</i> -dependency for the lateral force coefficient C_{F_y} , for D24 tested with M_{s2} rig (<i>left</i>) and for D37 (<i>right</i>).	74

4.11	Evaluation of A_1 parameter from the lateral force coefficient C_{F_y} , for the maximum Re of D24 model (<i>left</i>) and D37 (<i>right</i>) tested with M_{s2} rig.	74
4.12	St determined by changing angle manually (<i>top</i>), and automatically using the rotational rig (<i>bottom</i>).	75
4.13	(<i>left</i>) Positioning of the hot-film in the near wake of the body; (<i>right</i>) St results from hot-film anemometry.	76
4.14	St results for the highest Re for different techniques.	77
4.15	Schematic for force measurement correction [taken from Zhao (2012)].	77
4.16	An example of free decay tests of a $SR = 1.5$ rectangular cylinder with $m^* = 2.236$, that is D24-W1 test case reported in Tab. 4.2: (<i>a</i>)- <i>column</i> plots show free decay test in air while (<i>b</i>)- <i>column</i> ones show free decay test in still water. The <i>top row</i> plots report the displacements time traces showing the decay from the y_0 value (note that several test imposing different initial displacements were tested obtaining in practice always the same values in terms of characteristic frequency and damping of the system). The <i>middle row</i> shows the decay rate based on a logarithmic decrement algorithm, while the <i>bottom row</i> shows FFT calculation of the PSD normalised with respect to the spectrum peak.	80
4.17	(<i>top</i>) Reduced maximum amplitude response (A_{max}^*) and (<i>bottom</i>) dominant reduced body displacements frequency response ($f_{y,max}^*$) of D24 [\circ] superimposed to the response of square cylinder H25 [\blacksquare] (taken from Nemes <i>et al.</i> (2012)), vs. reduced velocity, U/U_r	82
4.18	(<i>top</i>) Reduced maximum amplitude response (A_{max}^*) and (<i>bottom</i>) dominant reduced body displacements frequency response ($f_{y,max}^*$) of D37 (\diamond) superimposed to the response of square cylinder H25 [\blacksquare] (taken from Nemes <i>et al.</i> (2012)), vs. reduced velocity, U/U_r	82
4.19	Test rig model sketch for cross-flow motion of a $SR = 1.5$ rectangular cylinder with variable angles of attack. The cylinder undergoes free vibrations constrained in the y direction, transversal to the free-stream U in x direction, being it allowed to be rotated of α , resembling a $B/D = 1.5$ rectangular body invested by a variable U_{rel} incidence flow velocity. D_f and B_f are referred to the body depth and width seen by the flow, being the first the only one of interest calculated as $D_f = D \cdot \cos(\alpha) + B \cdot \sin(\alpha)$	83
4.20	α -study comprehensive 2D and 3D results.	84
4.21	Different view angle for the same plot proposed in Fig. 4.20. <i>bottom right</i> , useful for D37 configuration.	85
4.22	Amplitude (<i>top</i>) and lift coefficient (<i>bottom</i>) nondimensional responses of $\alpha = 0^\circ$ case (D24). f_{vs} harmonics of order 1 (St) and 2, are indicated respectively in red continuous and blue dotted line while in orange dashed lines (<i>top</i> plot), the crossing point between two distinct linear trends is detected corresponding to the interacting super-harmonics of f_{vs} (order 1.5) and the dominant one in the instability branch (order 6).	86
4.23	Amplitude (<i>top</i>) and lift coefficient (<i>bottom</i>) nondimensional responses of $\alpha = 90^\circ$ case (D37). f_{vs} harmonics of order 1 (St) and 2, are indicated respectively in red continuous and blue dotted line while in orange dashed lines (<i>top</i> plot), the crossing point between two distinct linear trends is detected.	87

4.24	Test rig model sketches for cross-flow motion of the $SR = 1.5$ D24 (<i>left</i>) and $SR = 0.67$ D37 (<i>right</i>) rectangular cylinder. The cylinders undergo free vibrations constrained in the transverse y direction with respect to the free-stream U (x direction), while its mass ratio is increased by optional added masses.	88
4.25	(<i>top</i>) Reduced amplitude response (A_{10}^*), and (<i>bottom</i>) <i>rms</i> of the nondimensional amplitude (y/D) of D24 for the 7 mass ratios investigated, against reduced velocity (U/U_r).	90
4.26	(<i>top</i>) Reduced amplitude response (A_{10}^*), and (<i>bottom</i>) <i>rms</i> of the nondimensional amplitude (y/D) of D37 for the 3 mass ratios investigated, against reduced velocity (U/U_r).	90
5.1	Birkhoff-type wake-oscillator sketch presented in Tamura and Matsui (1979).	97
5.2	Funakawa (1969) extrapolated plot: in particular the curve was taken from Swanson (1961), Fig. 2. <i>top</i> (curve <i>a</i> with $Re = 3.58 \cdot 10^4$). The ratio U/V is the rotational-to-flow velocity ratio.	98
5.3	Sketch for the visualization of the separation point position in case $\Delta = 0.5$.	99
5.4	Fluctuation of the length and the angular displacement of the wake oscillator [Fig. 2 in Tamura and Matsui (1979)].	101
5.5	Birkhoff-type wake-oscillator sketch presented in Tamura and Shimada (1987).	106
5.6	Present results for the square section (<i>TS present</i> , solid line with markers) compared with the original ones in Tamura and Shimada (1987) (<i>TS paper</i> , dotted lines), galloping model implemented as already shown in Ch. 2 (<i>QS present</i> , dashed line) and Wawzonek experimental results (<i>WZ</i> , \circ and \square markers).	107
5.7	Second stable branch obtained for a constant Y_0 : by coloured filled triangle markers placed on $\nu = 1.6$ vertical dashed line are indicated the different values of Y_0 chosen, whose time traces are proposed in Fig. 5.8.	108
5.8	Different stable amplitude values Y_s obtained for $\nu = 1.6$ by changing the initial amplitude Y_0 respectively equal to 0.1 (<i>left</i>), 0.4 (<i>center</i>) and 0.8 (<i>right</i>); with filled red circles the values of Y_s are indicated.	108
5.9	A flock of sheep encounters a carousel demonstrating the Magnus effect.	110
5.10	Summary of previous lift coefficient vs. velocity ratio data. [reproduced from Swanson (1961)]. (a) ideal fluid (potential flow, $C_L = 2\pi\Delta$, $AR = \infty$, $Re = \infty$); (b) Thom (1934) ($AR = 12, 26$, $Re = 5.3 \div 8.8 \cdot 10^3$, end-disks of diameter $d_e = 3D$); (c) Reid (1924) ($AR = 13.3$, $Re = 3.9 \div 11.6 \cdot 10^4$); (d-i) Prandtl and Tietjens (1934) ($AR = 4.7$, $Re = 5.2 \cdot 10^4$, end-disks of diameter $d_e = 1.7D$ (<i>d</i>) and no disks (<i>i</i>)); (e) Thom (1925) ($AR = 8$, $Re = 1.6 \cdot 10^4$); (f) Swanson (1961) ($AR = \infty$, $Re = 3.5 \div 30 \cdot 10^4$); (g-h) Thom and Sengupta (1932) ($AR = 5.7$, $Re = 5.3 \div 8.8 \cdot 10^3$, rough sanded (<i>g</i>) and smooth <i>h</i> surface); (j) Schwartzemberg (<i>unpublished</i>) ($AR = 4.5$, $Re = 5.4, 18.6 \cdot 10^4$); (k) Swanson (1961) ($AR = 2$, $Re = 5 \cdot 10^4$, continuous end sections).	111
5.11	Birkhoff-type wake-oscillator sketch utilized in the experiments.	112
5.12	Examples for a measurement of varying lift coefficient for $U_{min} \leftrightarrow U \approx 0.04 \text{ ms}^{-1}$ for D25 (<i>left</i>) or D24/D37 (<i>right</i>) section mounted on the rotor rig.	112
5.13	Rotational rig study comprehensive results. U assumes mean values of 0.09, 0.15, 0.20, 0.25 ms^{-1} respectively from the top to the bottom. Plots reported in <i>left column</i> refer to D25 while <i>right column</i> to D24/D37 results.	118
5.14	$Re = 0.77 \div 4.63 \cdot 10^3$. D25 results for Magnus-related parameter. [see Fig. 5.15 for caption].	119

5.15	$Re = 0.99 \div 5.92 \cdot 10^3$. (<i>left</i>) Entire set of flow velocities results for D24/D37 rotating section: the value of the Magnus-related parameter is obtained through a linear regression obtained by collapsing all the data in only one vector. (<i>right</i>) Velocity ratio window selected to extrapolate the value to be used in numerical modelling.	119
5.16	Different polynomial approximations for the lateral force coefficient of some rectangular cylinder sectional model. [see Tab. 5.2]	120
5.17	Sensitivity study on TS -model parameters for the first study (Stage 1). [test cases ref. Tab. 5.3]	121
5.18	Final results on the test cases investigated after having empirically defined the model parameters. [see Tab. 5.4]	122
6.1	Experimental results in air and water for rectangular cylinder with $SR = 0.67$.	125
6.2	Experimental results reported in the reference literature, in air and water, for the square section. <i>Air flow</i> : Smith (1962) results are relative to a $m^* = 1163$ and damping ratios respectively [\blacklozenge] 1.07 and [\diamond] 1.96, whose relative QS -galloping theoretical velocity is indicated with markers and dashed lines [- -]. <i>Water flow</i> : Bouclin (1977) results are relative to [\circ] $m^* = 5.38$ with $\zeta = 0.0044$, [\bullet] $m^* = 9.69$ with $\zeta = 0.0044$ and [\times] $m^* = 15.24$ with $\zeta = 0.00489$; Zhao <i>et al.</i> (2014) reported a square cylinder having $m^* = 2.64$ with $\zeta = 0.00258$ [\blacksquare], while D25 case is relative to $m^* = 15.00$ with $\zeta = 0.00131$ [\square]. D25 square data (unpublished) are available by courtesy of Dr. Jisheng Zhao.	126
6.3	Experimental present and literature results in air and water for rectangular cylinder with $SR = 1.5$. <i>Air flow</i> : Smith (1962) results are relative to a $m^* = 857$ and damping ratios respectively [$+$] 1.03 and [\times] $5.94 \cdot 10^{-3}$, for which galloping instability onset velocity is indicated with markers at zero-amplitude and dashed vertical lines [- -]. <i>Water flow</i> : dynamical characteristics of the present tests sectional models are the same already mentioned.	127
6.4	(<i>top</i>) Competition zone found during hysteresis tests for D24-W1; (<i>bottom</i>) hysteresis test for D37-W1 section.	128
6.5	Experimental results from literature in air and water for rectangular cylinder with $SR = 2$. <i>Air flow</i> : Santosham (1966) reported $m^* = 2093$ for ζ respectively [\blacklozenge] 0.695 and [\diamond] $4.1 \cdot 10^{-3}$; Smith (1962) gave results for a $m^* = 643$ with ζ respectively [\circ] 1.03, [\bullet] 2.80 and [\times] $5.94 \cdot 10^{-3}$. With markers and dashed lines [- -] is indicated the relative QS -galloping theoretical velocity. <i>Water flow</i> : Bouclin (1977) proposed a rectangle having [$+$] $m^* = 11.52$ with $\zeta = 3.26 \cdot 10^{-3}$	129
6.6	Comprehensive overview of air and water experimental results on rectangular cylinder with $SR = 1.5$. Air flow (Feng (1968) [\bullet] $m^* = 248$ and $\zeta = 0.00103$) and water flow (Khalak and Williamson (1997) [\circ] $m^* = 2.4$ and $\zeta = 0.011$) data on the circular cylinder are superimposed together with Bouclin (1977) $SR = 2$ rectangle of $m^* = 11.52$ [$+$]. For square data the reader can refer to the caption of Fig. 6.2.	133
6.7	Comprehensive overview of air and water experimental results on rectangular cylinder with $SR = 0.67$. Air flow (Feng (1968) [\bullet] $m^* = 248$ and $\zeta = 0.00103$) and water flow (Khalak and Williamson (1997) [\circ] $m^* = 2.4$ and $\zeta = 0.011$) data on the circular cylinder are superimposed. For square data the reader can refer to the caption of Fig. 6.2.	134

B.1	Picture of the HBM S2M force sensor.	144
B.2	Picture of the ES Europe 535 QD force sensor.	144
B.3	(left) View of a laser triangulator device for displacement measurement; (right) Relationship between laser output voltage and actual object distance. [reproduced from Mannini (2006)]	144
C.1	Angle of attack's study for $m^* = 2.24$: nondimensional amplitude, oscillation and lift frequencies vs. reduced velocity with respect to resonance one, for $\alpha = 0^\circ$ ($SR = 1.5$)	148
C.2	Angle of attack's study for $m^* = 2.24$: nondimensional amplitude, oscillation and lift frequencies vs. reduced velocity with respect to resonance one, for $\alpha = 1^\circ$	149
C.3	Angle of attack's study for $m^* = 2.24$: nondimensional amplitude, oscillation and lift frequencies vs. reduced velocity with respect to resonance one, for $\alpha = 2.5^\circ$	150
C.4	Angle of attack's study for $m^* = 2.24$: nondimensional amplitude, oscillation and lift frequencies vs. reduced velocity with respect to resonance one, for $\alpha = 5^\circ$	151
C.5	Angle of attack's study for $m^* = 2.24$: nondimensional amplitude, oscillation and lift frequencies vs. reduced velocity with respect to resonance one, for $\alpha = 10^\circ$	152
C.6	Angle of attack's study for $m^* = 2.24$: nondimensional amplitude, oscillation and lift frequencies vs. reduced velocity with respect to resonance one, for $\alpha = 15^\circ$	153
C.7	Angle of attack's study for $m^* = 2.24$: nondimensional amplitude, oscillation and lift frequencies vs. reduced velocity with respect to resonance one, for $\alpha = 20^\circ$	154
C.8	Angle of attack's study for $m^* = 2.24$: nondimensional amplitude, oscillation and lift frequencies vs. reduced velocity with respect to resonance one, for $\alpha = 25^\circ$	155
C.9	Angle of attack's study for $m^* = 2.24$: nondimensional amplitude, oscillation and lift frequencies vs. reduced velocity with respect to resonance one, for $\alpha = 30^\circ$	156
C.10	Angle of attack's study for $m^* = 2.24$: nondimensional amplitude, oscillation and lift frequencies vs. reduced velocity with respect to resonance one, for $\alpha = 35^\circ$	157
C.11	Angle of attack's study for $m^* = 2.24$: nondimensional amplitude, oscillation and lift frequencies vs. reduced velocity with respect to resonance one, for $\alpha = 40^\circ$	158
C.12	Angle of attack's study for $m^* = 2.24$: nondimensional amplitude, oscillation and lift frequencies vs. reduced velocity with respect to resonance one, for $\alpha = 45^\circ$	159
C.13	Angle of attack's study for $m^* = 2.24$: nondimensional amplitude, oscillation and lift frequencies vs. reduced velocity with respect to resonance one, for $\alpha = 5^\circ$	160
C.14	Angle of attack's study for $m^* = 2.24$: nondimensional amplitude, oscillation and lift frequencies vs. reduced velocity with respect to resonance one, for $\alpha = 550^\circ$	161

C.15	Angle of attack's study for $m^* = 2.24$: nondimensional amplitude, oscillation and lift frequencies vs. reduced velocity with respect to resonance one, for $\alpha = 60^\circ$	162
C.16	Angle of attack's study for $m^* = 2.24$: nondimensional amplitude, oscillation and lift frequencies vs. reduced velocity with respect to resonance one, for $\alpha = 65^\circ$	163
C.17	Angle of attack's study for $m^* = 2.24$: nondimensional amplitude, oscillation and lift frequencies vs. reduced velocity with respect to resonance one, for $\alpha = 70^\circ$	164
C.18	Angle of attack's study for $m^* = 2.24$: nondimensional amplitude, oscillation and lift frequencies vs. reduced velocity with respect to resonance one, for $\alpha = 75^\circ$	165
C.19	Angle of attack's study for $m^* = 2.24$: nondimensional amplitude, oscillation and lift frequencies vs. reduced velocity with respect to resonance one, for $\alpha = 80^\circ$	166
C.20	Angle of attack's study for $m^* = 2.24$: nondimensional amplitude, oscillation and lift frequencies vs. reduced velocity with respect to resonance one, for $\alpha = 85^\circ$	167
C.21	Angle of attack's study for $m^* = 2.24$: nondimensional amplitude, oscillation and lift frequencies vs. reduced velocity with respect to resonance one, for $\alpha = 90^\circ$ ($SR = 0.67$)	168
C.22	Mass ratio's study for $SR = 1.5$: nondimensional amplitude, oscillation and lift frequencies vs. reduced velocity with respect to resonance one, for $m^* = 2.24$	170
C.23	Mass ratio's study for $SR = 1.5$: nondimensional amplitude, oscillation and lift frequencies vs. reduced velocity with respect to resonance one, for $m^* = 3.02$	171
C.24	Mass ratio's study for $SR = 1.5$: nondimensional amplitude, oscillation and lift frequencies vs. reduced velocity with respect to resonance one, for $m^* = 3.50$	172
C.25	Mass ratio's study for $SR = 1.5$: nondimensional amplitude, oscillation and lift frequencies vs. reduced velocity with respect to resonance one, for $m^* = 4.10$	173
C.26	Mass ratio's study for $SR = 1.5$: nondimensional amplitude, oscillation and lift frequencies vs. reduced velocity with respect to resonance one, for $m^* = 6.00$	174
C.27	Mass ratio's study for $SR = 1.5$: nondimensional amplitude, oscillation and lift frequencies vs. reduced velocity with respect to resonance one, for $m^* = 7.49$	175
C.28	Mass ratio's study for $SR = 1.5$: nondimensional amplitude, oscillation and lift frequencies vs. reduced velocity with respect to resonance one, for $m^* = 9.76$	176
C.29	Mass ratio's study for $SR = 0.67$: nondimensional amplitude, oscillation and lift frequencies vs. reduced velocity with respect to resonance one, for $m^* = 2.24$	177
C.30	Mass ratio's study for $SR = 0.67$: nondimensional amplitude, oscillation and lift frequencies vs. reduced velocity with respect to resonance one, for $m^* = 3.5$	178

C.31	Mass ratio's study for $SR = 0.67$: nondimensional amplitude, oscillation and lift frequencies vs. reduced velocity with respect to resonance one, for $m^* = 9.76$	179
C.32	Mass ratio variation study (general overview) for D24-W1-7; note that the dashed line indicates the critical velocity.	180
C.33	Mass ratio variation study (general overview) for D37-W1-3; note that the dashed line indicates the critical velocity.	180

List of Tables

3.1	Characteristics of sectional models employed at Stahlbau <i>WK</i>	33
3.2	Characteristics of sectional models employed at CRIACIV <i>WT</i>	38
3.3	Test cases for plywood model (D77) in smooth flow on F_{d1} rig. [Relative stability parameter and Strouhal number are $A_1 = 5.7$ and $St = 0.106$]. . .	47
3.4	Test cases for plywood model (D77) in smooth flow on F_{d2} rig. [Relative stability parameter and Strouhal number are $A_1 = 5.8$ and $St = 0.106$]. . .	47
3.5	Test cases for aluminium model (D30) in smooth flow tested on F_{d2} rig. [Relative stability parameter and Strouhal number are $A_1 = 6.2$ and $St = 0.106$].	47
3.6	Test cases for aluminium model (D45) in smooth flow tested on F_{d2} rig. [Relative Strouhal number are $St = 0.1255$].	47
3.7	Turbulent flow and dynamic characteristics of the aeroelastic tests performed with D77 on F_{d2} : Δx denotes the distance between the grid and the longitudinal axis of the model, I_u the turbulence intensity, L_u the longitudinal turbulence length scale.	60
3.8	Turbulent flow and dynamic characteristics of the aeroelastic tests performed with D30 on F_{d2}	60
4.1	Characteristics of sectional models employed at FLAIR <i>WC</i> . Note that the immersed length L has been proposed, while reporting the total length in round brackets.	67
4.2	Test cases for aluminium model $SR = 1.5$ (D24) in smooth water flow. . . .	79
4.3	Test cases for aluminium model $SR = 0.67$ (D37) in smooth water flow. . .	80
5.1	Scheme for the VIV models available in literature.	95
5.2	Polynomial interpolation coefficients: values determined in the present work (D37, H53, D77, D30, D24 sectional models), for two different odd polynomial degrees (7^{th} and 11^{th}) are proposed together with some contributions taken by literature for square and $SR = 2$ rectangle. Present and literature correspondent values of C_{L_0} are also given. In bold are indicated the models and values object of numerical simulations.	114
5.3	Model parameters for the sensitivity study.	115
5.4	Model parameters for the sensitivity study.	117
A.1	Aerodynamic parameters and relative test conditions for the rectangular cylinder with side ratio 3:2. The aspect ratio in case of confined 2D test cases is indicated as ∞ ; in case of 3D prisms I_u and L_u are meant to be measured at the top of tower models; the asterisk * indicates that the numerical value was inferred by the Writers from a published figure; the apex + identifies the results of numerical CFD simulations.	140

A.2	Aerodynamic parameters and relative test conditions for the square cylinder. See also caption of Tab. A.1	141
A.3	Aerodynamic parameters and relative test conditions for the rectangular cylinder with side ratio 2:1. See also caption of Tab. A.1	142
B.1	Technical specifications of the HBM S2M load cell employed in B_s static tests	143
B.2	Technical specifications of the ES Europe 535 QD load cell employed in F_{s1} static tests	144
B.3	Technical specifications of the ATI Model FT-Delta force balance employed in F_{s2} static tests	145
B.4	Technical specifications of the Micro-epsilon Model OptoNCDT-1605/200 laser employed in F_{d1} and F_{d2} dynamic test rig	145

Abbreviations

2D-3D	two-three dimensional
<i>a.n.</i>	author's note
AB	air-bearing
<i>AR</i>	aspect ratio
BL	boundary layer
block.	blockage ratio
BNC	Bayonet Neill-Concelman
CFD	computational fluid dynamics
DAQ	data acquisition
DC	direct current
<i>DE</i>	differential equations
DoF	degree(s) of freedom
ECD	eddy currents damper
FFT	fast-Fuorier-transform
FIV	flow-induced vibrations
IIE	Instability-Induced Excitation
LVDT	linear variable differential transformer
MIE	Motion-Induced Excitation
MULS	modified unifying least-squares (method)
<i>ODE</i>	ordinary differential equations
PCI	peripheral component interconnect
PSD	power spectral density
<i>QS</i>	quasi-steady (theory/model)
<i>SR</i>	side ratio
<i>TS</i>	Tamura & Shimada (numerical model)
<i>TTL</i>	transistor-transistor logic
vs.	versus
VIV	vortex-induced vibrations
<i>WT</i>	wind tunnel
<i>WK</i>	windkanal
<i>WC</i>	water channel

Physical Constants

air density	ρ_a	\approx	1.15	kgm^{3-1}
water density	ρ_w	\approx	998	kgm^{3-1}
air dynamic (absolute) viscosity	μ_a	$=$	$1.85 \cdot 10^{-5}$	Nsm^{-2}
air kinematic viscosity	κ_a	$= \frac{\mu_a}{\rho_a} =$	$1.57 \cdot 10^{-5}$	$\text{m}^2 \text{ s}$
water dynamic (absolute) viscosity	μ_w	$=$	$1.002 \cdot 10^{-3}$	Nsm^{-2}
water kinematic viscosity	κ_w	$= \frac{\mu_w}{\rho_w} =$	$1.004 \cdot 10^{-6}$	$\text{m}^2 \text{ s}$

Symbols

General notations

$(\dot{\quad})$	t or τ derivative	
$(\quad)' \equiv (\quad)_{rms}$	root mean square value of the signal	
$(\bar{\quad})$	mean value of the signal	
$\mathcal{O}(\quad)$	order of magnitude	
t	time	s
B	width (oncoming flow wise)	m
D	depth (in transversal direction)	m
D_H	hydraulic diameter	m
L	model spanwise effective/immersed length	m
$SR = \frac{B}{D}$	side ratio	-
$AR = \frac{L}{B \text{ or } D}$	aspect ratio	-
f_s	sampling frequency	Hz

Flow characteristics

ρ	density	kg/m ³
μ	dynamic viscosity	Nsm ⁻²
$\kappa = \frac{\mu}{\rho}$	kinematic viscosity	m ² s
U	free-stream velocity	ms ⁻¹
u	longitudinal flow velocity component	ms ⁻¹
v	transversal flow velocity component	ms ⁻¹
w	vertical flow velocity component	ms ⁻¹
I_u	turbulence intensity	-
L_u^x	longitudinal macro-scale of turbulence	m
U_{rel}	apparent flow velocity	ms ⁻¹
U_g	galloping onset dimensional velocity	ms ⁻¹
U_r	Kármán-resonance dimensional velocity	ms ⁻¹
α	angle of attack to the relative incident flow	°
$\vec{w} = \nabla \times \frac{d\vec{r}}{dt}$	vorticity	ms ⁻¹
$\Gamma = \iint_S \vec{w} \cdot d\mathbf{S}$	circulation	m ³ s ⁻¹
f_P	pump frequency	Hz

Aerodynamics of the body

f_{vs}	frequency of vortex shedding	Hz
$C_X = \frac{F_X}{\frac{1}{2}\rho U^2 DL}$	force coefficients	-
C_L	lift force coefficient	-
C_D	drag force coefficient	-
$C_{L_0} = \sqrt{2}C'_L$	C_L at $\alpha = 0^\circ$ amplitude on a stationary body	-
C_{F_y}	coefficient of lateral force	-
A_1, A_3, A_5, \dots	polynomial coefficients for C_{F_y}	-

Dynamics of the body

k	system stiffness	Nm^{-1}
m	oscillating mass	kg
m_d	fluid-displaced mass	kg
m_A	added mass	kg
m_{add}	additional external mass	kg
c	damping	Nsm^{-1}
$f = f_{osc}$	frequency of body oscillation	Hz
$c_{cr} = 2m\omega_n$	critical damping	Nsm^{-1}
$\zeta = \frac{c}{c_{cr}}$	fraction of critical damping	-
$f_n = \frac{\omega_n}{2\pi}$	natural frequency of the body	Hz
$\omega_n = \sqrt{k/m}$	fundamental pulsance	rad s^{-1}
$n = \frac{\rho D^2 L}{2m}$	mass parameter (ref. air-flow)	-
$m^* = \frac{m}{m_d} = \frac{1}{2n} \frac{D}{B}$	mass ratio (ref. water-flow)	-

Response parameters

\bar{y}	mean of $y(t)$	m
$\hat{y}(t) = A$	oscillation amplitude	m
$y(t) = \bar{y} + \hat{y}(t)$	displacements time history signal	m
$\tilde{y}(t)$	peak values in amplitude of the $\hat{y}(t)$ signal	m
$Y = \frac{y}{D}$	nondimensional oscillation amplitude	-
Y_s	stable Y (numeric solution)	-
A^*	general nondimensional response parameter	-
A_{10}^*	mean of the top 10% of A^*	-
A_{max}^*	maximum value of A^* of e	-
$f^* = f_y^* = \frac{f}{f_n}$	frequency ratio	-
$f_L^* = \frac{fL}{f_n}$	lift coefficient frequency ratio	-
ϕ	phase angle	$^\circ$

Velocity ratios

$(\nu = f_s^*)U/U_r$	reduced velocity respect to critical	-
$U^* = \frac{U}{f_n D}$	reduced flow velocity respect to frequency	-
$\tilde{U} = \frac{U^*}{2\pi}$	reduced flow velocity respect to pulsation	-

$U_r^* = \frac{1}{St}$	Kármán-resonance reduced velocity	-
$U_g^* = 2\pi \frac{2\zeta}{nA_1}$	quasi-steady galloping reduced velocity	-
$\Lambda = \frac{U_g^*}{U_r^*}$	onset velocity ratio	-
$\Delta = \frac{v_0}{U}$	rotational-to-flow velocity ratio	-

Models parameters

$\tau = \omega t$	non-dimensional time	s
ϑ	wake-oscillator angular displacement DoF	°
β	separation point angle for a spinning cylinder	°
l_c	mass and rotation centers reciprocal distance	m
l	half length of the wake-oscillator	-
$l^* = l/D$	nondim. half length of the wake-oscillator	-
h	thickness of the wake-oscillator	m
$h^* = h/D$	nondim. thickness of the wake-oscillator	m
G	gravity centre of the wake-oscillator	-
F_{LMag}	Magnus effect induced lift force	N
\tilde{f}_m	Magnus effect parameter (Funakawa)	-
\tilde{f}	Magnus effect parameter (Tamura & Matsui)	-
v_0	tangential velocity component, $v_0(r, \vartheta)$	ms ⁻¹
$\Upsilon_i, i = 1, \dots, n$	empirical constants	-
ϵ_a	absolute tolerance	-
ϵ_r	relative tolerance	-

Characteristic numbers

$Re = \frac{UD}{\nu}$	Reynolds number	-
$Sc = Sc_{BD} = \frac{4\pi m\zeta}{\rho LBD}$	Scruton number (respect to BD)	-
$Sc_{D^2} = \frac{4\pi m\zeta}{\rho LD^2}$	Scruton number (respect to D^2)	-
$St = \frac{f_{vs} B}{U}$	Strouhal number	-
$Ma = \frac{\dot{y}}{v_{sound}}$	Mach number	-
$Fr = \frac{\dot{y}}{\sqrt{gD}}$	Froude number	-

Dedicated to my mum.

Chapter 1

Introduction

1.1 FIV of low side ratio rectangular cylinders

It is common practice to observe objects which vibrate when invested by a fluid flow; it is sufficient to think about the crown of the trees, the power line cables, the pole of a flag and the flag itself or even a submerged rope holding a boat standing inside an under-sea stream. All these examples lie under the general concept of flow-induced vibrations (FIV). The interest around FIV phenomena is lively since many centuries¹ and it has never ceased during the last one. There has been a stream of works which develops from the dawn of Aeronautics till nowadays, and the interest of the scientific community has never given up regarding such themes. When the structure motion and aerodynamic forces interact significantly, the amplitude of self-excited vibration may grow in time, diverging or not, and induce some instabilities; we commonly refer to this behaviour as ‘aeroelasticity’. Aeroelastic phenomena were initially investigated in the aeronautical field and then, after the achievement of high-rise buildings or long-span bridges, also in civil engineering. The spectrum of instabilities possibly occurring, even for the structures belonging to the latter field, results to be quite large.

The trend in the design of slender civil structures is going toward sections prone to the existence or coexistence of some aerodynamic or aeroelastic effects. In fact, if we think about the general sections of high-rise buildings and bridge decks, we can easily derive that we are referring to variable side ratio rectangular cylinders, which can effectively be prone to more than one aeroelastic phenomenon under certain conditions.

A first step is to bound the analysis to bluff-bodies aerodynamics and aeroelasticity. The bodies characterized by a non-streamlined cross-section, such as an airfoil, are classified as bluff. In a bluff section the boundary layer does not remain completely attached over the whole extent of the surface, but it is subject to separation processes. It is possible to introduce here a first dichotomy based on the type of boundary layer separation point, which can be free or fixed. In smoothly curved bodies the separation point is free to move on the surface according the local condition of the boundary layer, and its position changes according to the flow condition, such as laminar or turbulent flow (generally delayed in turbulent case), surface roughness or dynamic condition of the body (*e.g.* rotating cylinders).

¹Some drawings representing flow visualizations of the near wake behind obstacles a river are reported by Da Vinci (1828)

Conversely, sharp-edges make the boundary layer separate independently of the flow conditions; in this case the separation points are determined by the section corners. Concerning sharp-edged bodies it is useful to introduce the *side ratio*, indicated as SR , which is defined as the ratio of the body cross-sectional width (B) on the body depth seen by the incident flow (D), $SR = B/D$, whereas the *aspect ratio* represents the body length immersed in the oncoming flow (L) nondimensionalized with respect to a reference length, that is $AR = L/D$ (or sometimes B depending on which side is considered).

Side and aspect ratios, together with other characteristics such as end-conditions or Reynolds number, promote different ways in which the vortex structure sheds from the body lateral surface, as we will see in the following. The present work deal with rectangular cylinders with low side ratio: from a general point of view the range $0.5 \lesssim SR \lesssim 3$ is considered, even if the discussion concerning experimental evidences and literature comparisons will be focused on a narrower range, namely $0.67 \lesssim SR \lesssim 2$.

1.2 Motivations

The principal motivation for the present work was the remarkable proneness to the interaction between vortex shedding and galloping demonstrated by the rectangular section having $SR = 1.5$ in particular conditions of flow and dynamical characteristics. Generally speaking, the side ratios range $0.67 \lesssim SR \lesssim 2$ are theoretically prone to both VIV and galloping phenomena. However, it is worth stressing that, in case the interaction manifest itself on a real structure, it leads to unrestricted growing amplitudes of vibration (galloping character) starting from low velocities (critical velocity at resonance for VIV); this is much more dangerous with respect to the two phenomena occurring separately. The interests of the present research are, from the engineering point of view, to precisely define the response behaviour in order to prevent structural crisis, and on the scientific point of view, to achieve a detailed knowledge of the causes promoting the occurrence of the interaction; nevertheless, while the former point can be satisfied by means of laboratory testing, the latter is still far from being well clarified.

This instability-type was observed in laboratory tests on a rectangular section with $SR = 1.5$, arisen unexpectedly during aeroelastic tests. It is worth noting that VIV and galloping separately were already extensively investigated during the decades. Thus, an updated state of the art showed an articulated amount of experimental and theoretical works, more unbalanced on the square section although higher SR bodies demonstrated to be prone to this kind of instability too. Hence, the possibility to cover a wide range of mass ratios has been undertaken. Such a choice presents several repercussions: from the point of view of theoretical research interest, the comparisons and interesting parallels with other sections in the same SR range but varying the mass and/or damping parameter are possible; on the other hand it could constitute a useful set of indications for structures' design. In fact, dealing with slender wind-sensitive structures or even submerged structures, a broad band of experimental evidences on which one can reliably rely is indispensable.

Therefore, aiming to extend our analysis to such different situations, wind- and water-sensitive structures, the mass ratios which have to be taken into account range from low (water) to high (air) values. Thus, a decision was made for investigating two completely different range of mass ratios, which led to the necessity to conduct two comprehensive

experimental campaigns in air- and water flow. This effectively gave, as it will be presented in Ch. 7, interesting results in terms of aero-/hydrodynamic and aero-/hydroelastic results.

1.3 Structure of the Thesis

The thesis consists of six chapters, each one preceded by a short introduction denouncing the aims of the relative content, and finalized by a brief summary recalling the main findings. The thesis is structured as follows.

- **Chapter 2 - Selective review** Selected ingredients necessary to describe the aspects involved in the interaction between VIV and galloping related to experimental tests, numerical modelling and theoretical issues on non-linear dynamics and aerodynamics of the involved systems.
- **Chapter 3 - Experimental campaign (*Air flow*)** Two campaigns performed in two wind tunnels, in order to collect static and aeroelastic data, on different SR , in smooth and turbulent flow.
- **Chapter 4 - Experimental campaign (*Water flow*)** An extensive campaign conducted in a water channel carried out in smooth flow conditions.
- **Chapter 5 - Numerical modelling** A short selective review on semi-empirical models available in literature about VIV and VIV-galloping, the implementation of the chosen predictive model for reproducing original results on $SR = 1$ and also that one conducted with the parameters determined by means of present laboratory measurements on $SR = 1.5$ section, in air- and water flow.
- **Chapter 6 - Discussion** A comprehensive comparison of present and literature experimental data and, finally, a brief overview to address the FIV behaviour of the investigated bodies.
- **Chapter 7 - Conclusions** The overall conclusions of the thesis, summarising the most relevant contributes of the work, providing some outlooks and recommendations for future researches.

Chapter 2

Interaction VIV-galloping: a selective review

2.1 Introduction

In this chapter an attempt has been made in unifying several contributions given by distinguished authors, around the main topic of the present dissertation. Dealing with the interaction between the two phenomena, vortex-induced vibrations (VIV) and galloping, generally treated as separated because different indeed in nature, implications on the practical structure design and even theoretical approach, a selective review for each separated phenomenon will be proposed; then, a selective state-of-art about the interaction is given, aimed at connecting the contributes of different disciplines participating to the comprehension of such a phenomenon. A brief description to purposely detect the aspects of VIV and galloping which characterize the interaction mechanism will be given, introducing a bit more the separated phenomena referring to the ideal case of the circular cylinder for vortex shedding and to the square section for galloping, then widening the sight on different geometries in the core of the chapter.

VIV is categorized as a type of instability-induced excitation (IIE) that is caused by an intrinsic flow instability, that is the vortex shedding, while galloping is a type of movement-induced excitation (MIE) that is caused by the aerodynamic instability of the structures under certain conditions of the fluid-structure system (Naudascher and Rockwell, 1993). For both the phenomena an appreciable afterbody is required for their occurrence.

Despite the laboratory observations, which constitutes the core of the present research, for the SR indicated to be the object of the present work the proneness to different mechanisms of different structures is hard to be univocally stated. In order to do this, a useful scheme was given by Matsumoto (1996) (Fig. 2.1), next to another one on aerodynamic instabilities occurring for different SR (Fig. 2.2).

The aeroelastic phenomena reported in Fig. 2.1 describe an articulated system of possibly occurring phenomena, to be taken into account in the flow-structure interaction based design. Among them, we will put our attention on those indicated as *Kármán Vortex-Induced Excitation* or Vortex-Induced Vibrations (VIV), and *High Speed Galloping*. It is worth pointing out that *Low Speed Galloping* refers to a different kind of instability, affecting rectangular section of very low side ratio, namely $0.2 \lesssim SR < 0.6$ (Nakamura and Hirata, 1991, Nakamura and Matsukawa, 1987), that builds up spontaneously from rest (in a very

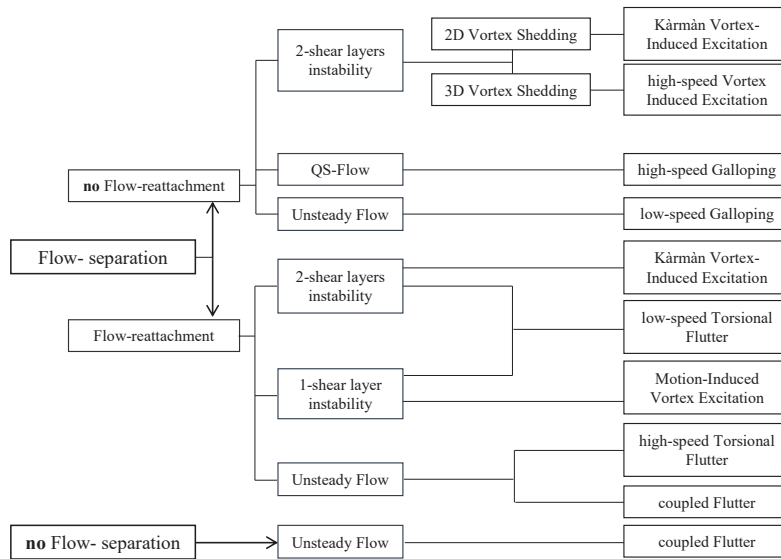


Fig. 2.1 Bluff-Body Aerodynamics. [reproduced from Matsumoto (1996)]

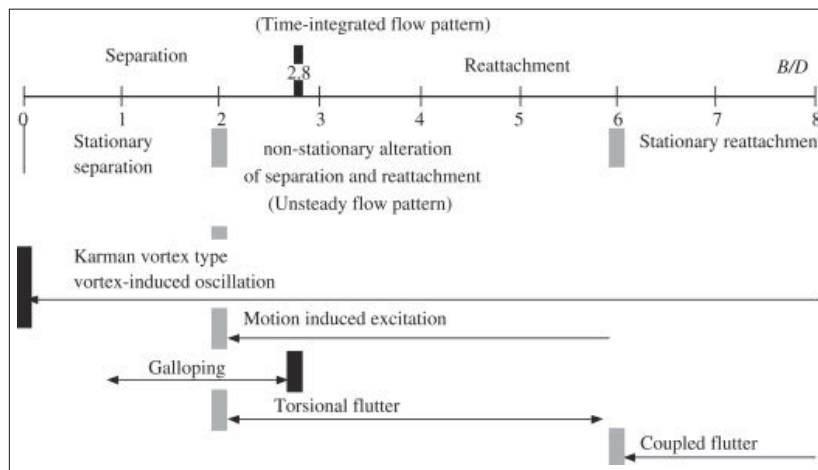


Fig. 2.2 Sharp edged bluff-bodies aerodynamics characteristics. [from Takeuchi and Matsumoto (1992)]

regular form), over a certain range of wind speeds, much lower than the vortex-resonance velocity. However, this aeroelastic phenomenon neither has been clarified so far nor it will be object of the present work.

2.2 Vortex-induced vibrations and lock-in

2.2.1 Flow past a stationary circular cylinder

The alternate shedding of vortices from the side of a body is probably one of the most studied phenomena in fluid mechanics. Fig. 2.3 refers to the change in flow pattern and wake structure of a stationary circular cylinder immersed in a fluid flow by increasing the flow velocity. The flow regimes experienced by the cylinder is dependent on *Reynolds* number, which is defined as

$$Re = \frac{UD}{\nu}, \tag{2.1}$$

where U is the free-stream velocity, D is the diameter of the cylinder and ν is the flow kinematic viscosity. These aspects were already investigated by *e.g.* Lienhard (1966), Williamson (1996), Sumer and Fredsøe (1997) and Zdravkovich (1997). At very low *Reynolds* number values ($Re < 5$), the flow dynamics around the cylinder is dominated by viscous effects of the fluid (creeping or Stokes flow). When Re is still lower enough, a steady recirculation bubble forms behind the body ($5 < Re < 40$), with two symmetrical counter-rotating vortices (cavity flow); the bubble length increase with increasing Re . When Re is increased above a certain critical value ($Re_{cr} \simeq 46$ for a circular cylinder *e.g.* according to Taneda (1956)), the steady configuration become unstable, and after a transient a new equilibrium configuration is obtained. This new flow however is no longer steady but is characterized by the alternate shedding of vortices from the two sides of the body ($40 < Re < 200$). In this range the flow undergoes its second major transition to the phenomenon of vortex shedding. The time-periodic vortices stagger in a two-row configuration in the wake to form a laminar


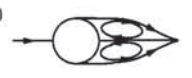




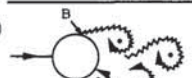


a)		No separation. Creeping flow	$Re < 5$
b)		A fixed pair of symmetric vortices	$5 < Re < 40$
c)		Laminar vortex street	$40 < Re < 200$
d)		Transition to turbulence in the wake	$200 < Re < 300$
e)		Wake completely turbulent. A: Laminar boundary layer separation	$300 < Re < 3 \times 10^5$ Subcritical
f)		A: Laminar boundary layer separation B: Turbulent boundary layer separation; but boundary layer laminar	$3 \times 10^5 < Re < 3.5 \times 10^5$ Critical (Lower transition)
g)		B: Turbulent boundary layer separation; the boundary layer partly laminar partly turbulent	$3.5 \times 10^5 < Re < 1.5 \times 10^6$ Supercritical
h)		C: Boundary layer com- pletely turbulent at one side	$1.5 \times 10^6 < Re < 4 \times 10^6$ Upper transition
i)		C: Boundary layer com- pletely turbulent at two sides	$4 \times 10^6 < Re$ Transcritical

Fig. 2.3 Re -dependent regimes of flow around a smooth, circular cylinder in steady flow.
[from Sumer and Fredsøe (1997)].

vortex street, which is well known as Kármán vortex street so-called in honour of Theodore von Kármán because of his observation and analysis based on the earlier observation of this vortex street by Bénard (1908). Investigations by von Kármán (1911) and Robinson and Saffman (1982) showed that the ratio of the transversal (cross-flow) spacing between the two rows to the longitudinal spacing of two consecutive vortices in the same row was 0.281 when the vortex street was stable. The vortex shedding exerts in turn fluctuating forces

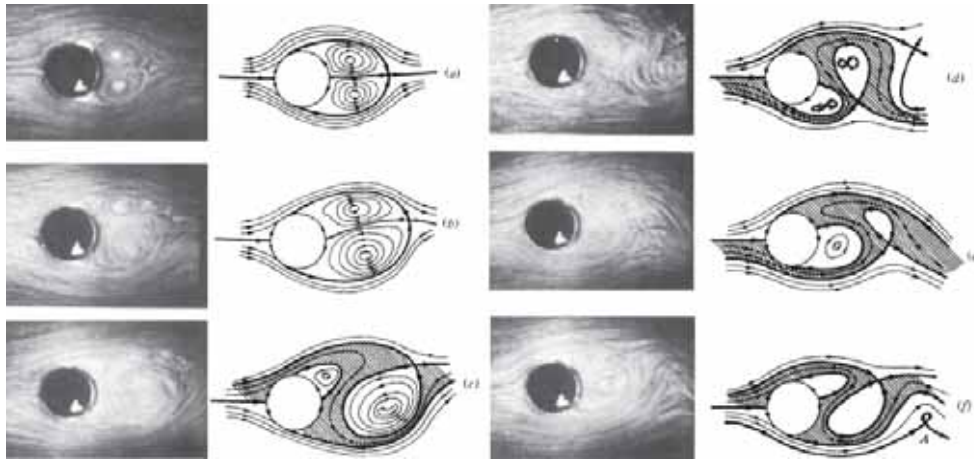


Fig. 2.4 Picture and interpretation of the flow in the near wake of a stationary cylinder in a flow starting from rest. Sequence of events begins at (a) and continues to (f). [from Perry *et al.* (1982)].

on the cylinder sides, exciting the cylinder so that to vibrate in case it was of distributed elasticity type or elastically mounted. Therefore, vortex shedding is highly significant with respect to vortex-induced vibration. Given that we will deal with Re ranging till the sub-critical range, and considering lately only sharp-edged bodies, it seems more useful here to introduce some elements about the formation of the near wake instead of deepening the analysis of Re -dependent flow regimes.

The development of vortex formation in the near wake of a circular cylinder has been described by Gerrard (1966), and a visualization of the mechanism of vortex shedding has been given by Perry *et al.* (1982).

The vortices shed with a defined frequency that depends on the shape of the body and which is directly proportional to the *Strouhal* number, according to the relation

$$f_{vs} = St \frac{U}{D}. \quad (2.2)$$

An empirical observation is the inverse proportionality between the shedding frequency and the width of the wake rather than to the body depth which means, for bodies with free separation point St to be a function of Re (Norberg, 2001); conversely, for bodies with fixed separation point St is not Re -dependent. It is worth noting that the boundary layer physical properties determine where shear layer separation occurs in a smooth section as in the case of circular cylinder.

In Fig. 2.4 is proposed the evolution of the flow pattern in the near wake of a circular cylinder at a Re inside the critical range ($Re = 100$), immersed in a fluid flow that starts from rest. The different oscillations phases are recorded in a way in which each of them represents the exposition of 40 consecutive frames on the photographic plate, given the nondimensional time exposure increment ($\Delta t \simeq 0.3D/U$) between each picture from the Prandtl 1920's movie (see Shapiro and Bergman (1962)), so that no instantaneous streamlines can be seen. As shown in Fig. 2.4 (a,b) the cavity which forms during the starting-up process, in a 'time-averaged sense', is closed and all the 'saddles' - identified by the **A** node in 2.4 (f) - are joined together, proposing a classic picture of a cavity flow. The relationship between the unsteady cavities and their convection into vorticity region, is the key feature

of the near wake and the first step in understanding vortex-shedding¹. The cavity should be seen of as a region where vortex sheets are undergoing a multiple-folding process and where each vortex shed is always ultimately connected back to the cavity by its own thread. In 2.4 (c) it is quite easy to observe the multiple-folding of streamlines, coloured in dark grey, which correspond with so called *instantaneous alleyways*: the fluid entering the cavity through the alleyways is bounded by the ‘separatrices’ (bold lines in the figure frames). It is well known these streaklines can never be broken, representing a flexible barrier which fluid can never cross, even though it may be stretched and become so highly convoluted that the original vortex sheet may become unrecognisable as a continuous sheet. On the next cycle the same applies to the next ‘body’ of fluid, and so on, so that the various bodies of fluid within the cavity are recognizable and separated from each other by separatrices. These bodies of fluid form a queue and are successively stacked up one behind the other and then move in jumps towards the solid body, awaiting their turn to be ‘squeezed’ out of the cavity and carried away by a Kelvin-Helmholtz-like roll-up (Perry *et al.*, 1982). Summarizing, during the vortex-shedding process (2.4 (c-f)), the cavity is open and the saddles are not necessarily joined by the separatrices, and alleyways penetrate the cavity.

The vortex-shedding process is characterized by strong three-dimensionality, also for two dimensional body. The correspondent shedding modes have distinct unstable spanwise wavelength bands and different topologies. The unstable shear layers roll up with a limited coherence and then the forming eddies stretch in the spanwise direction. A discussion of the physics standing behind this phenomenon is reported in (Buresti, 1998). The two-dimensional wake of a circular cylinder undergoes an hysteretic transition to three-dimensional flow at a $Re \approx 190$. The initial instability causing this transition gives rise to the first of a sequence of two shedding modes leading to the rapid evolution to fully turbulent flow (Williamson, 1996). A more recent work which explains the physical nature of the initial transition to three-dimensionality of flow past a circular cylinder using *Floquet instability analysis* has been published by Thompson *et al.* (2001).

Conversely with respect to smooth bodies the wake regimes generated by sharp edged sections are less sensitive to $Mach^2$ and $Reynolds$ numbers, because the separation points do not vary but are fixed in correspondence of the section corners which face the fluid-flow. Nevertheless other flow parameters can have a strong influence on the vortex formation process. For instance very important is the role played by local Re associable to the degree of sharpness of the corners and to the surface roughness of the body. Concerning real structures placed in a more or less developed boundary layer the oncoming turbulence too plays a key-role in the shedding mechanism, usually reducing its overall intensity (Simiu and Scanlan, 1996). Then, for not streamlined bodies, such as bridge deck sections, although the elongated and aerodynamically designed type prevailed on the compact ones, the process is much more complicated to predict, determining more than one dominant St , which correspond to different shedding structures (Bruno and Khris, 2003).

2.2.2 Vortex-induced vibrations

So far we have considered the case of a stationary two-dimensional elongated circular cylinders, but it is well known that the flow generated by vortex shedding around a vibrating

¹for a complete insight on the formation region mechanism describing reverse-flow and entrainment of growing vortices shear layers one can refer to Gerrard (1966)

²Mach number is defined as the ratio of flow velocity past a boundary to the local speed of sound.

bluff body can have very significant differences from that around a fixed one. In fact when a bluff body free to vibrate is immersed in a fluid flow it is quite easy to observe it to oscillate primary in the direction transversal with respect to the oncoming flow. In this situation vortex shedding is altered and the flow pattern around the body is significantly different from the stationary body case saw in the above paragraph. As a consequence of the discrete wake vortices formation, the flow field has a dominant periodicity, and the structure generating the wake is exposed to a periodic pressure loading which results in a transverse, or lift force at frequency f_{vs} , arising from the asymmetry of the vortex formation, while the drag force, in case of axisymmetric cross-sections, fluctuates at $2f_{vs}$ (Bishop and Hassan, 1964). Accordingly, if the structure is elastic with natural frequencies f_n , near f_{vs} it will tend to develop a resonant response in the form of bending oscillations normal to the wind direction. The lift force can induce the cylinder to vibrate in the cross-flow direction, while the drag force can induce the cylinder to vibrate in the in-line direction to the flow. The character of both the aforementioned vibration can be at first considered as harmonic. Attempting to easily describe the key features of the body response is useful to

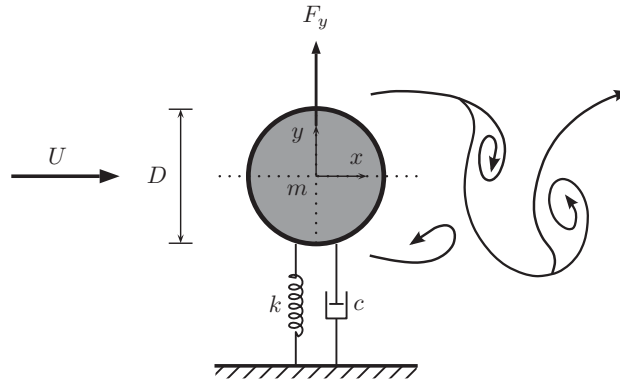


Fig. 2.5 Definition sketch for cross-flow VIV of a circular cylinder. The cylinder undergoes free vibrations constrained in the transverse y direction to the free-stream U in x direction.

refer to a schematic lateral view sketched in Fig. 2.5 where a circular cylinder is subject to a uniform smooth-flow, and is given to freely oscillate in the cross-flow direction due to the fluctuating forces F_y exerted by the vortex shedding, constituting a 1-DoF damped system. The governing equation of motion for cross-flow VIV of the body can be expressed by

$$m\ddot{y} + c\dot{y} + ky = F_y, \quad (2.3)$$

or in terms of natural frequency and damping ratio of the system by

$$\ddot{y} + 2\zeta\omega_n\dot{y} + \omega_n^2 y = \frac{F_y}{m}, \quad (2.4)$$

where m is the oscillating system's mass, c is the structural damping, k is the spring constant representing the system stiffness, $\omega_n = \sqrt{k/m} = 2\pi f_n$ is the natural pulsation of the system, $\zeta = c/(2m\omega_n)$ is the fraction of structural damping with respect to critical or simply damping ratio, and F_y is the lift force in the direction transverse to the free-stream.

2.2.2.1 Synchronization

One could understand synchronization as rhythms' adjustment in oscillating bodies due to their weak interaction. Avoiding to precisely quantify where the border between this "weak" and "strong" interaction lies, strong-coupling is a notion well defined at resonance only, whereas the level of detuning of two systems defines in a way how weak the coupling become. Anyway, our interest is in oscillators which are intended as weakly coupled non-linear autonomous systems, physically modelled by a system of ordinary differential equations. Nevertheless, a comparison with an externally excited system can be helpful in the phenomenon's understanding and its origins.

If a system with natural angular frequency ω_n is externally excited by a forcing term characterized by ω_e , one can observe that when ω_e is not too far away from ω_n there's the usual phenomenon of interference or *beating* as it happens in linear systems. If, however, ω_e approaches ω_n , the beats disappear suddenly and only one frequency ω_e remains. Everything happens if the oscillator frequency is *entrained* by the external frequency³, within a certain band $\omega_e - \Delta\omega < \omega_e < \omega_e + \Delta\omega$. Such a phenomenon is commonly known as lock-in (or synchronization), even if a wide nomenclature for the same phenomenon can be derived from the literature. It is worth noting that the here mentioned external excitation has to be seen as one of the two systems interacting each other. In practice, in the present work the role played by what we've just referred as the external forcing term, has been considered that of the periodic pressure loading acting due to the vortices structure shed from the body sides. The mutual interaction of these two systems (vortices structure and oscillating body), manifests itself as a non-linear resonance between the fluctuating pressure, externally driving the body, and transversal motion, which may give rise to the synchronization of the system.

Going back to 1665, the Dutch scientist Christiaan Huygens wrote to the Royal Society of London to tell them of his discovery of an "odd kind of sympathy" between two pendulum clocks hung together on a wall: they were unsynchronized with another one in this condition but became synchronized when suspended to a thin wooden board. Effectively Huygens's discovery was the first-ever observation of coupled oscillation⁴ (see Bennett *et al.* (2002) for the explanation of the phenomenon and further details about Huygens experiment details). For our purposes and in terms of frequencies, in case the oscillation and vibration frequencies are approaching each other the Strouhal relation shows to be violated, and the vortex-shedding is controlled by the body motion. In Fig. 2.6 two different types of such violation are reported: air differ from water flow case due to the contribution of the added mass, negligible in air while significant for an higher fluid density (for more details refer to §4.2.4.1). In such cases a resonance condition can occur when the vortex shedding frequency, f_{vs} , and that of the body oscillation, f , in bending or torsional DoF, are locked and close to the natural one, f_n , experiencing almost perfectly harmonic oscillations. However, this resonance has showed to be nonlinear: these nonlinearities can be easily observed although hardly reproducible through analytical models. Marra *et al.* (2011) after having reviewed a large amount of predictive analytical models reported that no model is actually able to properly predict vortex-induced vibrations, given that once the model parameters have been estimated for a certain value of the mass-damping parameter, response predictions for different values of it become unreliable. Above all it is important to underline that

³for details and a first attempted theory to model the phenomenon see Van der Pol (1927)

⁴according also to the opinion of Prof. Strogatz, applied mathematician at Cornell University

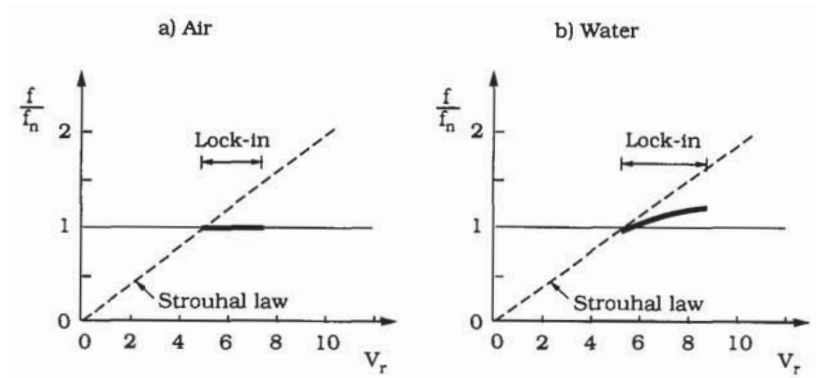


Fig. 2.6 Schematic illustrations of frequency response in air and water with regard to cross-flow vibrations. [from Sumer and Fredsøe (1997)]

the lock-in instability is a self-limited phenomenon, which means the stable amplitude of the harmonic oscillation response is bounded to a certain value for each velocity at which the body is subjected. Once the flow velocity overcomes the lock-in range the oscillations quickly disappeared.

A source of nonlinearity in VIV can be identified for example in the hysteretic behaviour

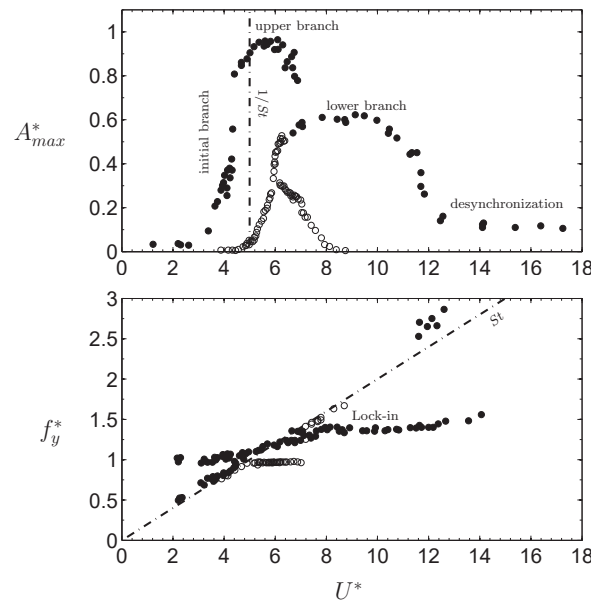


Fig. 2.7 Amplitude and frequency responses of VIV of a circular cylinder. \circ indicate $m^* = 248$ and $\zeta = 0.00103$ ($m^*\zeta = 0.255$) by Feng (1968) while \bullet represent $m^* = 2.4$ and $\zeta = 0.0045$ ($m^*\zeta = 0.011$). [reproduced from Khalak and Williamson (1997)]

originating from the different response branches obtained by increasing the velocity till overtaking the lock-in range and then decreasing the velocity backward, as reported in Fig. 2.7 for what concern Feng's results. It has been observed that phase angle (ϕ) expresses the same kind of behaviour. The oscillation hysteresis is a key feature of lock-in and some studies attempted to explain the base mechanism, *e.g.* the nonlinearities in the elastic system, namely the springs (Currie *et al.*, 1972), or in the system damping (Wood, 1976). Hysteresis in amplitude and phase angle response has been put in relation with the switching between different types of shedding modes addressed in Williamson and Roshko

(1988), together with the abrupt reduction in amplitude after the response peak. A detailed account of this relationship has been given by Brika and Laneville (1993). Moreover, significant super- or sub-harmonic resonances, in terms of energy content, are known to take place concerning the body response (Schewe, 1989).

Apart from the the capture of the vortex-shedding frequency by the body frequency over a range of reduced velocity, the second well-known aspect is the large increase in correlation length that occurs at lock-in, which is also another source of nonlinearity.

Looking at the literature results in terms of correlation between pressures at points separated by a variable distance along the cylinder axis, for a freely vibrating circular cylinder Novak and Tanaka (1972) demonstrated the coherence to strongly increase of with the vibration amplitude; from their results also the role of the turbulence intensity (I_u) in the oncoming flow is addressed, clearly showing the increase of it causing a strong reduction of the fluctuating forces due to vortex shedding. A square section subject to forced oscillations, with fixed oscillation amplitude, showed the increase of spanwise correlation of the flow at a reduced velocity where the vortex and body frequencies coincide (Bearman and Obasaju, 1982).

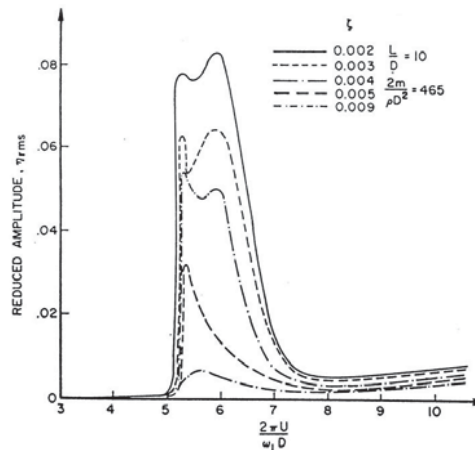


Fig. 2.8 Model stack nondimensional amplitude response of a circular cross-section for different values of structural damping ($Re < Re_{cr}$). (Wooton, 1969).

Another parameter strongly affecting the limit-cycle amplitude, in torsional or bending modes, is the mass-damping parameter. In air flow cases we can consider it in the coupled form of *Scruton* number general expression

$$Sc = \frac{\zeta m}{\rho D^2}, \quad (2.5)$$

even if we presently refer to two other forms of it, such as

$$Sc_{D^2} = \frac{4\pi\zeta m}{\rho D^2}, \quad \text{and} \quad Sc_{BD} = \frac{4\pi\zeta m}{\rho BD} \quad (2.6)$$

It is well-known Sc to play a key-role in motion amplitude response as showed in Fig. 2.8, where an increase of such a parameter produces a suppression of the limit-cycle oscillation peak. Aiming to model both aero and hydroelastic vibrations Eq.[2.7] can be employed

after having purposely nondimensionalized the quantities. It results:

$$\ddot{Y} + 2\zeta\dot{Y} + Y = C_y n U^2, \quad (2.7)$$

in which C_y is the exciting force coefficient and the *mass parameter* is used in the classical form

$$n = \frac{\rho D^2 L}{2m}. \quad (2.8)$$

In aeroelastic oscillations Y_{max} is in the order of magnitude of $\mathcal{O}(1)$, while for damping we usually get $\mathcal{O}(10)^{-3} \div \mathcal{O}(10)^{-2}$ in a laboratory environment⁵, and $\mathcal{O}(10)^{-4} \div \mathcal{O}(10)^{-3}$ for mass ratio. Thus, the contributes of damping and forcing terms are comparable, so that in the solution we are allowed to get rid of both of them obtaining an harmonic-like solution for the differential equation (*DS*) in the form $Y = \bar{Y} \cos(\tau)$, with \bar{Y} determined by the balance between small exciting and damping forces (Parkinson, 1989). On the other hand it is important to underline that in water, given the water on air density ratio $\rho_w/\rho_a \approx 800$ the only negligible term is the damping one, resulting the forcing term proportional to the increased mass ratio. Furthermore it is worth noting how useful is uncoupling the mass and damping parameters, to consider, especially in water, only the contribution of the former. In particular in case of hydroelastic oscillation we will refer to a different expression for the *mass ratio* like

$$m^* = \frac{\text{oscillating mass}}{\text{fluid displaced mass}} = \frac{m}{m_d} = \frac{m}{\rho B D L} = \frac{1}{2n} \frac{D}{B} \quad (2.9)$$

here reported in case of rectangular cylinders ($D \neq B$), which are the objects of the present dissertation. This crucial dependency from the mass ratio in case of hydroelastic oscillations is suggested in Fig. 2.7, being it responsible for the change of pattern and level of the limit-cycle amplitude oscillations as well as Sc in aeroelastic cases.

2.3 Galloping

The other aeroelastic instability object of the present work is, rather appropriately, referred as galloping, given that it takes its name from the visual impression given by its typical low-frequency, high amplitude occurrence. It is not just a spectacular and annoying phenomenon, because in some cases it may have very costly consequences which may range from very low to extremely high, depending on the circumstances of each case. Galloping occurs for long, flexible and slender structures with aerodynamically and non-axisymmetric bluff cross-sections, and it requires only one degree of freedom, either bending with translation of the structural section normal to its span and wind direction, or torsion about a span-wise axis (torsional galloping). Concerning the former type, tall buildings and high-rise structures (Parkinson and Wawzonek, 1981), lighting pole and isolated structural elements (Scruton, 1963) are typical examples of structures susceptible to galloping when the wind velocity exceeds certain critical velocity thresholds, although the origins of its study come from older evidences on different structures, such as ice-coated power lines cables. On the other hand Sisto (1953) studied the instability seen from the viewpoint of the so-called *stall-flutter* (torsional mode) applied to one and three blades cascades in axial-flow compressors. His results confirmed the previous deduction from nonlinear theory concerning

⁵either in a wind tunnel (*WT*) or a water channel (*WC*).

transient behaviour and equilibrium flutter amplitudes or limit-cycles.

The main concerns about galloping are that strong lateral self-excited oscillations can develop at a certain wind speed as a result of aerodynamic force components: in particular negative aerodynamic damping (ζ_a) can be produced even at velocities lower than the critical one, considerably reducing the total damping (ζ_{tot}) available to the structure (Novak, 1972).

$$\zeta_{tot} = \zeta + \zeta_a \quad (2.10)$$

In Lanchester (1907)⁶ was reported an instability triggered by an incipient motion in a interesting “aerodynamic puzzle” called *aerial turbillion*, essentially composed by a D -sections shaft mounted to revolve freely about the axis of an orthogonally placed support (a sort of helicopter rotor). It was found the rotor to have no tendency to go round in the one direction or the other. If, however, a considerable initial spin was given in either direction, the rotor will gather speed and spin at an enormous rate, as for a perfect windmill. By the way galloping of iced conductors has been a design and operating problem for electric utilities since the early 1900s: the phenomenon, in the form of large-amplitude oscillation of iced-up transmission lines, was suggested by den Hartog (1930) as due to the negative rate of change of cross-wind force varying the apparent angle of attack (α), defined as the angle between the chord line and the oncoming flow direction. When the ice-coating makes the section non-axisymmetric that instability can occur. If the body moves across the flow, thus producing a change of α which gives a force in the direction of its motion, a quantum of work is done on the body and the instability can occur. In den Hartog (1932) was stated a necessary condition for the instability obtains when the slope of the lift around $\alpha = 0^\circ$ is more negative than the drag force. However, since Glauert too previously studied an analogous aerodynamic problem of auto-rotation of a stalled airfoil (Glauert, 1919), and associated the instability to the section aerodynamic coefficients, the so called Glauert-den Hartog incipient instability criterion states the proneness to it in case

$$\left. \frac{dC_L}{d\alpha} \right|_{\alpha_0} + C_D(\alpha_0) < 0, \quad (2.11)$$

where α_0 stays for a neighbourhood of the zero angle of attack. From Eq.[2.11], valid under the hypothesis of no-torsion but only the plunging DoF allowed, it’s clear the reason why circular section are not prone at all to galloping, in fact it is always verified that $dC_L/d\alpha \equiv 0$ and $C_D > 0$. From the moment that galloping is driven by the instantaneous angle of attack between the body and the flow, which results in an asymmetric pressure distribution, it does not involve a mechanism of lock-in between the oscillation and vortex formation as opposed to VIV and can thus often be predicted through quasi-steady theory.

2.3.1 Nonlinear Quasi-Steady model for galloping

Although the large amount of studies concerning galloping of ice-coated power lines cables, the square section can be considered, as well as the circular one in VIV, the reference one for galloping instability, or at least the most studied. Ice-coated cables assume an

⁶reported in § 30, pp.44-45, with a note by the author: “[...] it was first brought to the notice of the author by Mr. Henry Lea, consulting engineer, of Birmingham, who, it would appear, had it communicated to him by Mr.A.S. Dixon, who in turn had it shown him when travelling in Italy by Mr. Patrick Alexander. The author has taken no steps to trace the matter further. The explanation here given is his own.”

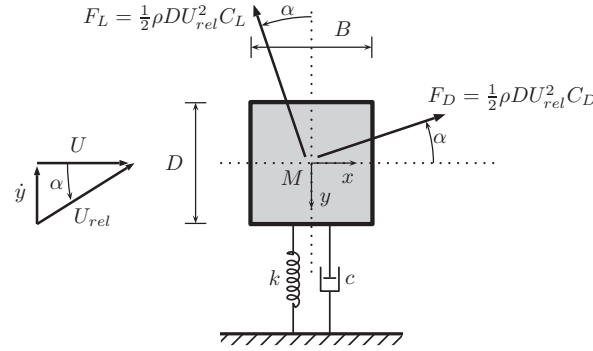


Fig. 2.9 Definition sketch for cross-flow galloping of a square cylinder moving in y direction with velocity \dot{y} , hence subject to the relative, or apparent, velocity U_{rel} .

indefinite variability of geometries, being not always prone to galloping instability. D -sections, despite the large oscillation amplitudes experienced, is commonly referred to as an hard-type galloping oscillator, which means $dC_L/d\alpha$ being so small that it needs a really high initial amplitude to trigger the vibrations, as it will be shown later. Conversely, the square section demonstrated to be a soft oscillator with respect to galloping instability. In case an elastically mounted bluff-section experiencing galloping (a schematic view is reported in Fig. 2.9) the reduced vibration frequency, f/f_n , is much lower than $U/f_n B$. This means, alternatively, that if the time needed for a particle in the fluid stream to cover the chord length of the section, B/U , is much lower than a complete body oscillation period, $1/f_n$, then it can be assumed that the instantaneous aerodynamic forces acting on the oscillating cylinder equals those one that it would if held stationary and subject to the relative velocity $U_{rel} = \sqrt{U^2 + \dot{y}^2}$, resulting from the apparent angle of attack α , given from the transverse cylinder velocity, \dot{y} , as from Eq.[2.12] (quasi-steady hypothesis).

$$\alpha = \tan\left(\frac{\dot{y}}{U}\right) \quad (2.12)$$

Another hypothesis is that of little displacements, so that to be allowed to approximate at the first order the apparent angle of attack. Under these assumptions the flow seen by the body in motion would be equivalent to that seen by the same body, but stationary, at the modified angle of attack and relative wind velocity.

In this configuration the steady aerodynamic drag and lift forces can be written as⁷

$$F_D = \frac{1}{2} \rho U_{rel}^2 D L C_D \quad (2.13)$$

$$F_L = \frac{1}{2} \rho U_{rel}^2 D L C_L \quad (2.14)$$

Composing aerodynamic forces in the vertical plane we can derive the lateral force

$$F_y = -F_L \cos \alpha - F_D \sin \alpha = \frac{1}{2} \rho U^2 D L C_{F_y}, \quad (2.15)$$

⁷we are here mostly taking as reference the passages developed in Blevins (1990)

giving the aerodynamic lateral force coefficient

$$C_{F_y} = -\frac{U_{rel}^2}{U^2} (C_L \cos \alpha + C_D \sin \alpha) . \quad (2.16)$$

For small values of angle of attack α , U and U_{rel} can be expanded in power series

$$\alpha \simeq (\dot{y}/U) + O(\alpha^2) , \quad (2.17)$$

$$U_{rel} \simeq U + O(\alpha^2) , \quad (2.18)$$

$$C_{F_y}(\alpha) \simeq C_{F_y}|_{\alpha=0^\circ} + \left. \frac{dC_{F_y}}{d\alpha} \right|_{\alpha=0^\circ} \cdot \alpha + O(\alpha^2) + \dots , \quad (2.19)$$

being $U_{rel} \simeq U$. Under this condition differentiating Eq.[2.19] with respect to α yields to

$$\frac{dC_{F_y}}{d\alpha} = -\left(\frac{dC_L}{d\alpha} \cos \alpha - C_L \sin \alpha + \frac{dC_D}{d\alpha} \sin \alpha + C_D \cos \alpha \right) , \quad (2.20)$$

leading, for α approaching zero, to

$$\left. \frac{dC_{F_y}}{d\alpha} \right|_{\alpha=0^\circ} = -\left(\left. \frac{dC_L}{d\alpha} + C_D \right) \right|_{\alpha=0^\circ} , \quad (2.21)$$

which means in turn

$$C_{F_y}(\alpha) \simeq -C_L|_{\alpha=0^\circ} - \left(\left. \frac{dC_L}{d\alpha} + C_D \right) \right|_{\alpha=0^\circ} \cdot \alpha . \quad (2.22)$$

The equation of motion for the system subject to an aerodynamic force can be written as

$$m\ddot{y} + 2m\omega_n\zeta\dot{y} + ky = F_y = \frac{1}{2}\rho U^2 DLC_{F_y} . \quad (2.23)$$

Taking $\alpha = 0$ we get $C_{F_y}|_{\alpha=0^\circ} \equiv -C_L$, and then substituting Eq.[2.22] in the above Eq.[2.23], we obtain

$$m\ddot{y} + 2m\omega_n\zeta\dot{y} + ky = \frac{1}{2}\rho U^2 DL \left[-C_L|_{\alpha=0^\circ} - \left(\left. \frac{dC_L}{d\alpha} + C_D \right) \right|_{\alpha=0^\circ} \cdot \frac{\dot{y}}{U} \right] , \quad (2.24)$$

that with some manipulations can be written as

$$m\ddot{y} + 2m\omega_n \left(\zeta - \frac{\rho U DL}{4m\omega_n} \left. \frac{dC_{F_y}}{d\alpha} \right|_{\alpha=0^\circ} \right) \dot{y} + ky = -\frac{1}{2}\rho U^2 DLC_L|_{\alpha=0^\circ} . \quad (2.25)$$

The term in round brackets represents the equivalent damping, expressed here as the difference between the structural and aerodynamic contribution:

$$\zeta_E = \zeta - \frac{U}{4\omega_n D} \frac{\rho D^2 L}{m} \left. \frac{dC_{F_y}}{d\alpha} \right|_{\alpha=0^\circ} , \quad (2.26)$$

making the system unstable (divergent oscillations) if and only if the equivalent damping results lower than zero, that is $\zeta_E < 0$. Hence, the critical velocity for galloping onset derives straightly imposing $\zeta_E = 0$

$$U_g^* = \frac{U_{crit}}{f_n D} = \frac{4m(2\pi)\zeta}{\rho D^2 L} \left(\left. \frac{dC_{F_y}}{d\alpha} \right) \right|_{\alpha=0^\circ}^{-1} . \quad (2.27)$$

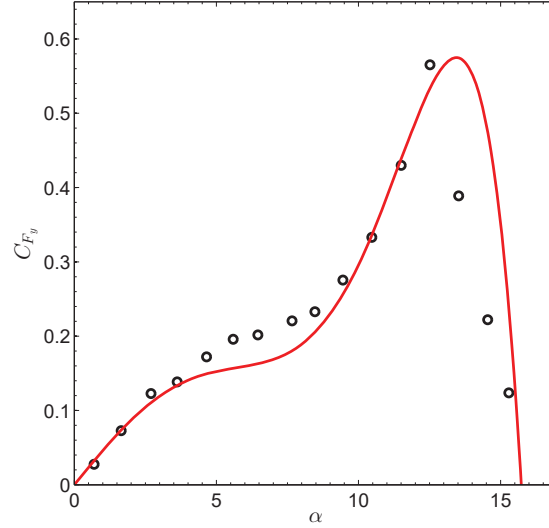


Fig. 2.10 Lateral force coefficient vs. apparent angle of attack for a square sectional model. \circ : experiment (Parkinson and Smith, 1964), $Re = 22300$, —: 7th order polynomial approximation using original paper coefficients ($A_1 = 2.69$, $A_3 = 168$, $A_5 = 6270$, $A_7 = 59900$).

As the aerodynamic lateral force coefficient C_{F_y} can be measured on stationary sectional models subject to a fluid-flow varying the angle of attack, the quasi-steady model provides to express it as a polynomial approximation. In order to predict the galloping onset velocity and the response of square cross-sectional body, such an approximation was firstly attempted Parkinson and Brooks (1961) considering an odd 5th order polynomial function for C_L and a 4th order for C_D , the formulation was revisited in Parkinson and Smith (1964) and substituted by a 7th order odd polynomial function justifying this choice “for a close approximation, because of the five important changes of curvature in the pertinent range”. In particular it is very important to be able to well detect 1) the slope of the C_{F_y} coefficient around 0° , 2) the inflection point given by the existence of intermittent shear layer reattachment (Luo *et al.*, 2003), 3) the maximum point indicating apparent angle of attack at which the shear layer will reattach definitely on the body side; moreover, to better describe the post-critical response, namely far away from the phenomenon onset, also 4) the tail of the descending branch after the maximum point should be interpolated. The following expression has been given by Parkinson and Smith (1964)

$$C_{F_y} = A_1 \left(\frac{\dot{y}}{U} \right) - A_3 \left(\frac{\dot{y}}{U} \right)^3 + A_5 \left(\frac{\dot{y}}{U} \right)^5 - A_7 \left(\frac{\dot{y}}{U} \right)^7, \quad (2.28)$$

being $A_1, A_3, A_5, A_7 > 0$: the experimental results reported by the authors have been reproduced in Fig. 2.10 and fit following the same polynomial. It is worth noting that in this notation the term A_1 represent the α -derivative of C_{F_y} in Eq.[2.27], so that to derive the equivalences:

$$U_g^* = \frac{4m(2\pi)\zeta}{\rho D^2 L A_1} = \frac{4\pi\zeta}{n A_1} = 2 \frac{S_{c_{D^2}}}{A_1} = 2 \frac{S_{c_{BD}}}{A_1} \frac{B}{D}. \quad (2.29)$$

Now substituting Eq.[2.28] in Eq.[2.23], and nondimensionalizing with respect to kD we can write

$$\ddot{Y} + Y = nA_1 \left[\left(\tilde{U} - \frac{2\zeta}{nA_1} \right) \dot{Y} - \left(\frac{A_3}{A_1 \tilde{U}} \right) \dot{Y}^3 \right] + nA_1 \left[\left(\frac{A_5}{A_1 \tilde{U}} \right) \dot{Y}^5 - \left(\frac{A_7}{A_1 \tilde{U}} \right) \dot{Y}^7 \right], \quad (2.30)$$

with $\tilde{U} = U^*/2\pi$, and $(\dot{})$ meaning here a nondimensional time derivative (*e.g.* $\dot{Y} = dY/d\tau$, with $\tau = \omega t$) determined using the *chain rule*; Eq.[2.30] represents an ordinary weakly nonlinear differential equation for the body transversal displacements.

Then, by using the polynomial coefficients identified through static tests, Parkinson and Smith solved the differential governing equation of motion, Eq.[2.30], using the method of Krylov and Bogoliubov (Minorsky, 1962): they successfully predicted the amplitude response for a freely vibrating square cylinder, the onset velocity U_g^* , and an hysteresis phenomenon. The two different stable limit cycles are predicted by theory to be related to a forcing term modelled as a 5th order polynomial, according to the Poincaré topological representation *SIS* (see Minorsky (1960) and §2.6.2). It is worth noting that the hysteresis in galloping oscillations, concerning the square section, has demonstrated to directly come from the existence of the inflection point in the C_{F_y} vs. α curve (Luo *et al.*, 2003). In

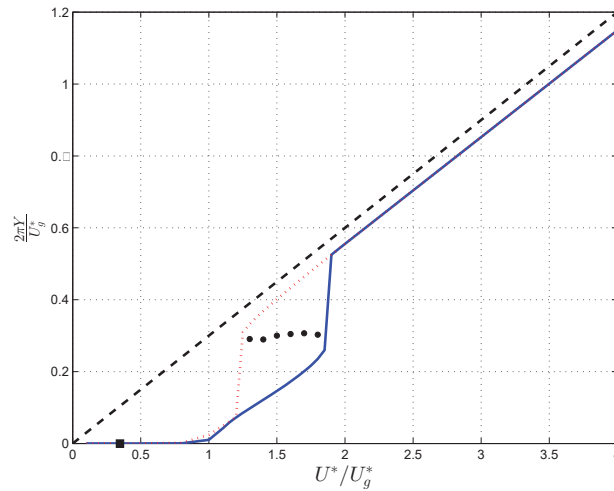


Fig. 2.11 Amplitude response of a square cylinder experiencing galloping ($f_n = 6.01$ Hz, $n = 4.3 \cdot 10^{-4}$, $\zeta = 0.00196$, $Re = 4000 \div 20000$) calculated with quasi-steady Parkinson's nonlinear model. —: *QS*-model stable amplitudes (Y_S) increasing flow velocity ($Y_0 = 0.05$); \cdots : decreasing flow velocity ($Y_0 = 2$); \bullet : unstable limit cycle; \blacksquare : resonance velocity ($U_r^* \approx 0.35$); - - -: Parkinson and Smith's rule of thumb from experimental results ($Y_S = 0.3 \cdot U$).

Fig. 2.11 are reported the results in terms of nondimensional stable amplitude increasing the flow velocity, reduced with respect to galloping nondimensional onset velocity, resulting from the implementation of the *QS*-model with *ODE45* function in MATLAB (MathWorks®), for a study case reported in the original paper. It is also interesting to note how this kind of plot allows the collapse of different study cases (varying ζ , n etc...), given that the results are divided by U_g^* that include all the model-dependent parameters (as reported in Parkinson and Smith (1964), Fig.5). It's easily visible the oscillation hysteresis obtained by increasing and then decreasing the flow velocity starting from different initial

nondimensional amplitudes (Y_0) according to the values proposed in the original paper, at least for the lower stable limit-cycle branch. In the study case $U_r^* \approx 7.41$, $U_g^* \approx 21.29$ giving a velocity ratio $\Lambda = U_g^*/U_r^* \approx 2.87$; this ratio represents a key-parameter in the interaction between VIV and galloping (see §2.6).

In a series of works Novak extended the nonlinear model to other prismatic structures extending the set of equations from rigid sections to continuous elastic systems (Novak, 1969), and turbulent shear flows in Novak (1972), Novak and Davenport (1970), Novak and Tanaka (1974). An extensive study on the effect of turbulence in rectangular cylinder was also conducted by Laneville (1973) testing different sectional models with two turbulence grids giving different turbulence intensities, I_u , and integral scales L_u^x : it was found the effect of the integral length scale to be small, although there is a consistent effect of I_u . As a common results all the authors reported that an increase of I_u implies a weaker response of the body, making a soft oscillator weaker, and an hard oscillator a soft-type one. One example of this effect can be found as an interesting common result in Novak and Laneville's works, reporting the change in proneness to galloping instability of the $SR = 0.5$ increasing I_u , given that in smooth flow it is considered an hard-type oscillator. Another effect of turbulence has been recognized in an earlier transition in the shear layers, which means in practice the anticipated reattachment (see *e.g.* $SR = 2$ results in Laneville (1973)), making the response to resemble that of a longer rectangle in smooth flow. Laneville and Parkinson (1971) have previously reported the results for a square and $SR = 2$ rectangular sections, showing the galloping behaviour being consistent with the C_{F_y} vs. α curve. Then after having progressively increased turbulence level, it was found the threshold to make the response change from weak oscillator to completely stable to be around $I_u = 12\%$.

Also Bearman *et al.* (1987) investigated a square section reporting the C_{F_y} vs. α curve to be turbulence-sensitive.

2.4 Afterbody effects and formation mechanism in rectangles of low side ratios

Since the afterbody plays a key-role in the vortex shedding and galloping phenomena in rectangular shaped bodies it will be attempted to propose a schematic and clear picture of the implications descending from its change in the range we already addressed to be of interest. First of all let us purposely and properly define the afterbody as the portion of the body downstream the separation point, which of course coincides with the leading edge in case of sharp edged body. Hence the afterbody is the entire cross-section. Aiming to demonstrate that all vortex streets behind bluff bodies are similar Bearman (1967) proposed to collapse all bluff body data relying only on C_D , St and the base pressure coefficient defined as

$$C_{p_b} = \frac{p_b - p_\infty}{0.5\rho U^2}, \quad (2.31)$$

where p represents the base pressure and p_∞ the free stream pressure. It goes without saying that given the presence of suction in the rear side of a body, the base pressure coefficient assumes negative values. Nakaguchi *et al.* (1968) have shown rectangular cylinders to have characteristic C_D and C_{p_b} a bit outside the range provided by Bearman (1967) for which C_D is about 2 and $C_{p_b} = -1.1$ were given as extreme values: as shown in Fig. 2.12 there's a narrow peak in the C_D vs. $\frac{B}{D}$ curve reaching $C_D = 2.94$ and $C_{p_b} = -2.2$ for $SR = 0.62$. Through

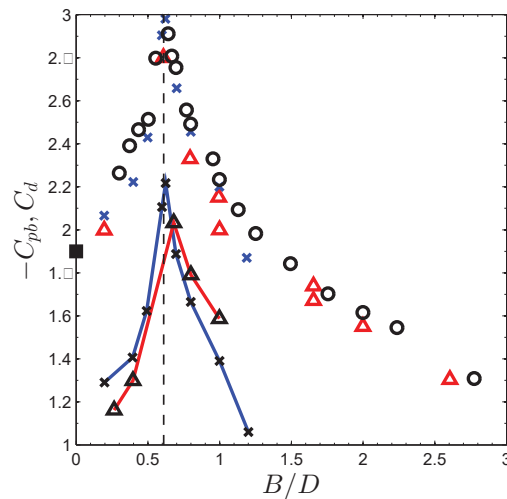


Fig. 2.12 Unified results for drag and base pressure coefficients.

C_D (only markers): \triangle Nakaguchi *et al.* (1968), \times Bearman and Trueman (1972), \blacksquare Fage and Johansen (1927) on a flat plate, \circ Courchesne and Laneville (1982).

C_{pb} (markers & coloured lines): $-\triangle-$ Nakaguchi *et al.* (1968), $-\times-$ Bearman and Trueman (1972). - - - reference line for the critical section $\bar{SR} = 0.62$.

flow visualization Nakaguchi *et al.* evidenced this behaviour of $SR \approx 0.6$, that we could call *critical section*, to be in the middle between the flat plate and square configuration.

The role of base pressure is to determine the amount of vorticity ($\bar{\omega}$) shed from each side of the body; it is also related to the distance of vortex formation (a_v in Fig. 2.14) and its strength when fully formed from the unstable shear layer rolled up. There's a equilibrium point developing among four elements: $\bar{\omega}$, a_v , C_{pb} and entrainment⁸, which has a stabilizing effect in the process. Bearman (1965) stated that the higher C_{pb} (in the sense we're moving towards less negative values) the higher a_v . We may consider the overall effect in shrinking the afterbody to very low value of SR as that of to increase the base cavity's volume behind the rear of the section to a shifted distance of vortex formation downstream. This implies in turns, as previously mentioned, an increase in base pressure. Summing up and referring to Fig. 2.12, if we start from the critical section ($SR = 0.62$ according to Bearman and Trueman (1972)), higher values of C_{pb} and lower ones for C_D are given by the afterbody effect, thus providing an increase in wake cavity volume.

It is also well known the same effect to be obtained just mounting a splitter plate, which delays the shear layer interaction beyond the wake length, hence increasing the separation zone and implying again an increase of a_v . This is determined by the above cited balance: the entrainment is no more able to sustain the low base pressure so that the vorticity has to be decreased to let a_v to adjust to a new equilibrium position. Bearman and Trueman worked on the critical section finding the same effect by placing trailing-edge spoilers normal to the flow variable in height, or just imposing angle of attacks, reaching the reattachment of the shear layer on the side for $\alpha = 20^\circ$.

Now, if we conversely move from a flat plate section orthogonally placed with respect to the flow, increasing the afterbody towards higher values of SR , it won't be possible indefinitely

⁸represented by line f in Fig. 2.14. The role of entrainment in vortex formation mechanism for the circular cross-section is discussed in Gerrard (1966); it is worth noting that even if it plays here a similar role in the above mentioned equilibrium, it is less dependent on Re for our particular case.

decreasing C_{pb} because at a certain *critical point* the shear layer will be impeded by the downstream corners during the shedding cycle. In particular an upper limit to shear layer curvature is fixed such that the flow cannot reattach on the side because the shear layer itself cannot sustain the low pressure behind the body, cutting off the bubble (see also Nakaguchi *et al.* (1968) about the maximum curvature of the shear layer for the critical SR). Fig. 7(c) proposed in Bearman and Trueman (1972) shows how close the shear layer comes to the downstream lower corner without crossing it, so to visually define the above mentioned maximum curvature. From the critical section on the flow pattern goes towards that of the lower SR range, with a larger base cavity.

Laneville and Yong (1983) updated the study of the afterbody effect on the formation process, in terms of SR , referred as *afterbody length* by the authors, showing how it strongly influences the distribution of initial vorticity in separation bubble minimum size and vorticity, and the interaction between the bubble and the forming vortex. They conducted a flow visualization campaign for better detailing the formation process in the near wake geometrically defined by the geometrical quantities reported in Fig. 2.14. The authors investigated rectangles with side ratio equal to $SR = 0.25, 0.64, 1.75, 5$ whereof some visualizations of interest is reported in Fig. 2.13. The geometrical features, derivable from the flow pattern, are schematised in Fig. 2.14: a_v is referred as the longitudinal distance between the position of forming vortices and the rear wall, d_v is the lateral spacing between the vortices and L_{ws} is the minimum size of the separation bubble, or wet length for the sake of brevity, and c_v is the distance to closure point. In is worth noting that the filaments in the figure represent both fluid and vorticity of the flow.

Part of the initial vorticity - a - is absorbed by the separation bubble - b -, and the evolution of the unabsorbed one - c - is controlled by the afterbody length. The c -relative shear layer feeds either the adjacent or opposite vortex while they are forming. The separation bubble plays as a buffer region filling itself so to grow and change in size as the adjacent vortex forms (see Fig. 2.13 *center*): when the vortex is shed the bubble shrink to the minimum size, measured by L_{ws} , exhausting itself either in forming wake vortex ($SR < 3$) or in patches of vorticity zones in case of reattached flow ($SR > 3$). In the former case B is too short to allow reattachment, trapping the bubble which instead vents its portion - d - into the adjacent vortex, in which also the c -part rolled up, together with the portion supplied from the wake - e - and opposite vortex formation region - f . Once the vortex is shed the opposite one starts to form.

For the side ratio range $0.5 < SR < 1.0$ the body width is partially wet by the bubble that,

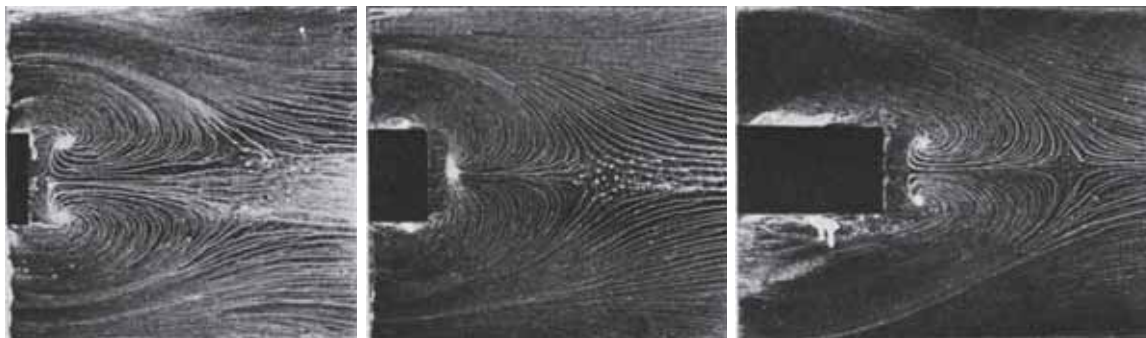


Fig. 2.13 Mean oil flow patterns around rectangular models of SR equal to 0.25 (*left*), 0.64 (*center*) and 1.75 (*right*). [partially reported from Laneville and Yong (1983)]

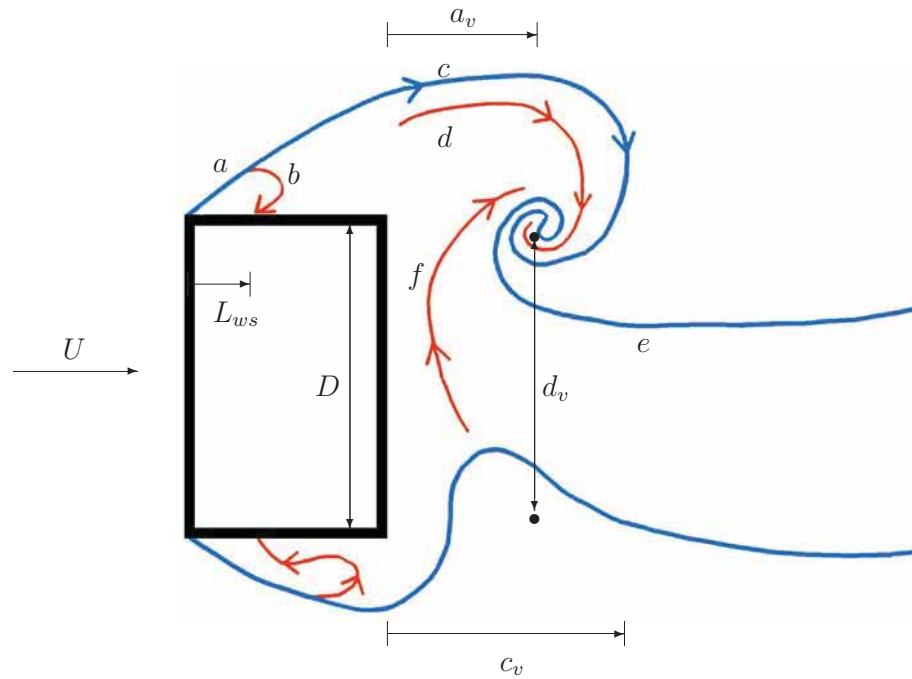


Fig. 2.14 Near wake vortex formation region as a filament line representation for a two-dimensional low side ratio rectangular cylinder; the upper (adjacent) vortex is on the verge to be shed while the lower one (opposite) has still to start growing up. [reproduced and revisited from Laneville and Yong (1983)]

when is fully expanded, extends over it. As mentioned, the initial vorticity divides, being in this case distributed mostly feeding the bubble to the expense of the portion feeding the adjacent vortex. The bubble interacts in turn with the forming vortex whose vorticity trigger a downwash effect, forcing the vortex to get closer to the center of the wake. In Fig. 2.13 (*center*) is clearly visible, concerning the critical section, that the two symmetric vortices collapse in the mid-height section line: as observed in Bearman and Trueman (1972) this entails the high suction local zone, which in turn corresponds to the low distance of the formation zone from the rear wall. The low base cavity volume corresponds to the lowest value of C_{pb} , as previously seen, as a result of the combined low values of lateral - d_v - and longitudinal - a_v - spacing. Laneville and Yong (1983) (see Fig. 4 of the original paper) showed that, after being linearly increased till $SR = 0.625$, for $0.625 < SR < 1.6$ the ratio L_{ws}/D vs. SR is a plateau, meaning the wet length to remain constant even increasing the afterbody length. At the same time L_{ws}/B increases in the range $0.25 \div 3.0$, while c_v/D moves towards the section rear till $SR = 1.0$, returning downstream with the same slope in the c_v/D vs. SR curve. In the critical section the shear layer curvature is maximal: this is supposed to be related to the interaction between the growing bubble and shear layer, which seems to be pushed away from the bottom (or top) side.

The range $1.0 < SR < 3.0$ is more complex to analyse since it extends from normal vortex shedding to reattachment on the side wall; we could have intermittent reattachment, even it is not detectable from the proposed visualization. In particular the reattached flow section regime ($2.8 < SR < 3.0$) is detectable from the St vs. SR curve, quite known in the classical literature (*e.g.* Brooks (1960)). Conversely the absence of a secondary region (or patch of vorticity) downstream with respect to the bubble, seems to indicate that no reattachment is possible, and to suggest the bubble to vent directly into the wake vortex

after being stretched during the growing process. Making comparisons with respect to a flat-plate normal to the oncoming flow regime, where the initial vorticity is almost completely released towards the wake, here a large amount of it is absorbed by the separation bubble, making the resultant wake vortex weaker, which implies in turn a lower value of drag.

Finally, for $SR > 3.0$, the reattachment makes this regime completely governed by the absorption of the initial vorticity by the trapped bubble; anyway its physics lies outside the interest of the present dissertation.

For the sake of completeness Parkinson (1963) addressed already rectangular cylinder with $0.75 < SR < 3 \div 4$ to be potentially unstable, being also able to gallop from rest (soft-oscillators); by contrast rectangular cylinders with shorter afterbodies, namely $0.375 < SR < 0.683$, need a quantum of external energy to reach the basin of attraction of a limit-cycle (hard-oscillators). He also identified the $0.75 < SR < 1.5$ rectangular cylinders to be unstable with respect to galloping, while for $SR = 4$ no gallop from rest was observed.

2.5 Turbulence effect

A detailed analysis about the joint effect of turbulence and afterbody is provided in Parkinson (1989). The overall effect exerted by the presence of turbulence intensity, and its increase in the flow, is the growing of the entrainment by the separated shear layers, thus thickening them and promoting first the above cited interference with the downstream corners, and then reattachment. Laneville and Parkinson (1971) showed the main consequences of turbulence are the switching from a hard-type to a soft-type oscillator behaviour for the rectangles with very low side ratio, as argued also by Novak and Davenport (1970), Novak (1972) and Nakamura and Ohya (1984), and a mitigating effect in reducing amplitude of vibrations. Nakamura and Tamonari (1977) showed the lowest SR for having soft-galloping switching from 0.75 in smooth flow to 0.5 for a $I_u = 12\%$; they also investigate the increase of entrainment effect above mentioned by placing spoilers in correspondence of the trailing edge corners, showing to affect the soft-galloping response of rectangular cylinder of SR ranging from 0.2 to 1.0.

Parkinson and Sullivan (1979) investigated the response of cantilevered square prisms in simulated boundary layer wind flow and reported that the turbulence effect fostered the interaction in their case. Bearman *et al.* (1987) showed that while for a low-damped system the turbulence always had a stabilizing effect, for medium and high damping the turbulence could either increase or decrease the amplitude of oscillations, depending on the range of reduced velocity of interest. Parkinson, relying on the work by Laneville (1973), empathized also the above underlined effect of turbulence in eventually stabilizing galloping instability by superimposing curves of constant angle of attack (data for $\alpha = 0^\circ, 3^\circ, 8^\circ, 16^\circ$) on I_u vs. SR map, aimed at showing soft, hard or stable galloping zones.

Some more elements about turbulence effect will be given in Ch. 3 in describing the present experimental rig for turbulence tests, and in Ch. 6 comparing the results of literature with those obtained by the author.

2.6 Interaction VIV-galloping

In the previous section we have seen that in certain situations the QS -theory constitutes a reliable basement in assessing the response of low-damped elastically mounted system

prone to galloping instability. Nevertheless the limitations of QS -theory have received extensive attention, even just after having demonstrated its reliability. Since the first formulation in Parkinson and Brooks (1961) the validity was discussed by the authors highlighting its limits, despite the good agreement between experimental and theoretical results showed in the paper. Several criteria have been reported by many authors indicating the boundaries for the applicability of the model, generally indicating that the QS -theory is applicable if an elastically-mounted body prone to the galloping instability is placed in a flow with sufficiently high reduced velocity. As implicitly suggested by Parkinson and Smith (1964), and reformulated later by Corless (1986), a limitation can be that the f_{vs} should be appreciably higher than f_n . Blevins (1977) proposed as a criterion $f_{vs} > 2f_n$, that means

$$\frac{1}{f_{vs}} < \frac{1}{2f_n} \Leftrightarrow 2\frac{U}{f_{vs}D} = U_r^* < U^* = \frac{U}{f_n D}.$$

Taking as example a square section we have $St = 0.135$ giving a requirement $U^* > 2(1/St) \approx 15$. This requirement was then revised by Blevins (1990) to $U^* > 20$, without further detailed explanation. Bearman *et al.* (1987) concluded the QS -theory is valid for galloping predictions if $U^*/2\pi > 4U_r^*/2\pi \approx 5$ that giving a threshold of $U^* \gtrsim 30$.

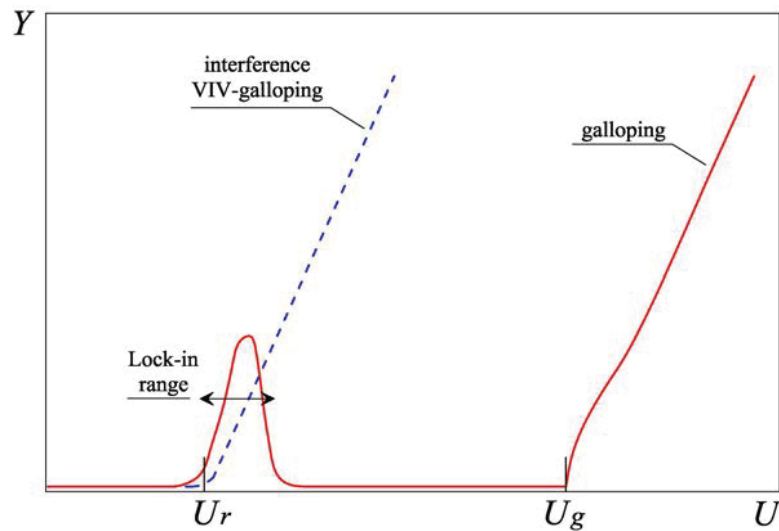


Fig. 2.15 Interaction sketch: — separated phenomena, - - - interaction VIV-galloping.

However, it has been observed that in case both VIV and galloping are possible, the interaction between the two form of oscillations can occurs. There are several factors playing a role in the eventual occurrence of this combined phenomenon; during the decades the different thresholds for each of them, always relating to the side ratio of the rectangular section which constitutes, so to say, a flow scenario apart, has been assessed through experimental and numerical investigations. In practice the interaction between VIV and galloping (from here on simply called as *interaction*) manifests itself as a phenomenon taking place at the resonance velocity. Hence, it exhibits the physical nature of galloping as an aerodynamic divergent instability triggered by the resonance condition. In Fig. 2.15 is proposed a schematic amplitude response plot related to a virtual study case for a square section. In the figure the dashed line simulates a possible so-called separated response in which the body experiences synchronization normally occurring at U_r^* ($St = 0.135 \Rightarrow U_r^* = 1/St = 7.4$),

and then exits from the lock-in bell; beyond a velocity range with no vibrations the galloping instability occurs at higher velocities. This happens for high value of U_g^* , that is in case of high damping or low values of mass parameter n as we saw in the previous section. In case U_g^* gets closer to U_r^* , the interaction can occur. The interaction between VIV and galloping constitutes a violation of *QS*-theory; however it has to be said that it can take place differently depending on how U_g^* gets close to U_r^* :

- $U_g^* > U_r^*$ *full interaction*: unrestricted oscillations starts at U_r^* instead of U_g^* , constituting the classic interaction mechanism (continuous line in Fig. 2.15);
- $U_g^* \gg U_r^*$ *partial interaction*: for some reasons the interaction onset occurs in-between U_r^* , as expected, and U_g^* ;
- $U_g^* < U_r^*$ or $U_g^* \ll U_r^*$ *quenching*: the vortex structure shed from the leading edges “freeze” the galloping instability till reaching U_r^* , when the oscillations can take place.

The third interaction-type will be treated apart in Sec.2.6.2, and will be better characterized, for what concern hydroelastic oscillations, in the following chapters.

2.6.1 Velocity and side ratio role on interaction

It is reasonable to figure out that what we call here velocity ratio $U_g^*/U_r^* = \Lambda$ is a crucial parameter, together with SR , that has to be taken into consideration in evaluating interaction. For the former suffice it to say that according to the actual European standards (*EC* 1, 2010) when Λ is either lower than 0.7 or larger than 1.5 the two phenomena can be considered separately. This has already to be dramatically inconsistent with specific literature and experimental evidences (Mannini *et al.*, 2013; 2014a;b), and it will be better analysed later. The importance of latter parameter relies more on fluid mechanics considerations, as reported in the above section, but some literature results may help to better understand the complexity of the phenomenon.

Since the first investigations about galloping on sharp-edged bluff section the interaction was observed and addressed as a failure of the *QS*-theory. In fact after a wide campaign, conducted on D-shaped and rectangular sections ($0.38 < SR < 2.48$), Brooks (1960) reported that “[...] results indicate that the steady state aerodynamic coefficients provide a useful approximation to the dynamic values; they also indicate that any theory which will completely predict the behaviour of such systems must include the effects of both negative aerodynamic damping and vortex resonance”. A low-damped square section response starting at resonance velocity was reported also in Parkinson and Brooks (1961). Parkinson and Smith (1964) observed the poorest agreement with theory for the lowest available damping on a square section model, namely the circle markers curve reported in Fig. 2.16 (*left*); the reason was addressed in the fact that the theoretical U_g^* lies too close to the correspondent U_r^* . For higher values of damping two stable limit cycles may be present in amplitude response. Despite the larger oscillation amplitudes experienced by a square section, it is particularly worth noting, with respect to the object of the present dissertation, that many authors put in light the more pronounced tendency to the interaction of rectangular section with $SR > 1$, which have shown a clear proneness to the interaction with vortex shedding, e.g. $SR = 1.5, 2.5$ (Smith, 1962) and $SR = 2$ (Parkinson, 1963, Parkinson and Modi, 1967, Santosham, 1966). Santosham (1966) in particular focused his investigation to the $SR = 2$

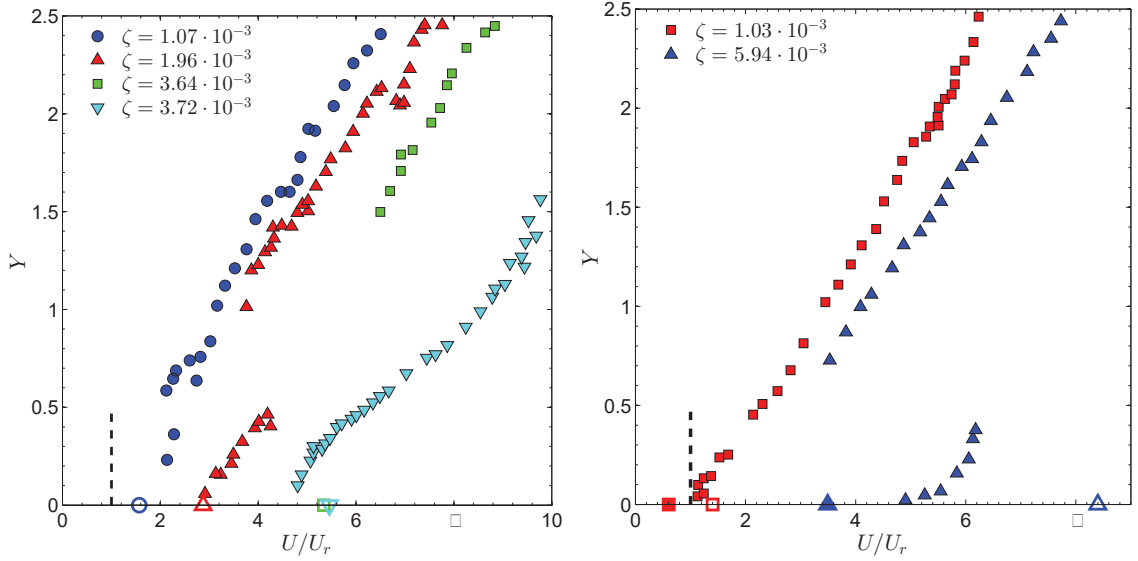


Fig. 2.16 response curves of a square section differently damped (*left*) and for a $SR=1.50$ section (*right*). - - -: resonance velocity, big empty markers: correspondent theoretical U_g^* derived from Smith (1962) and Parkinson and Wawzonek (1981), big filled markers: theoretical U_g^* proposed with the value of A_1 derived from present static tests (see Ch. 3).

rectangle. He started his investigations aimed at finding the causes of the discrepancy between Smith's results on square compared to a similar campaign on $SR = 2$ section, and to include the response function due to the formation of wake vortices in QS -theory. In some interaction-prone cases a partial interaction response was observed, recording the onset of oscillations at $U_g^*/3$ instead of U_r^* . He was also the first that identified the failure in QS -theory in the vortex shedding effect instead of the hysteresis in reattachment of the shear layers placing a splitter plate in the wake, suppressing it, obtaining a strong effect on the galloping response, although the QS -predictions continued to be in contrast with experiments. For example it was mentioned the failure in QS -predictions for $U_g^* < 10$, which means a velocity ratio $\Lambda > 10 \cdot (2\pi\bar{S}t) \approx 3.8 \div 5.6$, where the mean value of $\bar{S}t \approx 0.075$ can be derived from the range given in the literature for such a geometry, which varies from 0.06 (*EC 1, 2010*) to 0.9 (*Knisely, 1990*). A valuable and comprehensive database for the sections $SR=1, 1.5$ and 2 , reporting the whole set of aerodynamic characteristics and experimental conditions in deriving them, has been published by Mannini *et al.* (2014b), and reported in Appendix A for the sake of convenience and completeness.

Nakamura and Mizota (1975b) confirmed the QS -theory to be less reliable in predicting the response of a rectangular cylinder with $SR = 2$ with respect to a square prism because of its proneness to interaction with Kármán vortices.

A CFD study conducted on rectangle with $SR = 2$ by Itoh and Tamura (2002) gave a value of $Sc_{BD} = 112$ in order to separate the phenomena. It is worth noting that

$$U_g = 2 \frac{Sc_{D^2}}{A_1} \cdot f_n D \Rightarrow \Lambda = \frac{U_g}{U_r} = \frac{U_g^*}{U_r^*} = 2 \frac{Sc_{D^2}}{A_1} = 2 \frac{Sc_{BD}}{A_1} \frac{B}{D} St ; \quad (2.32)$$

one has also to take into account the remarkable variability of the stability parameter, namely $2.33 < A_1 < 7.82$ according to Mannini *et al.* (2014b), together with St as already seen, in order to derive a velocity ratio to have VIV and galloping not interacting between each other. Despite a possible range $\Lambda = 3.44 \div 17.3$, taking respectively $St = 0.06$ with

$A_1 = 2.33$ and $St = 0.09$ with $A_1 = 7.82$, it seems reasonable to assume $\Lambda \approx 11$ taking $\bar{St} = 0.075$ and $\bar{A}_1 = 3$.

Concerning the turbulence effect, Miyata *et al.* (1983) found the response of a $SR = 2$ rectangle to be still prone to instability even for a $I_u = 11\%$.

Fig. 2.16.*left* reported the galloping response curves for a $D = 1$ inch square section at four different values of damping, while in Fig. 2.16 (*right*) the response of a $SR = 1.5$ section for two different level of damping are reported. It is worth introducing the fact that the damping was varied through eddy currents dampers (ECD): this kind of technique allows to increase Sc , and in turns U_g^* , by just externally supplying almost completely viscous damping to the system; another common way to increase Sc is that of adding dead loads (masses) to the model. Without considering the limitation represented by the maximum weight that any test rig can sustain, the principal drawback is to decrease the system frequency that implies in turn two consequences: the first is to change the scale of reduced velocities and Re in turns (*e.g.* we could have the synchronization at a different U_r^* changing in this way the Re_{cr} values between two test cases), the second is that the rate of change of frequency is neither linearly dependent on damping nor predictable at all.

However, Fig. 2.16 (*right*) deserves some more comments. Given the lack of information available in Smith (1962), the QS -galloping onset velocity is reported with two different values, one derived Parkinson and Wawzonek (1981) for the two cases (empty big markers in figure), the other one (filled big markers) calculated with a representative value of A_1 proposed later on in this dissertation produced through static tests on different $SR = 1.5$ sectional models. In particular Parkinson and Wawzonek (1981) reported for the $\zeta = 0.00594$ case $\Lambda = 8.4$ and $\Lambda = 1.4$ for the $\zeta = 0.00103$ case. It turns out respectively $A_1 \approx 2.4$ and $A_1 \approx 2.5$ respectively for the two cases, while the value that will be proposed is $A_1 \approx 5.77$, giving two different values for the velocity ratio, respectively of $\Lambda = 3.49$ and $\Lambda = 0.6$. Parkinson and Wawzonek (1981) summarized the results of the experimental campaign conducted by Wawzonek (1979) overtly aimed at investigating also the interaction for the square section, giving, as principal result, a threshold for the velocity ratio of $\Lambda = 2.15$ necessary to separate the two phenomena. For the case reported in Fig. 2.16 (*right*) the interaction was attributed to the low-damped case given the linear increase of the oscillations departing from U_r^* , though not underlining the quenching ($\Lambda < 1$) effect because of the overestimation of both the galloping onset velocities. Nakamura and Mizota (1975b) indicated the threshold for the applicability of QS -theory in $\Lambda = 2 \div 3$, though remarking that for such low reduced velocities the agreement between theory and experiments could be fortuitous. Also Bouclin (1977) and Parkinson and Sullivan (1979) indicated a threshold for the QS predicted behaviour to be valid of $\Lambda = 2 \div 3$. Bearman *et al.* (1987) observed a critical velocity ratio of about $4 \div 5$ for the QS -theory to be accurate, while other interesting features were observed to be promoted by the variation on the angle of attack. Otsuki *et al.* (1971) studied this effect on the instability for rectangular sections with various SR , finding for $SR = 1.5$ a proneness to interaction for $\alpha < 7^\circ \div 8^\circ$. An extremely interesting study is reported in Nemes *et al.* (2012) concerning the α -variation of a square section, undergoing a wide range of FIV phenomena switching from galloping to VIV (diamond configuration that means $\alpha = 45^\circ$) to galloping ($\alpha < 15^\circ$). Besides the upper (UB) and lower branch (LB) of VIV nomenclature (Khalak and Williamson, 1997), they also addressed a new branch of vibrations called *higher branch* (HB) where the oscillations reach a maximum amplitude close to $\alpha = 20^\circ$, $U^* = 8$.

2.6.2 Quenching-effect

The theoretical treatment of a quasi-linear systems, as we hypothesized to have in our case, has been assessed since many decades and it will be proposed according to Minorsky (1960). In this *nearly linear domain* an electrical/mechanical 1-DoF can be handled by *DE* in the form

$$\ddot{x} + x + \mu f(x, \dot{x}) = 0 \quad (2.33)$$

where $f(x, \dot{x})$ is a non-linear function of x and \dot{x} , and μ is a small parameter. Being the system nonlinearity defined basically by the smallness of μ the solving method for such a problem is identified also as the method of small parameter(s). In fact either *Autonomous* (self-sustained oscillations) or *non-Autonomous* (subharmonic resonance, synchronization, parametric excitation etc.) problems are classified as nearly linear problems, for which μ is small. In cases in which the system is outside the synchronization range as defined in 2.2.2.1, that means no rational ratio with self-excited frequency exists, we can speak about *asynchronous quenching*. Where the auto-periodic exists we have the usual beats, while, when absent, there remains only a small hetero-periodic, forced frequency. Now let's focused on two cases reported in Minorsky (1960), namely:

- i** *asynchronous excitation*: this different nonlinear phenomenon can occasionally manifests itself when the nonlinear characteristic is represented by a polynomial of at least 5th degree to take into account an additional inflection point;
- ii** *asynchronous quenching*: in this case the hetero-periodic frequency is very high compared with auto-periodic one, $\omega_e \gg \omega_n$, the self-excited oscillation, whose frequency is ω_n , is destroyed or *quenched* by the external frequency ω_e .

The latter can be alternatively described as follows: in absence of the external frequency the system is at rest, but as soon as ω_e applied it begins to oscillate with his own frequency, ω_n , like if ω_e was a trigger source for the instability to occurs releasing the oscillations at ω_n . Here the magnitude of ω_e doesn't matter as in case of quenching .

It is quite easy to recognise here the *QS*-galloping (**i**) and quenching-type (**ii**) interaction mechanism. The physical interpretation of the Parkinson and Smith (1964) also referred to Minorsky (1962) in solving the nonlinear system through the method of the first approximation of Krylov and Bogoliubov, a small parameter method as well, although the interaction and the first attempt in explaining the phenomenon has been mentioned in Santosham (1966) with a nomenclature directly derived from Minorsky (1960). Moreover as from the definition of asynchronous quenching above reported it seems reasonable that Parkinson and Brooks (1961) were referring to this last contribute in publishing the first formulation of *QS*-approach for galloping, whereas the polynomial was varied in Parkinson and Smith (1964). Santosham (1966) tested numerically different approximation for the forcing term, reaching 11th order polynomial, attempting to insert also a periodical term in the second-kind *DE* system, in which the fluctuating lift coefficient C_{L_0} is taken into account, for modelling the interaction with wake vortices. He also perform numerical calculations to compare the response of $SR = 1$ and 2 rectangular sections in water and air. He also measured Y vs. U quenching response for a $SR = 2$ at a velocity ratio $\Lambda = 0.74$. Similar results were obtained also by Bouclin (1977) in a *WC* and Bearman *et al.* (1987) in a *WT*, respectively at $\Lambda = 0.54$ and 0.63. Bearman *et al.* (1987) also pointed out that the cause for the delay in the instability can be found looking at the forced-experiments carried

out by several authors (Bearman and Obasaju, 1982, Luo and Bearman, 1990, Nakamura and Mizota, 1975b, Otsuki *et al.*, 1974), in which the unsteady lift force may be subject to a sudden phase change near U_r^* , from negative to positive, thus leading to a generation of negative aerodynamic damping, and therefore to the onset of the excitation.

2.7 Chapter summary

In the present chapter a selective review on theoretical and practical aspects on the phenomenon of the interaction between vortex shedding and galloping is developed. The most interesting features and triggering mechanisms of the two separate phenomena are briefly illustrated in the first part as a basement for introducing the discussion on the interaction. Turbulence effect has been addressed too basing on literature evidences which can constitute a useful introduction for the experimental part performed in turbulent flow. Concerning the interaction VIV-galloping, experimental and theoretical aspects have been illustrated, leaving the numerical treatment of the phenomenon to Ch. 5. A specific section, rather very briefly treated, is dedicated to quenching effect being one of the most interesting expression of the interaction mechanism.

Chapter 3

Experimental methodology

Part. 1 - Wind tunnels testing

3.1 Introduction

As it has been reported in the previous chapter there are already several experimental campaigns to rely on in building a robust database for any kind of comparisons. Nevertheless, it is also true that sometimes it is necessary to put together tests carried out in different laboratories and experimental conditions, and this process necessarily leaves some gaps behind. For example, as reported in Appendix A, the data on aerodynamic characteristics are often quite scattered for the same geometry. Therefore, comprehensive experimental campaigns should be designed to characterize the sections here under investigation, putting the attention on the range of Λ and SR we want to describe.

The choice to principally test the $SR = 1.5$ derived from experimental evidences underlying its proneness to the interaction; in addition, given the large amount of data already reported in literature for the square cylinder in air (Bearman *et al.*, 1987, Parkinson and Brooks, 1961, Parkinson and Smith, 1964) and water (Bokaian and Geoola, 1984, Bouclin, 1977), and considering also the large campaign conducted on $SR = 2$ by Santosham (1966) in air (a response curve in water was given by Bouclin (1977) too for this section), it seemed useful to provide more details on that, trying to cover an as large as possible range of velocity ratios. Anyway, aerodynamic coefficients of $SR = 1$ has been tested by the author in air flow to make some comparisons with the literature. Obviously similar measurements were performed also for $SR = 0.67$, by rotating $SR = 1.5$ of an angle of $\alpha = 90^\circ$.

The test were conducted in air and water flow, so to investigate the largest spectrum of mass ratio ever. air flow tests, that is the object of the present chapter, were performed at *CRIACIV*¹ Boundary Layer (BL) Wind Tunnel (*WT*) in Prato (University of Florence, DICeA²) and at the boundary layer wind tunnel (in German *Windkanal*) of the Stahlbau (*WK*) in Braunschweig (Technical University of Braunschweig). The experimental rigs which are going to be introduced will be identified respectively by the a capital letter meaning the name of the city (*i.e.* respectively ‘*F*’ for Florence and ‘*B*’ for Braunschweig), while the type of the facilities, together with an eventual number identifying a different

¹Centro di Ricerca Interuniversitario di Aerodinamica delle Costruzioni e Ingegneria del Vento (Inter-university Research Center of Building Aerodynamics and Wind Engineering)

²Dipartimento di Ingegneria Civile e Ambientale (Department of Civil and Environmental Engineering)

set-up to perform the same test, is referred via subscript letters, meaning ‘s’ for static or ‘d’ for dynamic tests. It is also worth noting, given the crucial role played by the flow angle of attack with respect to the model, that in all the laboratories, wind tunnels and water channel, the zero angle of attack position was visually given at first and fixed through empirical expedients, and then double-checked by means of electronic inclinometers (or level gauges). For the laboratory instrumentation the reader can find detailed technical specifications in Appendix B.

3.2 Stahlbau *WK* experimental campaign



Fig. 3.1 View of the *Stahlbau* Boundary Layer Wind Tunnel (Windkanal) in Braunschweig.
[by courtesy of Dr.-Ing. Hodei Aizpurua Aldasoro]

For the first campaign here described the wind tunnel used for the experiments is an open suction Eiffel type one, whose length is 12.85 m including the cone-shaped fan. In case of necessity in developing the boundary layer the length could represent an issue to take into account, but given that we’re dealing with experiments to be conducted with an as smooth as possible flow it doesn’t affect the measurements. The laminar flow is obtained by flow straightener honeycomb; there’s also the presence of conditioning grilles, aimed to grasp eventual sources of filth (powder etc...). The aeroelastic section, whose dimensions are 1.40 m for the transversal width and from 1.20 to 1.35 m in height (given the presence of an adjustable ceiling), is placed at 1.25 m far from the sieve that is present up-wards with respect to the grilles, as reported with like ‘Test section 1’ in Fig. 3.2. To compensate the flow losses after passing through the rectifier section the nozzle is contracted with a ratio of $\approx 3.7 : 1$.

The flow is generated with an axial fan that is located at the end of the wind tunnel. This fan has fourteen blades and is capable of moving a volumetric flow of $50 \text{ m}^3 \text{ s}^{-1}$. The power is given by a three-phase motor with nominal power of 55 kW. The minimum and maximum wind speed is respectively 2 and 25 ms^{-1} . The turbulence intensity I_u in the wind tunnel in laminar conditions is less than 1%. The differential pressure micro-manometer, ManoAir500 (produced by Schiltknecht Messtechnik AG), allow to directly read the flow

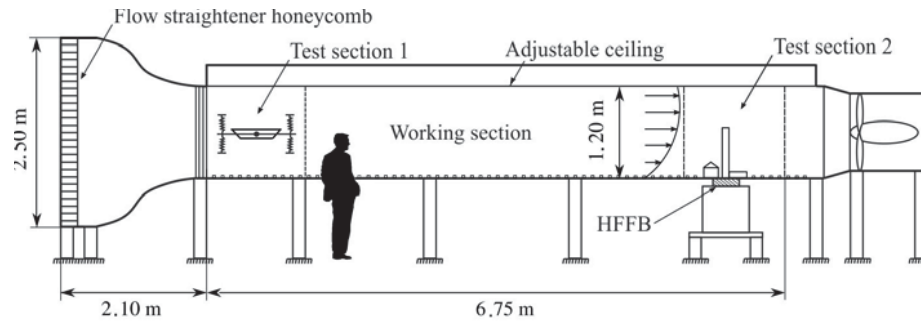


Fig. 3.2 Schematic lateral view of the windkanal; note that the test section utilized during measurements is the number one. [by courtesy of Dr.-Ing. Hodei Aizpurua Aldasoro]

velocity, as well as pressure, of gaseous media; furthermore temperature, effective ambient pressure and humidity are measured.

3.2.1 Static tests

Static measures are necessary in order to assess the aerodynamic characteristics of the section under investigation. The choice to start from a square section represents so to say a *benchmark* given the wide literature on it. After having designed the model and the set-up, the whole amount of measurements has been taken within the Master Thesis work by Marta Navarrete at Stahlbau.

The square sectional model designed by the author was built directly in the workshop of the Stahlbau thanks to the precious help of Dr. Mathias Clobes. Firstly a model made by aluminium tubing with dimensions $53 \times 53 \times 1600$ mm and thickness 2 mm, was sharpened, so that to reduce a bit the thickness and obtain very sharp edges. Then, four 2 mm thick aluminium plates, through which the carbon fibre model axis has been inserted and secured, were placed inside the model to increase its stiffness. The characteristics of the sectional model are reported in Tab. 3.1.

H53	
Section depth (D) [mm]	53
Section width (B) [mm]	53
Section length (L) [mm]	1200
$AR=L/D$	22.64
Model mass (M) [kg]	1.51
material	aluminium
Blockage [%]	3.8

Tab. 3.1 Characteristics of sectional models employed at Stahlbau WK.

Static rig (B_s) The static rig is reported in Fig. 3.3; the model was connected to six load cells (type HBM S2M), three at each model end, inserted in a purposely designed aluminium block with a hole in the center allowing to the model axis to slide in and to be blocked by means of three screws. Each force sensor is axially loaded (tension/compression) thanks to an hinged connecting rod that suppresses any bending stress because of the presence of a plate-shaped appendix able to flex in the measuring plain (*e.g.* for a torque exerted

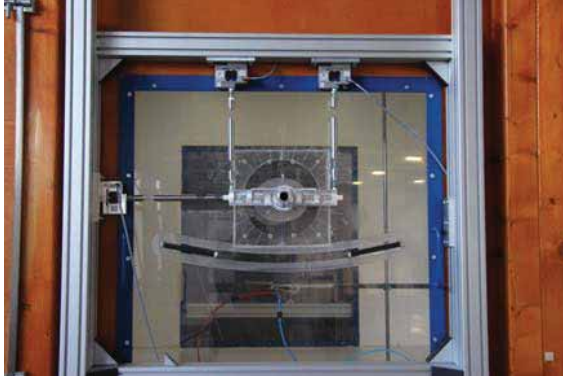


Fig. 3.3 Side view of the B_s static test rig composed by the three force sensors linked to the light and rigid aluminium arm sustaining the model.

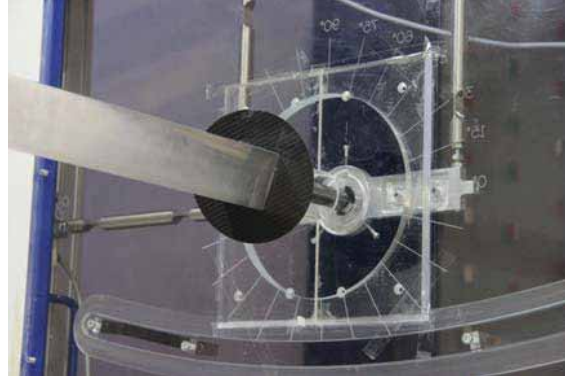


Fig. 3.4 View from the inside of the WK on a model end anchor point in which is visible the elliptical carbon fibre end plate.

by the model). The sensor (one per side) that measures the horizontal force is capable of a maximum load value equal to 100 N, while the limit for those placed and measuring vertically is 50 N. Hence, it is possible to measure F_D , F_L and M_z by simply composing the different 1D contributions of each cell. The model spanned through almost the whole WK width, while the portion of the axis between the end plates, visible in Fig. 3.4 and constituted by elliptical flat carbon fibre thin slabs, and the tunnel walls is protected by cylindrical shaped protection elements (not visible in the proposed pictures), and aimed at avoiding the vortex shedding from the model axis. The load cells were fixed to an external aluminium frame isolated from any vibration at which the WK could be subjected. The aerodynamic force coefficients were determined for angles of attack ranging approximately from -5° to $+20^\circ$, allowing to determine U_g^* and eventually the C_{F_y} polynomial coefficients. For the angle of attack detection a Pro3600 digital protractor was employed, providing a digital measurement; the absolute accuracy of the device is ± 0.05 for $\alpha = 0^\circ \div 10^\circ$, ± 0.10 for $\alpha = 10^\circ \div 90^\circ$.

The data acquisition (DAQ) system is constituted by a NI PXI-6284, an high-accuracy multifunction M Series module optimized for 18 *bit* analog input accuracy. This resolution is equivalent to $5\frac{1}{2}$ digits for DC measurements. The sensors are connected to this card. In Fig. 3.5 the results of C_D and C_L for a $Re \approx 11 \cdot 10^5$ are reported together with the evaluation for A_1 parameter. Generally speaking more attention has been given to the positive $\alpha = 0^\circ$ range, mirroring the negative drag and lift values to double-check the reliability of measured values (\square markers are superimposed to \diamond to identify mirrored values for C_D , $+$ markers are superimposed to \circ markers for C_L , while \square markers are superimposed to \circ markers in C_{F_y} results). The results for all the Re analysed, correspondent to $U = 10, 13, 17$ and 20 ms^{-1} , for the lateral force coefficient C_{F_y} is proposed in Fig. 3.6. It is possible to remark how the lowest Re result is scattered with respect to the two other central values, meaning the flow was too slow for a valid measurement. In Fig. 3.7, Eq. 2.21 is used to alternatively calculate A_1 parameter again for a $Re = 10.68 \cdot 10^5$; the value obtained is in good agreement with the value of 2.69 given in Parkinson and Smith (1964).

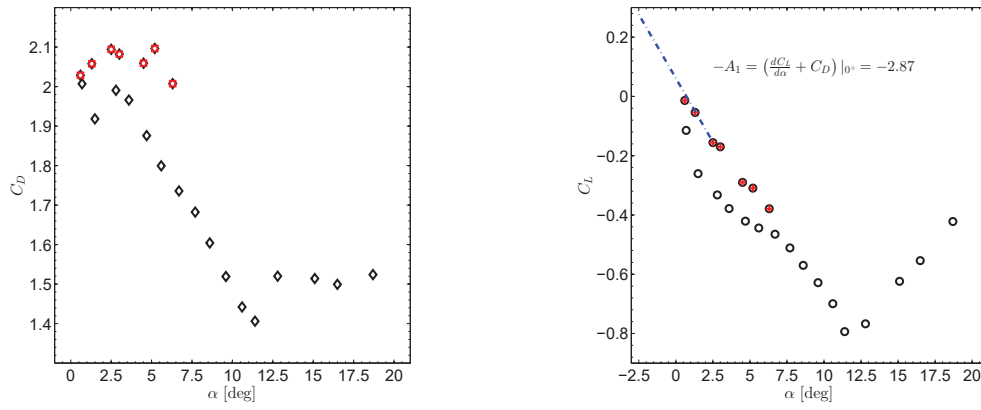


Fig. 3.5 Results of drag (*left*) and lift (*right*) coefficients for H53 tested with B_s rig, $Re = 10.68 \cdot 10^5$.

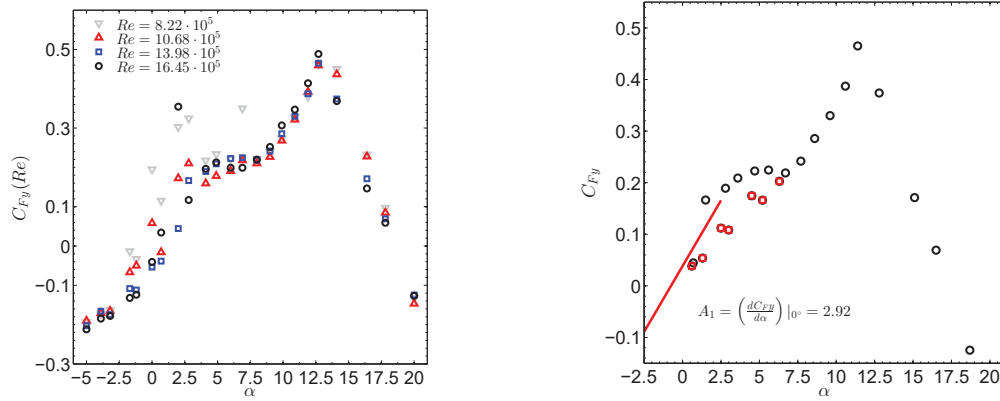


Fig. 3.6 Re -dependency for the lateral force coefficient C_{F_y} , for H53 tested with B_s rig.

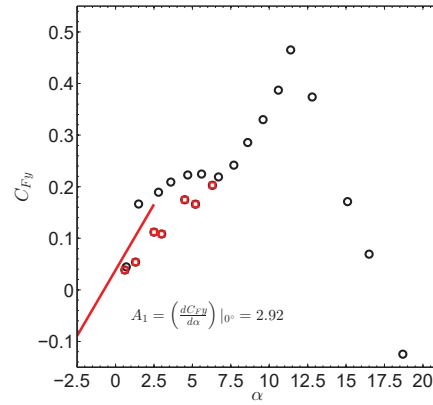


Fig. 3.7 Evaluation of A_1 parameter from the lateral force coefficient C_{F_y} , for a $Re = 10.68 \cdot 10^5$.

3.3 CRIACIV WT experimental campaign

A large part of air flow measurements has been performed at the CRIACIV WT (Fig. 3.8), which is an open-circuit Eiffel-type facility too with a contraction ratio of roughly 4:1. A schematic top-view of the tunnel, which develops on a total length of about 22 m is reported in Fig. 3.9. Apart from some specifications reported here below the reader can find additional further informations in Augusti *et al.* (1995).



Fig. 3.8 View of the CRIACIV-DICeA Boundary Layer Wind Tunnel in Prato.

3.3.1 Flow system and sectional models

The diffusers' "T-geometry" was designed to optimize the limited volume available, being indeed quite peculiar though very efficient. The height of the tunnel is 1.60 m, while the divergent side walls widen the section transversal width from 2.20 m right after the contraction to the 2.42 m of the BL test section; they were designed this way in order to compensate the formation of a boundary layer caused by the wall friction. The wind-speed is adjusted by means of a variable-frequency drive frequency (VFD, but also usually called *inverter* drive), and the pitch angle of ten blades by which the fan is composed: the higher the pitch the higher the suction acting on the air-volume up-stream in the tunnel. Such a system allows a maximum wind-speed around 30 ms^{-1} ; at the same time it ensures a high velocity resolution due to the fact that the inverter velocity can be precisely adjusted once an approximately velocity is imposed through the desired pitch angle. At the same time the flow can be assumed to be quite smooth indeed, as the resultant turbulence intensity obtained by means of hot-wire anemometry is much less than 1 %. In Fig. 3.10 are reported the results analysed after a recent measurement: the longitudinal turbulence intensity turned out to range between 0.69 and 0.73, depending on the range of velocities on which a mean value can be calculated. In the plots dotted lines are referred to the mean on the entire velocity range, while the dashed one is related to the velocities $U < 16 \text{ ms}^{-1}$: the step-shaped increment of I_u could derive from the effect of the larger scale vortices, usually not affecting the sectional models employed in aeroelastic tests; in any case I_u value is very low.

The pitch angle is manually controlled while the inverter frequency can be changed from

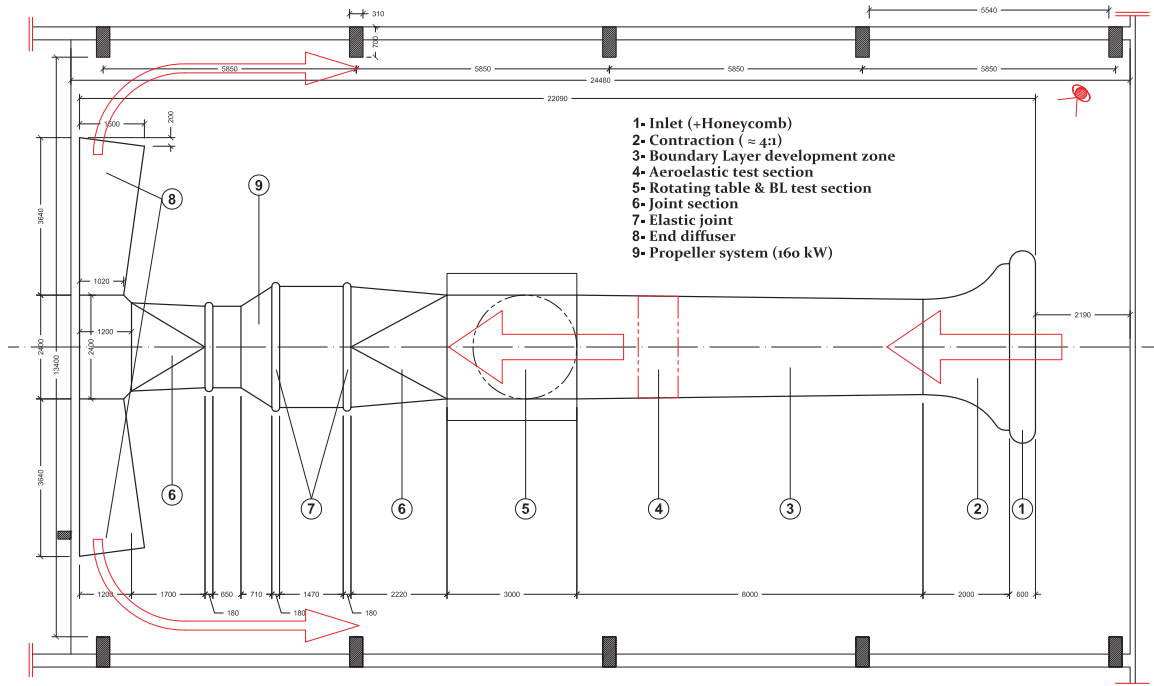


Fig. 3.9 Schematic view of the wind tunnel after the last survey conducted by the author (without office rooms and workshop); position 4 indicate the static and aeroelastic test section, while the symbol placed in the up-right position indicates the snapshot point of Fig. 3.8

remote using FRENIC Loader, a freeware software released by Fuji Electronics; all data (pressure, temperature, laser, force etc...signals), are simultaneously recorded via LabVIEW™, while data post processing and analysis were performed using MATLAB®. The

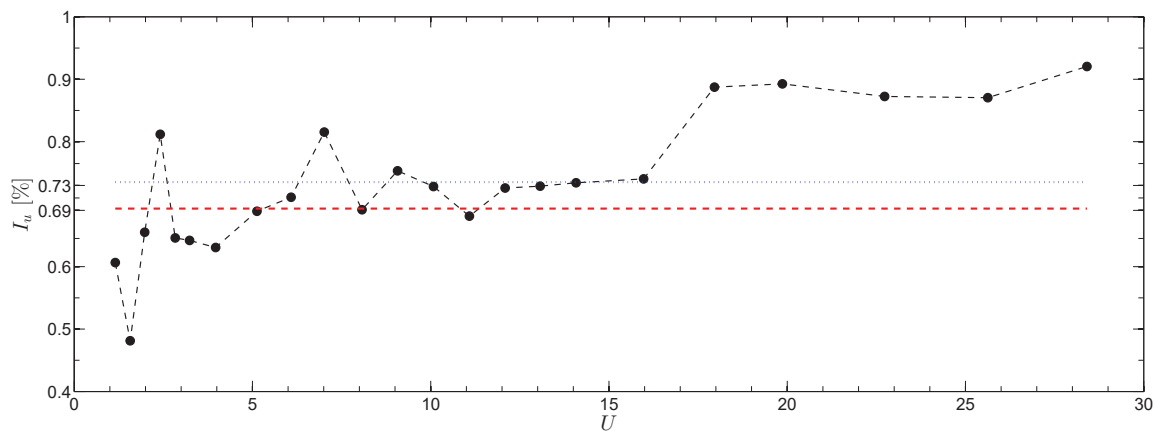


Fig. 3.10 Turbulence intensity variation by increasing flow velocity determined through hot-wire anemometry. [data recorded on December 2014]

characteristics of the sectional models employed in *WT* measurements are listed in Tab. 3.2; each section will be better characterized later on, within the paragraphs of interest.

	D77	D30/D45
Section depth (D) [mm]	77	30/45
Section width (B) [mm]	116	45/30
Section length (L) [mm]	986	1000
$AR=L/D$	12.8	33.3/22.22
Model mass (M) [kg]	1.73	2.63
material	plywood	aluminium
Blockage [%]	4.8	1.9/2.8

Tab. 3.2 Characteristics of sectional models employed at CRIACIV WT.

3.3.2 Static tests

Static tests are necessary in order to measure the aerodynamic forces exerted by the fluid on the body. Hence, they are needed to assess its proneness to the incipient instability by composing the lift and drag contribution (as already described in Ch. 2 §2.3). In order to get them, two different rigs have been used, referred as F_{s1} and F_{s2} , and 3D rendered in Fig. 3.11.

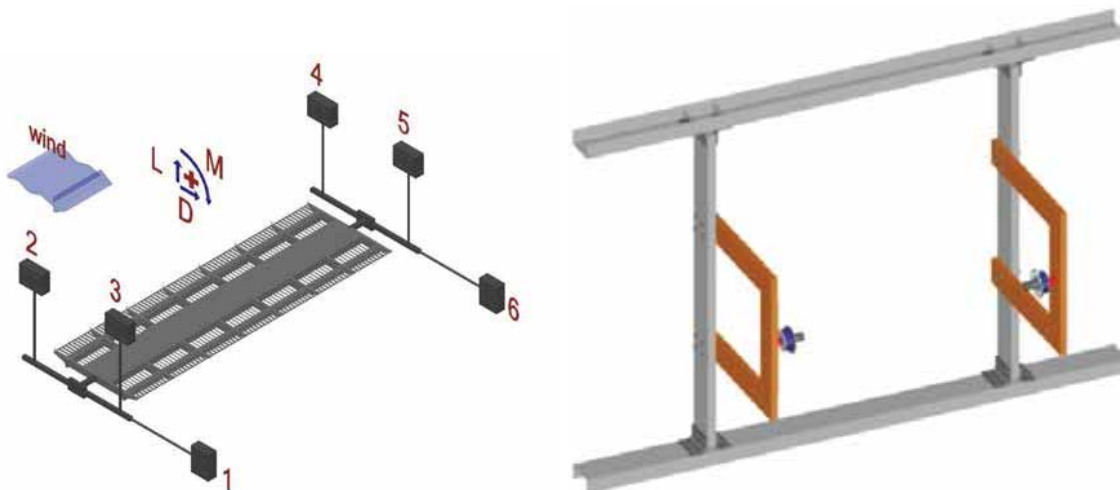


Fig. 3.11 (left) F_{s1} static test rig render view, with the position of the load cells with a generic cross-sectional bridge model suspended; (right) render view of the F_{s2} rig with the force balances connected to the rigid frames, without any sectional model suspended.

Static rig 1 (F_{s1}) For the static tests of the first campaign a wooden model was employed (D77); to promote 2D flow conditions, rectangular plates in plywood were provided at the model ends (their dimensions 450×150 mm, with thickness 4 mm), accordingly to the prescriptions given by Cowdrey (1963) and Obasaju (1979). The blockage ratio reported in Tab. 3.2 is calculated considering the model alone as D/H_{WT} , being H_{WT} the height of the WT test section. The model was also equipped with 28 pressure taps, located at the central section of the cylinder and along a longitudinal array, and registrations at a sampling frequency of 500 Hz were performed with piezoelectric pressure transducers and the system PSI DTC Initium.

F_{s1} is practically equivalent to B_s and alternatively referred as *load cells rig*. The model was connected to six load cells DS Europe 535 QD (three at each end as shown in Fig. 3.11 left) by means of a system of connecting rods with Cardan joints, which allowed the measurement

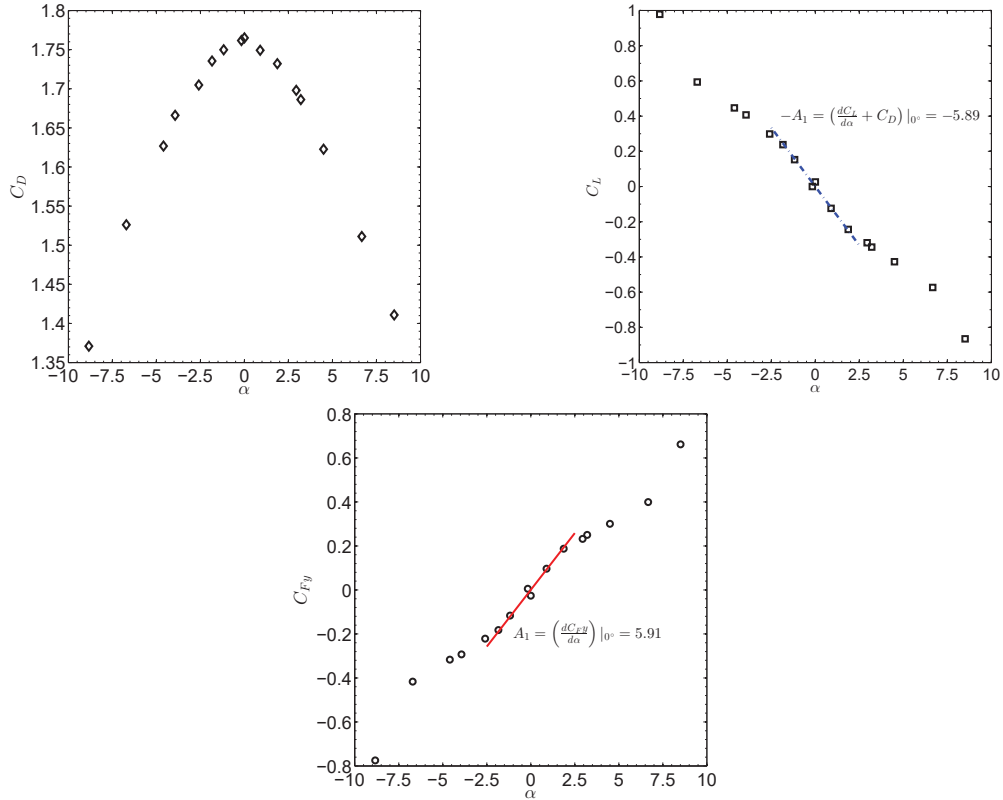


Fig. 3.12 (*top*) Results in terms of drag (*left*) and lift (*right*) coefficients for D77; the dashed line represents the linear regression of the lift around $\alpha = 0^\circ$, while the A_1 term is obtained from Eq. 2.21. (*bottom*).

of F_D , F_L and M_z by simply composing the contribution of each cell. The model was placed inside a rig consisting of two large plexiglass walls supported by two metallic frames connected both to the floor and the ceiling of the wind tunnel. The load cells were fixed to these frames. Aerodynamic coefficients were determined for angles of attack ranging approximately from -10° to $+10^\circ$, hence, for this experimental campaign, only the QS -galloping onset velocity, U_g^* , can be obtained from the results shown in Fig. 3.12 relatively to the highest Reynolds number tested ($Re \simeq 90 \cdot 10^3$). Present static tests results have already been published in Mannini *et al.* (2013), and here they are re-proposed slightly changed in terms of A_1 value. The model showed an appreciable symmetry in drag response, in good agreement with Norberg (1993) for the $\alpha = 0^\circ$ value, and a remarkable linearity around $\alpha = 0^\circ$, which makes the slope of $C_{F_y}|_{\alpha=0^\circ}$ easier to obtain. Given the presence of pressure taps with which the model was equipped, the Strouhal number of the section has been evaluated by spectral analysis of lift force (Fig. 3.13.*top*) and pressure coefficient at the midpoint of the lower side (Fig. 3.13.*bottom*) signals for D77, by which a resultant value of $St = 0.106$ was found. This value has been assumed, from here on, to be most reliable for $SR = 1.5$ in air flow. In the lift coefficient spectra the first natural bending frequency of the model fixed is present in addition to the dominant peak representing the St frequency. Then, it is also possible to notice the St super-harmonic resonance of order two for a higher velocity in the lift spectrum, which is even more visible in the pressure coefficient spectra.

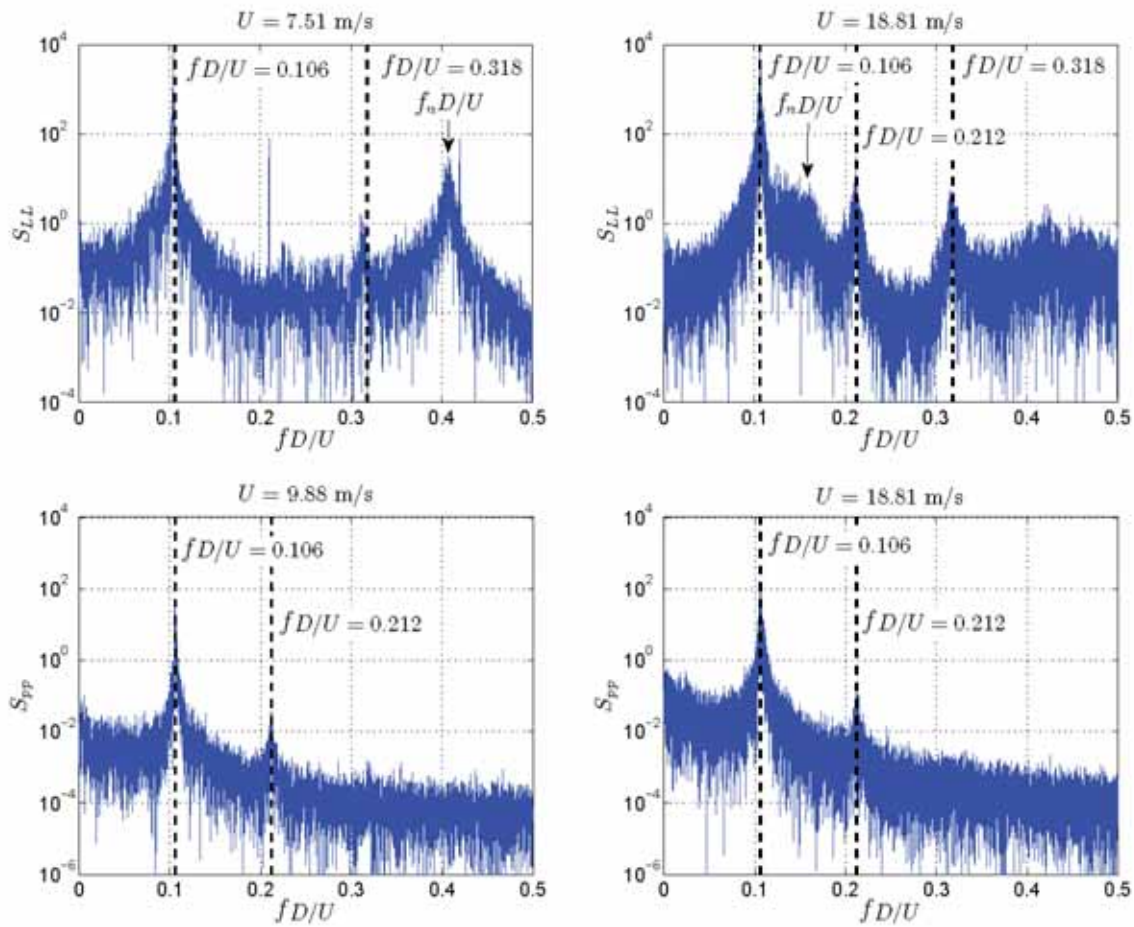


Fig. 3.13 (top) D77 sectional model's power spectral density of lift coefficient (S_{LL}) and (bottom) pressure coefficient at the midpoint of the lower side (S_{PP}), for four wind speeds; dominant peaks represent the St chosen value for $SR=1.5$.

Static rig 2 (F_{s2}) Another campaign has been conducted after the design of a new test rig, so-called *balance rig*. Tests on stationary cylinders were conducted not only on D77 but also using another model, purposely designed in aluminium with particular attention to the sharpness of the edges (D30 or D45 depending on which SR configuration is mounted). The aluminium model wasn't equipped with any pressure taps and resulted to be slightly heavier to get a higher stiffness with respect to D77, expressing also a lower Re range implying consequences in terms of aeroelastic response (see §3.3.3). It is worth noting that the same spectral analysis for deriving St values was not performed for F_{s2} . The measurement of the aerodynamic force coefficients at various angles of attack were performed by means of two six-components strain-gauges dynamometers ATI FT-Delta SI-165-15, characterized by a high resonance frequency. The force transducers are placed one at each end of the model and supported by a rigid steel frames jutting out from an upright steel columns. The results in terms of St for D77, D30 and D45 sections were determined via hot-wire anemometry and reported in Fig. 3.15: the probe was mounted $5D$ behind and $2.5D$ below the center of the midspan section of the model. Values equal to $St = 0.104$ and 0.1038 respectively for D77 and D30 models, were detected which is in line with the value given by Norberg (1993) of 0.105 . Just to give a more practical term of comparison, these values are remarkably different from that one reported in the standard *EC 1* (2010), in which



Fig. 3.14 Front view and zooming on one side of the D30 model in correspondence of the junction with the balance.

$St = 0.09$ is suggested.

Anyway, a St value of 0.106 for the $SR = 1.5$ was kept after having performed the spectral analysis previously addressed. Concerning D45 section, a value of 0.1255 was taken as valid, as indicated in Fig. 3.15.*right* in dashed line: in the plots for each sectional model the indication is not merely a mean value but it takes into account either the operational range in which the aeroelastic test were carried out, always considering that U_r^* to be generally in the lower velocity range, and the poorest reliability of near-zero velocities measurements.

In addition to the detection of the characteristic Strouhal numbers, for each model the results in terms of C_D , C_L , Re and C_{F_y} are proposed, for D77, D30 and D45 in Fig. 3.16-3.24. The slopes were obtained by calculating the linear regression of data in the range $-2.5^\circ < \alpha < +2.5^\circ$. Again, as showed for the square section tested in *WK*, attention has been given to the positive $\alpha > 0^\circ$ range, mirroring the negative values of drag and lift to double-check the reliability of measured values (the same notation for markers has been here used according to that in § 3.2.1). Both the A_1 parameter evaluations, either calculated by using C_D and C_L or simply C_{F_y} , have been reported. The Re - effect plots is very effective for D77 and D30 to assess the reliability of the measurements, although the highest value has always been chosen for final results.

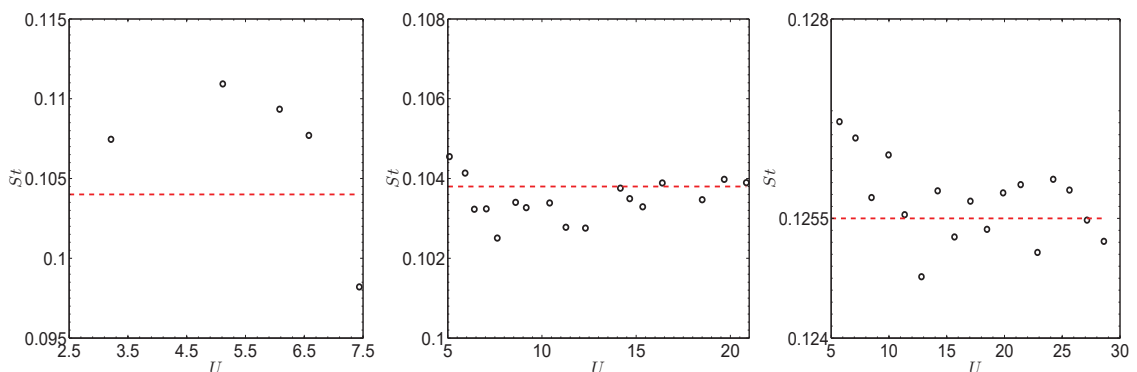


Fig. 3.15 (*left*) D77, (*center*) D30 and (*right*) D45: hot-wire anemometry results performed in different velocity ranges; the dashed line is placed in correspondence of the mean values in the range of velocity giving reliable values though the chosen values derive from spectral analysis.

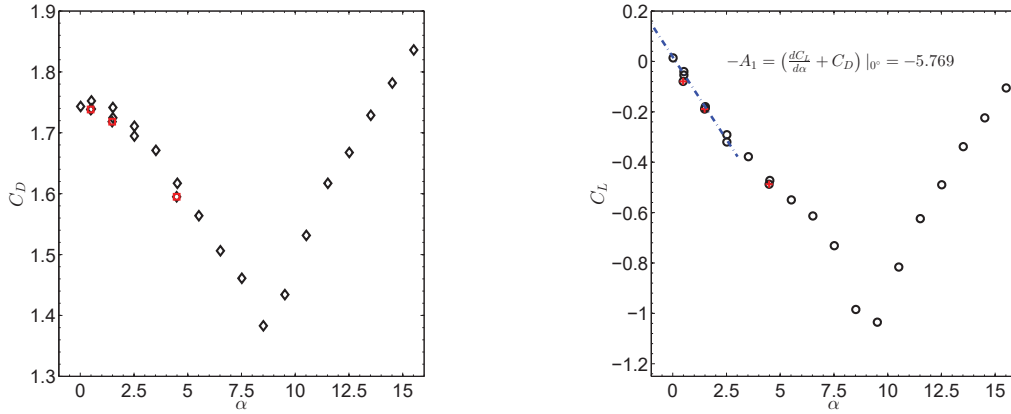


Fig. 3.16 Results of drag (*left*) and lift (*right*) coefficients for D77 tested with F_{s2} rig, $Re = 147095$.

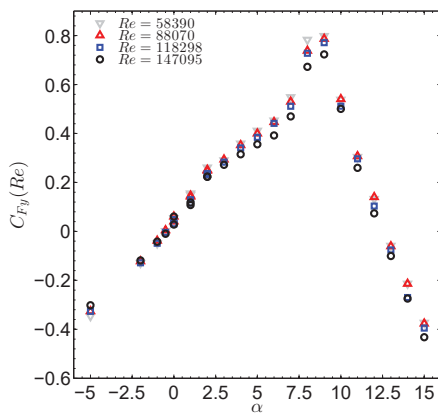


Fig. 3.17 Re -dependency for the lateral force coefficient C_{F_y} , for D77 tested with F_{s2} rig.

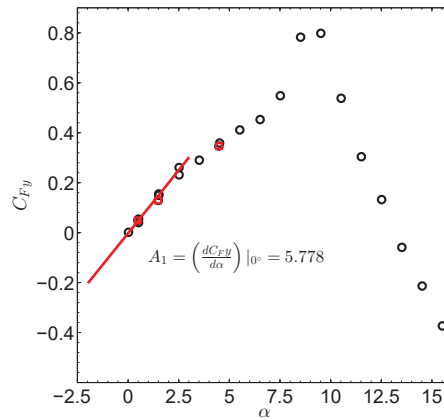


Fig. 3.18 Evaluation of A_1 parameter from the lateral force coefficient C_{F_y} , for a $Re = 14.71 \cdot 10^4$.

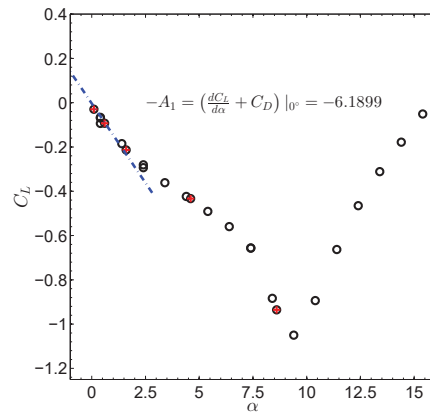
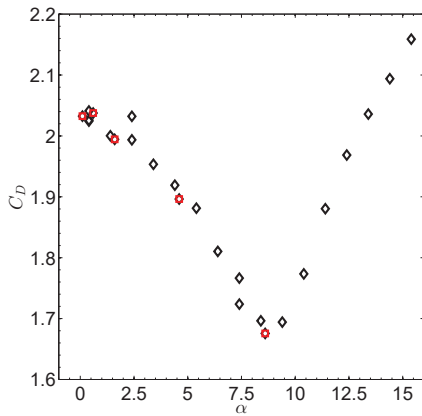


Fig. 3.19 Results of drag (*left*) and lift (*right*) coefficients for D30 tested with F_{s2} rig, $Re = 57455$.

There's a good agreement between the values of A_1 found with F_{s1} rig compared with F_{s2} results (a value of 5.9 against 5.7); a higher value has been derived for D30 ($A_1 = 6.2$). As expected from literature evidences D45 showed to be an hard-type oscillator, being negative the C_{F_y} slope around $\alpha = 0^\circ$. Moreover, Fig. 3.23 shows the Re -dependency of D45 section:

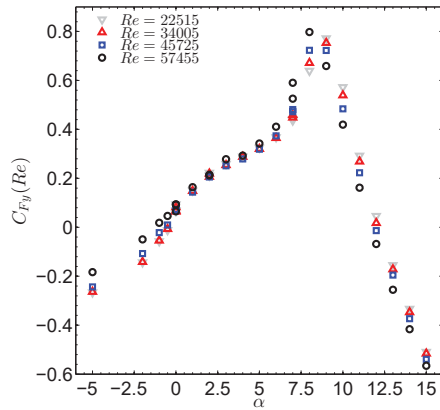


Fig. 3.20 Re -dependency for the lateral force coefficient C_{F_y} , for D30 tested with F_{s2} rig.

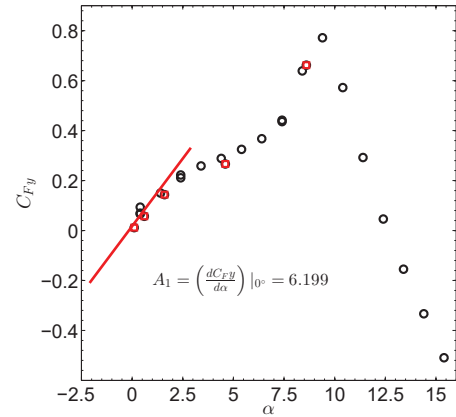


Fig. 3.21 Evaluation of A_1 parameter from the lateral force coefficient C_{F_y} , for a $Re = 57.45 \cdot 10^3$.

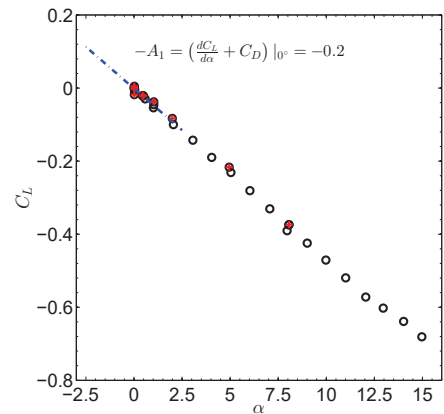
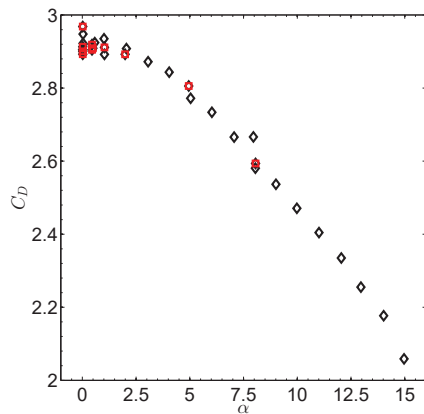


Fig. 3.22 Results drag (*left*) and lift (*right*) coefficients for D45 tested with F_{s2} rig, $Re = 85722$.

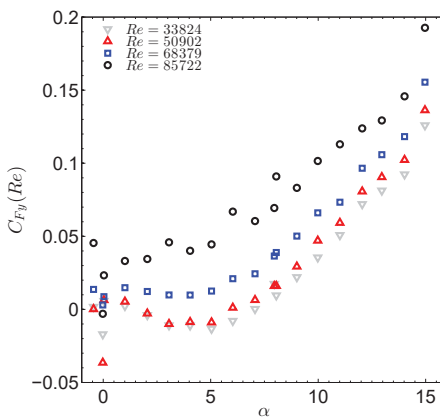


Fig. 3.23 Re -dependency for the lateral force coefficient C_{F_y} , for D45 tested with F_{s2} rig.

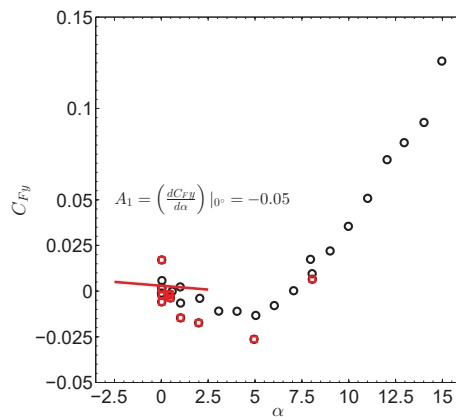


Fig. 3.24 Evaluation of A_1 parameter from the lateral force coefficient C_{F_y} , for a $Re = 85.72 \cdot 10^3$.

this should be considered as physically representative of the fact that static tests on this sectional models are critically sensitive to any change in the mounting system and other variables affecting the measures. In fact, for any chosen Re , the section can be considered as stable concerning its proneness to the galloping instability in this flow condition.

3.3.3 Aeroelastic tests

Response curves in terms of oscillation amplitudes by increasing the flow velocity represent the core of aeroelastic results. They were obtained by measuring displacement time histories which will be analysed after having well identified mechanical and dynamical characteristics of each test case; moreover they have to be analysed knowing the aerodynamic characteristics of the sectional models. The results will be here given in terms of standard deviation (*rms*) of nondimensional oscillation amplitudes vs. flow velocity reduced with respect to critical one: in this way it results easier to observe the interaction onset, eventually occurring at $U/U_r = 1$.

Two different dynamical test rigs will be introduced, thus the reported results belong to different campaigns performed at CRIACIV WT, in different periods of the Ph.D. work. It has to be remark that some of them were taken without the author presence, although the activities and the design of test rigs has been carried out in the laboratory together with the other colleagues. The author acknowledges all of them for the contributes made available for the present work.

Springs rig (F_{d1}) In this rig both plunging and pitching modes are allowed; the sectional model was elastically suspended, whose axis, realized by carbon fibre tubing, was clamped to a rigid suspension arm (one for each side), in turns elastically connected through eight vertical coil springs (four on each side), each one with a nominal stiffness of 5340 N/m (Fig. 3.25.*left*). The aluminium suspension arm minimizes the weight, though it was designed like a 3D truss with an high stiffness in its plane (Fig. 3.25.*right*). The system damping is minimized by realizing the connection between each spring and the arm with a thin line cable, so to maximally suppress the friction between steel parts. The springs are pre-stressed to promote an as linear as possible response. Then, in order to have only 2-DoF allowed to the system, the oscillation of the model in the along wind direction, as well as the rotation about a vertical axis have been constrained through four long steel cables which are connected to the model by means of two low-friction ball bearings, for suppressing the drag force though not interfering with the pitching DoF; such a system was realized by Mannini (2006), and it is still employed for this test rig. Each one of the two



Fig. 3.25 (*left*) View of the *springs rig* F_{d1} from the mounted D77 model rear towards the tunnel inlet; (*right*) close-up view on one side of the rig showing the suspension arm and the springs mounting system.

four-springs group is connected to a rigid aluminium square frame mounted inside the tunnel and screwed on the bottom and the ceiling. To enforce 2D flow condition, the volume in which the model is suspended is confined by means of 2 vertical plexiglass plates, whose edges facing the flow were purposely sharpened to ‘cut’ the flow aside.

Three non-contact optical laser transducers by Micro-epsilon Model OptoNCDT 1605 determine the displacements of the model in the aeroelastic set-up: these lasers use a semiconductor with 675 nm wavelength and a maximum output power of 1 mW and their functioning principle is based on triangulation. The output voltage range is ± 10 V which corresponds to a displacement of roughly ± 100 mm, then, the lasers are connected to a DAQ board which is the interface from the signals and the laboratory PC. Each laser pointed an aluminium plate jutting from the rigid horizontal arm.

In Tab. 3.3 the test cases identified by the capital letter ‘A’ were investigated through the F_{d1} rig, varying the Sc by adding external masses to the system or increasing the damping by wrapping some tape around the springs.

Blades rig (F_{d2}) A second dynamical test rig was realized in order to quicker mount and set-up the system plunging frequency and also to get the lowest possible damping. Two C-shaped steel profiles, welded below the bottom and above the ceiling of the *WT*, were equipped with threaded holes in which two vertical rectangular profiles with rounded corners (having $150 \times 50 \times 5$ mm along-, across-wind and thickness dimensions), can be easily screwed to fix their ends. The distance between this two vertical element defines the longitudinal length of the models tested. Two horizontally mounted shear-type frames connect the model to the vertical elements: the horizontal steel plates, so-called *blades*, measure 50 mm in across-wind direction and 5 mm in thickness, representing the columns of the shear-type frames. Each one of these frames horizontally jut out by means of extremely compact and thick steel blocks, so constituting the interface, or better the physical constraint, between vertical profiles and blades frames. The two blades of a frame are vertically connected through an arms in which the model axis is in turn pulled-on; these arms are designed as a Vierendeel steel truss to be as light and rigid as possible. Due to the very large flexural stiffness of the two vertical arms, at the first order, only a vertical displacement can be considered to be allowed. The system stiffness can be varied by simply changing the nominal length of the blades (L_b); the rigid blocks are horizontally divided into two parts which are shaped to be closed each other on the internally sliding blade pressing it tightly



Fig. 3.26 (left) View of the *blades rig* F_{d2} from the mounted D77 model rear towards the tunnel inlet; (right) render view of the test rig without any model mounted.

on two zones, guaranteeing a fixed support. Of course the oscillating blades percentage mass changes by changing L_b so that its value has to be calculated case by case. Two lasers were placed below each vertically moving frame, to measure the displacements as for F_{d1} . F_{d2} test cases are identified by the capital letter ‘B’ in Tab. 3.4; Sc was varied by varying L_b and/or by adding additional masses to the system.

3.3.3.1 Free-decay test

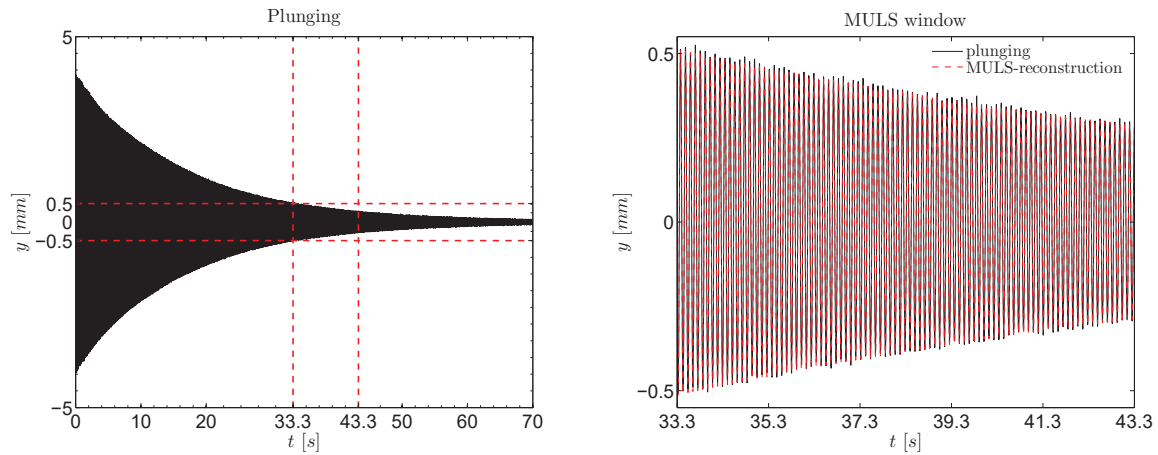


Fig. 3.27 (left) plunging window on which the Muls analysis has been applied; (right) Muls reconstructed signal superimposed to the windowed plunging signal.

To dynamically characterize the dynamical systems above introduced, a reliable identification procedure is needed. This was done by conducting still-air measurements to derive the mechanical characteristics of the moving parts of the system (rig, model, appendices eventually mounted like additional masses or tape to increase damping etc. . .), given its sensitivity to any change in the test environment or mounting process, either purposely induced or just resultant with no apparent reason after the identification procedure. Being F_{d1} is a 2-DoF test rig, it would need to be identified for both plunging and pitching vibrational modes, to uncouple the contributes in terms of mechanical damping ratio (ζ) and in terms of frequencies of vibration, although only the quantities related to plunging will be used in analysing present results. Nevertheless, a so to say ‘parasitic’ rolling mode is often present and arises from displacement’s time traces. This is due to the rig imperfections and/or unbalances of masses, though imperceptible, which give place to some asymmetries with respect to the center of the sectional model, and make this last one to roll, so that differential displacements from one model end to the other are present overlapped to those due to the heaving mode. On the other hand F_{s2} is theoretically designed to allow only plunging, but, even if if pitching is mechanically suppressed, a rolling mode caused by, again, the practical unlikelihood in building and mounting the set-up with perfect symmetry with respect to the midspan of the model, is still present. Furthermore, it was usually observed a different initial inflection for each blades-frame.

A part from the issues connected to the experimental rigs there are other aspects which has to be considered in performing a free-decay tests.

The test consists in recording the time histories of model displacement in one or more model control points which are analysed afterwards. In case that only plunging is allowed

test case	f_n [Hz]	m [kg]	ζ [%]	Sc_{BD} -	U_r [ms ⁻¹]	U_g [ms ⁻¹]	Λ -	Re_{cr} -	n -	m^* -
D77-A1	14.73	4.89	0.16	9.84	10.7	5.7	0.53	54965	6.81E-04	1101
D77-A2	9.84	10.96	0.08	11.05	7.1	4.3	0.60	36701	3.06E-04	2465
D77-A3	14.84	4.82	0.52	31.50	10.8	18.3	1.70	55417	6.91E-04	1084
D77-A4	8.98	13.16	0.42	69.74	6.5	24.6	3.76	33605	2.53E-04	2957
D77-A5	9.03	13.03	0.44	71.55	6.6	25.2	3.86	33606	2.56E-04	2929
D77-A6	9.09	12.83	0.83	134.25	6.6	47.9	7.24	34004	2.59E-04	2884
D77-A7	9.11	12.79	0.99	158.45	6.6	56.7	8.54	34077	2.62E-04	2876

Tab. 3.3 Test cases for plywood model (D77) in smooth flow on F_{d1} rig. [Relative stability parameter and Strouhal number are $A_1 = 5.7$ and $St = 0.106$].

test case	L_b [mm]	f_n [Hz]	m [kg]	ζ [%]	Sc_{BD} -	U_r [ms ⁻¹]	U_g [ms ⁻¹]	Λ -	Re_{cr} -	n -	m^* -
D77-B1	674	9.83	4.832	0.0841	4.79	7.1	1.9	0.27	36670	7.3E-04	1034
D77-B2	674	9.80	4.832	0.0899	5.12	7.1	2.0	0.28	36546	7.3E-04	1034
D77-B3	600	11.98	4.696	0.1313	7.20	8.7	3.5	0.40	44690	7.5E-04	996
D77-B4	600	11.72	4.916	0.1444	8.26	8.5	3.9	0.46	43700	7.2E-04	1039
D77-B5	674	5.93	13.060	0.0702	10.81	4.3	2.6	0.60	22110	2.7E-04	2795
D77-B6	490	9.94	12.856	0.1257	19.00	7.2	7.6	1.06	37072	2.7E-04	2744
D77-B7	490	16.40	4.494	0.5700	30.39	11.9	20.1	1.69	61148	7.7E-04	968

Tab. 3.4 Test cases for plywood model (D77) in smooth flow on F_{d2} rig. [Relative stability parameter and Strouhal number are $A_1 = 5.8$ and $St = 0.106$].

test case	L_b [mm]	f_n [Hz]	m [kg]	ζ [%]	Sc_{BD} -	U_r [ms ⁻¹]	U_g [ms ⁻¹]	Λ -	Re_{cr} -	n -	m^* -
D30-B1	674	8.98	5.815	0.0546	24	2.5	3.2	1.24	5084	9.5E-05	3522
D30-B2	590	8.92	8.947	0.0915	62	2.5	8.0	3.17	5047	6.2E-05	5379
D30-B3	545	8.70	11.881	0.1220	111	2.5	14.0	5.68	4927	4.6E-05	7210
D30-B4	490	9.43	13.785	0.1389	144	2.7	19.8	7.40	5340	4.0E-05	8254
D30-B5	490	9.45	13.785	0.1430	150	2.7	20.5	7.68	5347	4.0E-05	8321
D30-B6	490	15.01	5.476	0.1950	82	4.2	17.8	4.20	8496	1.0E-04	3336
D30-B7	490	15.19	5.476	0.2300	97	4.3	21.5	4.99	8597	9.9E-05	3361

Tab. 3.5 Test cases for aluminium model (D30) in smooth flow tested on F_{d2} rig. [Relative stability parameter and Strouhal number are $A_1 = 6.2$ and $St = 0.106$].

test case	L_b [mm]	f_n [Hz]	m [kg]	ζ [%]	Sc_{BD} -	U_r [ms ⁻¹]	Re_{cr} -	n -	m^* -
D45-B1	650	9.35	5.815	0.0546	10.26	3.4	10053	2.1E-04	3522
D45-B2	490	15.07	8.947	0.0915	28.52	5.4	16208	1.4E-04	5379

Tab. 3.6 Test cases for aluminium model (D45) in smooth flow tested on F_{d2} rig. [Relative Strouhal number are $St = 0.1255$].

one single time trace would be theoretically sufficient, while for detecting the pitching vibrational mode, as in the case of F_{d1} , at least two lasers on a the same model side are needed, plus another one on the other side to double-check the relative displacements of the model along the whole span and to control the rolling motion. However, for F_{d2} rig two lasers are enough, given that the model cannot rotate around its axis. The damping and frequency of the system are measured imposing several times an initial amplitude (y_0) condition and then recording the decay of the oscillations till a near-zero value. Sometimes

the initial condition has been imposed by suddenly releasing the model previously attached to two electro-magnets screwed on the tunnel floor, allowing to quite precisely set it up; alternatively an external impulse is given simply hitting the model by hands. It turns out that the test is conducted in still-air, while theoretically the damping should be measured in the void as the contribution of still air is slightly nonlinear and increases with the amplitude of the oscillation. Nevertheless, in still air this effect can be neglected by imposing small y_0 values. The overall nonlinearity of damping in still air was verified to be moderate in the present case.

The theoretical values of the oscillating mass for each test case is given by the model mass M , eventual externally mounted masses m_{add} , the system moving parts and participating mass of springs or blades; the effective value was anyway alternatively calculated by adding several sets of known masses and measuring the natural frequencies, according to the procedure outlined in Bearman *et al.* (1987). The system identification was performed by means of MULS method Bartoli *et al.* (2009): this algorithm assumes a coupled linear system with a given number of DoF and the pairs of complex conjugate eigenvalues and eigenvectors are iteratively estimated via nonlinear least-squares minimization of the sum of the squared differences between the measured and the reconstructed time histories of the displacements.

An example of identification result, performed in a test case on F_{d2} , is here proposed: from the time histories of two control points' displacements, the plunging mode signal is obtained by averaging their contemporary values recorded. Then, a maximum value of $y_0 = 0.5$ mm was selected for identification on a time-window of a few seconds, namely 10 s in the example reported in Fig. 3.27.*left*). In Fig. 3.27.*right* the MULS-reconstructed signal is overlapped to the original one. In the following section the detected frequencies and damping ratios have been derived accordingly to the procedure above outlined. It is worth noting that in general different values of damping can be detected by starting from different y_0 values in the time histories extracted for the identification procedure above described. This is due to the fact that the estimated damping value is non-linear with amplitude of vibrations. The y_0 values were taken, time by time, such that the decay test repeatability was kept for several tries in the same dynamic boundary conditions.

3.3.3.2 Smooth flow

In this section a general presentation of the results obtained in smooth flow experimental campaigns are described. Some results has already been published either in journals or conferences proceedings, and will be referenced time by time. It is worth underlying that each response curve is grouped by sectional model tested, collapsing different values in terms of Scruton number. The initial slopes of the main instability branches (those individuated by means of triangles in the figures) reported are different, even concerning the same sectional model, depending on the Sc (objective physical parameter) and the number and velocity range chosen (subjective parameters) for its detection.

Results coming from the campaign on D77-A1÷A7 underlined the proneness to the interaction of the $SR = 1.5$ cross-section; the characteristics necessary to fully define each test case are listed in Tab. 3.3, while the response curves are reported in Fig. 3.28 and 3.29³. In F_{d1} tests the system mass was varied by externally and symmetrically adding masses

³The data were re-elaborated with respect to those already published in Mannini *et al.* (2013; 2014a;b).

to the model, whereas the damping was modified by wrapping some tape around the coil springs; in tests A3÷A5 the tape was applied only to the four upper springs, while in tests A6 and A7 it was wrapped around all the eight springs. It is quite easy to note that up to the D77-A5 ($Sc_{BD} \approx 72$) the amplitudes of vibration show a linear growth starting from the critical velocity ($U/U_r = 1$): as expected a VIV-galloping type instability manifests itself with unrestrictedly growing oscillation amplitudes as the flow velocity is increased. The same effect is verified for D77-A1 and A2 where the *quenching effect* takes place given the ratio $\Lambda < 1$.

For the highest Sc test cases still interacting (D77-A4 and A5), for $U/U_r \approx 1.6 \div 1.7$ a *kink* is present as a deviation from the amplitude linear trend, not predicted by the QS -theory. With such a pattern the curve individuates an inflection point with sloped tangent, even if the kink is meant to be placed in correspondence of the first local maximum. This interesting feature was already detected by Miyata *et al.* (1983) and in a lesser extent by Bearman *et al.* (1987), in testing a low-damped square cylinder in smooth flow condition. The latter group of authors correlated it with a transverse force component occurring at $3 \cdot f_{osc}$: they did observe this effect in correspondence of a reduced velocity of $U^* \approx 3 \cdot 2\pi = 18.85 \Leftrightarrow U/U_r = U^*/U_r^* \approx 2.54$, assuming a St of 0.135; another cause for this behaviour was attributed by the authors to complex vortex formation caused by the high strain imposed by the sharp afterbody corners on the shear layers. The same phenomenon's observation has been reported in Nemes *et al.* (2012) at $U^* > 14 \Leftrightarrow U/U_r = 1.89$ (keeping the same assumption on St).

For higher Sc values, VIV-galloping interaction is suppressed, due to the reaching of a velocity ratio high enough to separate the two phenomena, that is $\Lambda = 7.24, 8.54$ respectively for D77-A6 and A7 test cases. In these cases the body experienced a low and narrow-peak resonance bell, showing however a non-negligible amplitude of vibrations even for such high Sc values. Comparing both Fig. 3.28 and Fig. 3.29, it is clear how the growth rate is slightly different depending on the regime: the QS -galloping instability branch seems to be steeper than the resonance one. Then, it is interesting to take a look at the characteristic displacement time traces recorded in some key-point showing different properties (sinusoidal shape, periodical, intermittent etc...) helpful for a better insight of the different nature of each response branch.

In Fig. 3.30 three response curves are proposed (namely D77-A1 relative to a *quenching* case, D77-A4 classically interacting and showing an upper kink with respect to the D77-A5 case), superimposing markers which specify the correspondent time histories reported below the figure. D77-A1 case response barely extends beyond the critical velocity, however, it is interesting how the modulation starting from $U/U_r = 0.98$ presents sharp peaks which get wider as the velocity increases towards $U/U_r = 1.2$. In D77-A4 case this effect is more evident: a different modulation-type is expressed, resembling a sawtooth wave, whose teeth become less steep by increasing the flow speed and finally becoming almost perfectly sinusoidal as the kink zone is reached. The same behaviour is shown by the D77-A5 test case too.

The same plywood model has been tested on F_{d2} rig, which is able to express even lower values of Scruton number as indicated in the comprehensive scheme in Tab. 3.4. The correspondent response curves in terms of *rms* of nondimensional amplitudes are reported in Fig. 3.34 and 3.35. The first difference with respect to F_{d1} results is the rising of a secondary resonance in correspondence of $U = U_r/3$ and at the natural frequency f_n , for test cases

going from D77-B1 to B4. This can be ascribed to a Sc -effect, considering that the D77-B4 relative value is lower than D77-A1 one (8.26 against 9.84). A different behaviour of D77-B2 case with respect to B1, B3 and B4 showed two segments in the secondary resonance branch divided by a jump at $U = U_r/2$, while the others are characterized just by the first segment which decrease in maximum amplitude and die out earlier and earlier as the Sc is increased. A second difference can be noticed from the comparison of triangles reporting the slopes of the instability branches: the interaction branch slope in this case is steeper than in the previous (0.233 against 0.147), while, given the lack of non-interacting test cases, only the comparison between the resonance branch related to F_{d1} (in Fig. 3.29 obtained through a linear regression of D77-A6 and A7 cases together) and the first segment of the secondary resonance of F_{d2} (in Fig. 3.35 indicated for the D77-B1 case) is possible (0.129 against 0.248). These differences in the slopes between the two set-up response curves, and maybe the presence of the secondary resonance region, are probably due to lower flow disturbance achievable with F_{d2} rig. Apart from these evident differences the instability clearly develops from U_r^* and unrestrictedly grows for the whole group of test cases, this time not showing any kink given that the reduced velocities range allowed by this test rig is lower, reaching $U \approx 1.5 \cdot U_r$ while, as mentioned previously, such an effect manifests itself afterwards ($U \approx 2.5 \cdot U_r$).

Again, some examples of signals taken from D77-B1 and B6 cases, the former expressing a marked secondary instability associated with *quenching* regime while the latter related to a classical interaction with $\Lambda = 1.06$. As expected the vibrations regime inside secondary resonance (Fig. 3.37.*left*) is almost perfectly sinusoidal, while it shows modulations at the main instability onset and also for higher velocities recalling the D77-A1 case reported in Fig. 3.31. In Fig. 3.38 the transition from the instability onset to higher reduced velocities is shown: it is quite interesting to observe the evolution of the time traces shape that clearly express the change from steeper and sharper to more flattened and lower peaks, looking like a sawtooth signal as in the previous case. One could speculate that such a progression would bring to the same pattern reported in Fig. 3.32.*center* or Fig. 3.33.*center*, assuming at higher velocities sinusoidal-like trace shapes (Fig. 3.32.*right* or Fig. 3.33.*right*).

The response curves results for the aluminium model D30 mounted on F_{d2} rig are shown in Tab. 3.5. The correspondent response curves are reported in Fig. 3.39 together with a close-up view on the instability onset zone proposed in Fig. 3.40. The principal difference between D77 and D30 model is the Sc number range of interest concurrently with a lower Re range, after having obviously considered the reduced D value, the construction material, the accuracy in the manufacturing and the corners sharpening process. In particular we can sum up writing down that approximately $Sc_{D30} \approx 5 \cdot Sc_{D77}$ and $Re_{D30} \approx 1/7 \cdot Re_{D77}$. At a very first observation of Fig. 3.39 it could seem the interaction to occur for the test cases ranging from D30-B1, B2, B6 and B7, although with a different and peculiar pattern. Nevertheless, by carefully considering the QS -galloping theoretical velocities beside Fig. 3.40, and by examining case by case, the picture is quite different from what was expected. In fact, although no *quenching* cases were allowed by the D30- F_{d2} combination, it can be said that D30-B1, B2, B6, B7 and possibly B5, taking also into account the results presented in the reference literature, could fall into the velocity ratio Λ range subject to the interaction VIV-galloping phenomenon. Conversely, in D30-B1 case ($Sc = 24$) a QS -galloping branch starts from $U/U_r \approx 1.2$ which almost matches the theoretical U_g value obtainable from $\Lambda = U_g/U_r = 1.24$ in Tab. 3.5; it is quite easy to note the contradiction

represented by such a behaviour. By increasing the Sc , case D30-B2 ($Sc = 62$), the instability onset is slightly delayed, though not matching the theoretical predicted value of 3.17, and the amplitude-velocity curve quickly leaves the linear trend assuming a reduced slope for probably recovering the pattern predicted by the QS -theory. Such a behaviour could be addressed as a partial interaction with the phenomenon onset placed in between the resonance and QS -galloping velocities. Similarly to the latter case, D30-B3 ($Sc = 111$ and $\Lambda = 5.68$), starts sooner with respect to QS -theory value but with a flatter pattern and much lower amplitudes, collocating itself again in a partial interaction instability regime. For the highest Sc values, 144 and 150 respectively for D30-B4 and B5 cases, the behaviour is that of a classical QS -galloping: the model is stable up to very high reduced flow speed showing limit-cycle oscillations after a small bump practically in correspondence of the theoretical onset velocity. Finally it is possible to observe two cases, D30-B6 and B7, showing an interaction mechanism more similar to the D77 wooden model results: increasingly vibration amplitudes start from U_r without sudden jumps, with a bit lower slope with respect to that of the D30-B1 galloping instability branch reported in Fig. 3.39; the initial linear trend is left at smaller amplitudes for higher values of the mass-damping parameter showing a plateau prior to increasing again. In addition, while for the D30-B6 case the first local maximum in correspondence of the deviation from the linear trend occurs around $U/U_r = 1.6$, following an ‘S’-shape, in D30-B7 the inflection point individuated by the change in the slope is an horizontal tangent type one, and the deviation point is rather anticipated. Despite these peculiar amplitude response curves may recall a kink occurrence, force or pressure measurements should be conducted to clarify this point, investigating the component of the force coefficient associated with frequencies near that of the body motion and its super-harmonics, the odd ones in general and the third one in particular, to check any eventual peak of the same order of magnitude of the fundamental harmonic at three times the body frequency (see Bearman *et al.* (1987) §3.4, Fig. 7). It is either interesting the way in which the D30-B7 curve rejoin the B6 case path from $U/U_r \approx 4$; from this point of view the lower amplitude response in the range $1.2 \lesssim U/U_r \lesssim 4.1$ is a clear Scruton effect. On the other hand, concerning the anomalous behaviour of this sectional model, particularly in D30-B1 case, the only possible consistent reason is represented by the different Re -regime with respect to D77. Of course this is an empirical speculation so far, meaning that further investigations need to be carried out in order to better explain this effect.

It is quite interesting now to look at some characteristic time histories pattern, like in previous cases. In Fig. 3.41 D30-B1, B4, B6 and B7 cases are reported, to be intended as representative of the other cases too. As in a typical galloping response for D30-B1 we have a modulation at the critical wind speed, while sinusoidal oscillations take place almost from the beginning of the instability branch. A similar behaviour can be observed in D30-B4, although the higher associated QS -galloping onset velocity. In D30-B6 the time histories character evolution is very similar to what happened in D77-A5 case (Fig. 3.33): right after the resonance velocity the time traces start to express periodic sawtooth shaped signals, with different modulations and characteristic period (*e.g.* as reported in Fig. 3.44.*center*), to become almost perfectly sinusoidal at $U/U_r = 1.55$, that is in correspondence of the local maximum which represents the amplitude response curve deviating point from the linear trend.

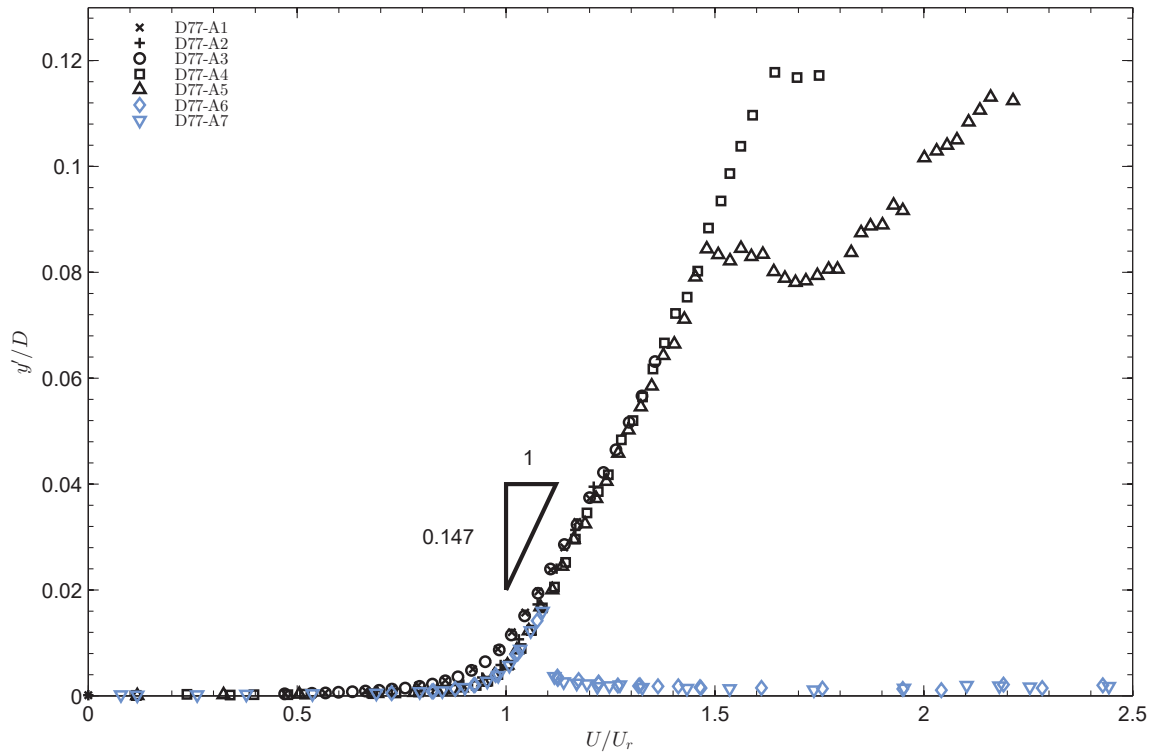


Fig. 3.28 F_{d1} aeroelastic response curves in terms of nondimensional amplitude *rms* D77 cases A1÷A7: light blue coloured markers, namely A6 and A7 ones, are related to the test cases not experiencing the interaction, but just a resonance.

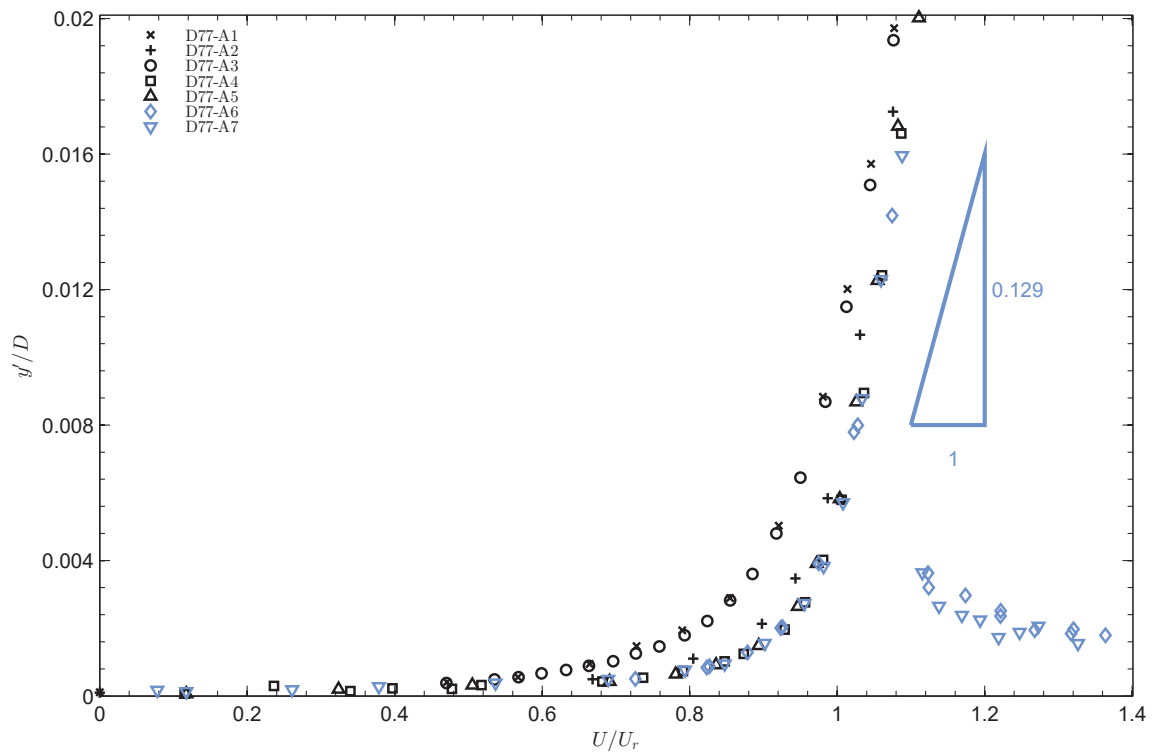


Fig. 3.29 Close-up window on the critical velocity range. [data already published in Mannini *et al.* (2013)].

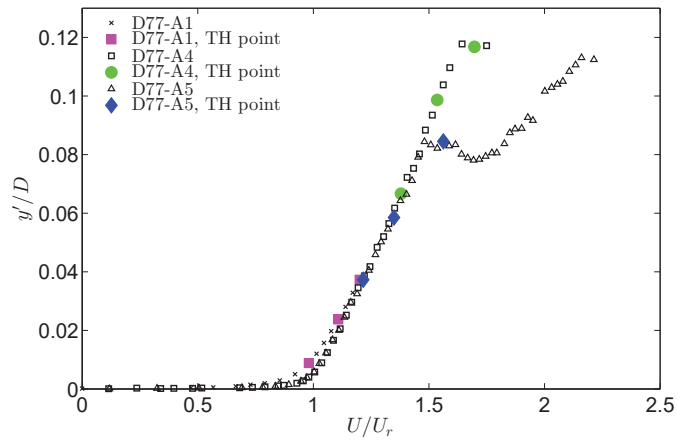


Fig. 3.30 Reference curves and velocity points for which nondimensional displacements are proposed for D77-A.

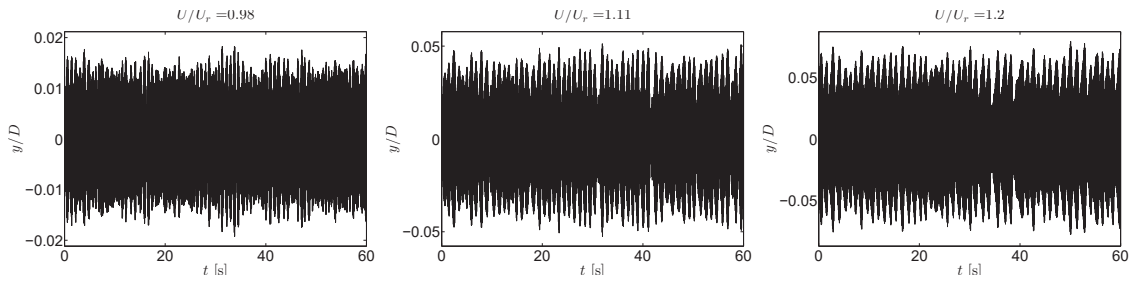


Fig. 3.31 D77-A1 [■] (*left*): $U/U_r = 0.98$: modulations around U_r . (*center*): $U/U_r = 1.11$: higher reduced velocity. (*right*): $U/U_r = 1.2$: change in time trace's profile.

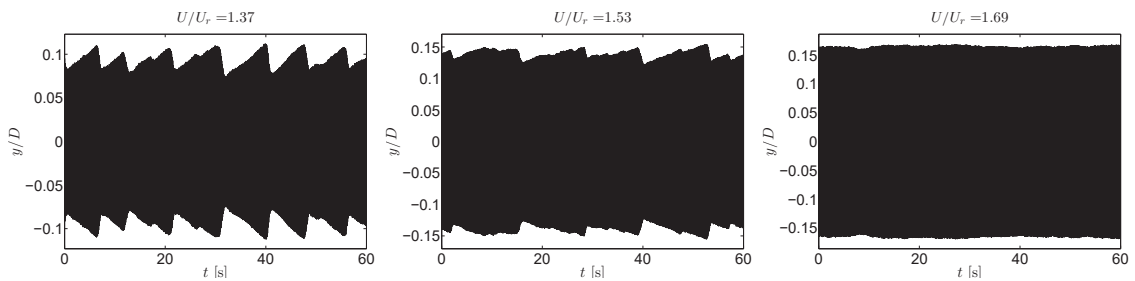


Fig. 3.32 D77-A4 [●] (*left*): $U/U_r = 1.37$: velocity in the mid-unstable branch. (*center*): $U/U_r = 1.53$: change of time trace's profile. (*right*): $U/U_r = 1.69$: point in the kink.

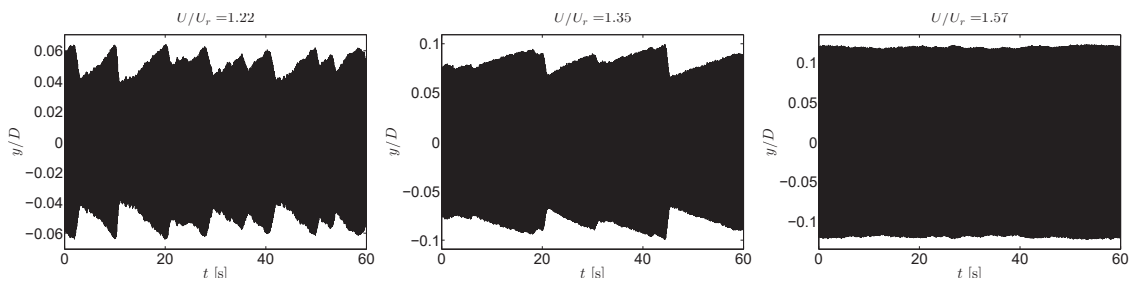


Fig. 3.33 D77-A5 [◆] (*left*): $U/U_r = 1.22$: point after U_r . (*center*): $U/U_r = 1.35$: higher reduced velocity but different time trace's profile. (*right*): $U/U_r = 1.67$: point in the kink.

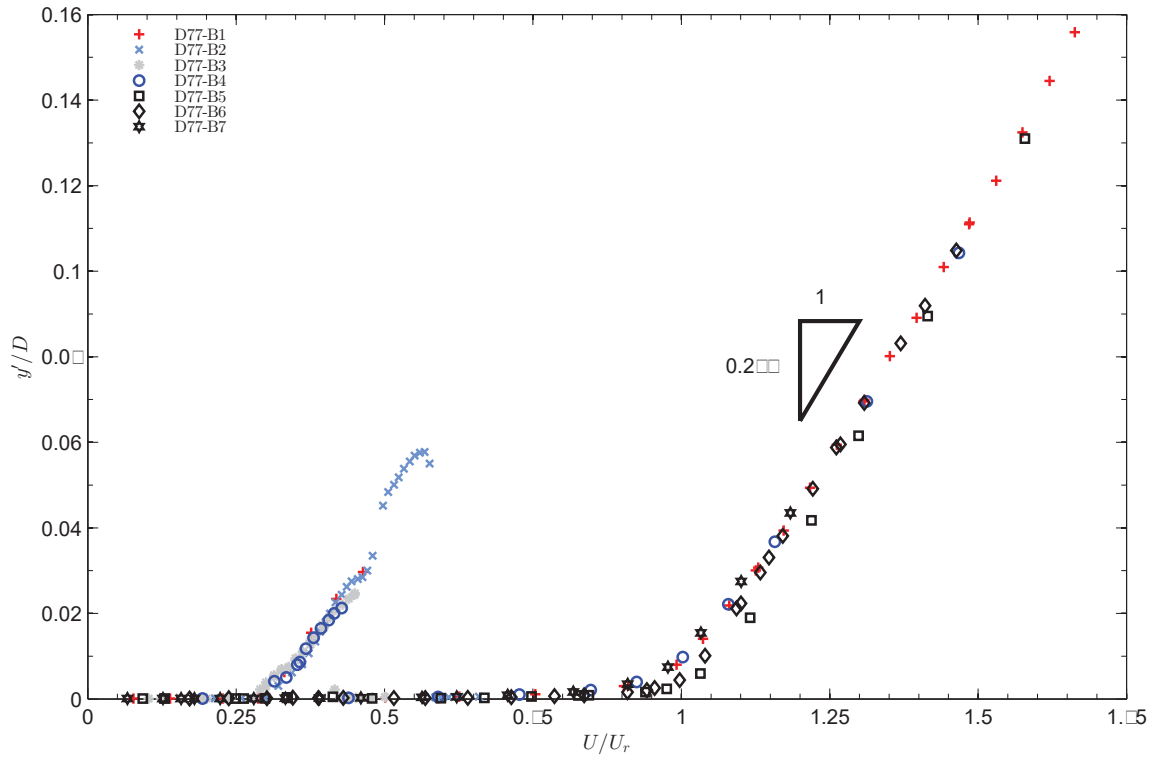


Fig. 3.34 F_{d1} aeroelastic response curves in terms of nondimensional amplitude *rms* D77 cases B1÷B7.

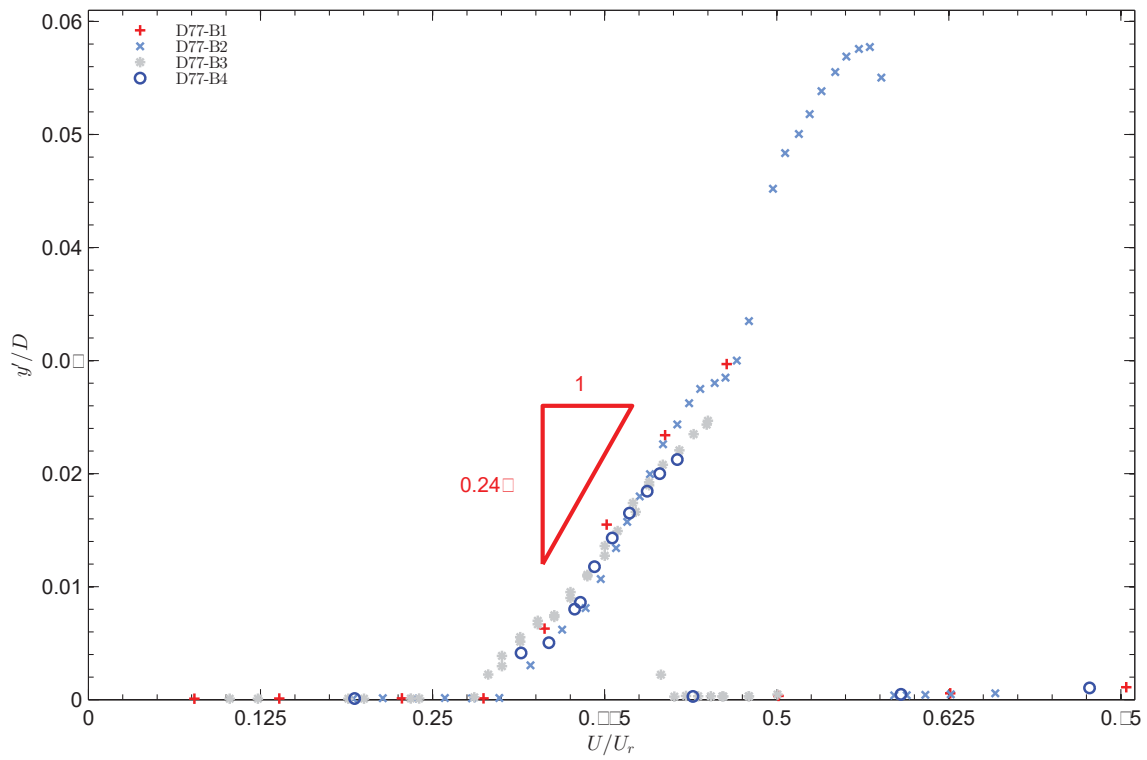


Fig. 3.35 Close-up window on the secondary resonance, where coloured markers (B1÷B4) are related to the test cases experiencing it.

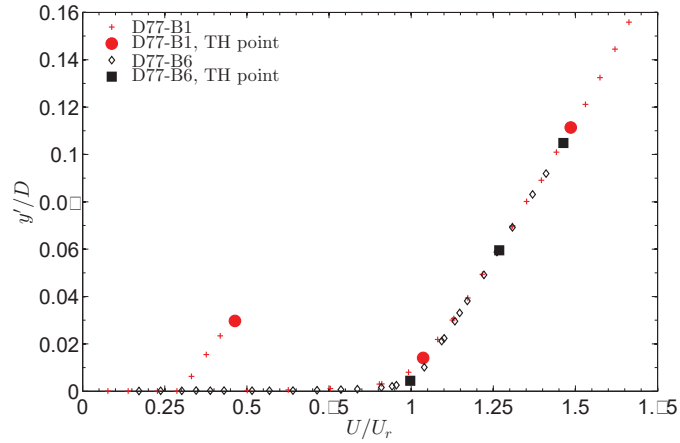


Fig. 3.36 Reference curves and velocity points for which nondimensional displacements are proposed for D77-B.

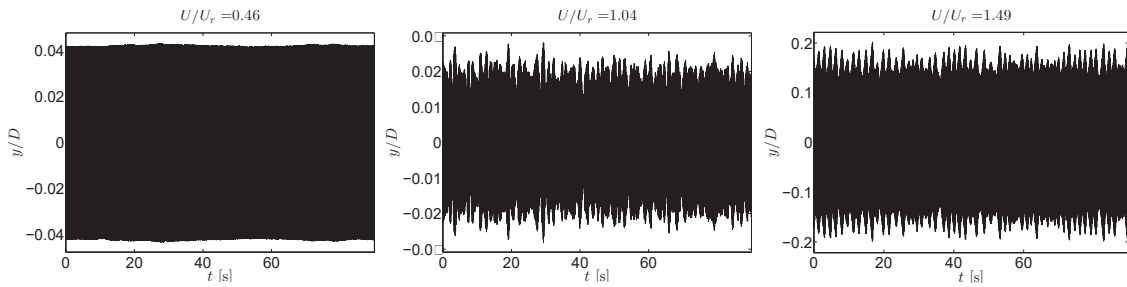


Fig. 3.37 D77-B1 [●] (left): $U/U_r = 0.46$, peak of the secondary resonance. (center): $U/U_r = 1.04$: instability onset. (right): $U/U_r = 1.49$: mid-branch of the instability.

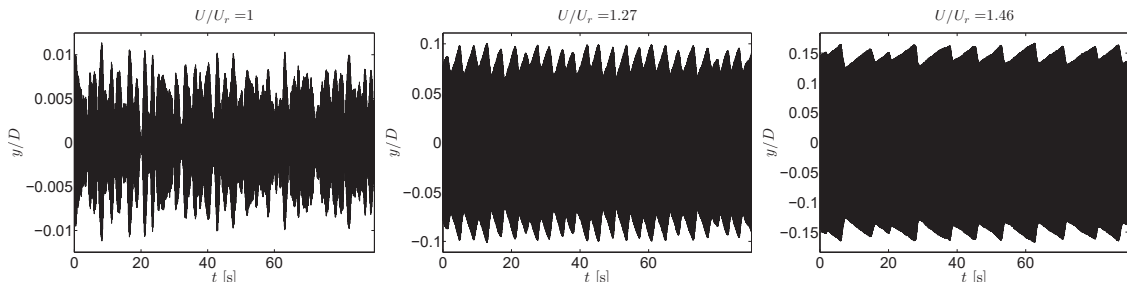


Fig. 3.38 D77-B6 [■] (left): $U/U_r = 1$: instability onset. (center): $U/U_r = 1.27$: mid-branch of the instability. (right): $U/U_r = 1.49$: highest reduced velocity.

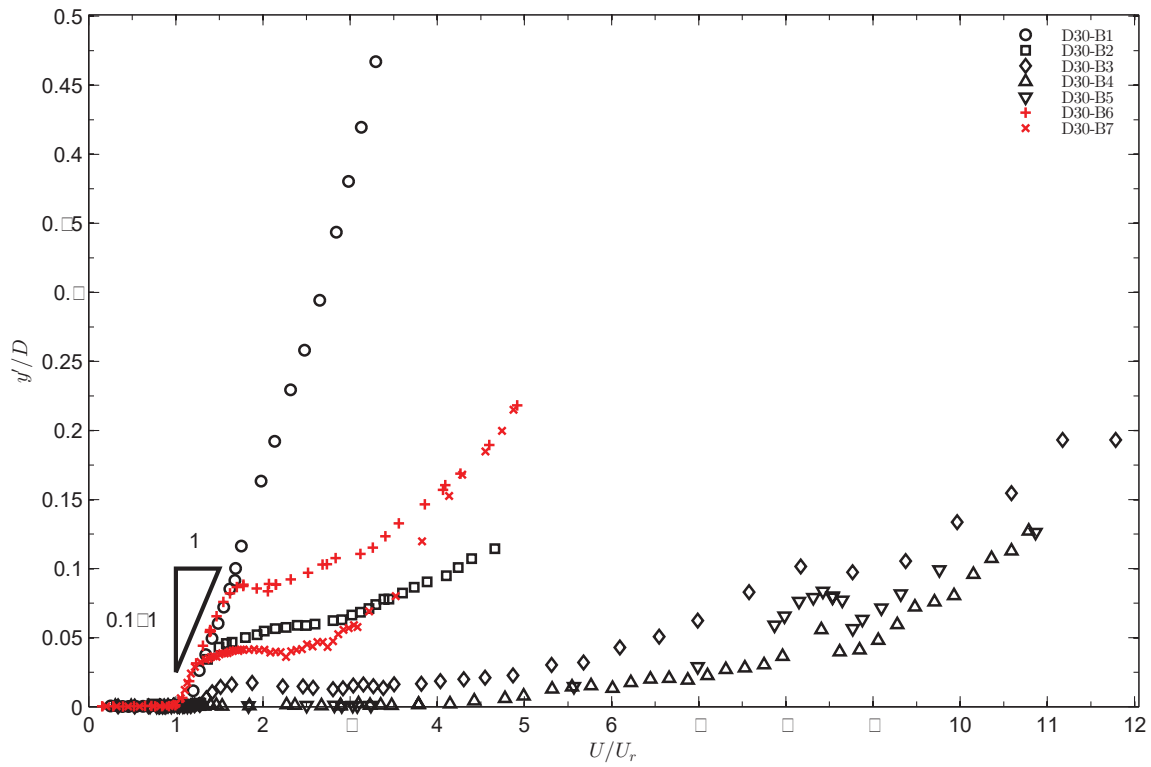


Fig. 3.39 F_{d1} aeroelastic response curves in terms of nondimensional amplitude rms D30 cases B1÷B7.

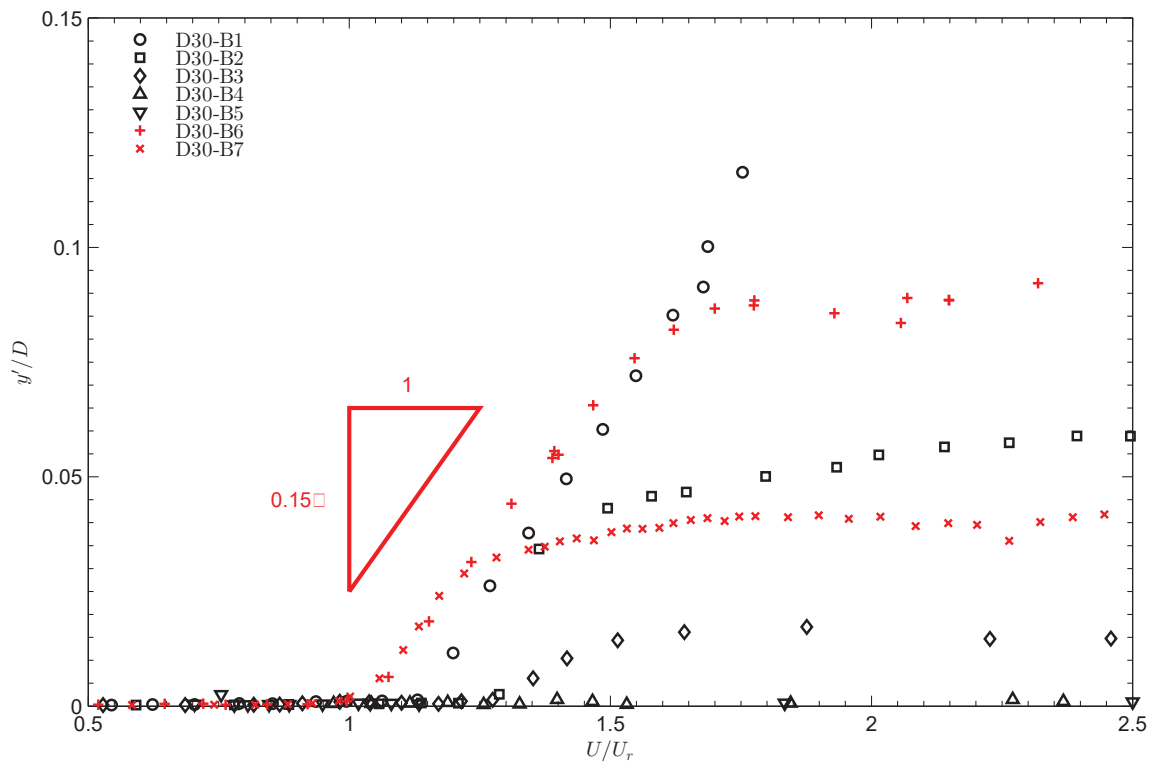


Fig. 3.40 Close-up window on the resonance region: red \times and $+$ markers (D30-B6 and B7) are related to test cases in which interaction occurs.

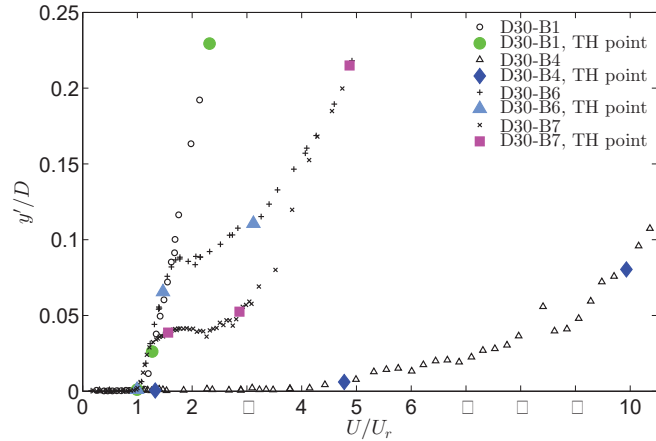


Fig. 3.41 Reference curves and velocity points for which nondimensional displacements are proposed for D30-B.

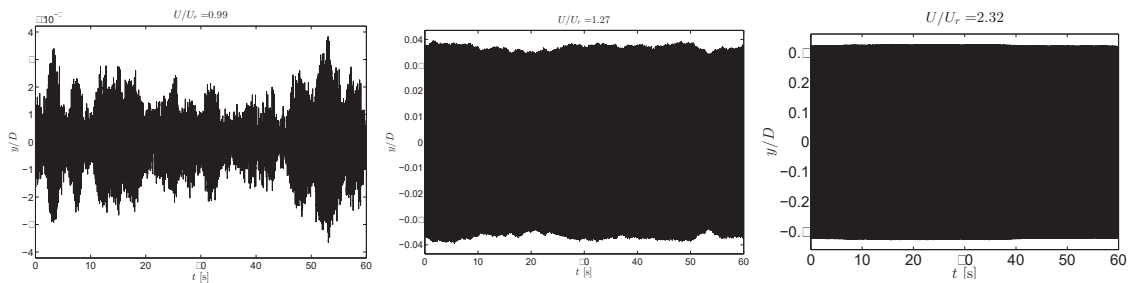


Fig. 3.42 D30-B1 [●] (left): $U/U_r = 0.99$: galloping-type instability onset. (center): $U/U_r = 1.27$: higher reduced velocity. (right): $U/U_r = 2.32$: mid-branch of the instability.

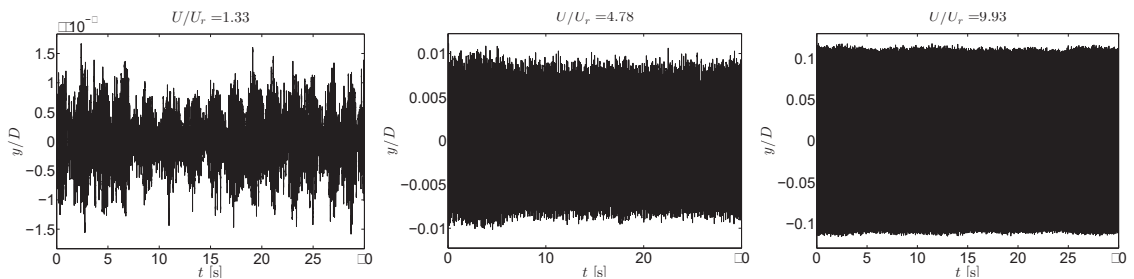


Fig. 3.43 D30-B4 [◆] (left): $U/U_r = 1.33$: beginning of stable zone. (center): $U/U_r = 4.78$: point before U_g^* (note that $\Lambda = 7.4$). (right): $U/U_r = 9.93$: mid-branch of galloping.

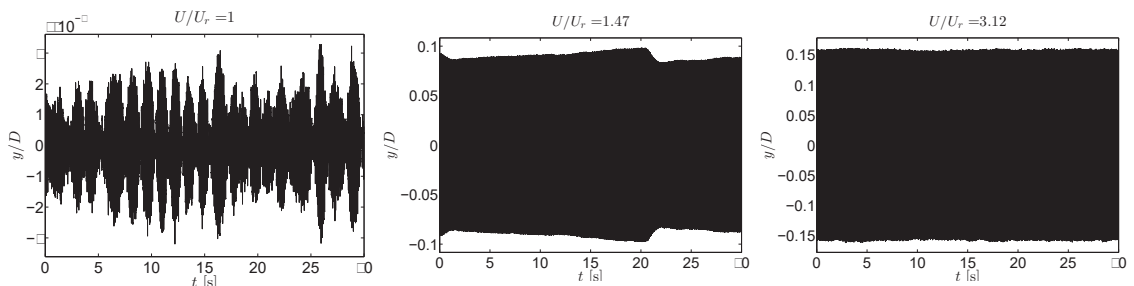


Fig. 3.44 D30-B6 [▲] (left): $U/U_r = 1.00$: phenomenon onset. (center): $U/U_r = 1.47$: mid-linear trend. (right): $U/U_r = 3.12$: second steeper branch of the instability.

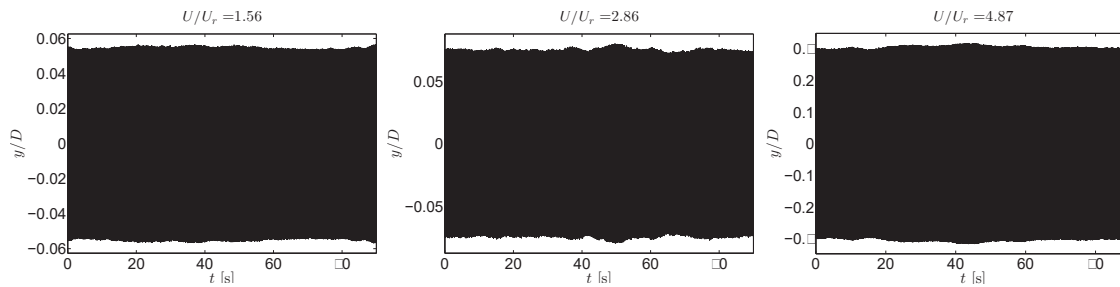


Fig. 3.45 D30-B7 [■] (*left*): $U/U_r = 1.56$: peak of the first increasing branch. (*center*): $U/U_r = 2.86$: end of the plateau. (*right*): $U/U_r = 4.87$: highest velocity point.

The behaviour of D30-B7 is different: after jagged modulations in the range $1 \lesssim U/U_r \lesssim 1.2$ the time traces start to be quite sinusoidal (Fig. 3.45.*left* and *right*), with only some slight modulations as in Fig. 3.45.*center*, till reaching the maximum allowed flow speed value. The second configuration for the aluminium model testing was the D30 section rotated by 90° , that is D45 configuration. As it was expected from the most amount of literature data such a section is stable, experiencing only a sharp and narrow resonance bell in correspondence of the critical velocity (Fig. 3.46). Clearly, the higher the Sc the lower the maximum peak in amplitude. However, the lowest Sc tested (D45-B1), shows a second and a third lower peaks at $U/U_r = 1.6$ and 5.6 before entering in a wake-induced vibrations regime experiencing amplitudes with the same order of magnitude shown also by D45-B2. In Mannini *et al.* (2013) an increase of the oscillations around a flow velocity corresponding to the third sub-harmonic of the system natural frequency was observed also for the test case correspondent to D77-A1, which is not visible in the previously reported figures because of the plot scale. On the other hand no sub- or super-harmonics were observed for D45-B2 case.

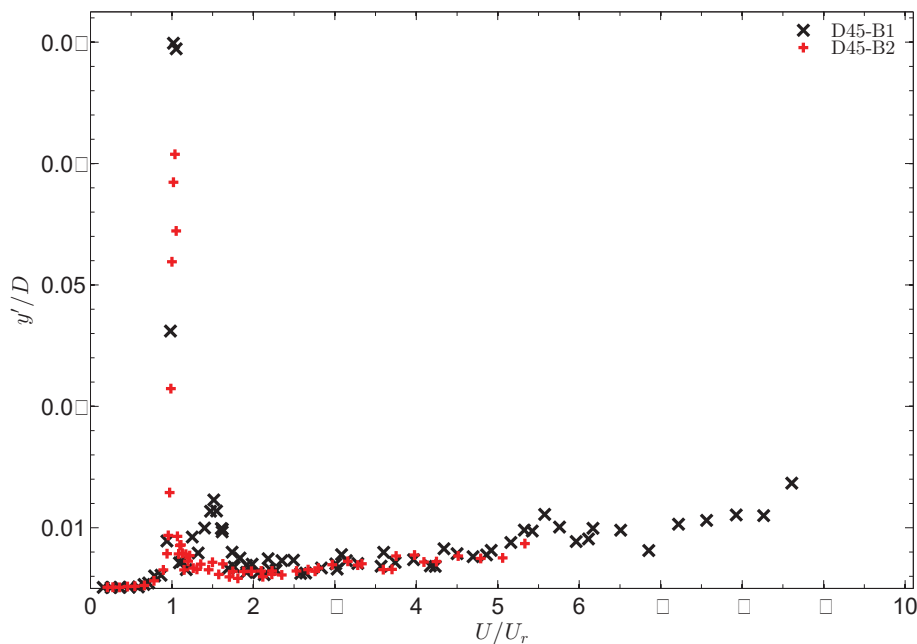


Fig. 3.46 F_{d1} aeroelastic response curves in terms of nondimensional amplitude *rms* D45 cases B1 and B2.

3.3.3.3 Turbulent flow

We already saw in Ch. 2 how the response characteristics are susceptible to variations since the oncoming flow become turbulent. Similarly way to the work carried out by Laneville (1973), an extensive campaign has been performed at CRIACIV WT, testing the $SR = 1.5$ rectangular cylinder in homogeneous turbulent flow. These test are interesting not only for a deeper insight on the response of such a body but also because it represents a useful dataset in addition to the literature results, which, as already mentioned, are more unbalanced on the square section.

The homogeneous turbulent flow was generated by two different wooden grids placed variably distanced upstream from the model. Grid G1 (Fig. 3.47.*left*) is characterized by a mesh of 100×100 mm with slats of a width of 25 mm, while grid G2 (Fig. 3.47.*right*) by a mesh of 550×550 mm with slats of 140 mm. The spectral properties of the generated oncoming turbulence were determined through hot-wire measurements. The spatial homogeneity of the flow at the position of the model was verified prior to start the tests. The various configurations considered are listed in Tab. 3.7 and 3.8 where the turbulence intensity and the longitudinal integral length scale are also reported.



Fig. 3.47 (*left*) View from the rear towards the tunnel inlet of the blades rig F_{d2} , with mounted D30 aluminium model and the turbulence grid type G1; (*right*) closer view of the G2 grid type.

Aiming to describe an oncoming turbulent flow it is difficult to detect an instantaneous snapshot of the boundary layer and all eddies formed within it. Hence, it is easier to make measurements of eddies at one point over a long period of time. We must invoke Taylor's hypothesis ('frozen turbulence' Taylor (1938)), stating that the advection velocity of the turbulence is much greater than the velocity scale of the turbulence itself. Quoting from the original paper "If the velocity of the air stream which carries the eddies is very much greater than the turbulence velocity, one may assume that the sequence of changes in u at a fixed point are simply due to the passage of an unchanging pattern of turbulent motion over the point.". The longitudinal integral length scale has been determined according to Taylor's frozen-eddy hypothesis, that is anyway a valid assumption invoked in most experiments designed to investigate turbulence physics with time resolving sensors (Higgins *et al.*, 2012); the results were confirmed by fitting the expression proposed by von Kármán to the measured spectrum.

As already saw in the D77-B1 case, in smooth flow (case T1=B1 for D77 in Fig. 3.48), the

test case	grid type	Δx [m]	I_u [%]	L_u^x/D -	ζ [%]	$S_{c_{B/D}}$ -
D77-T1	no grid	-	< 1	-	0.088	5.1
D77-T2	G1	4.95	3	1.0	0.086	4.9
D77-T3	G1	1.50	6	0.6	0.096	5.5
D77-T4	G1	0.90	9	0.5	0.081	4.6
D77-T5	G1	0.70	11	0.4	0.075	4.3
D77-T6	G1	0.50	16	0.4	0.110	6.3
D77-T7	G2	6.84	9	3.3	0.072	4.1
D77-T8	G2	5.00	14	3.0	0.110	6.4

Tab. 3.7 Turbulent flow and dynamic characteristics of the aeroelastic tests performed with D77 on F_{d2} : Δx denotes the distance between the grid and the longitudinal axis of the model, I_u the turbulence intensity, L_u the longitudinal turbulence length scale.

test case	grid type	Δx [m]	I_u [%]	L_u^x/D -	ζ [%]	$S_{c_{B/D}}$ -
D30-T1	no grid	-	< 1	-	0.057	24.4
D30-T2	G1	4.95	3	2.6	0.057	24.1
D30-T3	G1	1.50	6	1.6	0.059	25.3
D30-T4	G1	0.90	9	1.2	0.061	25.9
D30-T5	G1	0.70	11	1.1	0.054	22.9
D30-T6	G1	0.50	16	0.9	0.054	22.8
D30-T7	G2	6.84	9	8.5	0.055	23.7
D30-T8	G2	5.00	14	7.7	0.061	26.0

Tab. 3.8 Turbulent flow and dynamic characteristics of the aeroelastic tests performed with D30 on F_{d2} .

onset of a galloping-type instability interacting with vortex shedding is placed at U_r^* , continuously growing in oscillation amplitudes as the flow speed is increased. A secondary instability with limited amplitudes can be observed in the range of wind speeds $U_r/3 < U < U_r/2$ (Fig. 3.49), previously referred as secondary resonance. From the moment that there's practically no difference between the response curves of D77-T1 and T2 test cases, we can derive that a turbulence intensity of around 3% doesn't affect the response of D77 cylinder. On the other hand, higher values shift to higher velocities the onset of the principal branch and progressively reduce in amplitude the secondary instability (D77-T3 in Fig. 3.49). However, the post-critical slope of experimental curves is constant by increasing I_u (D77-T1 to T6 in Fig. 3.48), as long as the integral length scale L_u^x/D is kept below 3, as in the case of grid G1. In fact, a stronger influence of L_u^x/D is evident using grid G2 as its value results tripled, although I_u values fall in the same range of grid G1, and no clear instability pattern is observed. It is worth noting that the shift in the instability onset, expressed on the U/U_r abscissa, can be affected by the St value detected in smooth flow, instead through static measurements in turbulent flow; nevertheless it seems to be not enough to justify such large shifts in velocity onsets.

In spite of a QS -galloping onset velocity just a bit higher than the critical one (about $1.2 \cdot U_r$ in smooth flow, case D30-T1 in Tab. 3.8), no interaction between vortex shedding and galloping was observed (Fig. 3.48). The instability pattern shows a jump to a higher branch at a wind speed slightly higher than $1.2 \cdot U_r$ and a small hysteresis loop around the

instability threshold Fig. 3.51. This is in evident contradiction with the results of the tests with the larger plywood model, also for much higher Scruton numbers. Furthermore, as already seen in §3.3.3.2, a Sc -effect is that the secondary resonance is no more present for D30.

A similar turbulence intensity effect has been obtained for D77 test cases too in postponing the instability onset is verified; the instability branches' slope is kept practically the same till D30-T3, then decreases for D30-T5 and T7 cases; for this latter test case there's an effect induced by the integral length scale, while the section seems to be stable for a larger turbulence intensities value (D30-T6 and T8).

In §2.3 the results by Laneville (1973) have been introduced reporting the effect of the L_u^x/D to be small with respect to a considerable effect of I_u . Although that experimental campaign was conducted on a square section and considering that usually there are peculiar effects in different laboratories testing, it is evident this finding to be in contrast with what has been found and showed so far.

3.4 Chapter summary

In this chapter several experimental campaigns conducted in air flow at two different research laboratories are described. First, static tests on a square section in the Stahlbau *WK* have been analysed and commented: the results are in line with the reference literature in particular concerning the detection of the lateral force coefficient (C_{F_y}), which is crucial for present work's results. Then, static, hot-wire anemometry and aeroelastic tests, either in sooth and turbulent flow, performed at *CRIACIV WT* are illustrated. It is worth considering that both static and aeroelastic experiments were conducted with two different set-up and in turn instruments, so that to double-check the results obtained. Turbulent flow aeroelastic measurements showed to be partially in contrast with the literature mentioned in the former section; nevertheless, for the sake of completeness, further static test in turbulent flow should be conducted to get a comprehensive picture on turbulent flow results.

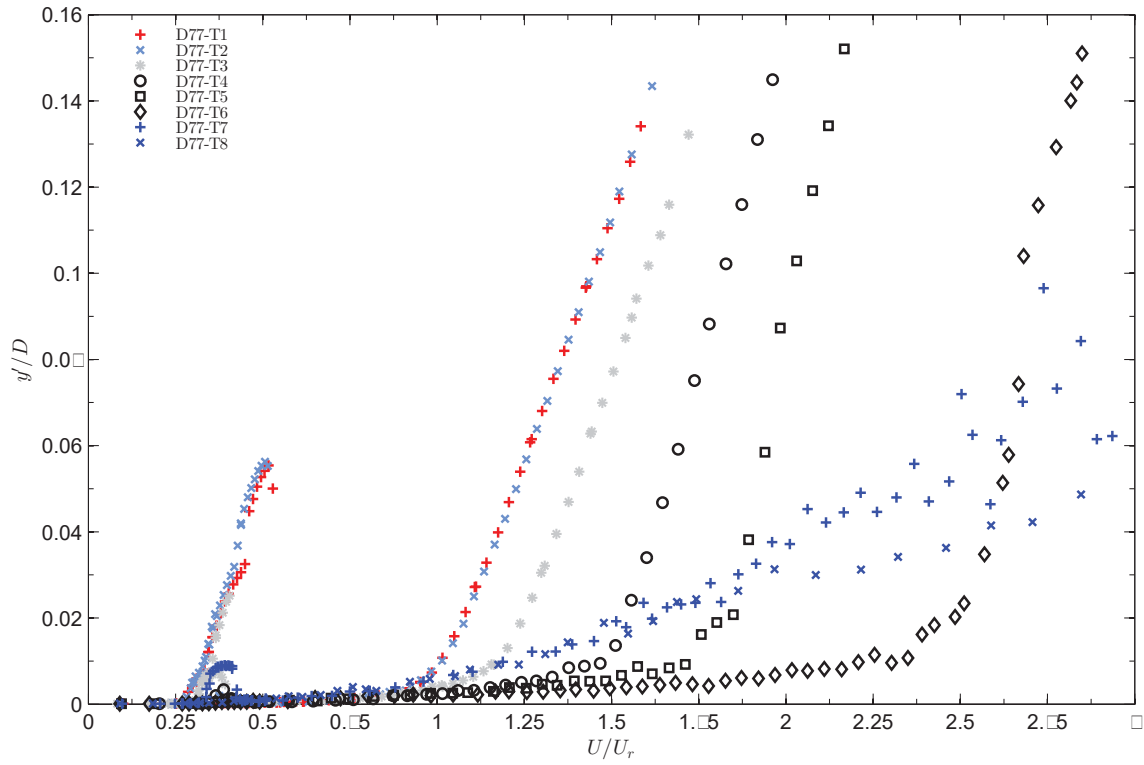


Fig. 3.48 F_{d2} aeroelastic turbulent flow response curves in terms of nondimensional amplitude rms D77 cases T1÷T8 (Tab. 3.7).

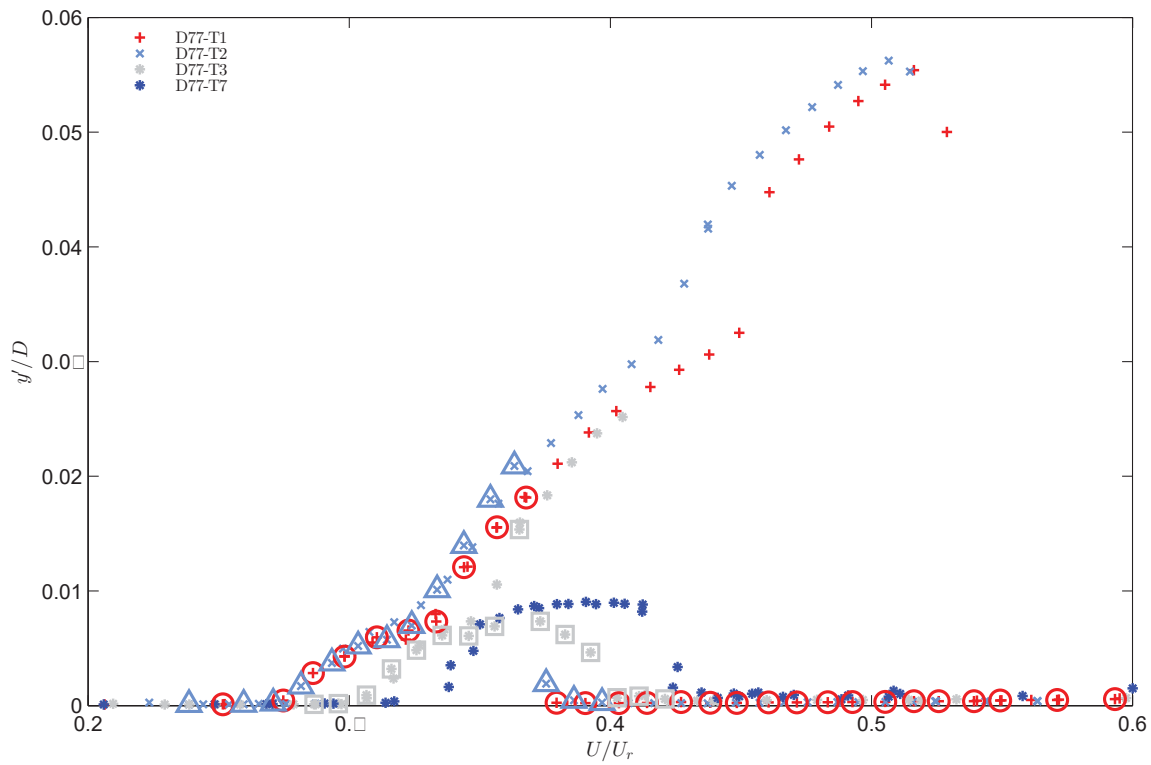


Fig. 3.49 Close-up window on the secondary resonances range; T1÷T3 and T7 show the secondary resonance starting at $U_r/3$. Superimposed empty markers (○, △, □ respectively for T1, T2, T3) denote the response by decreasing wind speed.

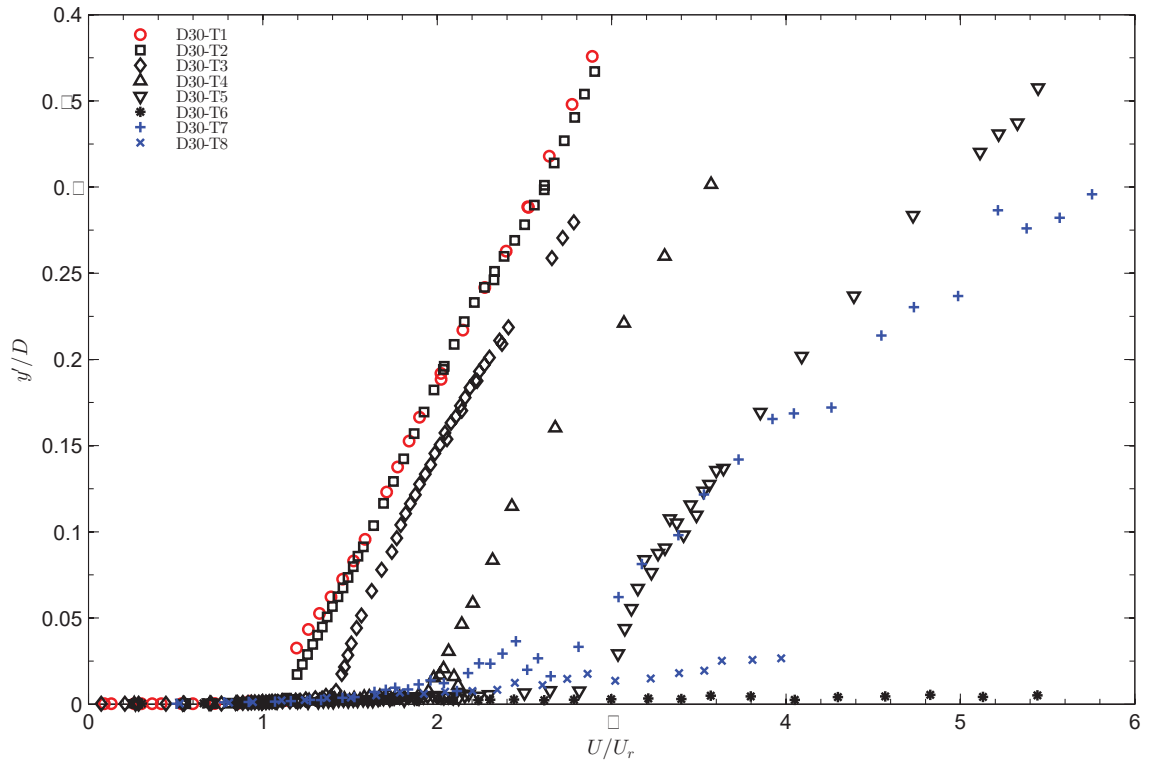


Fig. 3.50 F_{d2} aeroelastic turbulent flow response curves in terms of nondimensional amplitude rms D30 cases T1÷T8 (Tab. 3.8).

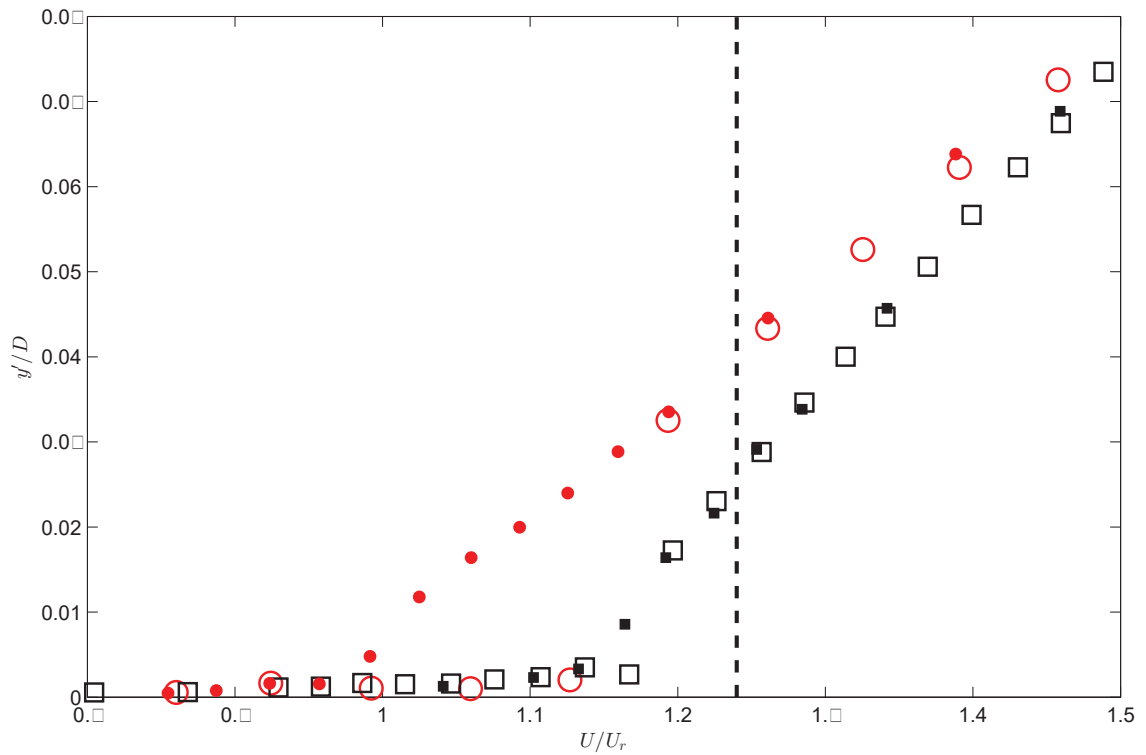


Fig. 3.51 Close-up window on the T1 and T2 instability onset velocity. Filled smaller markers denote the response by decreasing wind speed while the dashed line is placed in correspondence of the QS -galloping velocity.

Chapter 4

Experimental methodology

Part. 2 - Water channel testing

4.1 Introduction

One of the principal targets of the present work was the investigation of extremely low mass ratio regime, to comprehensively characterize every kind of flow condition. To this aim, an experimental campaign in water flow was undertaken, that is by basically changing the flow density. Such measurements in water flow were carried out entirely at *FLAIR*¹ Water Channel laboratory (*WC*) in Melbourne (Monash University, MAE²). This time the experimental rigs are identified by the a capital letter ‘*M*’, while the same criterion for identifying static/dynamic differentiation is kept.

4.2 *FLAIR WC* experimental campaign

4.2.1 Flow system and sectional models

Fig. 4.1 and 4.2 show respectively a view of the laboratory room and a schematic lateral and top view of the recirculating system of the free-surface water channel.

The closed-loop water flow is driven by a centrifugal pump system: the flow is conditioned by upstream combined sections of vane, mesh, settling chamber, honeycomb and fine mesh, before it proceeds through a 3D contraction section (ratio of 3:1), allowing a free-stream turbulence level in the test section of less than 1 %. The test section locates in between an upstream contraction section and a downstream diffuser, and its interior dimensions measure 4 m in length, 0.6 m in width, and 0.8 m in depth. The transparent glass walls of the test section are supported by steel frames, which eventually allow flow visualisation imaging. The free-stream velocity in the test section can be varied continuously in a range of $U_\infty = 0.048 \div 0.456 \text{ ms}^{-1}$ corresponding to the pump frequency range of $f_P = 5 \div 50 \text{ Hz}$. The pump frequency is programmed and controlled via LabVIEWTM software. More details can be found in Leweke (2002). The last calibration used for the present measurements was performed via two different techniques, namely by particle image velocimetry (PIV) and laser doppler velocimetry (LDV) (see Zhao (2012) for details). The experimental

¹Fluids Laboratory for Aeronautical and Industrial Research.

²Department of Mechanical and Aerospace Engineering.



Fig. 4.1 View of the *FLAIR* Water Channel Laboratory. [by courtesy of Dr. Jisheng Zhao]

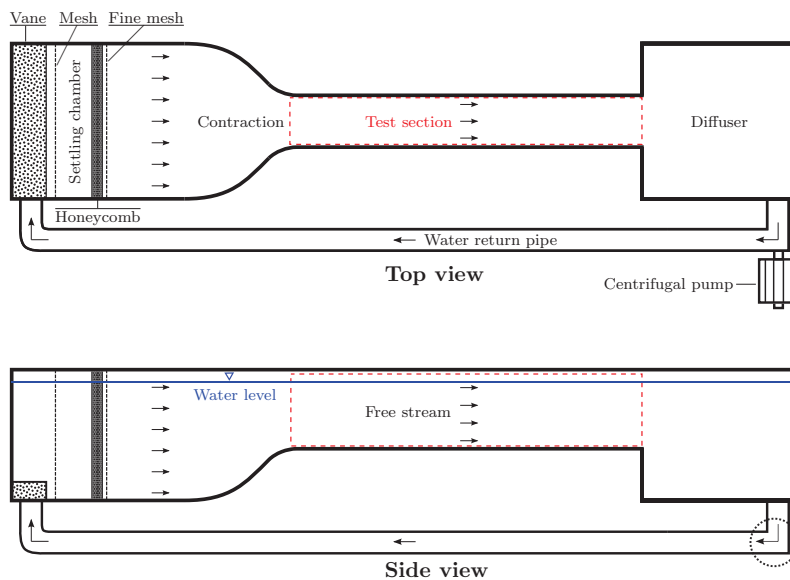


Fig. 4.2 Schematic view of the water channel . [from Zhao (2012)]

campaign was conducted on an aluminium sectional model designed by the author and manufactured directly in the department, thanks to the precious help of the workshop staff. The geometrical properties of the D24/D37 rectangular model, together with those of the square cylinder H25 tested by Dr. Zhao during his Ph.D. work (for which some comparisons will be given in Ch.6), are reported in Tab. 4.1. The rectangular cross-section rigid cylinder model was made from aluminium tubing; the immersed length and aspect ratio both calculated based on side length, are also reported in the table.

When building the model one should take into consideration that aluminium corrodes quickly in water, particularly when it is left in the water for a long time, as in the case of the present campaign: sometimes a single measurement session could take 20 hours and in any case once the configuration is mounted and identified it's better to conduct the test in the same configuration to avoid the modification of hydrodynamic characteristics. The

	D24/D37	H25
Section depth (D) [mm]	24.75/37.45	25
Section width (B) [mm]	37.45/24.75	25
Immersed length (L) [mm]	617.5 (702.5)	620 (750)
Wall thickness (t_w) [mm]	2.14	1.6
AR= L/D	24.9/16.47	24.8
material	aluminium	aluminium
Model mass (M) [kg]	0.648	0.497
Blockage [%]	4.2/6.4	4.3

Tab. 4.1 Characteristics of sectional models employed at FLAIR WC. Note that the immersed length L has been proposed, while reporting the total length in round brackets.



Fig. 4.3 (*left*) D25 and D24/D37 models; (*right*) view of a model mounted on the rig suspended above the perspex platform.

chemical process is called galvanic corrosion that leads to the so-called ‘pitting’, and the chlorine in the water accelerates this process. However, pitting is primarily an aesthetic problem that practically never affects neither strength nor surface finish. Therefore, the model employed were anodized in advance to counteract pitting. The result of this chemical process is the black colour of the models (Fig. 4.3.*left*).

A gap of 2 mm was given between the cylinder’s free-end and an end conditioning platform (Fig. 4.3.*right*), to minimize end effects, to promote parallel vortex shedding (see Williamson (1989)), and to prevent the entrainment of shear-layers passing from above the lower model free-end in the wake as a 3D effect. The platform has a top plate of $500 \times 500 \times 5$ mm and a height of 165 mm and it was already employed in Branković (2004), is alternative to the system previously experienced in several studies conducted at Cornell University by *e.g.* Khalak and Williamson (1996) and Govardhan and Williamson (2000); this latter consisted in connecting end-plates to the oscillating body, as in the case of the *WT* and *WK* experiments in the present dissertation. More details on the end effects promoted by these kind of aerodynamic appendixes on VIV of circular cylinders were reported

in Morse *et al.* (2008).

During the construction process, a 20 mm transparent window made by acrylic material was inserted, eventually allowing a laser sheet to illuminate through in case of PIV measurements; the continuity interface was finely polished and the corners carefully sharpened in order to prevent any imperfection..

The angles of attack values were set cross-checking them by means of different expedients: an acrylic thick rectangular plate purposely dimensioned was employed to initially place the body side parallel with respect to the WC walls, then, a digital angle measurement device with a resolution of 0.05° was used for double-checking the values. An empirical method was finally used for a visual check-out, that is setting an angle such to promote a clear symmetrical shedding in the body wake. Despite the simplicity this method showed a strong sensitivity to any imperceptible adjustment.

4.2.2 Rigs and instrumentation

DAQ The quantitative variable measurements in the experiments were the free-stream velocity (U), the cylinder's linear displacement (y), the resulting hydrodynamic lift and drag forces (F_L , F_D) and the transistor-transistor logic (TTL) standard signal eventually triggering signals to the lasers or camera shooting system. These measurements were conducted simultaneously by using a data acquisition (DAQ) system consisting of a National Instruments™ BNC-2110 connector block interfaced with a PCI-6221 (37pin) DAQ board which was embedded in a PC desktop. The DAQ system provided 8 channels of ± 10 V DC analog input and 2 channels of ± 10 V DC digital output with a 16-bit resolution, and two 32-bit digital counters. Even if the maximum sampling frequency (f_s) of the DAQ system could reach 250 kHz, experimental measurements were sampled at 100 Hz, whose Nyquist frequency was more than 50 times higher than that of FIV system, being f_n always less than 1 Hz, as it will be reported later on. The data sampling and recording of the measurements were controlled via LabVIEW™ 8.5 VI programs, customised by the author, while the data post processing and analysis were performed using MATLAB® codes.

Air-bearing system (AB) AB rig was designed by Dr. Jisheng Zhao during his Ph.D. work (Zhao, 2012). To promote only transversal motion in exciting cross-sectional bodies through FIV several researchers employed since many decades air-bearing systems whether in wind tunnel (Bearman *et al.*, 1987, Brooks, 1960, Feng, 1968, Ferguson, 1965, Smith, 1962) and in water flow experiments (Bokaian and Geoola, 1984, Bouclin, 1977).

A photograph of the system used in the present campaign is shown in Fig. 4.4. A fine machined aluminium base frame, measuring 208 mm in width, 800 mm in length and 16 mm thick, is mounted on four screw-threaded pads at the corners allowing a vertical height adjustment and levelling in the horizontal plane. Four commercial porous carbon media air bushings (Model: S302502) from NEWWAY™ Air Bearings (USA) are individually mounted in four aluminium pillow blocks screwed on the base: a light carbon fibre tube (measuring 700 mm and 600 mm in length respectively with a wall thickness of 1.5 mm), can pass through each couple of air-bushings without friction once the compressed air system is on. The original thicker carbon fibre tubes were fine polished down by machine to obtain a tolerance of $10 \mu\text{m}$, to satisfy the specifications on the recommended shaft tolerance for the air-bushings diameter ($\varnothing 25.0000^{+0.0000}_{-0.0076}$). The resulting 2 parallel carbon

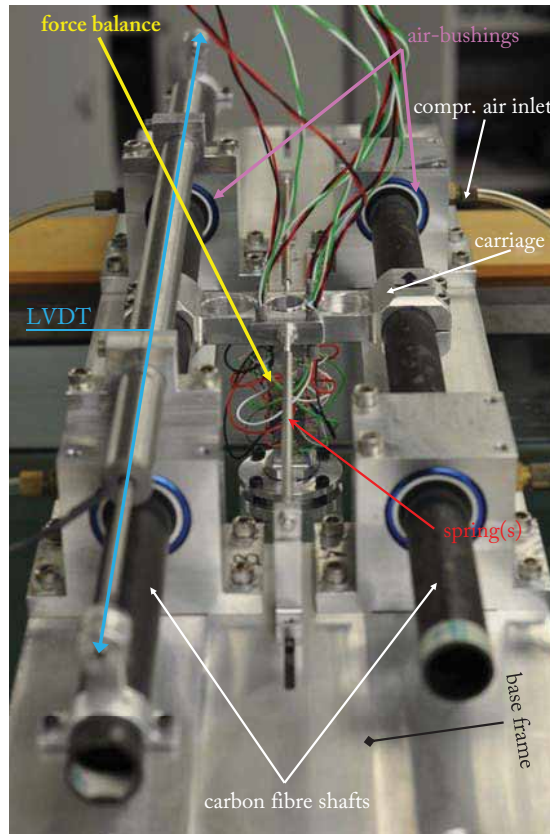


Fig. 4.4 Air-bearings system view.

parallel shaft are clamped together through an aluminium cross carriage; in this geometrical configuration the system allows a total stroke length of 160 mm, providing enough space (± 80 mm from zero-position in the channel midspan) for FIV movements; it goes without saying that a remarkable attention has been paid at the shafts alignment for maximizing its straightness. The performance of air bearings also requires proper quality air flow without any contaminant (oil, water, pollution in general), thus the compressed air supply was conditioned by a general-purpose filter, an air dryer, and then a pressure regulator with gauge. The outlet pressure, read on the regulator gauge, has to be kept at approximately 90 *psi* for the present set-up.

The system stiffness, and the frequency in turn, can be purposely tuned by mounting a variable number of springs connecting the fixed base frame with the carriage: the system allows to anchor till 3 spring on each side, which extend in the same direction of the shaft-carriage alignment one, allowing this system to be modelled like a 1-DoF very low-damped system. Then, the choice of the light weight elements minimized the moving system mass. The springs employed are produced by Lee Spring (UK), model LE014B13S: they are made of stainless steel, and each had an outside diameter of $D_n = 4.775$ mm, a wire diameter of $d_w = 0.355$ mm, 151.9 counting coils, and a free length of $L_s = 63.50$ mm. Since the system is a one-pair-spring-one-mass arrangement, this pair of springs act in parallel, thus the system can be reduced to an equivalent single-spring-mass system given by the sum of the participating springs. The mass of each spring was 1.77 g, hence, even increasing their number the oscillating mass doesn't grow appreciably (see Tab. 4.2): the number of springs was varied for tuning the desired natural system frequency of oscillation.

Displacements measurement In order to precisely measure the displacements of the model a friction-free non-contact magnetostrictive linear variable differential transformer (LVDT) was embedded in the *AB* system. The LVDT (Model: SE 750-10000, Macro Sensors, USA) is placed on top of one pair of pillow blocks. It takes 24 V input and provides 250 mm range of measurement, which is higher than the total stroke allowed by the shafts. The sensor has been previously statically calibrated and the repeatability of the linear response has been assessed.

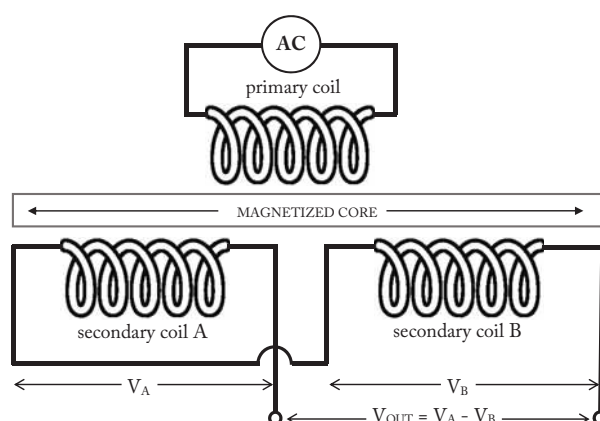


Fig. 4.5 Circuit scheme of the LVDT transducer.

Force balance A four-component force balance based on sensitive semiconductor strain gauges was also designed and built by Dr. Jisheng Zhao. The ‘head’ of each model needs to be equipped with an aluminium adapter allowing to screw them directly into the free end of the jutting part (sting) of the force balance (see the top of the models in Fig. 4.3.*left*). The strain gauges are bonded onto the lateral surface of the sting. The strain gauge model used was SB1-1000-P2, manufactured by BCM Sensor Technologies (Belgium), and were configured to form a Wheatstone bridge, helping to improve temperature compensation of the circuit³. The four channels measure respectively Lift Force, Lift Moment, Drag Force and Drag Moment, whose signals are amplified separately. The measurement range was designed to be ± 2.5 N with accuracy of 0.01 N, which was sufficient to measure the forces (within a range of ± 1.5 N) in that, as well as in the present, FIV study.

4.2.3 Static tests

Static tests in *WC* represent a double-check for what was found in the *WT*. The model was rigidly attached and the aerodynamic forces were measured for different values of flow velocity for different attack angles (α), set using different expedients. After having mounted any model in the *AB* rig, the air pressure was switched off in the air-bearings circuit, and then the shafts were clamped to the levelling platform to suppress any transversal motion. The investigated angles of attack cover a range $-5^\circ \leq \alpha \leq 95^\circ$ so to describe the transition from D24 to D37 configurations.

³For further information, calibration procedure or working principles the reader may refer to Zhao (2012)

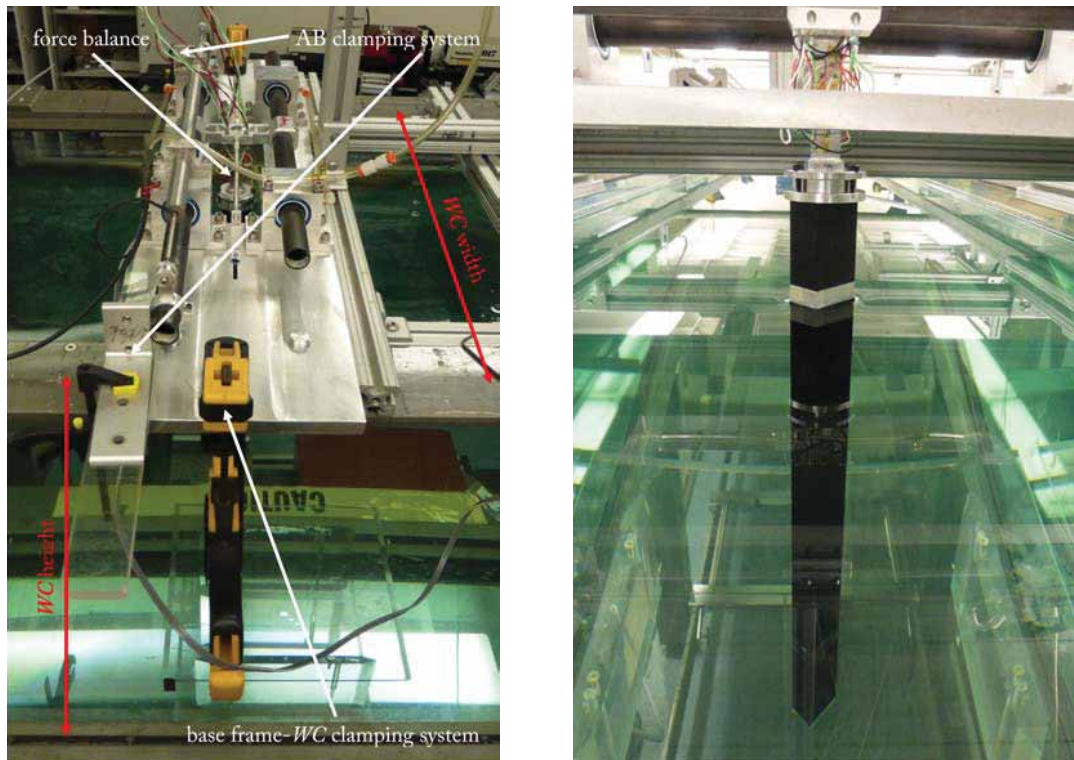


Fig. 4.6 (left) static rig in M_{s1} configuration obtained by clamping the AB system; (right) view of submerged rectangular aluminium model attached to the force balance.

Static rig 1 (M_{s1}) In the first series of static test the angle of attack was imposed by manually rotating the model, that means unscrewing and then screwing it again once reached the next angular position on the force balance sting. This modality was really time-consuming for two reasons: the first was the mere mounting and effective angle double-checking process, while the second was the fact that the measurements for the tested water speeds have to be conducted angle by angle, waiting to let the flow stabilizing around the cylinder. Therefore, five different flow-velocities were tested, equally distributed in the range allowed by the channel pump. An offset measurement was recorded for each angle variation. The length of each measurement was fixed in 120 s, while the recovery time, necessary to reach a steady state from a velocity to another, was empirically derived to be quite below 180 s, so that this time gap has been kept as a suitable value.

The results underlined that probably the repeated unscrewing-screwing procedure possibly put in force the strain gauges differently for each angle affecting first of all drag measuring. For the sake of completeness the overall results for C_{F_y} are proposed in Fig. 4.7: as clearly visible, C_{F_y} values are out from the expected range. Moreover, the points related to the lowest flow-velocity value don't follow at all the qualitative pattern of the higher Re curves. These results, though unsatisfying, have been here proposed mostly to make clear the motivations which led to the realization of the second static test rig which follows.

Static rig 2 (M_{s2}) A different technique set-up during the period at WC was obtained by the union of the rotator designed by Lawrence Wong (currently a Ph.D. candidate at MAE), for investigating the circular cylinder in forced rotations undergoing hydroelastic oscillations (Wong *et al.*, 2014), in order to optimize the static test technique just seen, and save a huge amount of time. The rig consists in a rotary engine that can be screwed to the

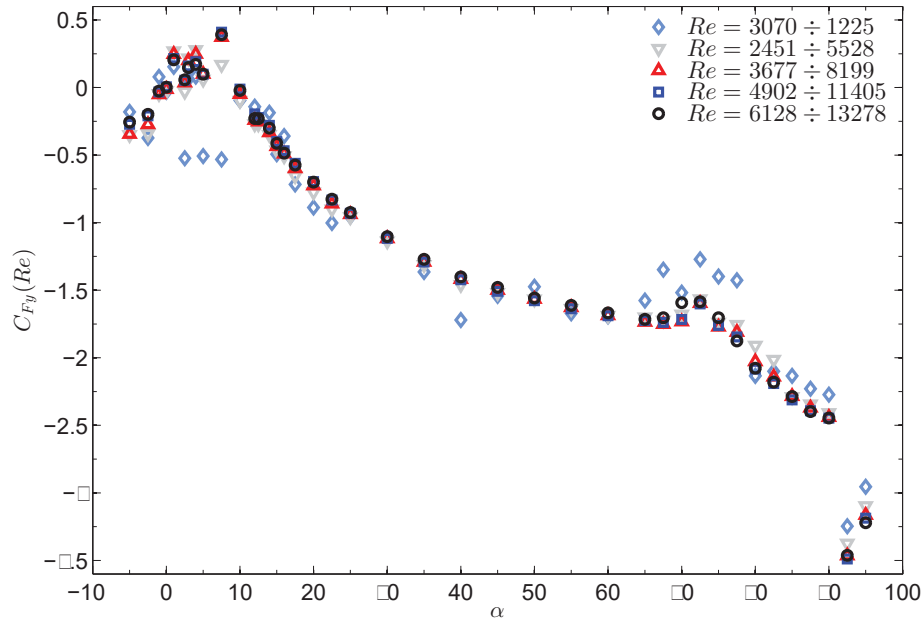


Fig. 4.7 M_{s1} results in terms of C_{F_y} for the entire range of imposed α .

bottom of the force balance, like it were a sectional model, after having inserted the model inside it by means of a purposely turned aluminium adapter, and fastened with four lateral grab screws (Fig. 4.8). The aluminium adapter was refined to prevent wobbling or parasite undesired effects. The rotor is externally controlled by using Parker 6K2 Motion Controller which allows to impose the desired constant angular velocity to the cylinder: the controller was re-programmed to obtain angular rotations instead of velocities.

The procedure for the detection of effective angles was made independent on the precise assignment of the perfect $\alpha = 0^\circ$ position: the cylinder was simply adjusted in a reference near-zero position, then it was programmed to automatically start from -0.5° and moving with a fixed angular step of roughly 0.5° to reach $\alpha = 105^\circ$. In this way the α range is well discretized. Each position assumed by the cylinder was captured using a PCO.2000 camera (2072×2072), triggered with the motion controller sending a TTL signal every time the angle was changed: once received the TTL signal, which was also recorded together with forces



Fig. 4.8 View from below AB system towards the rotor rig.

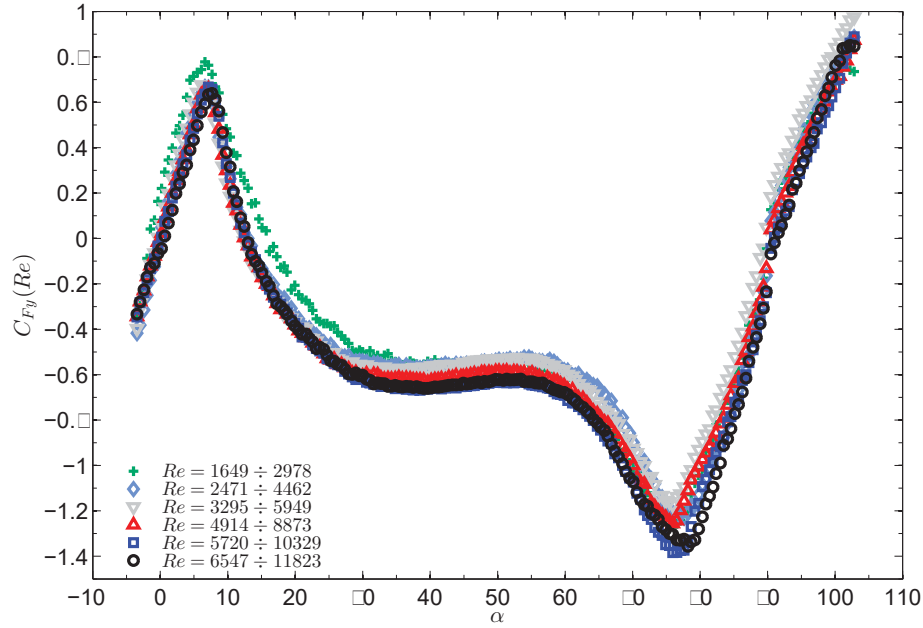


Fig. 4.9 Results in terms of C_{F_y} for the entire range of α imposed with M_{s2} .

and other signals, an image was automatically acquired with the software for the camera control (Camware). The procedure was completely automatic; an offset signal recorded was taken for each flow-velocity increment. It is worth noting that such a procedure is time-saving because such a slight increment in the angle of attack, meaning a slight variation of the near wake at each step, is almost instantly recovered around the body, much faster than a change in the flow speed for which a larger waiting time is needed to let the flow reach a steady state regime. After having recorded the results in terms of images and signals, the real values of each angle was determined by means of a iPhyton routine that precisely calculate the angle comparing the actual image with the initial one captured at near-zero angle. Then, the angles vector obtained with this procedure is shifted taking into consideration the crossing from negative to positive values of the lateral force coefficient C_{F_y} in correspondence of $\alpha = 0^\circ$. Given the rapidity of such a method, six different flow-velocities were tested; again, each measurement lasts 120 s, but this time the recovery time from an angle to the next one is only 10 s.

The results for the whole set of water speeds tested is reported in Fig. 4.9. The order of magnitude of the maximum reached by C_{F_y} is consistent with the results given previously for D77 and D30 models in the *WT* (see Fig. 3.17 and Fig. 3.20 in §3.3.2). Of course there are differences even at a first sight. First of all it is evident (see also Fig. 4.10.*left*) the lack of any inflection point; a linear trend is kept till reaching the maximum point correspondent to the apparent angle of attack from which the section experiences the reattachment of the shear layer on the side making the section stable, placed around $\alpha \approx 7^\circ$ (value reported in Parkinson (1963) for a $SR = 2$ rectangular section), instead of $\alpha \approx 9^\circ$ in D30 and D77 cases. Secondly Fig. 4.11.*right* was obtained by horizontally flipping the α -vector detected and then changing sign to the ordinates of lateral force coefficient to obtain a similar C_{F_y} vs. α curve for D37 model. The section resulted a soft-type oscillator in contrast with results obtained for D45 section in *WT*, even showing a steeper slope with respect to D24 one. Although in the literature $SR = 0.67$ section has been most of the time referred to

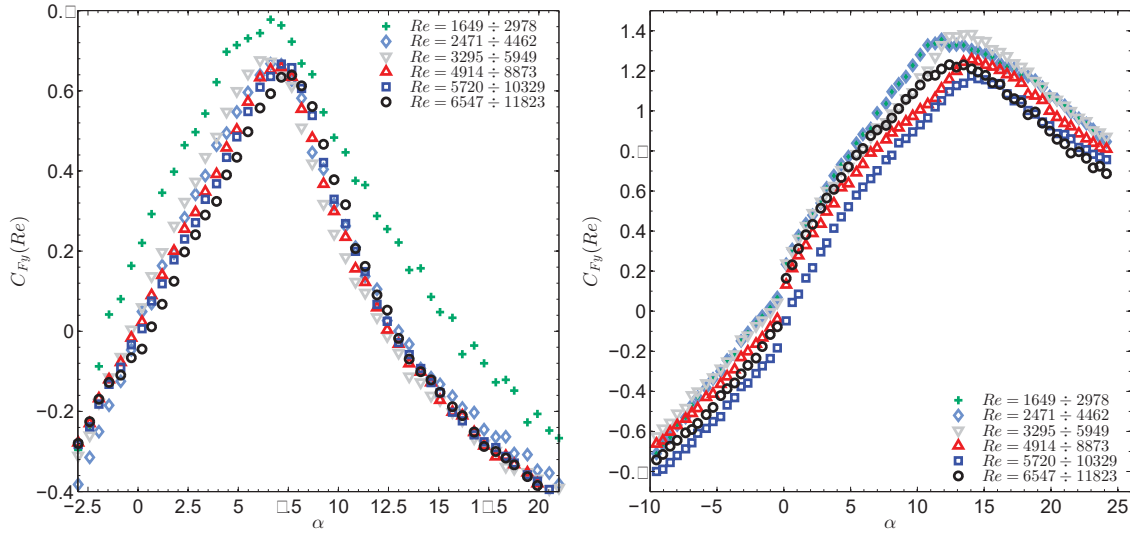


Fig. 4.10 Re -dependency for the lateral force coefficient C_{F_y} , for D24 tested with M_{s2} rig (left) and for D37 (right).

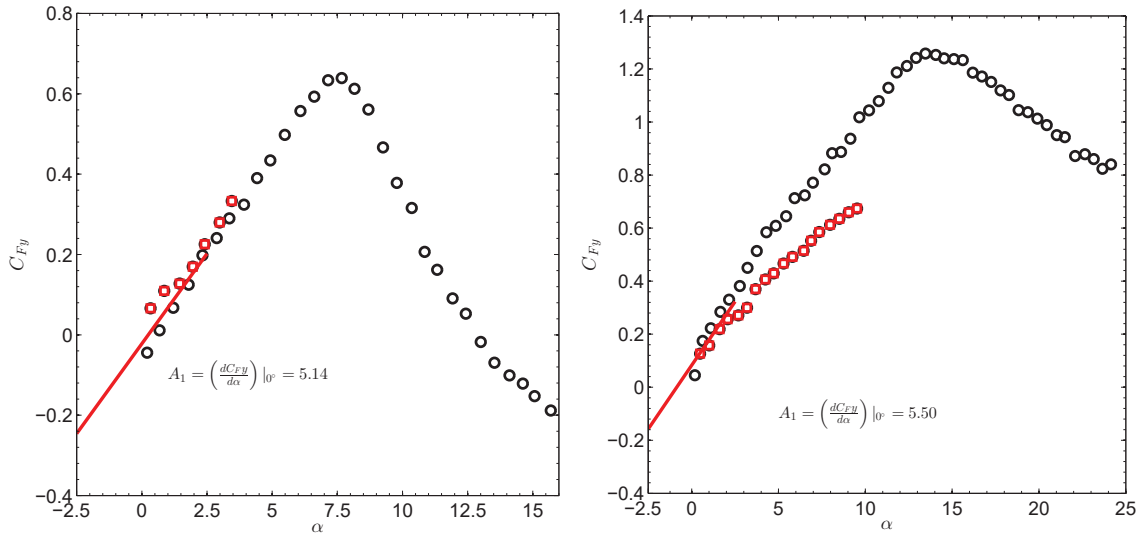


Fig. 4.11 Evaluation of A_1 parameter from the lateral force coefficient C_{F_y} , for the maximum Re of D24 model (left) and D37 (right) tested with M_{s2} rig.

as a hard-type oscillator in air flow cases, in the present conditions it turned out it to be unstable, consistently with respect to hydroelastic and static tests given in Bokaian and Geola (1983). For D37 the maximum point reached by C_{F_y} was around $11^\circ < \alpha < 14^\circ$ depending on Re .

After these general remarks it is interesting to report the results as previously done for D77 and D30 cases, by showing the A_1 parameter resulting from C_{F_y} curve slope around $\alpha = 0^\circ$. The plot reported in Fig. 4.11 relatively to D24 and D37, also show a not perfect superposition of the mirrored negative values, so that the slope of the C_{F_y} has been obtained through the linear regression in the range $-0.5^\circ < \alpha < +2.5^\circ$ instead of starting from $\alpha = -2.5^\circ$ like it has been done before. The reason for this discrepancy has not been fully detected. Nevertheless the values obtained for the rectangular cylinder are assumed to be consistent with dynamic tests and reliable for the purposes of the present dissertation.

Strouhal number measurements Particular attention was paid to the characterization of the Strouhal number over such a wide range of angles of attack. In addition to the measurements on M_{s1} and M_{s2} rigs, hot-film anemometry measurements were also performed. The spectral analysis on lift did provide the St detection for each angle. In addition, an hot-wire anemometer was placed 15 cm downstream with respect to the trailing edge of D24 cylinder and $\approx 1.2D$ in transversal direction, as indicated in Fig. 4.13.*left*. The measurements were recorded for two different flow velocities, correspondent to pump frequencies of 10 and 20 Hz, four angles of attack, 0° , 40° , 70° and 90° , and two durations for measurements, 5 and 20 *min*. While the Re -dependent results for St analyses with M_{s1} and M_{s2} are respectively reported in Fig. 4.12.*top* and *bottom*, hot-film measurements are proposed in Fig. 4.13.*right*. A comprehensive representation of all the above exposed results is summarized in Fig. 4.14.

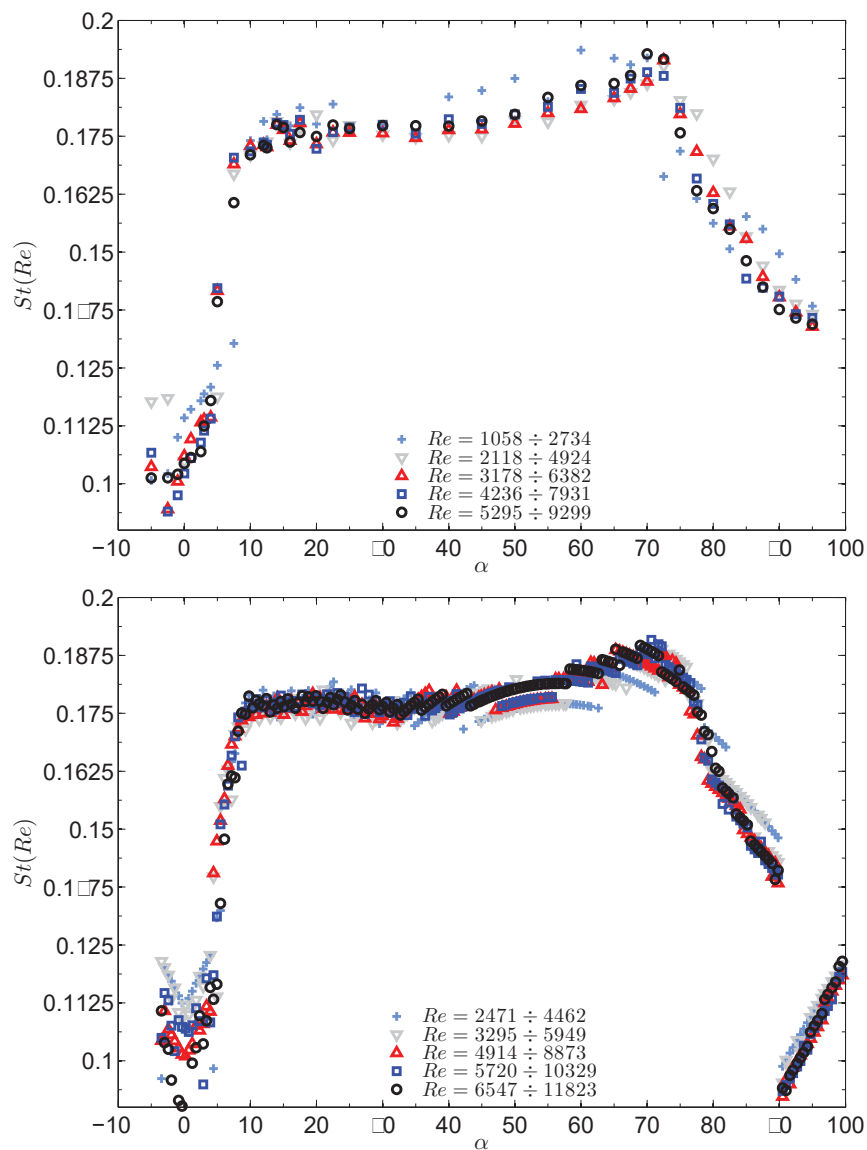


Fig. 4.12 St determined by changing angle manually (*top*), and automatically using the rotational rig (*bottom*).

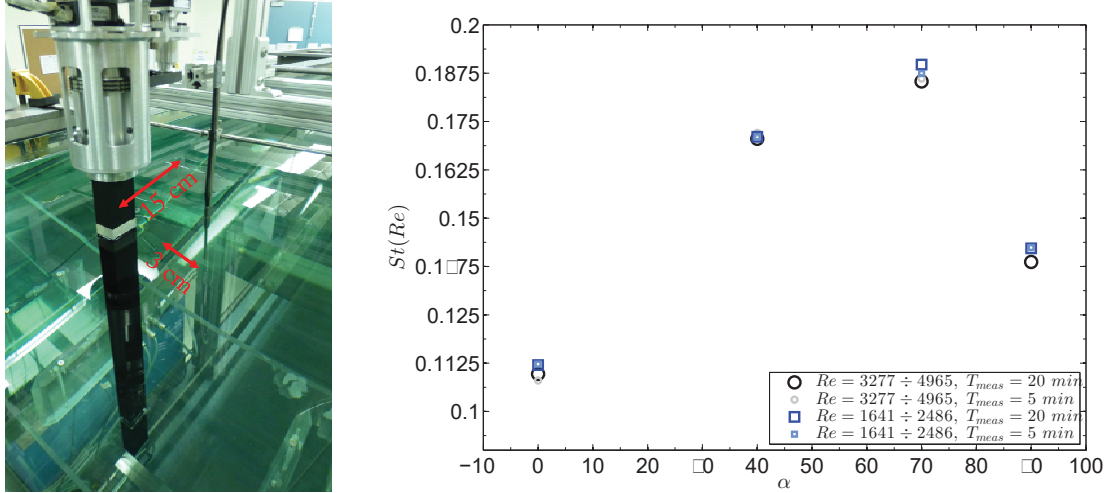


Fig. 4.13 (left) Positioning of the hot-film in the near wake of the body; (right) St results from hot-film anemometry.

An attempt has been made in choosing the most reliable values, in particular for D24 and D37 configurations; the Re -range matching the best superposition between different techniques is proposed, together with a curve (dashed light gray line) fitting the entire amount of experimental points. Some comments are needed when reading these results: St value of D24 is in good agreement with the literature and WT data (0.1044 against 0.105÷0.106), while that of D37 section is close to the square section case⁴ (0.137 against a St value for the square section in the range 0.127÷0.135 is reported in Tab. A.2). However, even hot-film anemometry provide a value practically identical to that expressed by static measurements (note that in Fig. 4.14 the St value provided via hot-film anemometry for D37 configuration is covered by the red filled circle marker indicating the chosen value). In practice, each St value was assessed by three different kind of test.

4.2.4 Hydroelastic tests

While for the stationary cylinder the fluid forces are directly recorded by the force balance, for hydroelastic tests the body experiences an inertial force induced by the acceleration. Hence, corrections are needed for the force component recorded by the force balance. The scheme reported in Fig. 4.15 can be taken as a reference for detecting the net fluid force F_y exerted on the body; the dashed line separate the moving system into two parts, the top and bottom part, for which the equation of motion can be expressed respectively by

$$F_s - c\dot{y} - ky = m_t\ddot{y}, \quad F_y - F_s = m_b\ddot{y}, \quad (4.1)$$

where m_t and m_b are the mass of the upper (top, subscript t) and lower (bottom, subscript b) system parts. It turns out that the transverse fluid force is then determined by using Eq. (4.1) as

$$F_y = F_s + m_b\ddot{y}. \quad (4.2)$$

In this case, only one dynamical test rig was employed, as the AB^5 rig guaranteed a

⁴It will be also shown in the following how $SR = 0.67$ behaves differently from square in general and from the same section ratio in air flow for this Re -regime

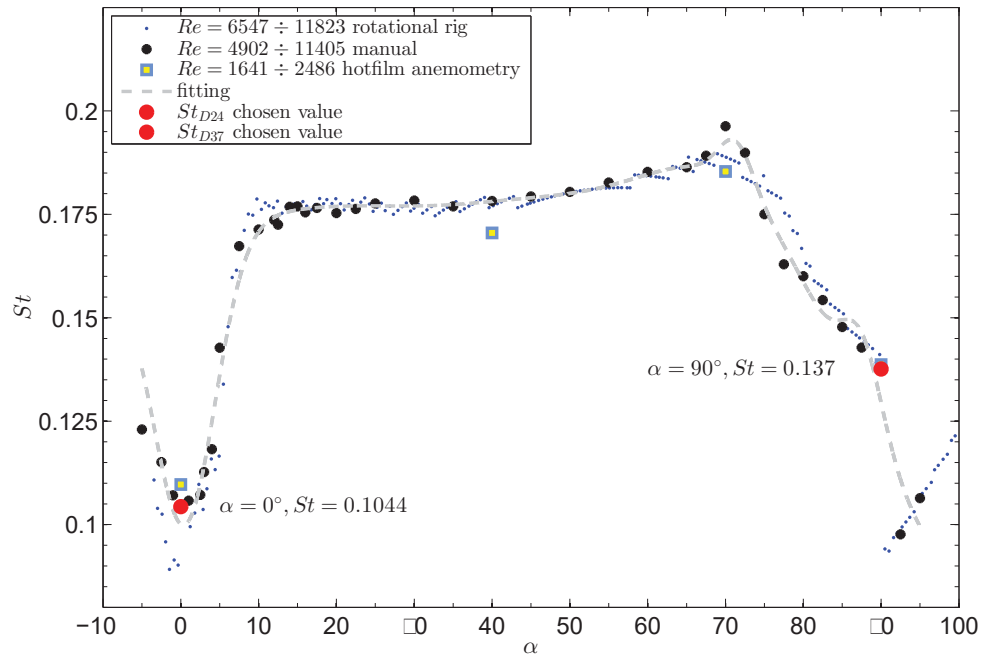


Fig. 4.14 St results for the highest Re for different techniques.

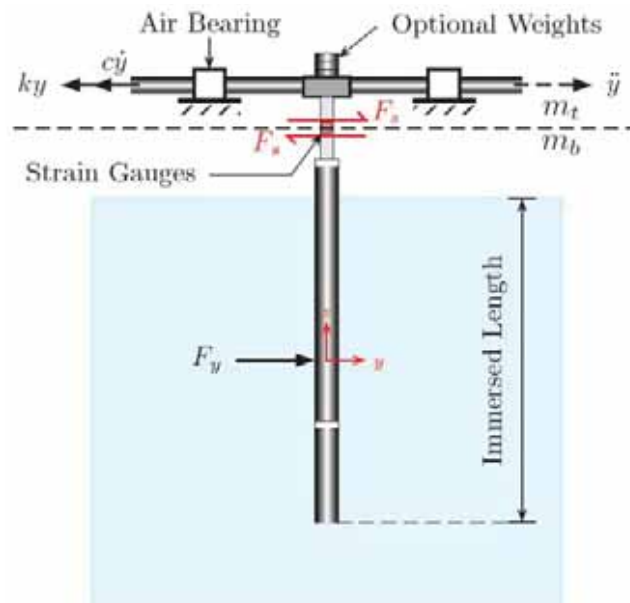


Fig. 4.15 Schematic for force measurement correction [taken from Zhao (2012)].

perfectly 1-DoF low-damped transversally moving system, allowing to easily attach any kind of 2D prismatic elongated body and to impose whatever angle of attack. However, an identification needs to be performed before each test case.

For aeroelastic tests the *rms* of nondimensional amplitude has been proposed as the main response parameter, being considered as statistically representative of the signal types recorded; the same parameter has been kept when illustrating hydroelastic results too, together with another one so-called A_{10}^* : it is defined as the mean of the top 10% of the peaks, as used by Hover *et al.* (1998) and Morse *et al.* (2008). This scalar provides a

⁵see §4.2.2

more appropriate and statistically robust measure for comparison of different, independent studies and different cross-sections. The same parameter was employed in the researches on FIV of circular and square cylinder performed at FLAIR laboratory on *AB* rig.

In Appendix C the complete set of results is reported: each angle of attack and mass ratio configuration investigated has been described by proposing three plots reporting on the top part the amplitude response curves in terms of both y'/D and A_{10}^* , while in the center and bottom there are two gray scale coloured plots representing the logarithmic-scale frequency power spectrum contour plots of the body oscillation (f_y^*) and transverse lift (f_L^*). They were formed by Fourier-transforming the time histories in correspondence of each U^* , then normalizing the resulting spectrum by the maximum energy peak. The normalized spectrograms so obtained were then placed continuously side by side. It goes without saying that the higher the number of velocities investigated the smoother the resulting plot; unfortunately the time schedule made the results for some angles of attack less refined. Note that the frequency ratio, either for displacement or lift, is normalized with respect to the system natural frequency f_n .

In the following, after having described the identification procedure here adopted, the obtained results will be commented.

4.2.4.1 Free-decay test

Generally speaking, the damping of the present FIV system is given by at least two contributes, the structural damping due to friction and relative motion between parts of the system (*i.e.* the shafts moving through air bearings) and fluid damping due to hydrodynamic force of the surrounding fluid. While the first contribution can be obtained by free-decay tests in still-air, as it is a characteristic of the mechanical system not depending on the fluid density, the procedure needs to be conducted twice to determine the natural frequency of system in water, representing the natural frequency to be used for nondimensionalization. The damping ratio in water gives also information about the added mass, m_A , negligible in air but significant in water flow. The added mass (or virtual mass) represents the inertia added to a system because of the deflection of a portion of fluid volume impressed by the cylinder as it tries to accelerate/decelerate; it can be defined by $m_A = C_A m_d$, being C_A the potential added mass coefficient ($C_A = 1$ for a circular cylinder), while m_d is the fluid displaced mass. It is worth noting that m_A is not involved in the calculation of m^* , being the oscillating mass the sum of the sectional model and the moving system parts. The system is subjected in this case to an hydrodynamic force F_y ; the Morison force can be written according to the formulation proposed in Sumer and Fredsøe (1997):

$$F_y = - \underbrace{\frac{1}{2} \rho_w C_D D L |\dot{y}| \dot{y}}_{\text{fluid damping force}} + \underbrace{m_A (-\ddot{y})}_{\text{added mass inertial force}} = m \ddot{y} + \underbrace{c \dot{y}}_{\text{structural damping force}} + k y \quad (4.3)$$

making the inertial \ddot{y} -dependent term no more equal to m but to $(m + m_A)$. In this case the total damping in water, ζ_w is given by two terms, the *structural* damping with added mass in still water (ζ_{sw}) and the *fluid* damping in still water (ζ_{fw}). Then, the undamped natural angular frequency in still water is similarly defined as

$$\omega_{nw} = \sqrt{\frac{k}{m + m_A}} = 2\pi f_{nw} , \quad (4.4)$$

test case	m^* -	m [kg]	m_{add} [kg]	springs -	f_{na} [Hz]	$f_n = f_{nw}$ [Hz]	Δf_{a-w} [%]	$\zeta = \zeta_a$ [%]	Λ -
D24-W1	2.24	1.28	0.0000	2	0.704	0.519	26.29	0.24697	0.0028
D24-W2	3.02	1.73	0.4504	4	0.835	0.656	21.46	0.21330	0.0033
D24-W3	3.50	2.00	0.7222	4	0.778	0.629	19.12	0.22076	0.0039
D24-W4	4.10	2.34	1.0658	4	0.721	0.599	16.93	0.18945	0.0040
D24-W5	6.00	3.43	2.1526	6	0.721	0.629	12.70	0.15076	0.0046
D24-W6	7.49	4.28	3.0006	6	0.648	0.576	11.18	0.15037	0.0058
D24-W7	9.76	5.58	4.3002	6	0.565	0.519	8.11	0.15207	0.0076

Tab. 4.2 Test cases for aluminium model $SR = 1.5$ (D24) in smooth water flow.

while the damped pulsation is defined as in the air-flow case by $\omega_{dw} = \omega_{nw} \sqrt{1 - \zeta_w^2}$. The total damping is the result of energy dissipation caused by the total damping force F_d , given by the sum of the fluid and structural part in Eq. (4.3), and it is proportional to the ratio of the energy dissipated in one cycle of vibration E_d and the total stored energy E_T , expressed by

$$\zeta_w = \frac{1}{4\pi} \frac{E_d}{E_T} \quad (4.5)$$

Now, being E_d determined by integration of the total damping force in one cycle, that is

$$E_d = \oint F_d, dy = \int_t^{t+T_{dw}} F_d \dot{y}, dt = \int_t^{t+T_{dw}} c \dot{y}^2, dt + \int_t^{t+T_{dw}} \frac{1}{2} \rho_w C_D D L |\dot{y}| \dot{y}^2, dt \quad , \quad (4.6)$$

while the total stored kinetic energy is simply given by $E_T = 1/2 (m + m_A) \dot{y}_{max}^2$ for a simple harmonic motion . The substitution of both the energy expressions into Eq. (4.3) gives

$$\zeta_w = \zeta_{sw} + \zeta_{fw} = \underbrace{\frac{c}{2(m + m_A)\omega_{dw}}}_{structural \ damping} + \underbrace{\frac{\rho D^2 L}{4\pi(m + m_A)} \frac{8}{3} C_D \frac{A}{D}}_{fluid \ damping} \quad , \quad (4.7)$$

helpful in clarifying that the value of damping, ζ , which will be reported in the future experimental results is the ζ_{sw} one, as expressed in Eq. (4.7), and also given by the combination of

$$f_{na} = \frac{1}{2\pi} \sqrt{\frac{k}{m}} \quad , \quad \zeta_{sa} = \frac{c}{2\sqrt{km}} \quad , \quad (4.8)$$

respectively the frequency and damping in still air, with Eq. (4.7) and Eq. (4.4) by

$$\zeta = \zeta_{sw} = \frac{f_{nw}}{f_{na}} \zeta_{sa} \quad . \quad (4.9)$$

An example of the identification procedure for the system natural frequency and damping ratio with respect to critical is described in Fig. 4.16: for still-air measurements it is only necessary to dismount the model and replace its mass with a dummy one, carefully weighted and placed on the moving parts of the AB rig. The results for the seven mass ratios tested for D24 model are listed in Tab. 4.2, while the three cases tested for D37 in Tab. 4.3; it is worth nothing that for all the test cases $m_d = 0.571$ kg given that the immersed volume of the model was not changing.

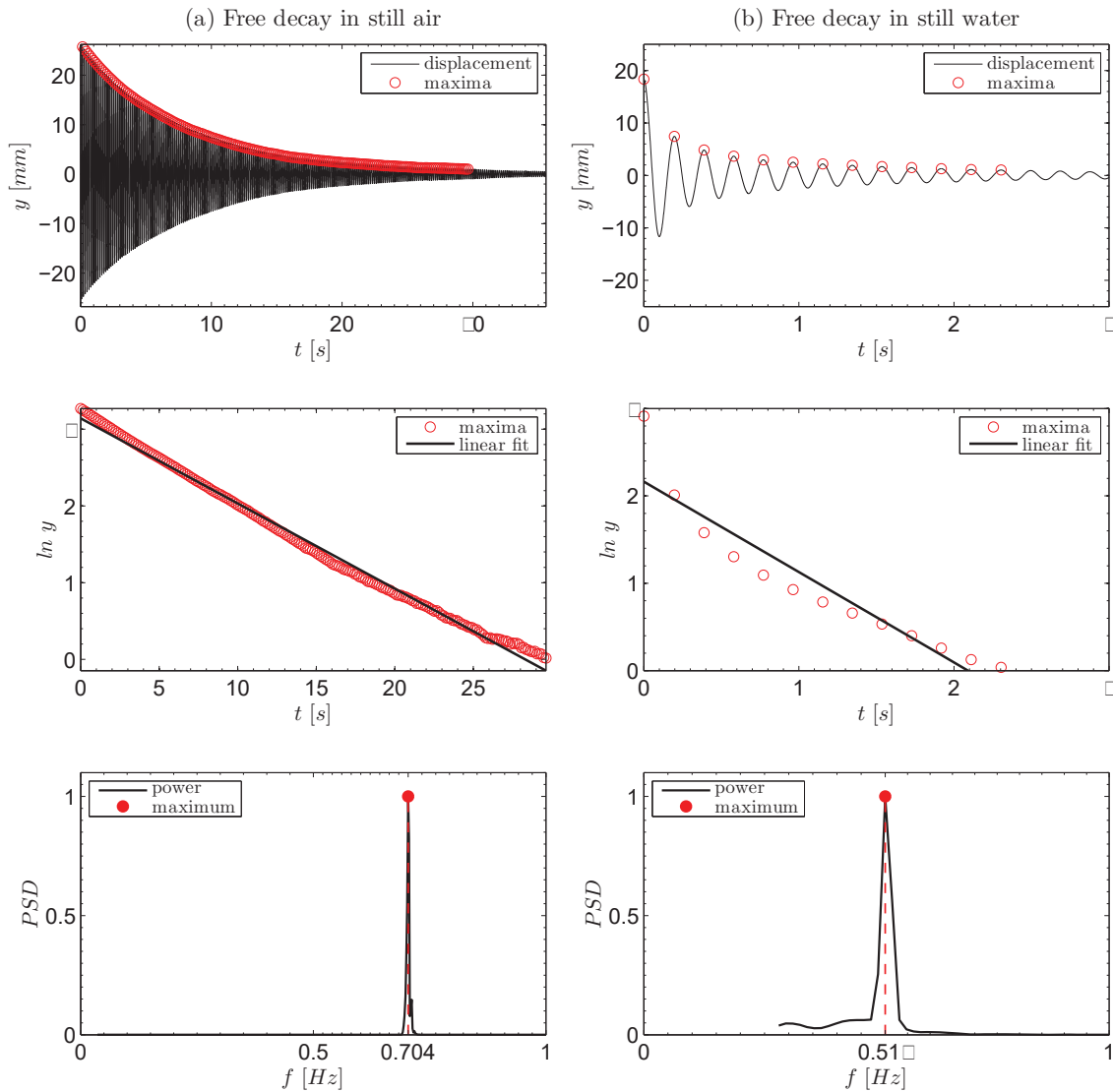


Fig. 4.16 An example of free decay tests of a $SR = 1.5$ rectangular cylinder with $m^* = 2.236$, that is D24-W1 test case reported in Tab. 4.2: (a)-column plots show free decay test in air while (b)-column ones show free decay test in still water. The top row plots report the displacements time traces showing the decay from the y_0 value (note that several test imposing different initial displacements were tested obtaining in practice always the same values in terms of characteristic frequency and damping of the system). The middle row shows the decay rate based on a logarithmic decrement algorithm, while the bottom row shows FFT calculation of the PSD normalised with respect to the spectrum peak.

test case	m^*	m [kg]	m_{add} [kg]	springs	f_{na} [Hz]	$f_n = f_{nw}$ [Hz]	Δf_{a-w} [%]	$\zeta = \zeta_a$ [%]	Λ
D37-W1	2.24	1.28	0.0000	2	0.704	0.595	15.45	0.24697	0.0028
D37-W2	3.51	2.98	0.7247	4	0.774	0.690	10.84	0.21904	0.0039
D37-W3	9.79	4.32	4.3163	6	0.565	0.530	6.08	0.14478	0.0073

Tab. 4.3 Test cases for aluminium model $SR = 0.67$ (D37) in smooth water flow.

Before showing the two main studies carried out in the *WC*, it seems interesting to make some remarks on the fundamental cases, namely D24-W1 and D37-W1. These constitute

the base for any further analysis and comparison will help in the comprehension of the other tests cases investigated. In Fig. 4.17 and 4.18 the reduced maximum amplitude and dominant displacement frequency response curves are shown respectively for D24 ($\alpha = 0^\circ$) and D37 ($\alpha = 90^\circ$). The data taken from Nemes *et al.* (2012) relative to a comparable low mass ratio square cylinder, H25, was superimposed in filled blue square markers.

Dark and light gray patches zones correspond to synchronization and galloping velocity range for D24 test case. A super-harmonic lock-in range, starting at $U_r/3$ whose local maximum is placed roughly at $2/3U_r$, is recognizable from the reduced frequency values $f_y/f_n \approx 1$ (not perfectly flat as reported in Fig. 2.6); on the other hand, only one locked point is visible for H25. Afterwards, a desynchronization region occurs in a wide velocity range, during which the amplitudes linearly decrease, for reasons which are still not clear, while f^* branch follow a slope equal to that of $2St$. Then, there's a sudden transition to galloping instability branch, at $U/U_r \simeq 1.6$, characterized by a dominant frequency response agreeing with the square section one ($f^* \approx 0.5$), and by an amplitude response unrestrictedly increasing as the reduced velocity gets higher. It is interesting to note how the amplitude response line identified by the square-related markers meets the galloping branch of D24 section, showing also a similar slope in pre- and post-critical response branch.

The same meaning for patches colors are kept for D37 case in Fig. 4.18: in this case, after an initial FIV branch in which the vibration amplitudes grow following the Strouhal law, a lock-in region is present right before the galloping instability onset. It is worth noting that this transition is denounced by the frequency response, given that the reduced frequency drop to lower values around $0.7 \div 0.8$, but not by the amplitudes domain which keeps almost the same slope, being indeed quite similar to that expressed by H25 section. The only deviation for the almost linear trend shown in the entire velocity range is constituted by the lock-in range, in which the body experiences an increased response.

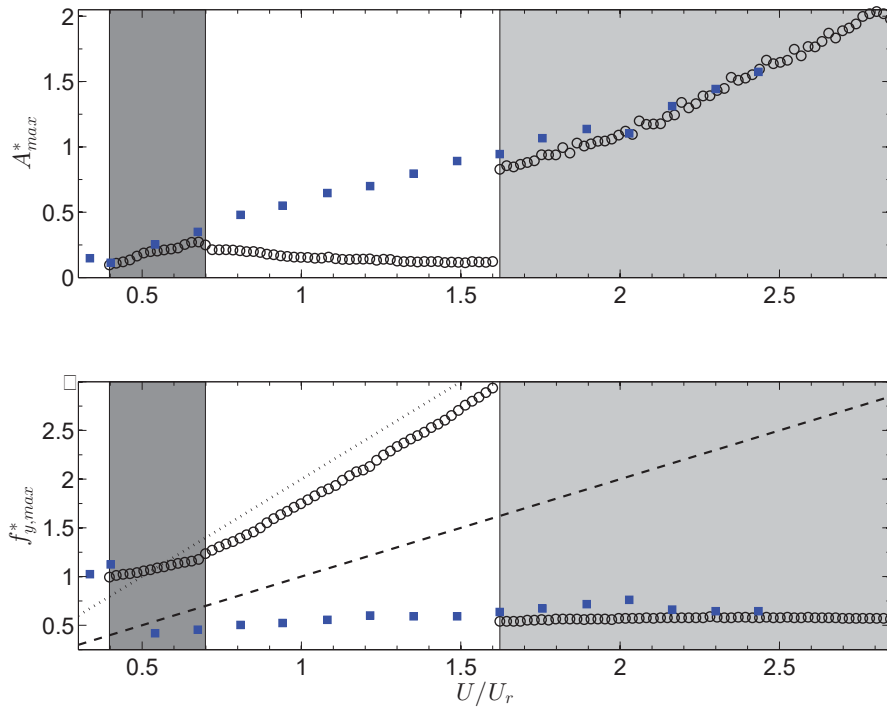


Fig. 4.17 (top) Reduced maximum amplitude response (A_{max}^*) and (bottom) dominant reduced body displacements frequency response ($f_{y,max}^*$) of D24 [\circ] superimposed to the response of square cylinder H25 [\blacksquare] (taken from Nemes *et al.* (2012)), vs. reduced velocity, U/U_r .

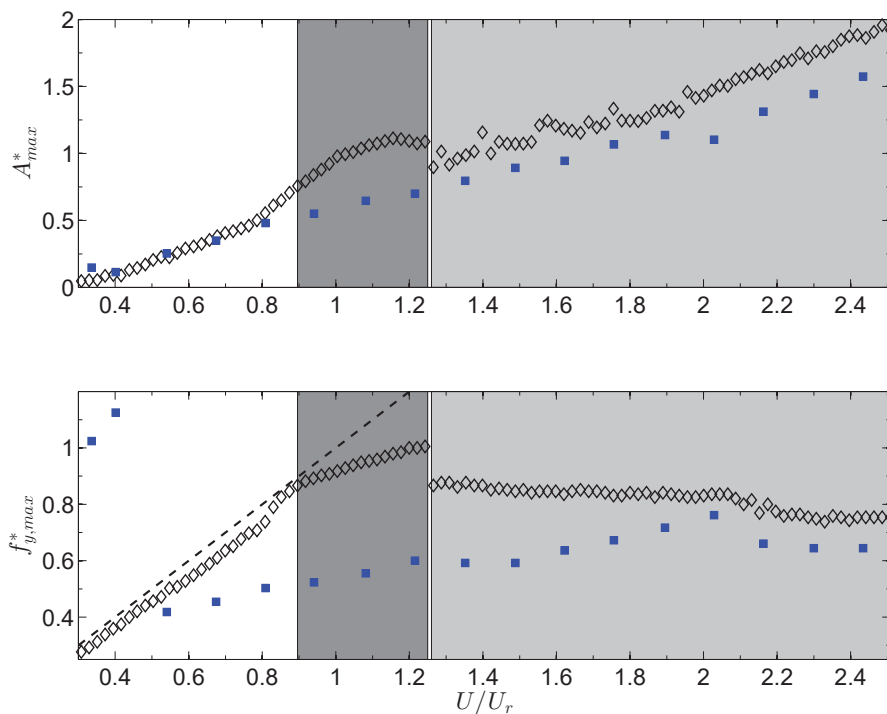


Fig. 4.18 (top) Reduced maximum amplitude response (A_{max}^*) and (bottom) dominant reduced body displacements frequency response ($f_{y,max}^*$) of D37 (\diamond) superimposed to the response of square cylinder H25 [\blacksquare] (taken from Nemes *et al.* (2012)), vs. reduced velocity, U/U_r .

4.2.4.2 Angle of attack study (α -study)

This first study originated from the observation of the different amplitude response type showed by changing α , starting from D24 and imposing wide increments to cover the α -range till reaching D37. The idealized sketch for such a kind of test is proposed in Fig. 4.19. Always referring to the lowest mass ratio, that means without any optional

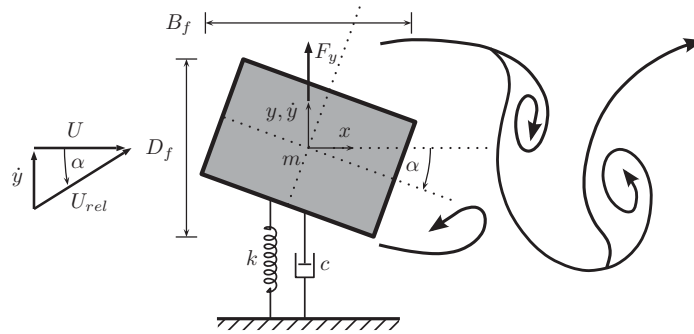


Fig. 4.19 Test rig model sketch for cross-flow motion of a $SR = 1.5$ rectangular cylinder with variable angles of attack. The cylinder undergoes free vibrations constrained in the y direction, transversal to the free-stream U in x direction, being it allowed to be rotated of α , resembling a $B/D = 1.5$ rectangular body invested by a variable U_{rel} incidence flow velocity. D_f and B_f are referred to the body depth and width seen by the flow, being the first the only one of interest calculated as $D_f = D \cdot \cos(\alpha) + B \cdot \sin(\alpha)$.

(m_{add}) mass added to AB system, the transition from D24 to D37, already presented in Fig. 4.17 and Fig. 4.18, was refined to describe as carefully as possible the transitions between α -responses; an attempt to collapse all the results in a 2D and 3D views is proposed in Fig. 4.20, containing a large amount of information. The α -range has been discretized by 5° angular steps, except for the near-zero range for which 1° and 2.5° were investigated too. The plots group shows 2D (left column) and 3D (right column) amplitude response curves by increasing the flow velocity (U/U_r on X-axis), and for the entire range of α investigated (α on Y-axis); concerning the Z-axes, the plots group rows propose in the top and middle rows the y'/D and A_{10}^* already introduced, while the mean value of the nondimensional amplitude is shown in the bottom row, to control primarily the degree of accuracy of the $\alpha = 0^\circ$ position, either for D24 or D37 case. The alternate shadowing for each angle step are helpful to read *e.g.* the almost zero-mean response of the D24 curve. A different view angle has been reported in Fig. 4.21, showing in this case too the zero-mean response of the D37 \bar{y}/D response curve.

The near-zero α -range has been refined because of the remarkable difference manifested from 0° to 5° , and which was found later to qualitatively already happens from 1° to 2.5° . In the following, from time to time, we will refer to the plots reported in Appendix C to better explain the observed phenomena which are summarized in the images proposed in the present chapter for the sake of brevity.

Response type 1 ($0^\circ \leq \alpha < 2.5^\circ$, Fig. C.1-C.2). D24 response already described qualitatively keeps the same patterns for $\alpha = 1^\circ$, a bit anticipating the onset of unstable branch and jumping more smoothly to a higher amplitude while experiencing a similar super-harmonic resonance whose local maximum doesn't change. It is quite interesting to observe the

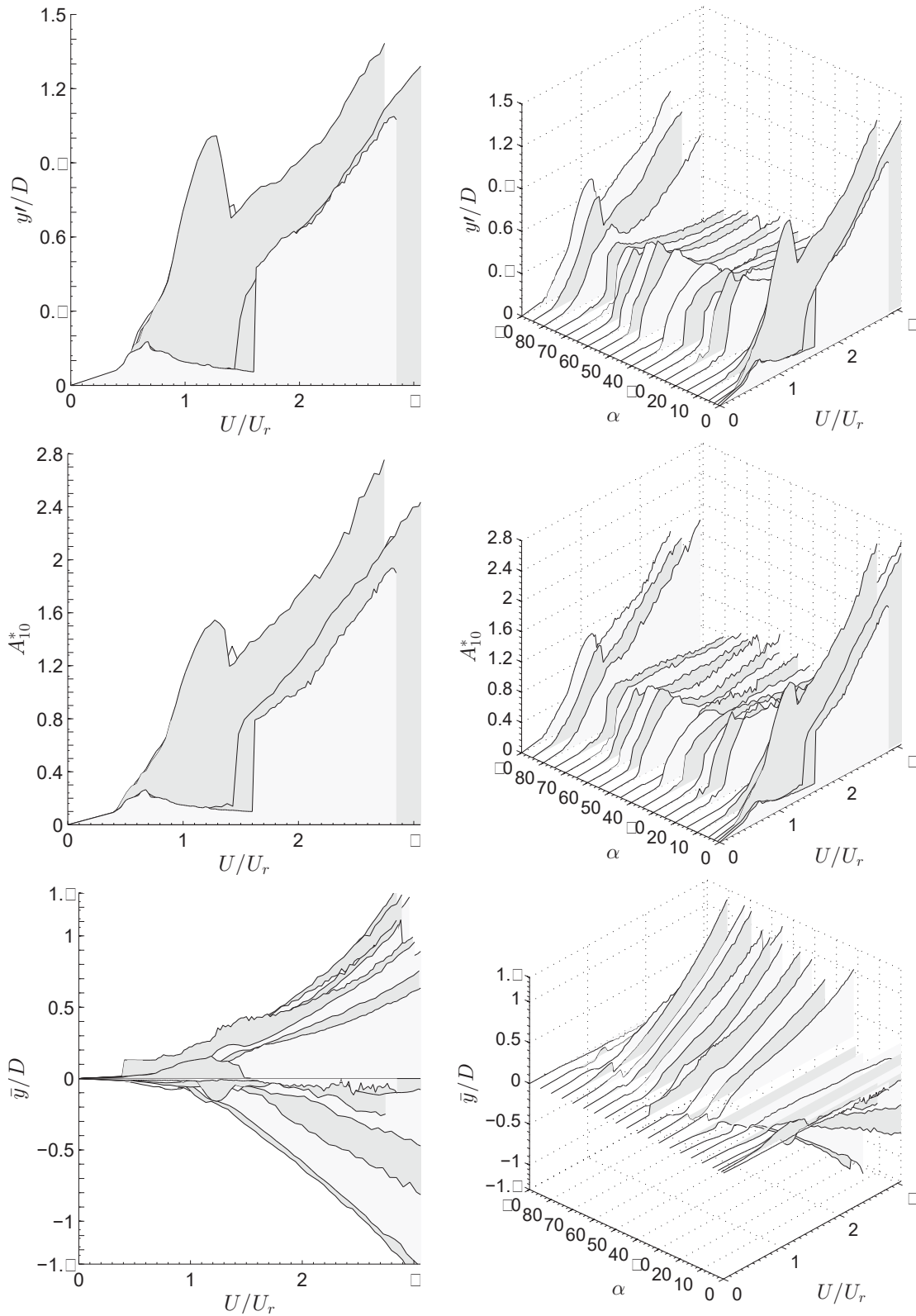


Fig. 4.20 α -study comprehensive 2D and 3D results.

nondimensional frequency plot in Fig. C.1: the narrow black line which lasts till $U/U_r \approx 1.6$ means the energy to be concentrate on the dominant frequency of oscillation, locking on f_n in the range $0.4 < U/U_r < 0.7$; the surrounding zone assumes a lighter gray colour showing

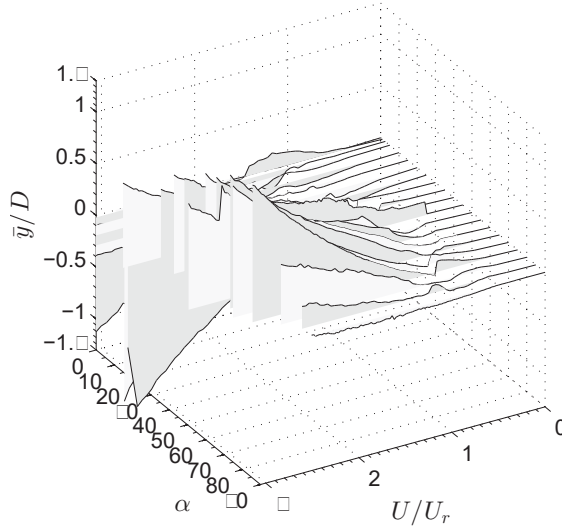


Fig. 4.21 Different view angle for the same plot proposed in Fig. 4.20.*bottom right*, useful for D37 configuration.

no super-harmonics on f_y^* plot, while for f_L^* the 2nd and 3rd order harmonics are visible. The desynchronization region, $0.7 < U/U_r < 1.6$, curiously assumes a slope corresponding to $2St$ in the reduced frequency domain (meaning the f_{vs} harmonic of the 2nd order), as showed in Fig. 4.22.*bottom*. However, a justification for such a behaviour have not been yet understood. At the onset of the galloping instability, $U/U_r \approx 1.6$, there's a sharp cut in the frequency domain too, leading to a dominant value of about 0.5, which is not in line with an expected value around 1, as usually happens in air flow cases. Within this highest velocity range the signals are more noisy than in synchronization and desynchronization zones (as denounced by darker gray colors around the dominant frequency line); in addition, there's the more marked presence of higher harmonics which interact each other; on the other hand those ones of order 2, 4 and 5 are barely visible. By observing Fig. 4.22, in correspondence of the crossing point between 6th order galloping super-harmonic and the first visible f_{vs} one, that seems to correspond to $1.5 \cdot f_{vs}$, as indicated in the figure caption, a sort of kick in A_{10}^* amplitude response, less visible but still present in y'/D curve reported in Fig. C.1, was recorded, implying an increased slope in the response curve. From a closer examination of the relative time histories of displacements it turned out that in correspondence of such a phenomenon the signals showed modulations with higher wave length compared to the lower velocity points.

Response type 2 ($2.5^\circ \leq \alpha \leq 10^\circ \cup 80^\circ \leq \alpha \leq 90^\circ$, Fig. C.3-C.5 and Fig. C.19-C.21). A completely different response curve shape abruptly manifests itself at $\alpha = 2.5^\circ$ showing vortex-induced vibration starting practically from the lowest flow velocity and following exactly the Strouhal slope up to a lock-in region (which is variable in the onset velocity and extension depending on α), then regularly reaching a local maximum point, which is around 1.5 for A_{10}^* in the range $2.5^\circ \leq \alpha \leq 10^\circ$, and around 1 for $80^\circ \leq \alpha \leq 90^\circ$. An evident synchronization, with f captured by f_n , is present for $\alpha = 2.5^\circ$ case in the interval $0.9 < U/U_r < 1.3$ (Fig. C.3), where lighter shade of gray colors underline sharper peaks (darker lines) in the spectra evidencing the dominant frequency and, especially for f_L^* case, the super-harmonics of 2nd and 3rd order. Then, there's a drop down in amplitude response, falling onto the

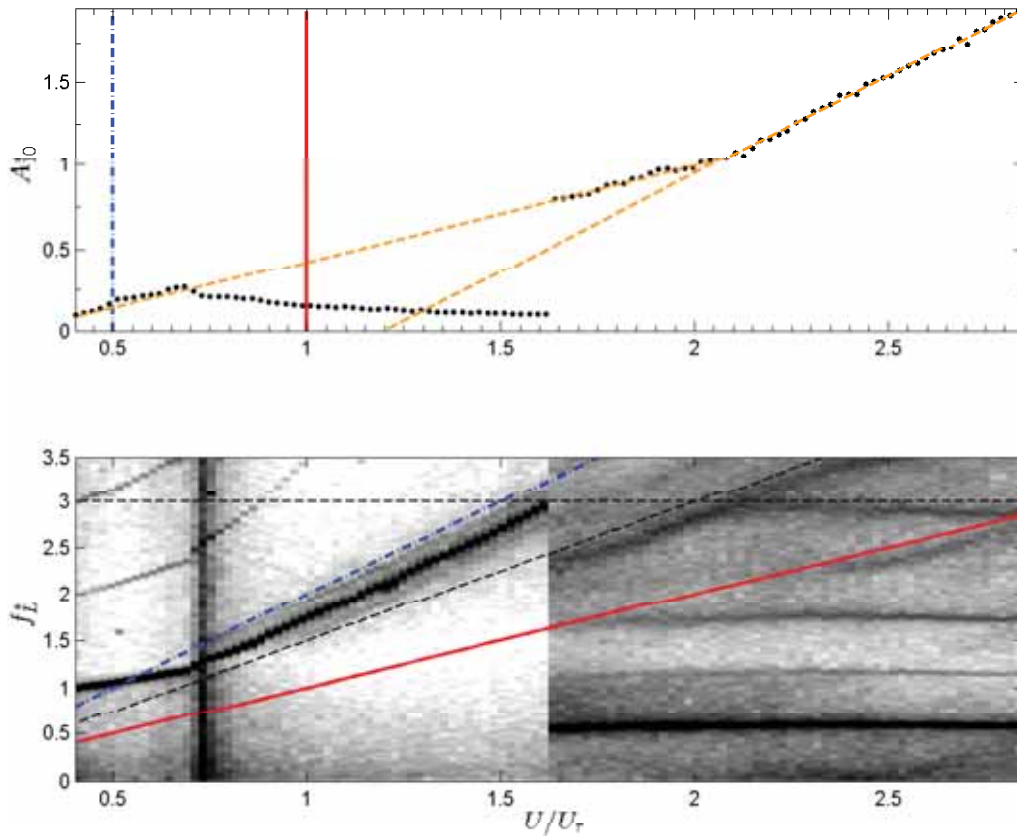


Fig. 4.22 Amplitude (*top*) and lift coefficient (*bottom*) nondimensional responses of $\alpha = 0^\circ$ case (D24). f_{vs} harmonics of order 1 (St) and 2, are indicated respectively in red continuous and blue dotted line while in orange dashed lines (*top* plot), the crossing point between two distinct linear trends is detected corresponding to the interacting super-harmonics of f_{vs} (order 1.5) and the dominant one in the instability branch (order 6).

galloping branch associated to more noisy signals, denounced by a dominant frequency a bit lower than $f^* \approx 1$. Either the amplitude and frequency response are of the same kind for the two α -ranges treated in this paragraph. Nevertheless, the analysis of the reduced frequency domain is clearer for D37 case ($\alpha = 90^\circ$): as for the D24 case a couple of more useful plots are reported in Fig. 4.23, where St and $2 \cdot St$ reference lines are indicated in both amplitude and frequency domain. Again, an interaction between galloping and f_{vs} super-harmonics can be observed causing a change in the A_{10}^* slope at a certain flow speed ($U/U_r \approx 2$).

Response type 3 ($\alpha = 15^\circ$, Fig. C.6). Here, a pretty messy amplitude response could be divided into two main region looking at the frequency domain: in the first one ($U/U_r < 1.8$) a trend line in reduced frequency domain follows the Strouhal law although a ‘competition’ between several harmonics seems to cause such a scattered amplitude response; in correspondence of some reduced velocities in the scattered zone some sub-harmonic lock-in is visible though never prevailing so to constitute a proper range. In addition, also for the lowest velocity range an high peak is present at the same time around $0.5 < U/U_r < 0.75$ expressing $f_y^* \approx 1$, indicating a super-harmonic lock-in which is apparently not detectable in amplitude domain. Then, a wake-induced vibrations zone ($U/U_r > 1.8$) showing slowly increasing amplitudes given by the vibration induced by the wake vortices and also a peak

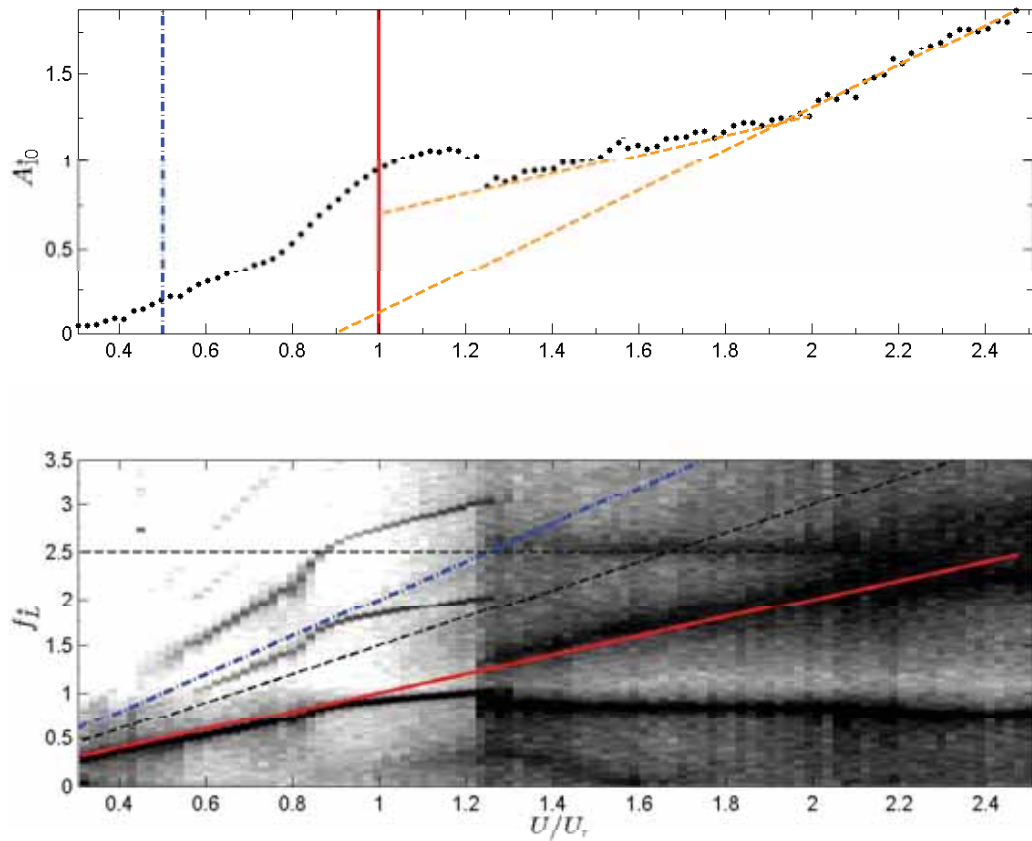


Fig. 4.23 Amplitude (*top*) and lift coefficient (*bottom*) nondimensional responses of $\alpha = 90^\circ$ case (D37). f_{vs} harmonics of order 1 (St) and 2, are indicated respectively in red continuous and blue dotted line while in orange dashed lines (*top* plot), the crossing point between two distinct linear trends is detected.

in the spectrum much wider around the Strouhal trend line. As a matter of fact $\alpha = 15^\circ$ marks the switching from *type 2* to *type 4* response: according to the static tests the proneness of the instability to develop from rest holds till about $\alpha = 8^\circ$, and even if $\alpha = 10^\circ$ case response has been categorized in the previous *type 2*, the transition to a different pattern is evident. Therefore the present case seems to represent boundary for unstable configurations.

Response type 4 ($20^\circ \leq \alpha \leq 75^\circ \setminus \alpha = 45^\circ$, Fig. C.7-C.11 and Fig. C.13-C.18). Without considering numerous local features by changing angle in the present range, which indeed did not fit any recognizable trend, the response shows negligible amplitudes till the occurrence of a lock-in region (with variable width of the correspondent bell and of the velocity onset), followed by a desynchronization branch characterized by a more or less pronounced prevalence of f_{vs} . The peculiar feature, variable from angle to angle, is the shape of the resonance bell which can be more or less steeper, presents a pronounced peak or different transitions to desynchronization branch. The local nondimensional amplitude maximum values slightly change from an angle to another. Furthermore, from the observation Fig. 4.20.*bottom-right* at $\alpha = 30^\circ$ an inversion in the mean value sign can be observed.

Response type 5 ($\alpha = 45^\circ$, Fig. C.12). In this configuration no synchronization is clearly

visible, except for $U/U_r \simeq 0.38$ where an almost imperceptible super-harmonic lock-in is present. In the frequency domain the dominant contribute widen the visible black trace, mainly where the amplitude response shows a plateau. Then, starting from $U/U_r = 1.2$ there's a jump in amplitude upwards, after which the reached amplitude value is kept constant also by increasing the flow velocity. It is interesting to underline that from a closer examination of displacement time histories lots of them showed an intermittent behaviour, more than any other α case.

The above proposed differentiation by response type is quite easily appreciable in Fig. 4.20 although, given the lack of frequency domain comparison, it is impossible the discrimination of $\alpha = 15^\circ$ and 45° , or the visualization of $5^\circ \leq \alpha \leq 15^\circ$ which result hidden by $\alpha = 2.5^\circ$ gray-filled curve. The fact that the two kind of nondimensional response parameters, y'/D and A_{10}^* , showed a good qualitative agreement implies an equivalence from the view point of statistical significance.

4.2.4.3 Mass ratio variation study (m^* -study)

As already addressed (§ 2.2.2.1) the main parameter used in discriminating different hydroelastic test cases is the mass ratio m^* . A comprehensive study has been conducted aimed at assessing the transition, where detectable, from lowest to highest m^* -range: seven mass ratios were investigated for D24 and three for D37, whose dynamical characteristics were already reported in Tab. 4.2 and 4.3, where the amount of external mass added to the system is reported too. The reference geometrical scheme for the two oriented cylinders is shown in Fig. 4.24.

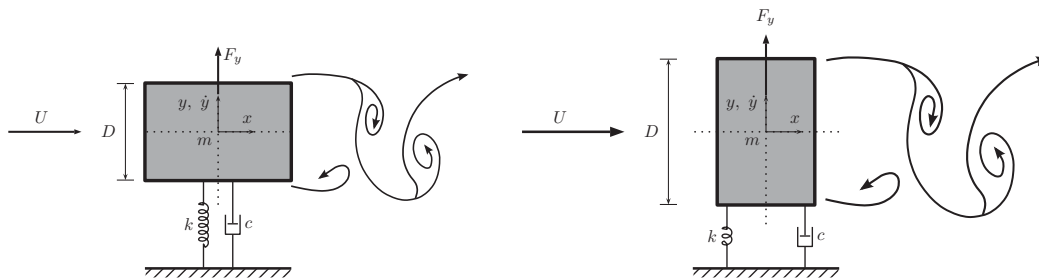


Fig. 4.24 Test rig model sketches for cross-flow motion of the $SR = 1.5$ D24 (*left*) and $SR = 0.67$ D37 (*right*) rectangular cylinder. The cylinders undergo free vibrations constrained in the transverse y direction with respect to the free-stream U (x direction), while its mass ratio is increased by optional added masses.

D24 rectangle The amplitude response can be categorized into three regimes already put in evidence by means of patches in Fig. 4.17. The super-harmonic resonance occurs at $U \approx U_r/3$, with amplitude peak in correspondence of $U/U_r \approx 0.67$ for $m^* = 2.24$, that progressively moves, as the mass ratio is increased, till reaching $U/U_r \approx 0.6$ for $m^* = 9.76$. Then, a flow-induced vibrations central branch is present, in de-synchronization regime with decreasing oscillation amplitudes (no patch in Fig. 4.17). Finally, galloping instability branch starts with a sharp upward jump in the oscillation amplitude.

A comprehensive figure reporting A_{10}^* (Fig. 4.25.*top*), and y'/D (Fig. 4.25.*bottom*) responses

are here usefully proposed below. The evolution of the amplitude response branch consists in shrinking the de-synchronization central region: in particular the galloping branch onset velocity get closer and closer to U_r as the mass ratio increases. By comparing the transition to higher mass ratios it is evident that the jump in amplitude at the instability onset disappears from $m^* \geq 4.1$, while it is still present, even if it is reduced in height, for $m^* = 3.02$ and 3.50 .

By referring to the plots in Fig. C.22 to Fig. C.28 the same kind of comparison with frequency domain is possible. The unstable branch onset evolution by increasing m^* reflects itself on the pattern around the onset zone. In fact, while for $m^* \leq 3.02$ the transition from desynchronization to galloping response suddenly manifests itself, showing in the unstable branch an horizontal straight dominant frequency line, for higher mass ratios a more or less clear cut in frequency domain is still present. For some m^* , a competition among harmonics and a noisier transition velocity range is present, but it is followed by a range in which the slope of the dominant frequency trace gets a bit steeper, before reaching a reduced velocity value for which the reduced frequency response gets flattened. The interaction between harmonics is present till $m^* = 4.1$, where some different interesting features are shown: in Fig. C.25 there's an interaction between the 3^{rd} and 6^{th} galloping super-harmonics with a not well detectable f_{vs} harmonic causing a bifurcation till $U/U_r \approx 2$, that seems to cause a similar phenomenon underlined in the previous paragraph for $m^* = 2.24$ in D24 and D37 configurations, which is present also for $m^* = 3.02$ and 3.5 (Fig. C.23 and Fig. C.24). In addition, for $m^* = 4.1, 7.49$ and 9.76 , a kink seems to occur at $U/U_r \geq 2.5$ without any apparent consequences in the frequency response.

D37 rectangle As previously shown, the response branch is still divided in three regimes; the first regime is a flow-induced vibrations response with the oscillation amplitude increasing linearly following the Strouhal line up to $U/U_r \approx 0.8$. As the reduce velocity is further increased, a lock-in range occurs for $0.9 < U/U_r < 1.1$ (dark gray in Fig. 4.18), which represents the second regime of the response branch (light gray in the right side of Fig. 4.18), featured by a low-height lock-in bell that 'meets' the beginning of galloping branch with a slight jump downward, which appears to increase linearly with the same slope as the first regime.

In Fig. 4.26 it is interesting to observe that the higher the mass ratio the higher the jump in amplitude downwards, and also the lower the mass ratio the higher the peak in resonance. Apart from the slight horizontal translation towards higher velocities there are not relevant differences among the three mass ratios tested. For both the A_{10}^* and the y'/D curves the galloping branch keeps a linear trend up to $U/U_r \approx 2$, then the response branch gets steeper, particularly for the lowest mass ratio, as happened also in D24 case.

The examination of the frequency domain plots (Fig. C.29-C.31) does not denounce any remarkable difference but the presence for higher mass ratios of appreciable reduced frequency trace with an opposite slope with respect to that of f_{vs} , crossing it around $U/U_r \approx 1.6$ and $U/U_r \approx 1.75$ respectively for $m^* = 3.5$ and 9.76 (in the former case such a phenomenon is less evident).

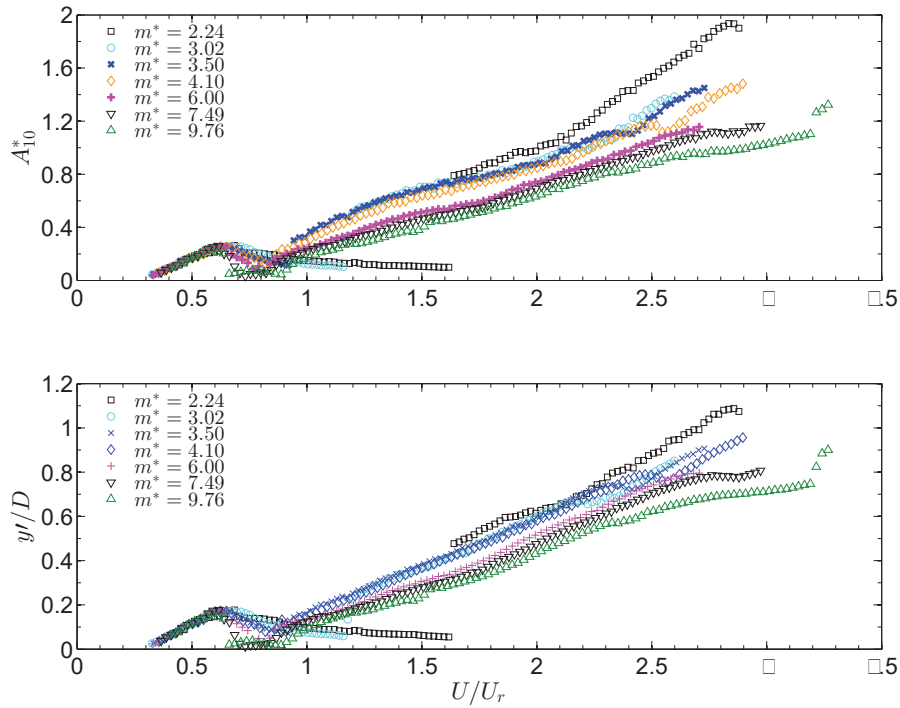


Fig. 4.25 (top) Reduced amplitude response (A_{10}^*), and (bottom) rms of the nondimensional amplitude (y_t/D) of D24 for the 7 mass ratios investigated, against reduced velocity (U/U_r).

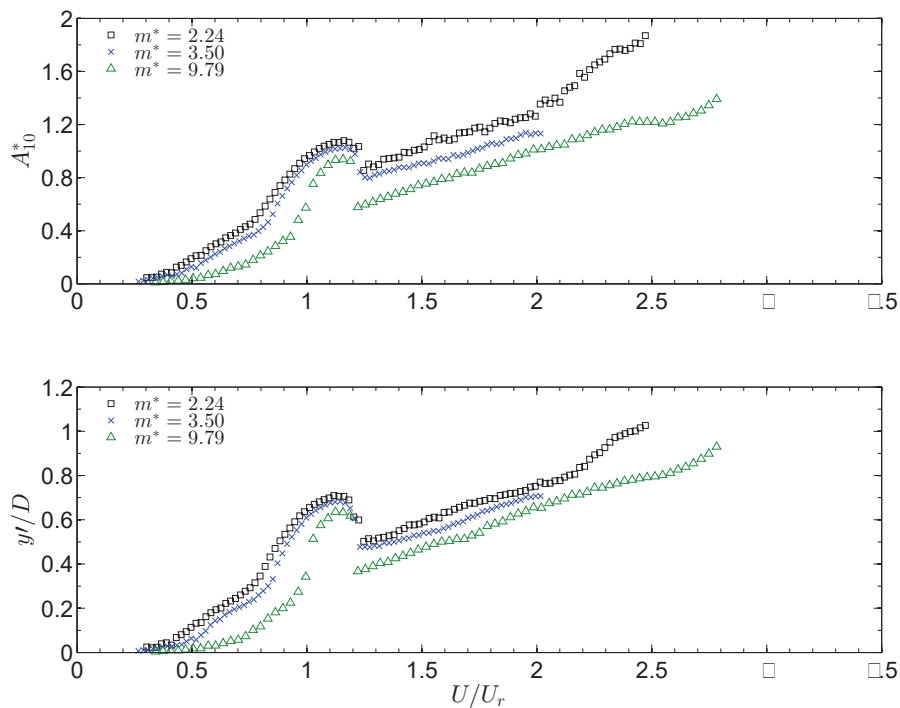


Fig. 4.26 (top) Reduced amplitude response (A_{10}^*), and (bottom) rms of the nondimensional amplitude (y_t/D) of D37 for the 3 mass ratios investigated, against reduced velocity (U/U_r).

4.3 Chapter summary

Two different sectional models were tested in the *FLAIR* water channel, a square section (investigated within previous campaign in the same laboratory concerning hydroelastic tests), and a rectangular section of side ratio $SR = 1.5$, characterized by a very low mass ratio allowing comparisons with a number of literature data. An articulated experimental campaign involved several test rigs with which static, hydroelastic, forced-rotations and hot-film anemometry tests were carried out. A wide range of Strouhal number values has been determined for the rectangular section only, densely varying the angles of attack in getting such a measurement; from the same test hydrodynamic coefficients $C_L - C_D - C_{F_y}$, *i.e.* lift-drag-lateral, were extrapolated for applying afterwards numerical models for the prediction of the instability. Two different studies, on the angle of attack variation for the lowest mass ratio ($m^* = 2.24$) and on the mass ratio variation for $\alpha = 0^\circ$ and $\alpha = 90^\circ$, that is D24 and D37 section, were mainly investigated concerning the hydroelastic response. The reliability of the obtained results has been addressed in order to make any comparison with literature as consistent as possible.

Chapter 5

Modelling of the VIV-galloping interaction

5.1 Introduction

It is common practice to perform aeroelastic measurements to simulate the response of a structure supposed to be prone to some aeroelastic instability. Although the classical example for these kind of laboratory tests is given on bridge deck sections, there are also other structures susceptible to self-excited phenomena when invested by a fluid flow, such as submerged pipes and off-shore structures pylons, or power-line cables and slender high-rise towers. They present more compact cross-sections than bridges ones, like squares or rectangles. The possibility to numerically predict the dynamical behaviour of such bluff sections in terms of maximal amplitude response, and additionally to have the knowledge of the range of velocity in which some instability occurs, could represent a huge advantage. In fact, the choice to conduct static and dynamic laboratory tests, is meant to increase their real cost of construction. On the other hand, from the theoretical point of view, the precise prediction of a phenomenon implies a complete insight of its causes and consequences. The answer to all the problems of this nature is directly given by the integration of Navier-Stokes equations, for the solution of any arbitrarily shaped moving boundary; nevertheless, any numerical approaches are possible, and CFD application to whatever engineering problems still results limited by reasons of accuracy of the solution and computational time costs. Aiming to overcome such a prediction demand, semi-empirical models represent a convenient way. Therefore, the present chapter deals with the attempt to purposely implement an analytical model for the VIV-galloping interaction prediction; by starting from literature models related to VIV and its interaction with galloping, the analysis was oriented on the $SR = 1.5$ rectangular section, given that the square one already received enough attention.

5.2 VIV and galloping modelling in literature

For what concern VIV it is possible to talk about an evolution of analytical models, not only chronologically but also concerning many other aspects ; on the other hand, for galloping, and in particular when QS assumption holds, Parkinson QS nonlinear model is able to qualitatively and quantitatively predict the response. A plenty of VIV models have been

developed, primarily for predicting the circular cylinder response and sometimes specifically extended or modified for bridge deck sections, as in the case of Scanlan (1998) who tried to reconcile lock-in analysis with flutter formulation. To this end, in addition to the most important comprehensive literature reviews like those reported by Bearman (1984), Berger and Wille (1972), Sarpkaya (1979; 2004), the one recently provided by Marra *et al.* (2011) specifically focused on VIV mathematical models, provides information about the practical capability in predicting VIV and lock-in characteristics of an arbitrary dynamical system. It was inferred that so far no model is able to well predict the maximum amplitude of vibration by changing the mass-damping value, meaning to ideally change the prototype scale structure, for which the model parameters were estimated. However, at least a couple of models, always developed for circular cylinders but not accounted for in the mentioned review, seemed to adequately reproduce amplitude but also hysteresis and phase response evidenced by laboratory tests. Nevertheless, according to Parkinson (1989) no model has yet provided an explanation for the interesting occurrence of modulations in surface pressures against a perfectly sinusoidal amplitude and lift signals reported in both Ferguson (1965) and Feng (1968) time traces.

An updated review was conducted leading to the composition of a brief scheme to differentiate the groups and provide chronological information on their formulation. In Tab. 5.1 a list and classification of VIV semi-empirical models is proposed and divided into two main categories based on the assumption that the fluid dynamic effects detected through the across-wind response are sufficient (**S-DoF**), or the coupling with the near wake oscillation, treated as a separate oscillator, is needed in order to predict the response (**2-DoF**). According to Billah (1989) the former group is in turn divided in two approach: negative-damping models (**ND**), in which the physical mechanism of energy transfer from the wake to the locked body is modelled as an instability which is caused by the drop towards zero of the total system damping. Among them, linear and nonlinear models were proposed, although, for a reliable modelling of VIV, nonlinear effects shouldn't be neglected. Then, semi-empirical models based on forced vibration tests (**FV**), performed in order to obtain force coefficients are listed; however, forced-vibration tests are employed in 2-DoF models too, having the drawback to require a purposely designed experimental facility for the model parameters detection.

Two different approaches distinguish the models of the 2-DoF class. As firstly suggested by Birkhoff (Birkhoff (1953), **Bc**) the low recirculation flow region between the two shear layers behind the cylinder could be modelled as a plate swinging from side to side, literally “*like the tail of a swimming fish*”. The same experimental evidence was observed in Bishop and Hassan (1964): once a perturbation was imposed to the body the wake behaved like a mechanical oscillator in free vibrations with a frequency depending on the flow velocity (**BHc**). Although not giving any geometrical characterization the wake was modelled as a nonlinear fluid oscillator. Among the listed models further details will be given about some of them when considered more interesting or helpful in the characterization of the models developed for the interaction VIV-galloping.

Hartlen & Currie model (1970) A coupled *ODE* system was developed to predict the circular cylinder amplitude response starting from the experimental evidences available till then. The obtained final results were not sufficiently satisfactory: peculiar features are not predicted (such as hysteresis or the jump in phase amplitude originated by the

Tab. 5.1 Scheme for the VIV models available in literature.

	S-DoF	2-DoF
	Harmonic [†] (Wyatt and Scruton (1981))	Hartlen and Currie (1970)
ND^a	Scruton (1963) [†]	Skop and Griffin (1973)
	Scanlan (1981) [†]	Iwan and Blevins (1974)
	Scanlan (1981)	Landl (1975)
	Ehsan and Scanlan (1990)	Wood (1976)
	Vickery and Basu (1983)	BHc^c Berger (1978)
	Goswami (1991), Goswami <i>et al.</i> (1992; 1993)	Dowell (1981)
	Larsen (1995)	Benaroya and Lepore (1983)
	Scanlan (1998) [†]	Berger (1987)
	D'Asdia and Noé (1998) ^e	Krenk and Nielsen (1999)
	D'Asdia <i>et al.</i> (2003) ^f	Diana <i>et al.</i> (2006)
FV^b	Sarpkaya (1978)	Bc^d Funakawa (1969)
	Staubli (1983)	Nakamura (1969)
	Iwan and Botelho (1985)	Tamura and Matsui (1979)

[†] Linear model.

^a Negative damping (Billah, 1989).

^b Forced-Vibrations derived force coefficients (Billah, 1989).

^c Bishop & Hassan concept (Bishop and Hassan, 1964).

^d Birkhoff concept (Birkhoff, 1953).

^e Developed for circular cylinder.

^f Developed for bridge sections.

transition from 2P to 2S mode and observed in Feng (1968)), and it did receive critics from *e.g.* Sarpkaya (1979). Nevertheless, the model has always been quite referenced by many authors and constitutes the base from one of the main model for the interaction.

In the following coupled *ODE* system the non-dimensional form for body displacement equation is formulated (the same of Eq. (2.7) with $C_y = C_L$); the nonlinearity of the system is concentrated in the van der Pol type equation for transverse aerodynamic force coefficient C_L :

$$\left\{ \begin{array}{l} a) \quad \ddot{Y} + 2\zeta\dot{Y} + Y = C_L n \tilde{U}^2 \\ b) \quad \ddot{C}_L - \Upsilon_1 f_s^* \dot{C}_L + \frac{\Upsilon_2}{f_s} \dot{C}_L^3 + f_s^{*2} C_L = \Upsilon_3 \dot{Y} \end{array} \right. , \quad (5.1)$$

where $f_s^* = U^*/U_r^* = St \cdot U^* = f_{vs}/f_n$, Υ_i ($i = 1, 2, 3$) are empirical constants, $\tilde{U} = U/2\pi$, and $(\dot{})$ are τ -derivatives as already mentioned for *QS* model¹. The process to determine the empirical constants takes into account three possible situations:

i *Cylinder mounted rigidly*. The right side of Eq. (5.1).*b* vanishes so that the equation represents the oscillating pressure force on a stationary bluff cylinder, solvable by theory of weakly nonlinear equations. In this case C_L ‘oscillates’ at f_{vs} whose amplitude is given by $C_{L_0} = \sqrt{4\Upsilon_1/3\Upsilon_2}$; here experimental values of C_{L_0} can be used to determine the ratio Υ_1/Υ_2 to be used in the oscillating cylinder analysis. Instead, the parameters Υ_2 and Υ_3 must be determined by fitting the experimental response.

ii *Cylinder actuated mechanically* By using forced-vibrations tests, *i.e.* with specified amplitude and frequency harmonic oscillations imposed to the body, only Eq.

¹§ refNLQsmodel

(5.1).*b* is needed, as from Minorsky (1962) is known that when the imposed frequency (f_i) is sufficiently close to the vortex shedding one, say $f_i \approx f_{vs}$, the solution of Eq. (5.1).*b* predicts the lock-in of f_{vs} to f_i .

iii Cylinder mounted elastically. In this case the authors attempted to seek a solution for the *ODE* system, in particular in the range in which f_{vs} is very close to f_n (lock-in range), where both the cylinder motion and lift fluctuation are approximately sinusoidal (Eqs. (5.2)) at a frequency close to f_n .

$$Y = Y_s \sin(f^* \tau) , \quad C_L = C_{L,s} \sin(f^* \tau + \phi) , \quad (5.2)$$

being τ the non-dimensional time. If Eqs. (5.2) are substituted in Eq. (5.1).*a*, equating to zero the coefficients of $\sin(f^* \tau)$ and $\cos(f^* \tau)$ resulting from the derivation process to satisfy the equation, two new equations can be written

$$(1 - f^{*2}) Y_s = n \tilde{U}^2 C_{L,s} \cos(\phi) , \quad (5.3)$$

$$2\zeta f^* Y_s = n \tilde{U}^2 C_{L,s} \sin(\phi) . \quad (5.4)$$

Dividing Eq. (5.4) by Eq. (5.3) it results

$$\tan(\phi) = \frac{(1 - f^{*2})}{2\zeta f^*} , \quad (5.5)$$

allowing a direct solution of the system represented by Eq. (5.1).*b*, Eq. (5.3) and Eq. (5.5) for the unknowns f^* , ϕ , Y_s and $C_{L,s}$, showed also in the original paper relying on the experimental results given by Ferguson (1965).

Berger's models (1978,1987) Interestingly the most successful improvement of the previous model was given by Berger (1978), whose results showed excellent agreement in comparing with Feng's data, namely in predicting the oscillation hysteresis. The governing equation derives from Eqs. (5.1) leading to:

$$\begin{cases} a) & \ddot{Y} + 2\zeta \dot{Y} + Y = n C_L \tilde{U}^2 \\ b) & \ddot{C}_L + \Omega^* \dot{C}_L + f_s^{*2} C_L = \Upsilon_3 \dot{Y} , \end{cases} \quad (5.6)$$

being Ω^* an even-power polynomial in C_L . It can be solved by assuming, as we saw previously, steady-state oscillations in the lock-in range. The principal difference is that now $C_{L,s}$ and Y_s solution equations are more flexible, so that one of the main achievements of the model was to incorporate what was necessary for a realistic simulation of the response. Ω^* polynomial coefficients were calibrated on Feng's low-damped experiments data. The agreement for the Y_s vs. reduced velocity curve was remarkable, and more important is the fact that the prediction for a test case with an higher damping ratio value was well predicted too. It is also interesting to mention the promising results of the 1978 model in predicting the response of a D-shape section; on the other hand the phase jump was not detected. Hence, the author re-examined the governing equations substituting to the linear coupling term $\Upsilon_3 D$ a more suitable nonlinear one, namely a polynomial in \dot{Y}^2 ; given

that in Feng's results the ζ parameter was shown to be motion-dependent (Wood, 1976), in the new model (Berger, 1987) the constant ζ became a polynomial in \dot{Y}^2 too. From a stability analysis conducted by Parkinson (1989) it emerged that limit cycles characterized by $\phi \approx 90^\circ \pm 9^\circ$ were found to be unstable, as well as those with $0^\circ < \phi < 9^\circ$ and $\phi > 120^\circ$, providing results in a good agreement with Feng's findings concerning the jump in phase angle.

Tamura & Matsui model (1979) - TM In this work the authors developed a second version of the model firstly proposed in Nakamura (1969), in which the vortex wake was represented by a finite cavity attached to the cylinder in torsional oscillations and then utilized the formulation proposed by Funakawa (1969) for the Birkhoff-type fluid oscillator. This VIV model is important for our purposes because it constitutes the basement for the model given by Tamura and Shimada (1987) that will be addressed later on. This mathematical model, which results to be similar to the model proposed by Iwan and Blevins (1974) to a closer inspection, was developed for predicting the response of a circular cylinder in a smooth fluid stream; it was numerically integrated by means of the Runge-Kutta method and, afterwards, compared with experimental results published by Ferguson (1965), Feng (1968), Yamaguchi *et al.* (1970) and Okajima (1976). In the equivalent Eq. (5.1).a for this model the variable is the angular position of the wake oscillator ϑ (see Eq. 5.25) and the nonlinear term comes from an assumed oscillatory cavity length, creating a nonlinear spring effect in the contribution estimated for the aerodynamic restoring torque of the flow around the cylinder; the nonlinear terms are linear in $\dot{\vartheta}$ and quadratic in ϑ expressing again a van der Pol-type equation. Although the oscillation hysteresis effect was not even here predicted the amplitude response comparisons showed good agreement with experimental data.

The theoretical background was given by Nakamura (1969) which developed and published his work right after Funakawa (1969): as reported by the former author, the principal difference between the two models is that while Nakamura treated the system as a binary flutter one, consisting of the cylinder displacements and the dead fluid region, Funakawa considered that the motion of the dead air region is a forced-oscillation which is driven by the body oscillations. Therefore, each model did come to a flutter formulation of different type: Nakamura's formulation coincided exactly with a binary (coupled) flutter, whereas Funakawa's one treated it as a 1-DoF instability. In reading the two papers it is evident the two formulations speak each other borrowing assumptions considered reliable for the

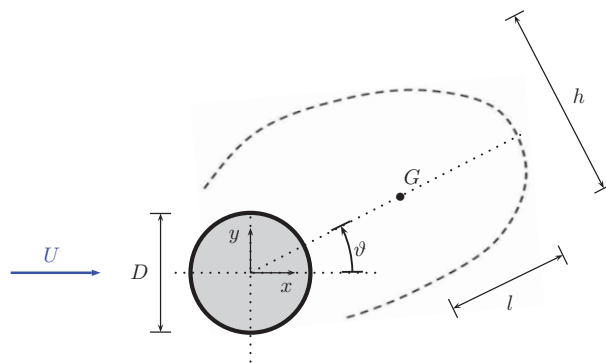


Fig. 5.1 Birkhoff-type wake-oscillator sketch presented in Tamura and Matsui (1979).

circular cylinder. Anyway, in exposing the models we will follow Nakamura's approach, even if some key parameters were taken from Funakawa (1969) experimental results.

The governing equation for a Birkhoff-type wake oscillator with variable length assumes the following formulation:

$$I\ddot{\vartheta} + K\vartheta = 0, \quad (5.7)$$

where $I = 2\rho lh(D/2+l)^2$ and $K = 2\rho\pi U^2 l(D/2+l)$ are respectively the wake-oscillator moment of inertia about the center of the cylinder and the coefficient of fluid dynamical restoring moment (taken from Nakamura (1969)). Then, assuming $h = 1.25D$ and $l = 1.1D$ in Fig. 5.1, the characteristic frequency of the dead air region can be given by:

$$f_{\vartheta} = \frac{\omega_{\vartheta}}{2\pi} = \frac{StU}{D} = \frac{1}{2\pi} \sqrt{\frac{K}{I}} = \frac{U}{\sqrt{4\pi h(D/2+l)}}. \quad (5.8)$$

Let us consider now the case of an elastically sustained cylinder treated, as previously said, as a binary flutter whose DoFs are y and ϑ : the two governing equations should be one for the cylinder motion and one for the fluid, the latter theoretically represented by a time-dependent Navier-Stokes equation. The Birkhoff analogy employed allows to reduce the problem in seeking the coupling between the two DoFs. It has to be underlined that the angular motion of the wake-oscillator is directly connected to the back-and-forth motion on the cylinder surface of the separation point, and hence it is associated with a change in the flow circulation. A way to derive this dependency was proposed to be the lift force due to Magnus effect (Magnus, 1853), which is proportional to the angular displacement of the dead air region, that is

$$F_L = -\tilde{f}\vartheta \quad \Leftrightarrow \quad C_L = \frac{-\tilde{f}\vartheta}{\frac{1}{2}\rho U^2 DL}. \quad (5.9)$$

A crucial contribution in determining the \tilde{f} parameter was given in Funakawa (1969) relying on experimental data originally measured by Ludwig Prandtl (Prandtl and Tietjens, 1934; 1957) for a spinning circular cylinder at a fixed flow velocity but varying the angular velocity (see Fig. 5.2), subsequently reported in Swanson (1961) together with the whole amount of experimental data available till then. Funakawa was interested in deriving the slope of

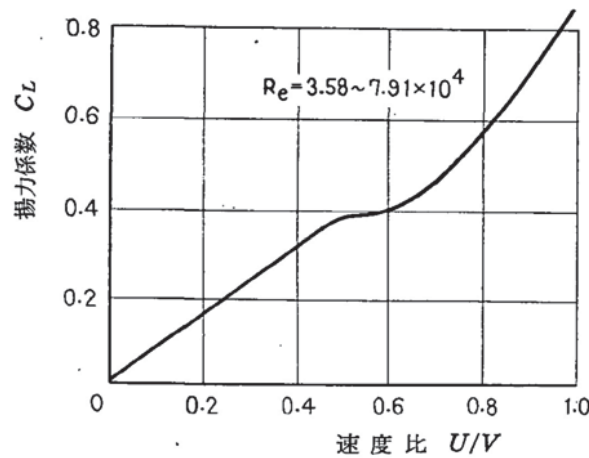


Fig. 5.2 Funakawa (1969) extrapolated plot: in particular the curve was taken from Swanson (1961), Fig. 2.top (curve *a* with $Re = 3.58 \cdot 10^4$). The ratio U/V is the rotational-to-flow velocity ratio.

the C_L vs. $\Delta (= v_0/U)$ curve², hence only the branch approximating a linear trend was considered. From the figure it is possible to derive that

$$\frac{|C_L|}{\Delta} \approx \frac{0.4}{0.5} = 0.8 \quad (5.10)$$

Now it has to be taken into account another crucial information coming from Prandtl experiments, namely a flow visualization showing that the separation point changed its angular position from the side of the cylinder, collocating itself at an angle $\beta = 20^\circ$ far from the vertical direction, when the velocity ratio assumes the value of $\Delta = 0.5$ (Fig. 5.3). Then,

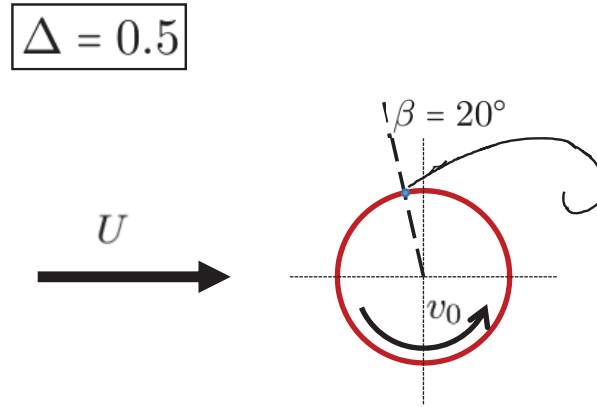


Fig. 5.3 Sketch for the visualization of the separation point position in case $\Delta = 0.5$.

a strong assumption was made, that was to consider this latter angle as roughly equal to ϑ ; it turns out that

$$\frac{|\vartheta|}{\Delta} = \frac{20^\circ \frac{\pi}{180}}{0.5} \approx 0.698 . \quad (5.11)$$

By making a system with Eqs. (5.10) and (5.11) in a differential form we get

$$\begin{cases} \frac{dC_L}{d\Delta} \approx 0.8 \\ \frac{d\vartheta}{d\Delta} \approx 0.698 \end{cases} \quad (5.12)$$

and then

$$\left\{ \frac{dC_L}{d\vartheta} = \frac{dC_L}{d\Delta} \cdot \frac{d\Delta}{d\vartheta} \right. , \quad (5.13)$$

giving $dC_L/d\vartheta \approx 1.146$. Nevertheless, the commonly used value for this last expression was defined by Funakawa considering a slightly different effective angle. In fact, a system in which the damping term derives from the wake-oscillator angular velocity, while the forcing term is caused by the cylinder sinusoidal self-induced motion $y = a \sin(\omega t)$ (forced system 1-DoF system as previously underlined) was given in the form:

$$I\ddot{\vartheta} + c\dot{\vartheta} + k(\vartheta - \vartheta_0) = \omega^2 I \bar{\vartheta} \sin(\omega t) , \quad (5.14)$$

²note that the the rotational-to-flow velocity ratio Δ is indicated in Funakawa (1969) with a different notation indicating the tangential velocity (v_0) with U , and the oncoming free-flow velocity (U) with V Fig. 5.2.

where

$$\bar{\vartheta} = \frac{a}{\frac{D}{2} + l} = \chi \frac{a}{D} = 0.625 \frac{a}{D} \quad (5.15)$$

was determined relying on the proportion of the dead stream (see the original paper by Funakawa (1969)) and

$$\vartheta_0 = -\frac{\dot{y}}{U} = -\frac{a\omega}{U} \sin(\omega t) \quad (5.16)$$

is the relative velocity. The effective angular displacement, that causes the lift induced by the Magnus effect, was indicated by $\vartheta_{eff} = (\vartheta - \vartheta_0)$. By substituting $\sqrt{K/I} = \omega_\vartheta$, that is the pulsation of the wake oscillator, and through some mathematical manipulations, the expression of ϑ_{eff} was given in the form

$$\vartheta_{eff} = \frac{\sqrt{(\bar{\vartheta}^2 \omega^4) + (\omega_\vartheta^2 \frac{a\omega}{U})^2}}{\sqrt{(\omega_\vartheta^2 - \omega^2)^2 + 4\epsilon^2 \omega^2}} \sin(\omega t - (\delta_1 + \delta_2)) \quad (5.17)$$

being $2\epsilon = c/I$, where

$$\delta_1 = \tan^{-1} \frac{\omega_\vartheta \frac{a\omega}{U}}{\omega^2 \bar{\vartheta}},$$

$$\delta_2 = \tan^{-1} \frac{2\epsilon\omega}{\omega_\vartheta^2 - \omega^2}.$$

The Magnus effect correlated parameter was given in Funakawa (1969) as

$$\tilde{f}_m = -\frac{F_L}{\vartheta_{eff}} = \frac{1}{2} \rho U^2 DL \frac{d|C_L|}{d\vartheta_{eff}} = 0.58 \rho U^2 DL, \quad (5.18)$$

from which a value of $(dC_L/d\vartheta_{eff}) = 1.16$ was fixed in Funakawa (1969). Nakamura stressed that such an estimate of \tilde{f}_m has a tentative nature and there would need further refinements, which are still left to be performed.

Going back to Tamura and Matsui model (*TM*), the authors started from the assumption that a linear relation exists between lift coefficient and angular displacement of the wake, $C_L = \tilde{f}\vartheta$, and recalling Eq. (5.9) they considered

$$\frac{dC_L}{d\vartheta} = \frac{\tilde{f}_m}{0.5\rho U^2 DL} = \tilde{f} = 1.16 \quad (5.19)$$

With reference to Silvio (1969) they considered the minimum oscillator length, ($2l_{min}$), when the vortex is completely discharged: the distance of $2l$ from the cylinder center were put in relation to ϑ , and described a ‘8-trace’ whose crossing point is placed in correspondence of $\vartheta = 0^\circ$ (see Fig. 2 in Tamura and Matsui (1979)). Therefore, they assumed that such a fluctuating length affected the secondary wake system like a parametric damping, giving an expression for the fluctuating wake-oscillator length, and then deriving the formulation for the spring constant of the oscillator.

The model took into account also the effect of the growing vortex that shed after having reached its maximum size, as a moment of force given by the lateral force induced by the increasing vorticity whose point of action was in the center of gravity G of the wake-oscillator. Such a force is directly derived using the Kutta-Joukowski theorem (Eq. 5.20) which applying to cases in which circulation is induced by fluid interaction, such as airfoils,

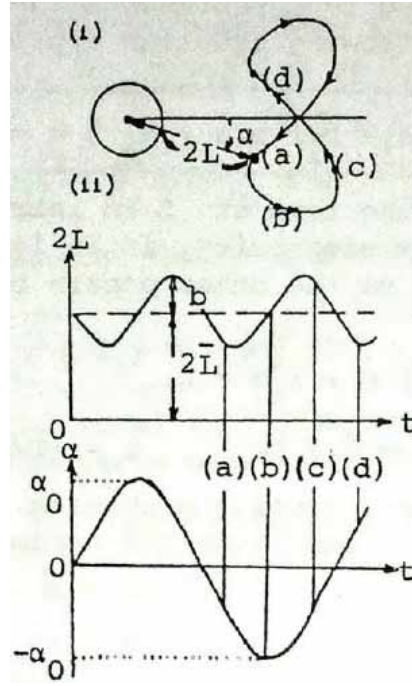


Fig. 5.4 Fluctuation of the length and the angular displacement of the wake oscillator [Fig. 2 in Tamura and Matsui (1979)].

or around spinning objects where the circulation is induced mechanically:

$$F_{L,\Gamma} = \rho U \Gamma \Rightarrow M_{\Gamma} = \underbrace{\rho U \Gamma}_{\text{force}} \underbrace{\frac{D}{2} + l}_{\text{distance}} = R \cdot \frac{D}{2} + l. \quad (5.20)$$

Then, it was considered the non-linear damping mechanism to the undamped oscillator: from a balance between the work done by the viscous damping force ($c_0 \dot{\vartheta}$) and that of the R force during a period, a negative damping effect resulting by the shed vortex was defined as

$$c_0 \approx -C = \frac{2\sqrt{2}U\Gamma(D/2 + l)}{\pi \vartheta_0 \omega_{\vartheta}}, \quad (5.21)$$

and a value of the damping ratio

$$\xi = \frac{C}{2\omega_{\vartheta} I} \approx \frac{\tilde{f}}{2\sqrt{2}\pi^2 l} \quad (5.22)$$

leading to the expression of the equation of motion of the wake-oscillator in the form:

$$I \ddot{\vartheta} - C \left[1 - \left(\frac{4\tilde{f}^2}{C_{L_0}^2} \right) \vartheta^2 \right] \dot{\vartheta} + K \vartheta = 0. \quad (5.23)$$

Hence, the effect of the cylinder motion on the wake-oscillator, which have to be coupled each other, was accounted for by considering the inertial contribute of a moment of force proportional to the acceleration of the horizontal movement of the axis of rotation ($-I\ddot{y}/(D/2+l)$) and the apparent angular displacement induced by the vertical motion (\dot{y}/U). Then, lift and drag forces, the latter only relating to the projection in y direction, were

accounted for by writing:

$$\begin{cases} F_L = -\tilde{f} \left(\vartheta + \frac{\dot{y}}{U} \right) \frac{1}{2} \rho U^2 DL \\ F_D = -\frac{1}{2} \rho (U^2 + \dot{y}^2) C_D DL \frac{\dot{y}}{(U^2 + \dot{y}^2)} \simeq -\frac{1}{2} \rho U \dot{y} C_D DL \end{cases} \quad (5.24)$$

where a value for the drag coefficient of 1.2 is taken from Funakawa (1969). After the nondimensionalization the coupled system can be written in the following form

$$\begin{cases} a) \ddot{\vartheta} - 2\xi\nu \left[1 - \left(\frac{2\tilde{f}}{C_{L0}} \right)^2 \vartheta^2 \right] \dot{\vartheta} + \nu^2 \vartheta = -\chi \ddot{Y} - \nu St^* \dot{Y} \\ b) \ddot{Y} + \left[2\zeta + n(\tilde{f} + C_D) \frac{\nu}{St^*} \right] \dot{Y} + Y = -\tilde{f} n \vartheta \left(\frac{\nu}{St^*} \right)^2 \\ c) C_L = -\tilde{f} \left(\vartheta + St^* \frac{\dot{Y}}{\nu} \right) \end{cases} \quad (5.25)$$

where $\chi = 1/(0.5 + l^*)$, $St^* = 2\pi St$, $\nu = U/U_r$, and $(\dot{})$ denotes the differentiation respect the nondimensional time.

5.3 Brief review on interaction VIV-galloping models in literature

Santosham model (1966) The very first attempt in combining the response of a section prone to galloping instability with the effect of the formation of wake vortices, was conducted by Santosham (1966); for this reason and because of interesting data on $SR = 2$ and $SR = 1$ cylinders, it seemed useful to quickly introduce his model in this section. He started from the discrepancy represented by the disagreement between Smith experimental results (Smith, 1962) and the nonlinear oscillator theory in the case of a rectangle with $SR = 2$, and decided to add an harmonic force at the Strouhal frequency to the quasi-steady self-excited forces. Recalling Eq. (2.30), the quasi-steady analysis without a vortex excitation term leads to a quasi-linear differential equation, of autonomous type, in the form

$$\ddot{Y} + Y = \varpi f(\dot{Y}) \quad , \quad [1^{st} \text{ kind ODE}] \quad (5.26)$$

while when the vortex excitation is included it can be written as

$$\ddot{Y} + Y = \varpi g(\tau, \dot{Y}) \quad , \quad [2^{nd} \text{ kind ODE}] \quad (5.27)$$

being the functions $f(\dot{Y})$ and $g(\tau, \dot{Y})$ determined by approximating the lateral force coefficient using Chebyshev polynomials. It is worth noting that the Author employed a 11th order polynomial of in approximating C_{F_y} of $SR = 2$, while a 7th order formulation was kept for the square section. The equation of motion Eq. (5.27) can be reformulated as

$$\ddot{Y} + Y = \varpi f(\dot{Y}) + Y_{vs} \sin(f_s^* \tau + \phi_{vs}) \quad , \quad (5.28)$$

where $f_s^* = \omega_{vs}/\omega = (2\pi f_{vs})/\omega$, $\tau = \omega t$ is the non-dimensional time, $\varpi = nA_1$ and $Y_{vs} = F_0/(m\omega^2 D)$. In case $f_s^* \neq 1$ the dimensional form of the equation of motion is given by

$$m\ddot{y} + c\dot{y} + ky = \underbrace{C_{F_y} \left(\frac{1}{2} \rho U^2 DL \right)}_{QS \text{ self-excited}} + \underbrace{F_0 \sin(\omega_{vs}t + \phi_{vs})}_{\text{harmonic at } f_{vs}}, \quad (5.29)$$

where $F_0 = C'_L \left(\frac{1}{2} \rho U^2 DL \right)$, being $C'_L = (C_L)_{rms} = C_{L0}/\sqrt{2}$ and ϕ_{vs} a phase angle. The Kryloff and Bogoliuboff linearised equation were solved. Now, let the nondimensional amplitude steady state solution be

$$Y = \bar{Y} \sin(\tau + \phi) + \Psi_s \sin(f_s^* \tau + \phi_{vs}), \quad (5.30)$$

where $\Psi_s = Y_{vs}/(1 - f_s^{*2})$; the solution was derived by substituting Eq. (5.30) in Eq. (5.28). The steady state solution has term in power series of Ψ_s , which is a function of the mass parameter (n), lift coefficient (C_L), flow velocity (U) and Strouhal number (St), given that

$$St = \frac{f_{vs} D}{U} = \frac{\omega_{vs} D}{2\pi U} = \frac{f_s^*}{U^*} \quad (5.31)$$

and

$$Y_{vs} = \frac{F_0}{m\omega^2 D} = \frac{\rho U^2 DL}{2m\omega^2 D} C'_L = \frac{nU^{*2}}{(2\pi)} C'_L, \quad (5.32)$$

giving

$$\Psi_s = \frac{Y_{vs}}{(1 - f_s^{*2})} = \frac{n\tilde{U} C'_L}{[1 - (U^* St)^2]} = \frac{C'_L}{4\pi^2} \frac{n}{\frac{1}{U^{*2}} - St^2}. \quad (5.33)$$

If $\Psi_s = 0$, that is when there's no response function, the steady state amplitude reduces to the solution of Eq. (5.26) given also in Parkinson and Smith (1964). Any contributions given by wake interactions can be neglected as long as $\Psi_s \ll 1$; conversely, by assuming $St^* = 2\pi St$, when U is large $\Psi_s = nC'_L/(-St^{*2})$. Heine (1964) reported values for C'_L equal to 1.1 and 2.2 respectively for rectangular $SR = 2$ and $SR = 1$, hence the ratio $C'_L/(St^{*2})$, considering values of St of 0.09 and 0.135 respectively, is of $\mathcal{O}(1)$ and the magnitude of Ψ_s is determined by n . In air flow n has an order of magnitude of $\mathcal{O}(-4)$ hence Ψ_s can be neglected. In waterflow n has the same order of magnitude of $C'_L/(St^{*2})$ (see §2.2.2.1), and the steady state solution is given by:

$$Y = Y_s \sin(\tau + \phi) + \Psi_s \sin(f_s^* \tau + \phi). \quad (5.34)$$

In Santosham (1966), the amplitudes predicted in waterflow case were determined also by means of a sensitivity analysis by varying C'_L values, showing that for values lower than 0.5 the response type was more similar to that one obtained in air flow. Then, the unstable limit cycle is not visible in numerical results as the onset velocity has been pushed towards the origin; in addition the magnitude of Y_s is inversely proportional to C'_L . Interestingly, for $C'_L > 0.5$ a response affected entirely by auto-periodic asynchronous quenching (§2.6.2) is obtained for both square and rectangular $SR = 2$ sections, although it failed to predict any interaction in air flow test cases.

Bouclin model (1977) The model was developed by Bouclin (1977), called by the Author *Fluid oscillatory mathematical model*, and it is considered the first real attempt for the interaction prediction. It combined *QS*-model with Hartlen and Currie's model for *VIV*, even if at first, Bouclin gave a modified solution of the *QS*-model applied in waterflow case which applies for $\tilde{U} > 2$. In fact by recalling Eq. (2.23) in a nondimensional form like

$$\ddot{Y} + 2\zeta\dot{Y} + Y = n\tilde{U}^2 C_{F_y} \frac{\dot{Y}}{\tilde{U}}, \quad (5.35)$$

the parameter $n\tilde{U}^2$ is not always less than 1 given that, as already mentioned, if in air the order of magnitude of n ranges from $\mathcal{O}(-4) \div \mathcal{O}(-3)$, in water we get $\mathcal{O}(-2) \div \mathcal{O}(1)$. A fundamental intuition of Bouclin, supported by experimental evidences, was the accounting of strongly nonlinear effects present in water for a velocity higher than a certain threshold. The response for $U^*/2\pi > 2$ agreed with classical *QS*-theory for the amplitude response but not for frequency one: he noted that while amplitude response was set to derive from a component of perturbational force in phase with velocity, that of the frequency depends on a component in phase with acceleration. For $n\tilde{U}^2 < 1$ ($\Leftrightarrow \tilde{U} \approx 2$) *QS*-model predicts the fluid force and cylinder displacements to have $\phi = 90^\circ$, and no component of fluid in phase with acceleration to reduce the frequency, as it happens in waterflow case together with a $\phi \neq 90^\circ$ between F_y and y . For $n\tilde{U}^2 > 1$, which means higher velocity range, surface effects appear such as the rising above the surface of the water on the front of the cylinder and the correspondent flow separation cavity forming in the rear face; these effects would decrease the effective immersed length on which hydrodynamical forces act and also the mass ratio, implying a decrease in amplitudes and frequencies. Furthermore he noted that for $\tilde{U} > 2$ one gets $n\tilde{U} \gg 2\zeta$, so the damping can be neglected, as also from the considerations on a totally uncoupled contribute of mass and damping parameter in waterflow case (see § 2.2.2.1). Therefore, an 'hydroelastic galloping' theory was given in the form

$$\ddot{\tilde{Y}} + \dot{\tilde{Y}} + \tilde{Y} = \tilde{U} C_{F_y} \left(\frac{\dot{\tilde{Y}}}{\tilde{U}} \right), \quad (5.36)$$

where $\tilde{Y} = nY$ and $\tilde{U} = n\tilde{U}$.

Subsequently, the fluid oscillator theory was developed whose and a *ODE* system can be given in the same notation as

$$\begin{cases} a) & \ddot{Y} + 2\zeta\dot{Y} + Y = n \left(C_{F_y} \frac{\dot{Y}}{\tilde{U}} + C_L \right), \\ b) & \ddot{C}_L - \Upsilon_4 \left[C_{L_0}^2 - \frac{4}{3} \left(\frac{\dot{C}_L}{f_s^*} \right)^2 \right] \dot{C}_L + f_s^{*2} C_L = \Upsilon_3 \dot{Y}. \end{cases} \quad (5.37)$$

Here the functional $\Upsilon_1 f_s^*$ is a constant value equal to $\Upsilon_4 C_{L_0}^2$ for unstated reasons (Corless, 1986). Some interesting remarks on the choice of the value to be assigned to C_{L_0} is given by the Author; actually the fluctuating lift coefficient is a key-parameter to which each model for the interaction has demonstrated to be really sensitive: it depends on AR , I_u , end conditions and Re . Despite in literature different values in smooth flow, such as 1.87 (Vickery, 1966), and 1.27 for $AR = 3$ and $Re = 5000$ (Chaplin and Shaw, 1971). In turbulent flows Vickery (1966) obtained a value of 0.96 and then a value of 0.65 for $AR = 20$ and

$Re = 5000$ having $I_u = 10\%$ (Vickery, 1969). Nevertheless a value of 0.7 was chosen for C_{L0} in the model.

Concerning Υ_3 and Υ_4 , experimental data on forced vibrations tests were used (Nakamura and Mizota, 1975b, Otsuki *et al.*, 1974) to give an estimate: in particular it was mentioned that for Υ_4 , affecting on the width of the resonance region, a value of 0.05 was chosen, while a ratio of $\Upsilon_3/\Upsilon_4 = 35$, that is $\Upsilon_3 = 1.75$, was given to obtain the best agreement for C_L at $f_s^* = 1$ (resonance). It was also interestingly noted that no forced vibrations result is affected by n and ζ , hence fitting of Υ_3 and Υ_4 on forced vibrations tests has any dependence on inertial/dynamical parameters. The comparison between numerical and experimental results showed a good agreement between $\sqrt{2}Y'$ and Y'_s amplitude response in the post-critical branch and an over estimation in the super-harmonic resonance ($U^* = 1/3 \cdot U_r^*$) region, whereas a decreasing trend for f^* by increasing velocities was predicted though not experimentally observed. The major error in numerical results derived from the inaccurate prediction of phase angle between excitation and response leading to an overestimation of f^* in the region which separates from Strouhal reference line.

Corless model (1986) Corless (1986)³ developed a varied version of Bouclin's system, here written in the form

$$\left\{ \begin{array}{l} a) \quad \ddot{Y} + 2\zeta\dot{Y} + Y = n \left(C_{F_y} \frac{\dot{Y}}{U} + C_L \right) , \\ b) \quad \ddot{C}_L - \Upsilon_1(f_s^*) \dot{C}_L + \frac{4\Upsilon_1(f_s^*)}{3C_{L0}^2 f_s^*} \dot{C}_L^3 + f_s^{*2} C_L = \Upsilon_3(f_s^*) \dot{Y} + \Upsilon_5(f_s^*) \ddot{Y} . \end{array} \right. \quad (5.38)$$

His work was more unbalanced on the mathematical approach to the problem, as the Author reports that the greatest contribute of his model is to be found more in the proposals for analytically solving the system of *DE* than in the originality of it from the fluid-dynamics point of view, being a slight variation of Bouclin's model. He considered four different approaches, three analytical, *van der Pol* (1), *multiple scales* (2) and *bifurcation solution* (3) methods, in addition to the direct numerical one (4). It is also interesting to note that he purposely left free all the model parameters, except C_{F_y} -related ones and C_{L0} , although remarking it is not strictly true for the last one. Any other parameter was modelled as a simple functional to keep the number of parameters empirically determined as low as possible, which is the opposite of any semi-empirical approach.

Data from forced vibrations tests (Bearman and Obasaju, 1982, Obasaju, 1983) were used for estimating the free parameters, while comparisons were made with the results published in Bearman *et al.* (1987) in air flow. The new term Υ_5 was inserted to improve the prediction of the sub-harmonic resonance: to this aim an *ad hoc* functional $\Upsilon_5(f_s^*) = B_0 + B_2 f_s^{*2}$ was used to get a right response. It is worth noting that Corless addressed, rather not rigorously, an explanation for the overestimation of f^* in the super-harmonic region in Bouclin's model, stating that the Hartlen and Currie expression for $\Upsilon_1 f_s^*$ works better in this respect.

Corless model well agreed with Bearman *et al.* results even if it was the way of conditioning the system parameters that played a key-role on the solutions; furthermore, the attempt to

³A misprint is present in the equation corresponding to Eq. (5.38).a, not reporting the nondimensional damping force term, as also in Eq. (2) in Corless and Parkinson (1988) and Eq. (1) in Corless and Parkinson (1993)

model the waterflow response for comparing also with Bouclin's hydrostatic tests allowed to determine that a numerical method is to be preferred when $n = \mathcal{O}(-1)$.

5.3.1 Tamura & Shimada's model (1987) - TS

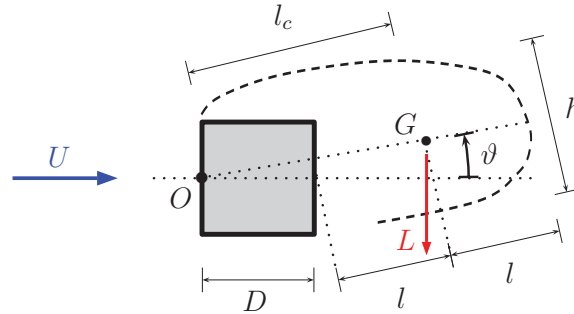


Fig. 5.5 Birkhoff-type wake-oscillator sketch presented in Tamura and Shimada (1987).

One of the main original contributions of the present dissertation was a deeper analysis of the rectangular cylinder of $SR = 1.5$, which implied the purpose to include numerical predictive simulations too. Hence, after having analysed each pros and cons, the model given by Tamura and Shimada (1987) was chosen. Its principal advantage derives from TM one, is that it just needs C_{L_0} and the \tilde{f} parameter to be implemented.

It is a combination of QS and TM models; it was developed for the prediction of the response a square section prone (or less) to the interaction between vortex shedding and galloping, hence some parameters of TM model were changed attempting to adapt the system to a geometry with completely different characteristics. In particular the center of rotation of the wake-oscillator was moved from the cylinder axis (as in Fig. 5.1) to the mid-point of the square side facing the oncoming flow, making l_c to become equal to $(D + l)\sin(\vartheta) \simeq (D + l)$ (Fig. 5.5), for a small ϑ . Then, the determination of two nondimensional parameters, namely the width of the wake-oscillator, $h^* = h/D$ and the nondimensional half length of the wake-oscillator $l^* = l/D$ can be determined by starting from flow pattern visualization for one of them, while the other one was obtained by means of the system

$$\begin{cases} \chi = \frac{1}{1+l^*}, \\ S^* = \sqrt{\frac{\pi}{h^*(1+l^*)}}. \end{cases}$$

The authors suggested to determine h^* first and then substitute into the system, but one may chose another way, or either determines such 'geometrical' coefficients entirely by means of flow visualizations, purposely conducted to visualize the wake angular motion during the shedding process. In the paper a value of $h^* = 1.8$ was derived from flow visualization by Mizota and Okajima (1981). However, the system equations were given as

follows

$$\begin{cases} a) \ddot{Y} + \left\{ 2\zeta + n(\tilde{f} - A_1) \frac{\nu}{St^*} - \sum_{i=1}^N \left[nA_i \left(\frac{St^*}{\nu} \right)^{i-2} \right] \dot{Y}^{i-1} \right\} \dot{Y} + Y = -\tilde{f}n \left(\frac{\nu}{St^*} \right)^2 \vartheta, \quad i = 3, 5, 7, \dots \\ b) \ddot{\vartheta} - 2\xi\nu \left[1 - \left(\frac{2\tilde{f}}{C_{L0}} \right)^2 \vartheta^2 \right] \dot{\vartheta} + \nu^2 \vartheta = -\chi \ddot{Y} - \nu 2St^* \dot{Y}, \end{cases} \quad (5.39)$$

where there has been used the original paper notation with the reduced velocity $\nu = U/U_r = StU^*$ ($\Leftrightarrow \nu/St^* = U^*/2\pi = \tilde{U}$). Then, the unsteady aerodynamic lift coefficient has been derived from Eqs. (5.39).a, b:

$$C_L = - \left[(\tilde{f} - A_1) \frac{St^*}{\nu} - \sum_{i=1}^N A_i \left(\frac{St^*}{\nu} \right)^i \dot{Y}^i + \tilde{f}\vartheta \right]. \quad (5.40)$$

5.4 Implementing TS model for $SR = 1$

Before implementing TS coupled model for predicting the dynamical response of the test cases investigated, the code was firstly validated by reproducing the original paper results with the parameters reported by the authors for a square section. In the original paper numerical results were compared with experimental data measured by Wawzonek in his wind tunnel experiments on a square cylinder (Wawzonek, 1979). Three different velocity ratios were taken as examples related to different scenarios, namely $\Lambda = 1.06, 1.49, 2.15$. Interaction with vortex shedding was apparent for the first two cases while in the third one the phenomena were separated. C_{F_y} polynomial coefficients were taken from Wawzonek too, and a value of $C_{L_0} = 0.7$ was assumed. The Runge-Kutta scheme was used for the numerical solution of the system, with a fixed nondimensional time step of $\Delta\tau = 2\pi/100$. Each velocity step calculation was stopped as soon as Y' and C'_L became smaller than 10^{-5} , or anyway when the nondimensional calculation time reached 400π ; each nondimensional stable amplitude of vibration was chosen by using these criteria.

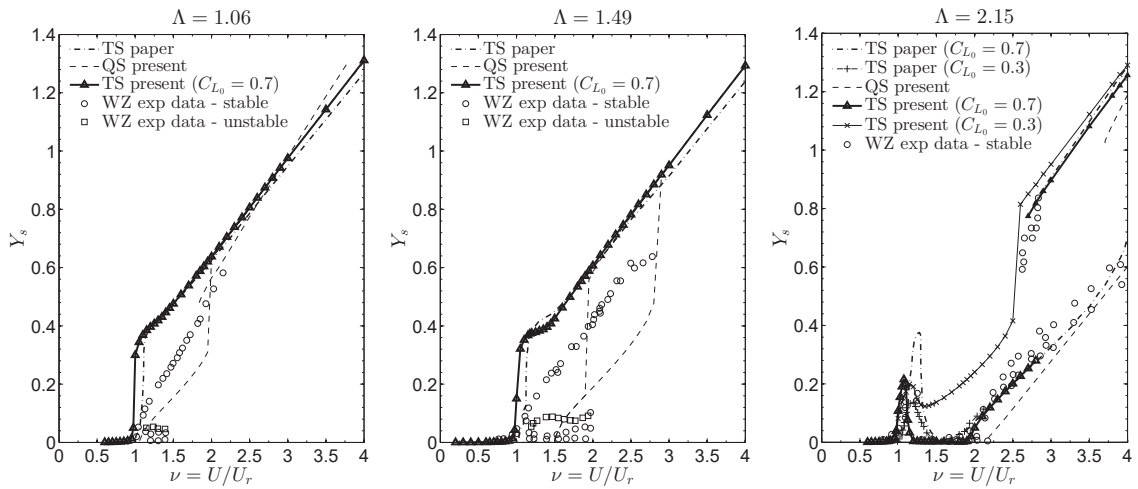


Fig. 5.6 Present results for the square section (TS present, solid line with markers) compared with the original ones in Tamura and Shimada (1987) (TS paper, dotted lines), galloping model implemented as already shown in Ch. 2 (QS present, dashed line) and Wawzonek experimental results (WZ , \circ and \square markers).

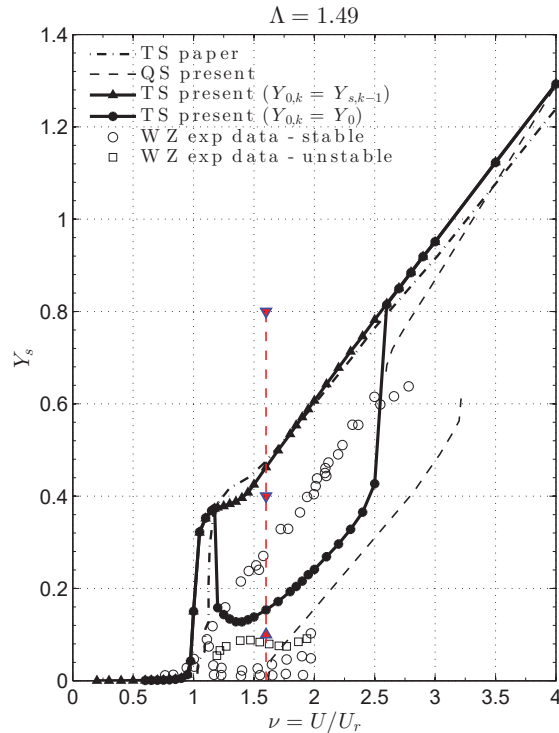


Fig. 5.7 Second stable branch obtained for a constant Y_0 : by coloured filled triangle markers placed on $\nu = 1.6$ vertical dashed line are indicated the different values of Y_0 chosen, whose time traces are proposed in Fig. 5.8.

In the present work a set of routines for solving the *ODE* system was solved using *ODE45* function in *MATLAB*®), by finally setting a relative and an absolute tolerance $\epsilon_a = \epsilon_r = 10^{-9}$ (stated after a sensitivity analysis). As in the original paper, the initial nondimensional amplitude has been fixed at $Y_{0,TS} = 0.1$; the results are shown in Fig. 5.6. The present model seems to reproduce quite well the original results, except for the $\Lambda = 2.15$ for $C_{L_0} = 0.3$ case, in which the resonance branch does not drop down on negligible amplitudes but remains at a mid-height before going on the upper post-critical branch; moreover the maximum height of the $C_{L_0} = 0.7$ case in the present results shows a lower peak at resonance, better matching indeed experimental points. Nevertheless some remarks have to be done for *TS*-model. The results shown in Fig. 5.6 are relative to an updated Y_0 , which means to take as initial amplitude of each reduced velocity calculation point as equal to that one of

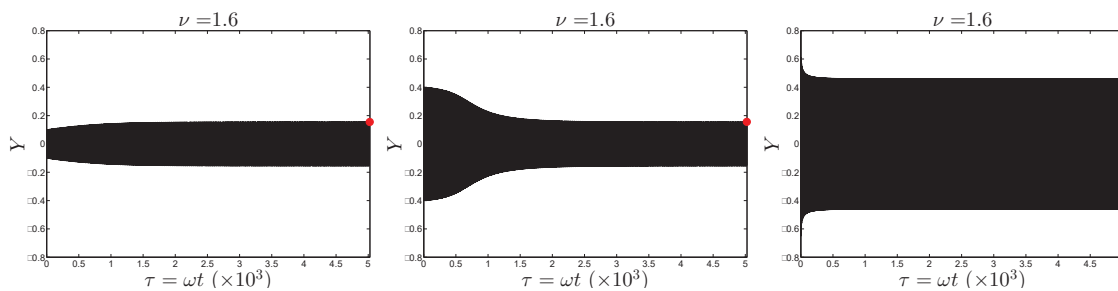


Fig. 5.8 Different stable amplitude values Y_s obtained for $\nu = 1.6$ by changing the initial amplitude Y_0 respectively equal to 0.1 (left), 0.4 (center) and 0.8 (right); with filled red circles the values of Y_s are indicated.

the previous one, that is:

$$\begin{cases} Y_{0,k} = Y_0, & k = 1 \\ Y_{0,k} = Y_{s,k-1}, & k > 1 \end{cases}$$

In fact considering a fixed initial amplitude $\forall \nu$ different stable limit cycles are detectable. An example is proposed for $\Lambda = 1.49$ and $C_{L_0} = 0.7$ in Fig. 5.7: the lower stable branch correspond to a fixed Y_0 value of 0.1 or even 0.4, whose time traces are reported in Fig. 5.8.*left* and *center* respectively, while the upper branch was reached only starting from a value of $Y_0 = 0.8$ (Fig. 5.8.*right*). It is also worth noting the length of the nondimensional time traces reported as examples: those in Fig. 5.8 correspond to $\tau = 1600\pi$, which is in this case long enough to visually check that a stable amplitude (Y_s) was reached but it's not like this in all the cases. For this reason a maximum calculation time was not fixed, but a 'trial-and-error visual process' has been chosen for the determination of each stable amplitude. On the contrary if a maximum time length was fixed, as in the original paper, one should have accounted for $1/4$ of calculation time used in the present case.

5.5 Rotational rig testing

Apart from flow visualizations related information about the wake-oscillator geometry, it has been previously shown how TS -model rely on mainly two parameters: while C_{L_0} is already obtained from static measurements, for \tilde{f} specific tests have to be conducted for measuring the variation of the lift induced by the variation of the velocity ratio, Δ , as in Prandtl experiments mentioned above.

Conversely, with respect to the sharp-edged bodies, the Magnus force effect on the circular section received a great attention because of military purposes related to the change of trajectory of a spinning missile or a body travelling through the air experiencing a rotation. In a technical report of U.S.A. NAVSEA (Borg, 1986) a detailed study on the state of the art starting from the half of XIX century was conducted, showing all the possibilities connected to the phenomenon which was also considered as a propulsion mechanism; a very intuitive image for explaining the phenomenon is reported in Fig. 5.9 The state of the art was proposed by Swanson (1961), who collected experimental and historical data about it, so to become a milestone in the reference literature. A comprehensive plot reporting all the data for the circular section with different end conditions, roughness, Re and AR is reproduced in Fig. 5.10. It would be misleading to the present dissertation purposes to enter in a detailed discussion on it, although the argument is really fascinating. The curves reported are helpful for a comparison between the 'classical' situation of a circular cylinder and the present one. The experimental rig described in §4.2.3 was employed to measure hydrodynamic forces on two rectangular sectional models, D24/D37 and D25, held in a stationary configuration, as in the case of M_{s2} rig experiments, in forced rotation at the desired constant tangential velocity v_0 . As sketched in Fig. 5.11 in addition to the physical quantities and numerical parameters already mentioned it is possible to individuate the hydraulic diameter, defined by Eq. (5.41), and used to get hydrodynamic coefficients starting from the recorded forces.

$$D_H = \frac{4DB}{2B + 2D} \quad (5.41)$$

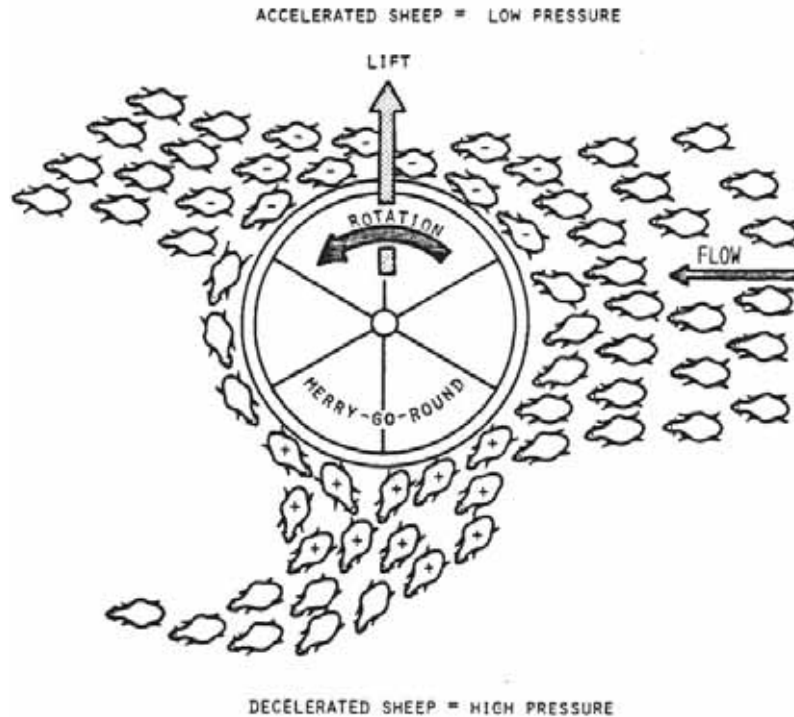


Fig. 5.9 A flock of sheep encounters a carousel demonstrating the Magnus effect.

Limitations on the range of Δ ($= v_0/U$) were given by the rotor power in relation to the oncoming flow forcing effect; the entire range allowed for v_0 was tested, measuring a suitable number of signals, 13 for D25 and 14 for D24/D37, for each U value. It is worth noting that the nondimensional velocity ratio Δ only matters in the present experimental campaign. Moreover, it will be reported that oncoming velocity steps have been kept quite low because of the limited power of the rotor engine allowing to the model to rotate properly. An automatic procedure has been employed to set up the v_0 levels, determining Δ values to suitable values.

The procedure for both the models provided to start from a $\Delta = 0$, given by the $v_0 = 0 \text{ ms}^{-1}$ at first, and then move to the next v_0 value, till reaching its maximal value. An offset measurement of 60 s for the force balance was always taken at the beginning of each U level and the measurement is recorded continuously until the maximal v_0 level for each flow velocity was reached; the recording time for each v_0 value was set to 360 s by sampling at $f_s = 100 \text{ Hz}$. The pump frequency of the water channel was set to obtain for both D24/37 and D25 values for $U \approx 0.04, 0.09, 0.15, 0.20, 0.25 \text{ ms}^{-1}$: in this way 2 datasets of 5×13 and 5×14 values of $C_L(\Delta)$, respectively for D25 and D24/D37, were obtained. The numbers of study cases, different from D25 to D24/D37 were chosen to fit the laboratory time available.

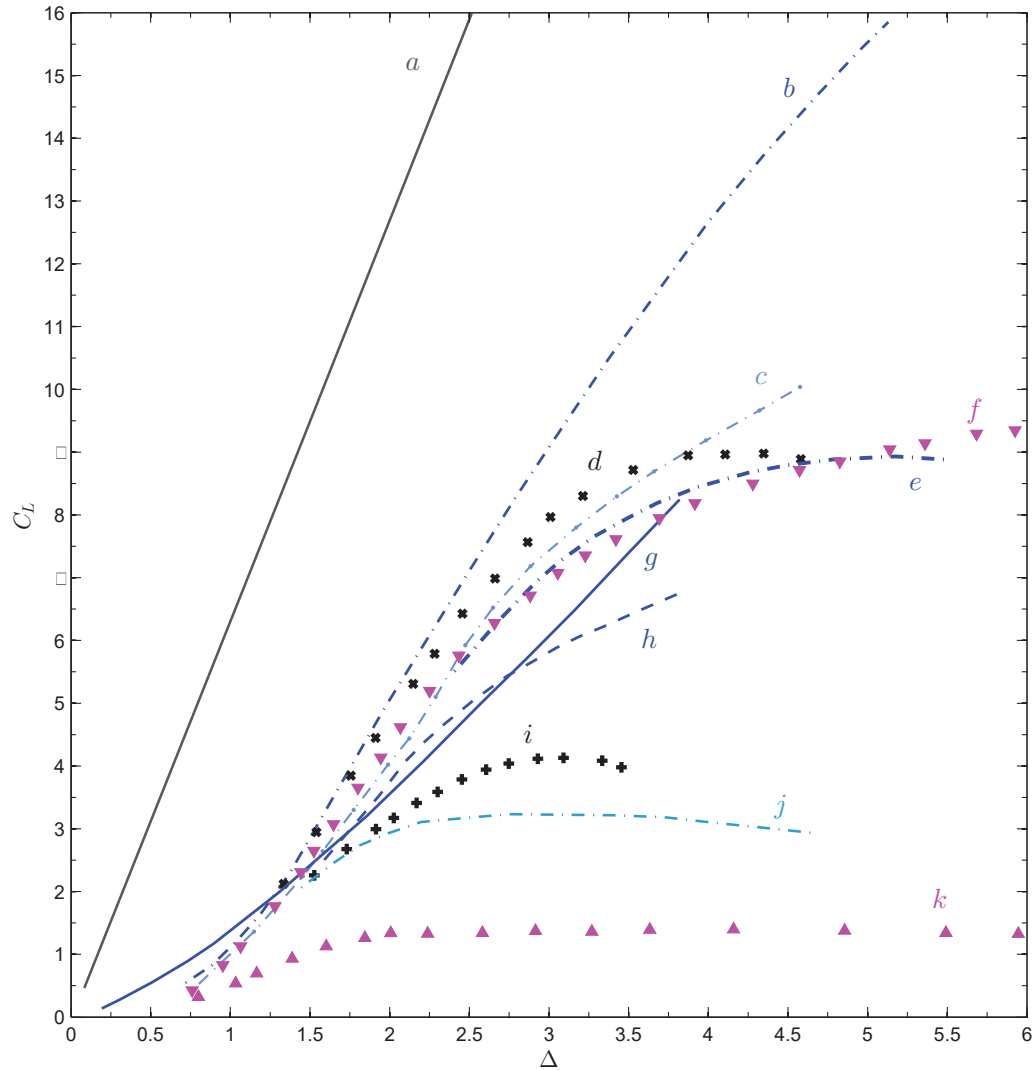


Fig. 5.10 Summary of previous lift coefficient vs. velocity ratio data. [reproduced from Swanson (1961)]. (a) ideal fluid (potential flow, $C_L = 2\pi\Delta$, $AR = \infty$, $Re = \infty$); (b) Thom (1934) ($AR = 12, 26$, $Re = 5.3 \div 8.8 \cdot 10^3$, end-disks of diameter $d_e = 3D$); (c) Reid (1924) ($AR = 13.3$, $Re = 3.9 \div 11.6 \cdot 10^4$); (d-i) Prandtl and Tietjens (1934) ($AR = 4.7$, $Re = 5.2 \cdot 10^4$, end-disks of diameter $d_e = 1.7D$ (d) and no disks (i)); (e) Thom (1925) ($AR = 8$, $Re = 1.6 \cdot 10^4$); (f) Swanson (1961) ($AR = \infty$, $Re = 3.5 \div 30 \cdot 10^4$); (g-h) Thom and Sengupta (1932) ($AR = 5.7$, $Re = 5.3 \div 8.8 \cdot 10^3$, rough sanded (g) and smooth (h) surface); (j) Schwartzemberg (*unpublished*) ($AR = 4.5$, $Re = 5.4, 18.6 \cdot 10^4$); (k) Swanson (1961) ($AR = 2$, $Re = 5 \cdot 10^4$, continuous end sections).

To the author knowledge such measurements have never been performed or published; only some contributes about the *autorotation* of rectangular prisms is available in military or transport engineering research field (Greenwell and Garcia, 2014), which is relative to the rotation induced on a 3D body free to rotate around an axis, such as a container transported by an helicopter, which has not much to do with our purposes. Hence, we couldn't referred neither to experimental nor to theoretical comparisons or considerations in tests designing. The plots in Fig. 5.12 report the lift coefficient signals for the entire evolution of each test case. The plot on the *left* contains H25 section's results while the *right* one those of D24 one, both reporting the lowest value of flow velocity. The dashed lines help in dividing the each acquisition in spinning velocity steps, though continuously recorded. By observing this

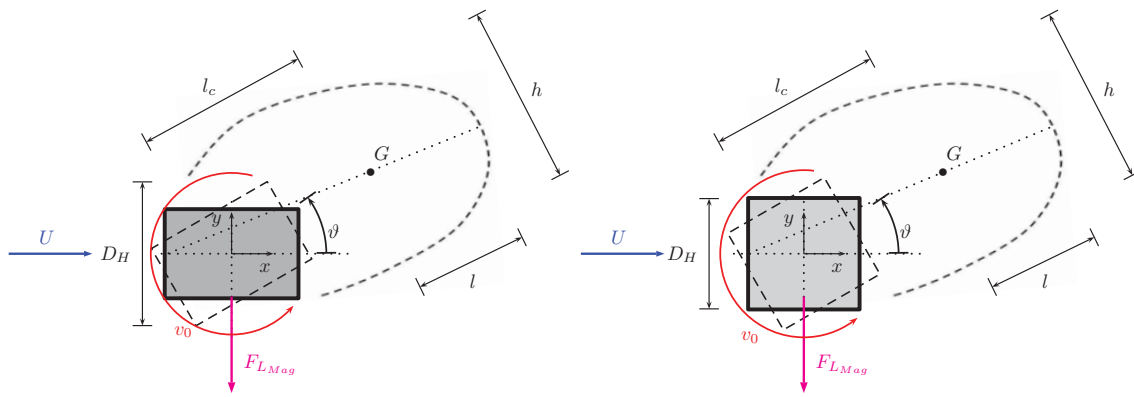


Fig. 5.11 Birkhoff-type wake-oscillator sketch utilized in the experiments.

two plots it is possible to make some observations. The first time window of each plot is related to a zero spinning velocity, so that it is representative of a measurement with fixed body. Nevertheless, its starting position was not carefully imposed to obtain a zero angle of attack given that it wasn't a static test but only the first programmed stage of a longer acquisition. Hence, the explanation for the mean lift value $\bar{C}_L \neq 0$ for $v_0 = 0$, is due to the arbitrary position of each measurement; only by chance for D24/D37 a zero position with respect to the flow seems to be set, obtaining $\bar{C}_L \approx 0$. However, such circumstances were completely fortuitous. Then, the comparison of the two plots says that by increasing v_0 keeping U constantly quite low, the increasing of C_L is impressive in modulus and observe a certain trend for both the bodies; nevertheless the signals get more chaotic, in particular for D24/D37 rectangle, even if apparently still stationary by increasing v_0 . The magnitude of C_L depends in part on the low flow velocity, having a quadratic inverse proportionality with F_L , in part on the fact that the flow 'sees' especially the continuously varying velocity making the shedding mechanism chaotic and the lift magnitude governed by the spinning body sides which behave like a paddle. This is, to the author opinion, the main reason which justify such higher C_L values of rectangular sections compared to cylinder case. Therefore, the C_L magnitude is increased from square to $SR = 1.5$ case. The examination of the others flow velocity levels supports this explanation: even if a similar trend is detectable, rather reasonably the lift increases by increasing angular velocity, though showing a completely

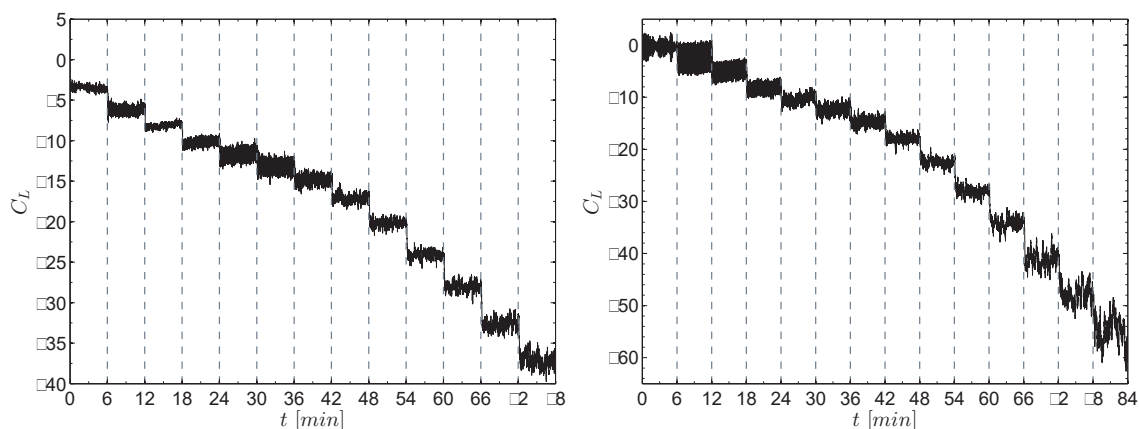


Fig. 5.12 Examples for a measurement of varying lift coefficient for $U_{min} \Leftrightarrow U \approx 0.04 \text{ ms}^{-1}$ for D25 (left) or D24/D37 (right) section mounted on the rotor rig.

different order of magnitude for more or less all the others flow velocities. Roughly speaking the spinning sharp-edged body can be ideally considered, from the point of view of the nature of the obstacle the fluid is investing, to a circular section as v_0 gradually gets faster and faster. This is a first approximation of course, as one can observe that the effect of the body edges on the boundary layer created in the fluid volume near to the so-called ideal circular section should be subject to a completely different mechanism.

From a practical point of view, we were more interested in obtaining experimentally consistent data to derive a variation law linking C_L to Δ , and this was the best empirical finding the author was able to conduct. Nevertheless, such an heuristic proof seems to be confirmed by another possible observation: in each time trace there seemed to exist a v_0 level, readable as a characteristic Δ for each configuration, at which the signals start showing lower amplitudes modulation in which no sharp edged is present and the separation point are governed by Re and v_0 by anticipating, or postponing, its position on the body surface interfering with the formed boundary layer (Swanson, 1961). On the other hand the v_0 levels below this threshold are characterized by quite different time histories patterns, maybe denouncing several transitions between more complicated flow states around the body, until a certain velocity ratio is reached for which only the Magnus effect prevails.

Now let us look at results in a more similar form with respect to what reported usually by the other investigators, such as the above showed *S-traces* given by Prandtl or Swanson. To this end \bar{C}_L value for each time window correspondent to a single Δ is reported, showing the range of variation of Re , for D24/D37 and D25. The final plots are proposed in Fig. 5.14 and 5.15, reporting in the *left-hand* plots a linear regression performed on all the data recorded to get the \tilde{f} -magnitude (\tilde{f}_{tot}), which is indeed quite higher than for circular cylinders as already noted. However, the perplexities on the lowest flow velocity set of measurements previously mentioned seems to be correct: the related curves ($U_{min} \approx 0.04 \text{ ms}^{-1}$) is moved away from the other flow velocities general trends, which seemed to collapse more or less on a unique pattern, showing either a different ‘local derivative’ by changing slope differently with respect to other flow velocities. Such an effect is a bit more pronounced for the square section. Moreover, from the observation of Fig. 5.10 a maximum peak is present for a $\Delta \simeq 4$; Swanson himself reported one of the main objectives of his investigation to be that of determining whether or not a maximum peak in the lift existed for a $AR = \infty$ cylinder, as indicated by Prandtl for a $\Delta = 4$ basing on previously mentioned flow visualization. However, he also remarked how Prandtl experiments were conducted with restrictions affecting a realistic situation (Swanson, 1961). Nevertheless, there seems to be a trend in decreasing the slope of the *S-traces* increasing the velocity ratio for both the bodies, although for $U > 0.04 \text{ ms}^{-1}$ the value $\Delta = 4$ hasn’t been reached because of the insufficient rotor power. For all these reasons the U_{min} dataset was neglected in calculating the effective \tilde{f} to be used in numerical modelling. In Fig. 5.14 and 5.15, on the *right-hand* plots, is reported the range $0 < \Delta < 1$ for the remaining *S-traces* and the linear regression utilized to obtain each \tilde{f} parameter value.

5.6 Implementing TS model for $SR = 1.5$

In § 5.4 how the TS model was implemented and validated with literature reported results for the square section, for which the model was conceived. The same predictive model was used presently, for reproducing the experimental curves, available for both the flow regimes, air and water, for the rectangular $SR = 1.5$. Thus, two step forward will be proposed in the following: a preliminary study on three test cases on $SR = 1.5$ in air flow associated to the sensitivity study on the main parameters of the model, and, at last, a study aimed to the prediction of the main air flow and water flow experimental data, showed in Ch. 3 and 4.

test case	A_1	A_3	A_5	$A_7 (\times 10^3)$	$A_9 (\times 10^6)$	$A_{11} (\times 10^6)$	C_{L_0}
D37	5.503	20 54	-561 -1685	1.87 13.95	- -0.051	- 0.07	2.15
H53	2.92	-23 -219	-10 13822	-0.323 -331.8	- 3.23	- -11.04	3.34
Heine (1964), $SR = 1$	-	-	-	-	-	-	3.11
Parkinson and Smith (1964)	2.69	168	6270	59.9	-	-	-
Wawzonek (1979), $SR = 1$	4.0	260	-10000	100	-	-	-
Tamura and Shimada (1987)	"	"	"	"	-	-	0.7
D77	5.78	18 -537	-3940 53750	32.2 -2003.6	- 29.48	- -150.14	1.2
D30	6.19	-38 -849	-2584 75713	21.1 -2593.7	- 36.37	- -179.78	3.07
D24	5.13	-101 92	303 -10910	766 204.9	- -1.48	- 3.78	0.62
Heine (1964), $SR = 2$	-	-	-	-	-	-	1.56
Santosham (1966)	2.33	1100	74240	1664.3	16.07	57.29	

Tab. 5.2 Polynomial interpolation coefficients: values determined in the present work (D37, H53, D77, D30, D24 sectional models), for two different odd polynomial degrees (7^{th} and 11^{th}) are proposed together with some contributions taken by literature for square and $SR = 2$ rectangle. Present and literature correspondent values of C_{L_0} are also given.

In bold are indicated the models and values object of numerical simulations.

First of all, static data on the investigated sectional models have been analysed for determining the best possible fit for the polynomial approximation of the lateral force coefficient. In Fig. 5.16 some examples of the fitted data are proposed, in which are reported two different polynomial degree, that is the 7^{th} , as in Parkinson's theory for the square section, and the 11^{th} , which demonstrated to improve the fitting accuracy. The fitting results, together with the amplitude of the fluctuating lift coefficient detected from static data are reported in Tab. 5.2, differentiated by SR and providing also some literature results adopted by previous investigators; in bold are highlighted the test cases object of the numerical results finally shown.

Stage 1 This first numerical study was restricted to D77 section on which the deepest work on fitting analysis was performed. Experimental curves for comparisons were chosen for representing the three situations (quenching, interaction, phenomena separation), often mentioned, are reported in Fig. 5.16, from the parameters reported in Tab. 5.2. As saw before, apart from the polynomial coefficients, TS -model has to be implemented by taking into account three key-parameters, h^* , \tilde{f} and C_{L_0} . For the moment, the first two are

based on the values given in TS , while for C_{L_0} the value derived from static tests data was taken as the reference value for the sensitivity study involving all the three parameters: in Tab. 5.3 their values are highlighted in bold, while in round brackets the other two tested values are reported. The results are reported in Fig. 5.17. It is worth specifying that the response parameters are the stable amplitude, Y_s , for the numerical model and $\sqrt{2}Y'$ for experimental data, even if in the plots will always refer to the same previously used general parameter A^* . In reading Fig. 5.17 note that the plots rows are relative to each test

test case	m [kg]	ζ	f_n [Hz]	Sc	Λ	h^*	C_{L_0}	\tilde{f}
I	4.89	0.0016	14.74	10	0.53	1.8 (0.58,2.32)	1.2 (0.7,1.8)	1.16 (1.2,2.4)
II	12.86	0.0017	9.94	26	1.43	1.8 (0.58,2.32)	1.2 (0.7,1.8)	1.16(1.2,2.4)
III	4.82	0.0052	14.86	32	1.73	1.8 (0.58,2.32)	1.2 (0.7,1.8)	1.16 (1.2,2.4)

Tab. 5.3 Model parameters for the sensitivity study.

case while the columns to each single parameter values. In addition to TS -model results, as a reference, the QS -model outcome is reported, both increasing (continuous line) and decreasing (dashed line) the flow velocity, respectively from $Y_0 = 0.01$ (whereas the value suggested in Parkinson and Smith (1964) was 0.05), and $Y_0 = 1$, which is significantly higher than the expected stable amplitude. From QS vs. TS model, it is straightly evident the capability of the interaction model to better predict the the onset of the instability. In fact, in all the plots presented in Fig. 5.17, in every interaction scenario or empirical parameter value, QS theoretical critical velocity goes wide with respect to TS one, which is quite obvious indeed given that QS one is the first value that intrinsically define the interaction scenario. Hence, when the theoretical QS galloping critical wind speed is lower than the Kármán-vortex resonance wind speed ($\Lambda < 1$, **I**) the model correctly predict the onset of a velocity-unrestricted instability around U_r . Then, also when it's more or less slightly higher ($\Lambda > 1$, **II-III**), the coupled model keep holding the onset at resonance velocity, contrarily to QS one; however, even in these cases, the model predicts a quick growth of the vibration amplitude not observed in the experiments.

By focusing on the interaction model only, it can be noticed that the amplitude of vibration predicted by TS -model is always markedly overestimated; in particular its tendency to sustain the reached amplitude is evident in case **I**. From C_{L_0} study it can be derived TS model to be almost not affected by its variation, so contradicting the results of the simulations performed for the square section in Ch. 5 for $\Lambda = 2.15$. Then, looking at the results of h^* parameter the model showed to be even less sensitive to it, given that both the different values chosen, 1.2 and 2.4, produced practically no difference in the numerical solutions. On the other hand the Magnus-effect parameter strongly affects the numerical response in determining the width of a sort of resonance bell, and the possibility to predict the two phenomena as separated or not. This result is more evident in cases **II** and **III**, where, given that $\Lambda > 1$, the separation can be somehow numerically induced through the parameters, while in case **I** it only affects the presence of a slight reduction in amplitude after the resonance peak. In particular, the lowest \tilde{f} value, 0.58, caused a little super-harmonic bell at $U/U_r \simeq 0.75$ and the most marked drop dawn in amplitude after the peak to return on the QS post-critical branch, whereas the highest one did not present the same

feature, remaining with a slope parallel to the QS one although with a certain offset with respect to it.

Stage 2 From Stage 1 it turned out the insensitivity of the model to the geometry of the coupled wake-oscillator, that is the h^* parameter. Anyway, the principal progress is here represented by the introduction of the ‘real’ \tilde{f} value, or at least those detected from empirical data on rectangles.

For this final stage only the most representative test cases were chosen in order to offer an overview of TS -model capability for predicting the response of $SR = 1.5$ rectangular cylinder in air and water flow. Therefore, in Tab. 5.4 the cases object of the present analysis are reported, namely three cases in air flow (cases **IV**, **V** and **VI**), whose experimental curves for comparisons come from tests conducted at *CRIACIV* (respectively D77-B1, B6 and A7), and one more case from hydroelastic tests (case **VII**, D24-W1). The value of C_{L0} was the one from Tab. 5.2 as reported in results legends. No simulation on the square section has been performed because dynamical tests available for D25 do not correspond to any static measure, and vice versa for H53 model. The results of the four cases are proposed in Fig. 5.18. Case **IV** is relative to a quenching scenario: as saw before the QS -galloping branch starts at the Λ value while TS one correctly predict the onset occurred during laboratory tests. Then, due to the high value of \tilde{f} , stable amplitudes are sustained, giving a trend for which the TS branch will tend to the QS one with the same slope. Similarly, in case **V** TS model overestimates the amplitudes whereas, given the velocity ratio is close to 1, QS model seems to better fit the experimental curve, overlapping on its branch, though again not matching the onset; then, the increment in amplitude predicted by the classical galloping response makes the numerical curve to diverge from laboratory data, in the range in which an hysteresis cycle occurs. It is worth noting that even if the experimental data (red filled circles in the second row of Fig. 5.18) extend up to $U/U_r = 1.5$ it is quite unlikely the unstable branch to develop following the curve described by the QS -model prediction (blue line in the same figure).

For what concern case **VI**, representing a separated phenomena scenario, as from what was expected, in the range of resonance region only the VIV-related part of the TS model effectively simulates the narrow resonance peak, though overestimating again its height and not predicting the sub-harmonics of order 2 and 3 barely visible in experimental data; on the other hand QS model response is completely flattened on a zero-amplitude response, being $\Lambda = 8.54$: to this end it goes without saying that the QS -theory correctly predict the galloping critical velocity and the slope of unstable branch in case an extended velocity range were shown here in the plot.

Case **VII** shows the results in predicting the response for $SR = 1.5$ section in water flow. In this case the experimental curve for comparisons with is that one coming from *FLAIR* experiments, for which some interesting remarks arise from the results proposed. TS numerical response curve seems to match the onset of the super-harmonic resonance, but then, maybe due to the high value of \tilde{f} , the amplitudes unrestrictedly grow up by increasing the flow velocity. However, QS model qualitatively predicts the trend of the amplitude response obtained in laboratory, not only the theoretical onset, which is as mentioned close to zero in water, but also the unstable branch shape, for which the QS curve shows a comparable trend, though slightly overestimating the amplitudes, going from the super-harmonic

test case	m [kg]	ζ	f_n [Hz]	Sc	Λ	h^*	C_{L_0}	\tilde{f}
IV	4.83	0.00084	9.83	5	0.27	1.8	1.2	5.32
V	12.86	0.00126	9.94	19	1.06	1.8	1.2	5.32
VI	12.79	0.0099	9.11	158	8.54	1.8	1.2	5.32
VII	1.28	0.0025	0.519	0.468	0.024	1.8	0.62	5.32

Tab. 5.4 Model parameters for the sensitivity study.

resonance to the higher velocities experimental amplitude values; nevertheless, the central region, that is the desynchronization range, has not been reproduced.

In conclusion, the TS semi-empirical model showed to be able to capture some of the physical phenomenon features observed in laboratory but fail to predict the actual trend of the experimental data.

5.7 Chapter summary

In the present chapter an overview on the most referenced numerical and semi-empirical models has been given. Given that QS -model was already discussed in Ch. 2 the review here proposed has been focused on the main VIV models used in the past to construct interaction VIV-galloping predictive models, introduced afterwards. Then, more details on TS -model were reported, characterizing the parameters for its implementation on the cross-sections of interest through an experimental campaign conducted employing the rotor rig. At the end of the chapter, final results on $SR = 1.5$ section have been proposed, showing the capability of the model to predict only some features of amplitude response; however, it demonstrated its necessity to be optimized for water flow predictions.

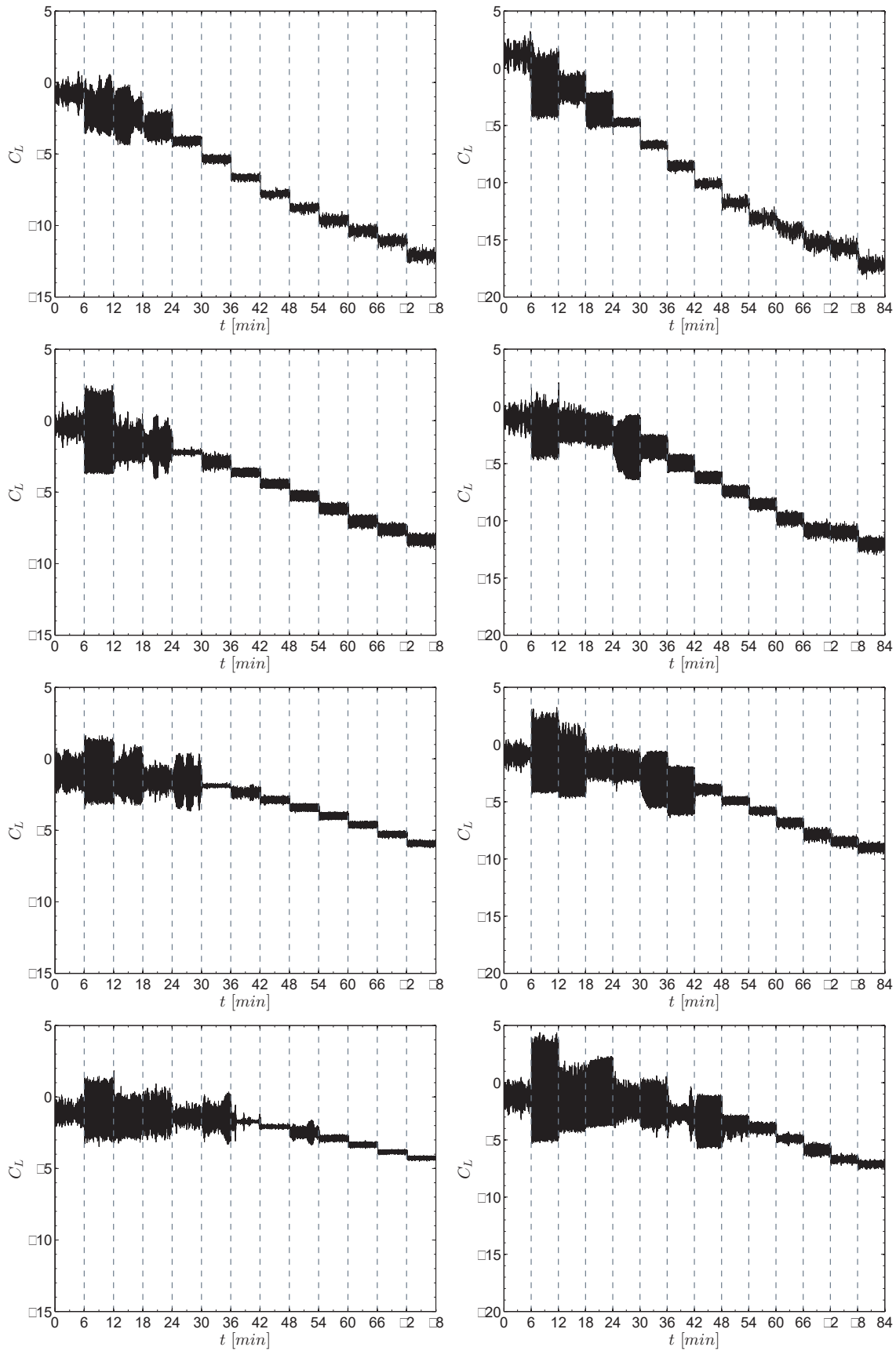


Fig. 5.13 Rotational rig study comprehensive results. U assumes mean values of 0.09, 0.15, 0.20, 0.25 ms^{-1} respectively from the top to the bottom. Plots reported in *left column* refer to D25 while *right column* to D24/D37 results.

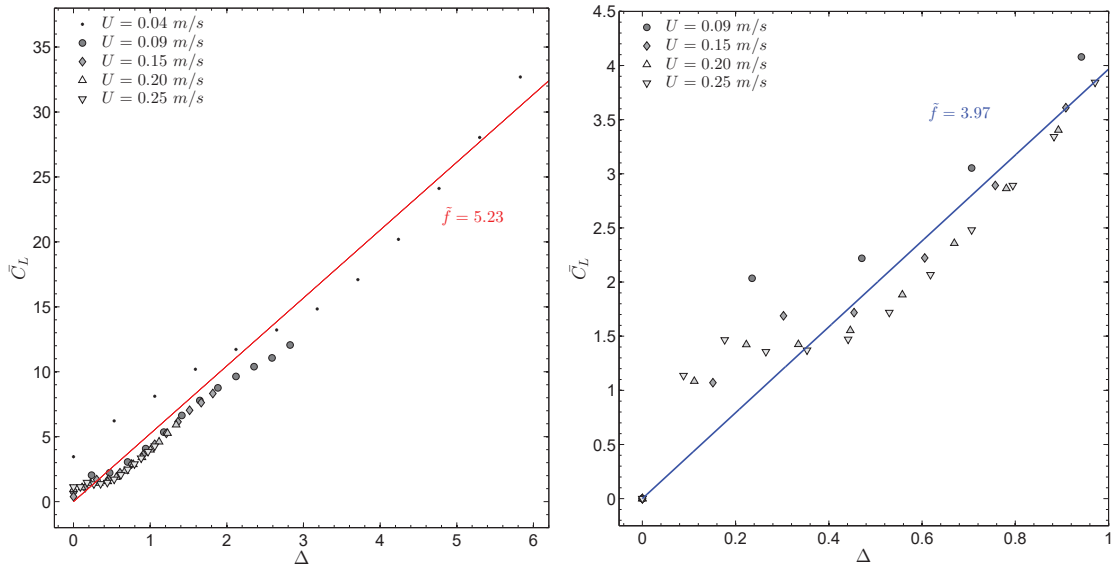


Fig. 5.14 $Re = 0.77 \div 4.63 \cdot 10^3$. D25 results for Magnus-related parameter. [see Fig. 5.15 for caption].

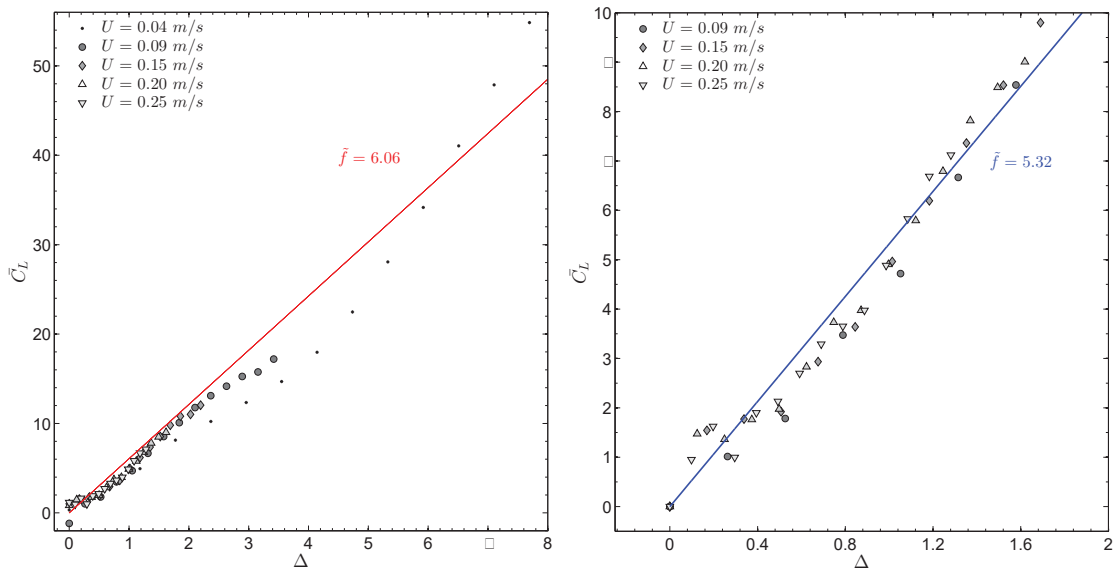


Fig. 5.15 $Re = 0.99 \div 5.92 \cdot 10^3$. (left) Entire set of flow velocities results for D24/D37 rotating section: the value of the Magnus-related parameter is obtained through a linear regression obtained by collapsing all the data in only one vector. (right) Velocity ratio window selected to extrapolate the value to be used in numerical modelling.

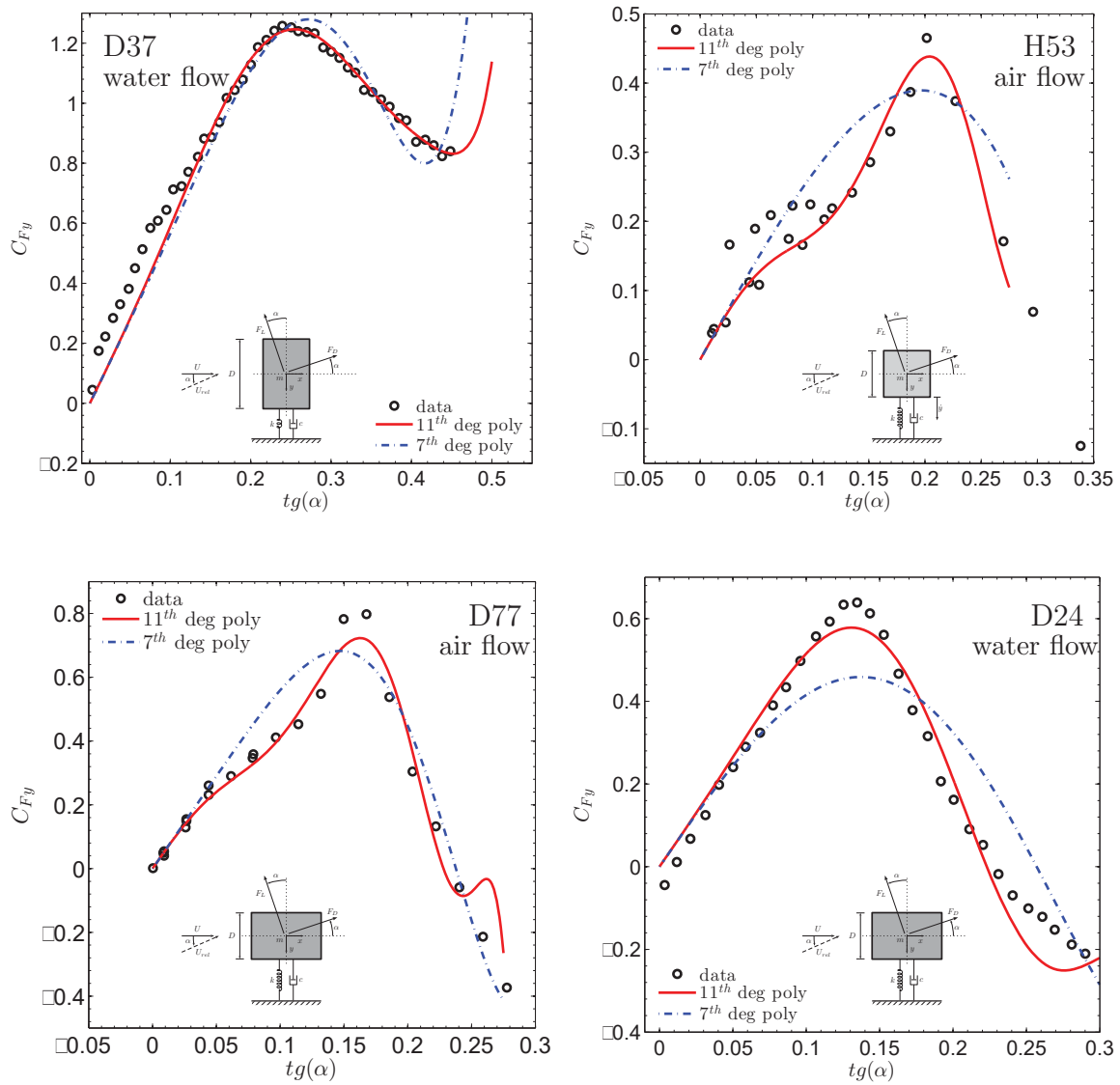


Fig. 5.16 Different polynomial approximations for the lateral force coefficient of some rectangular cylinder sectional model. [see Tab. 5.2]

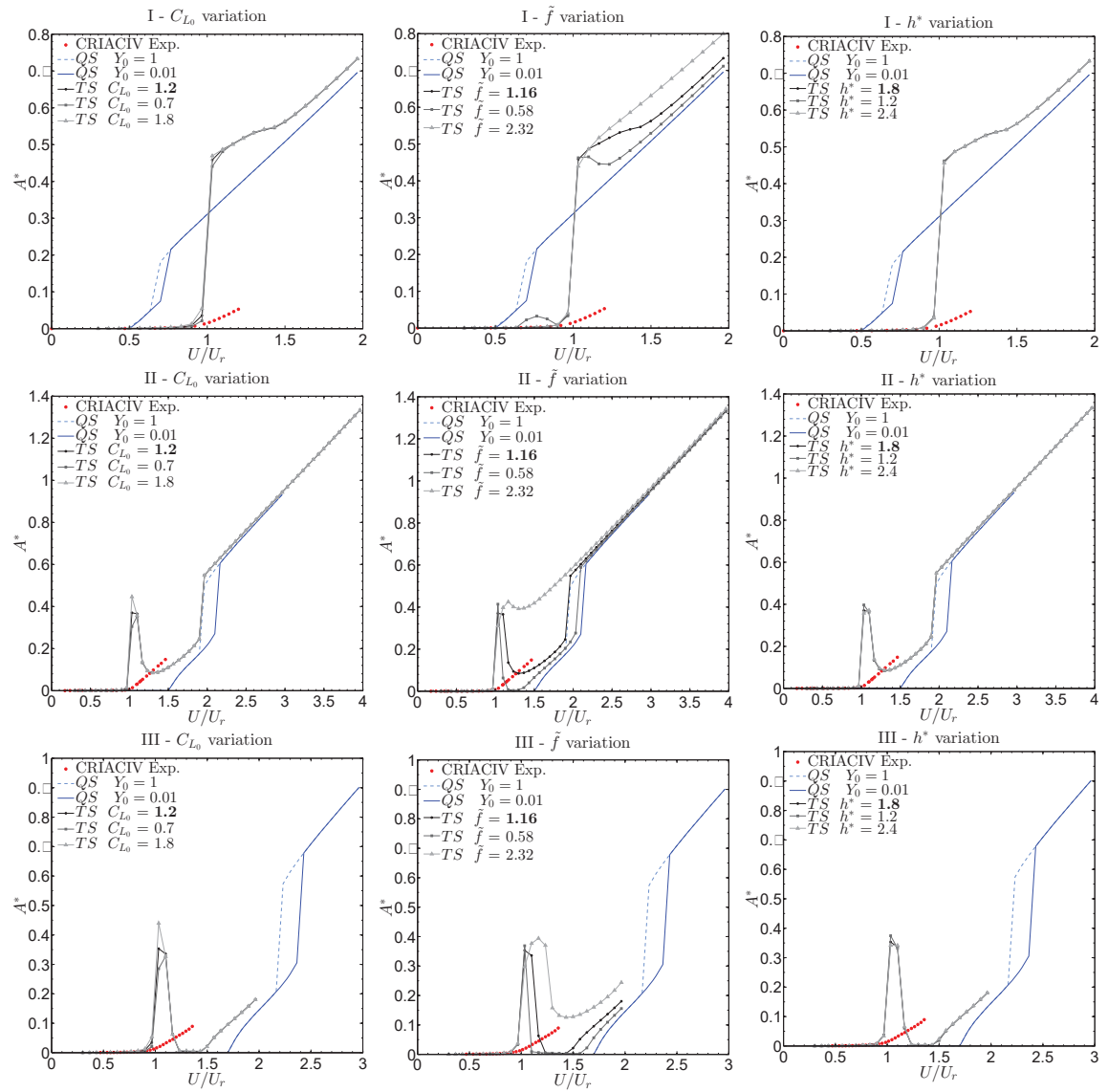


Fig. 5.17 Sensitivity study on *TS*-model parameters for the first study (Stage 1). [test cases ref. Tab. 5.3]

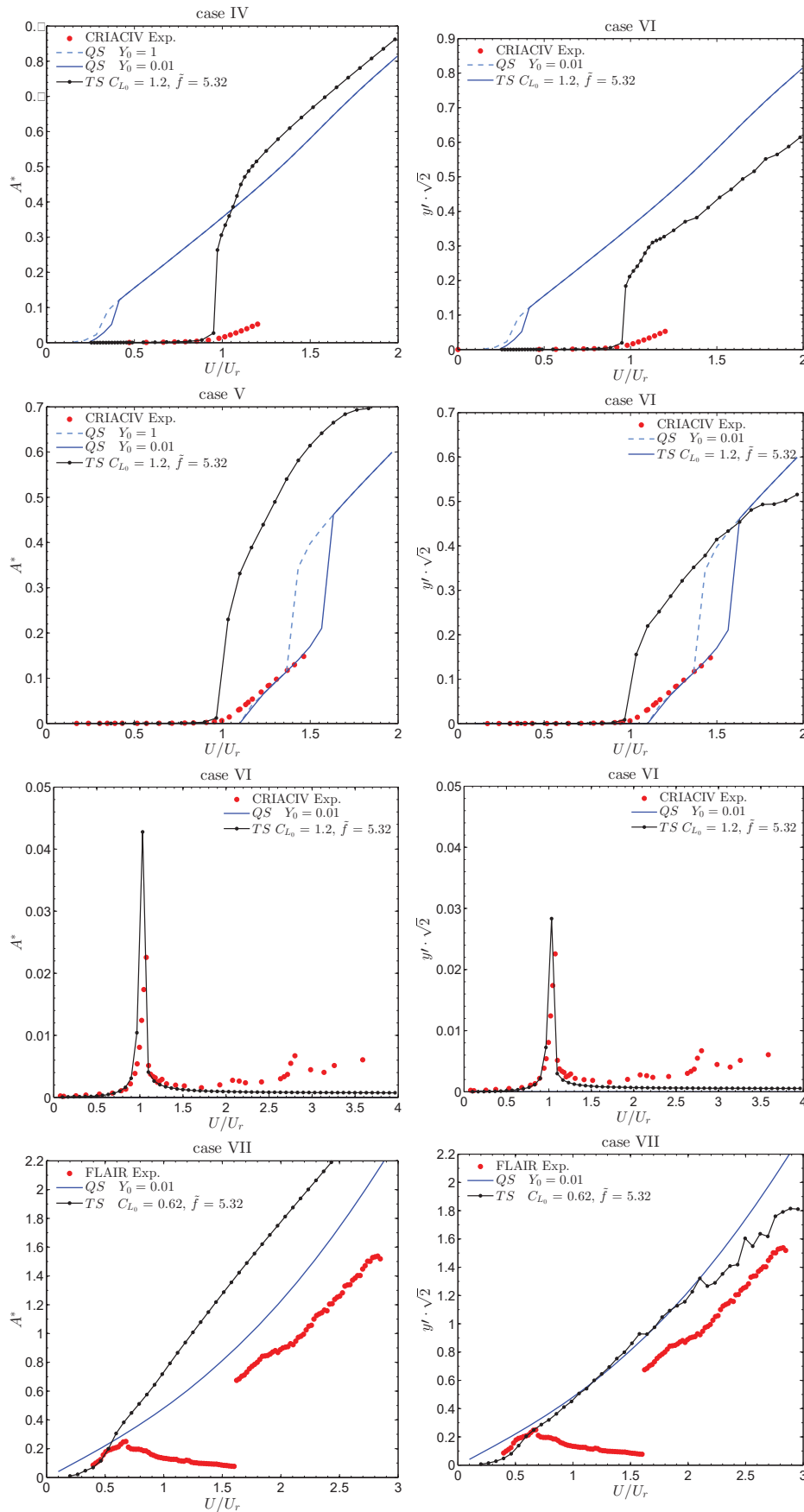


Fig. 5.18 Final results on the test cases investigated after having empirically defined the model parameters. [see Tab. 5.4]

Chapter 6

Discussion

6.1 Introduction

In the present chapter the different contributions coming from experimental and numerical results will be assembled in order to have a comprehensive insight of the interaction phenomenon. Although a more precise understanding about the behaviour of low side ratio rectangular cylinder came out from present laboratory experiences and obviously from researches previously published by several distinguished investigators, the capability of a semi-empirical model, which reliably predicts at least the main features of the dynamical response, can make the difference from the engineering point of view. However, the physics behind the possible interaction between VIV and galloping demonstrated to be quite complicated, so that in the near future it will be hard to skip any laboratory observations. Unfortunately, the flow-visualizations are lacking in the present work for several reasons, though obviously necessary in order to have more information about the causes and not just on the effects which often did induce in the investigators involved misleading conclusions. Nevertheless, aero- and hydroelastic results did contribute to the development of a wider and comprehensive framework in which our ‘story’ on low side ratio rectangular cylinders can find its own place.

6.2 Comparing experimental data in air & water flow

The dynamical data, previously shown in their completeness, are in the following just recalled time by time for what it seemed to be worthy. In this section, some considerations on presently investigated $SR = 1.5$ and $SR = 0.67$ rectangles, together with other experimental data taken from the literature, also with different side ratios, will constitute the preamble to give rise to a wider perspective in which the circular section will be included too. In this way the effectively considered side ratio range will extend from 0.67 to 2, fully covering the cases for which the literature already showed the proneness to the interaction between VIV and galloping.

It is here worth remarking for the reader to put attention on which form of nondimensional amplitude each time will be used in the legends, given that only a general parameter A^* will be proposed in ordinates; this was caused by the different sources from which data for comparisons were taken, so that from time to time A_{max}^* , $\sqrt{2}A_{rms}^*$, and A_{10}^* will be utilized.

Although some critics could arise from this choice, it is important to consider that different investigators did chose, during the years and depending on experimental circumstances and recorded output, different response parameters, evidently considered as statistically representative in each case. While in Khalak and Williamson (1997) the maximum value (A_{max}^*) was considered reliable, Bouclin (1977) assumed the signals to be almost perfectly sinusoidal¹ by using the theoretical definition of the *rms* of a sine wave ($\sqrt{2}A_{rms}^*$), which was also our choice for air flow results; unfortunately Smith (1962) and Santosham (1966) did not specify anything about the criterion used to extract a significant amplitude parameter. On the other hand A_{10}^* represented for some authors the best choice for water flow signals, but still, it is considered here to be consistent to compare all these response forms parameters.

Another operated choice was to characterize the test cases showed by the mass-damping parameter, not with Scruton number expression but with the mere product between the mass ratio, m^* , and the damping ratio with respect to critical, ζ ; to the author opinion this improved a clear comparison of results having such a different character in the very end of this section. However, all these quantities will be punctually indicated allowing to easily detect each curve properties.

Data measured in air and water have to be analysed always keeping in mind some important facts which are important to remark for the sake of clarity, even if occasionally mentioned so far.

- Water flow regime is theoretically out from the boundaries of *QS*-theory, thus the use of parameters such as U_g^* has to be carefully made. However, U_g^* in water is always near-zero, in fact for the present experiments we got $\Lambda = 2 \div 7 \cdot 10^{-3}$ (Tab. 4.2 and 4.3), while in Bouclin's tests on square section values of $\Lambda = 3 \div 9 \cdot 10^{-2}$ were obtained.
- Nondimensionalized quantities of literature data are proposed at the best of the knowledge of parameters (such as A_1 , St , n etc...) declared by Authors, being replaced by tentative, though likely, values always consistent with literatures.
- Measurements taken in the *WT* are of an order of magnitude smaller in terms of nondimensional amplitude response because the test rigs did not allow higher displacements. In fact, dynamical rigs employing air-bearings² have as the only limitation in amplitude the maximal stroke resulting from rig geometry and the transducer position, also considering that the springs connecting the model to the fixed reference usually allows large displacements standing below the maximal elongation allowed; on the other hand the systems like those described in Ch. 3, F_{d1} and F_{d2} , cannot sustain large displacements because of some components yielding limit.

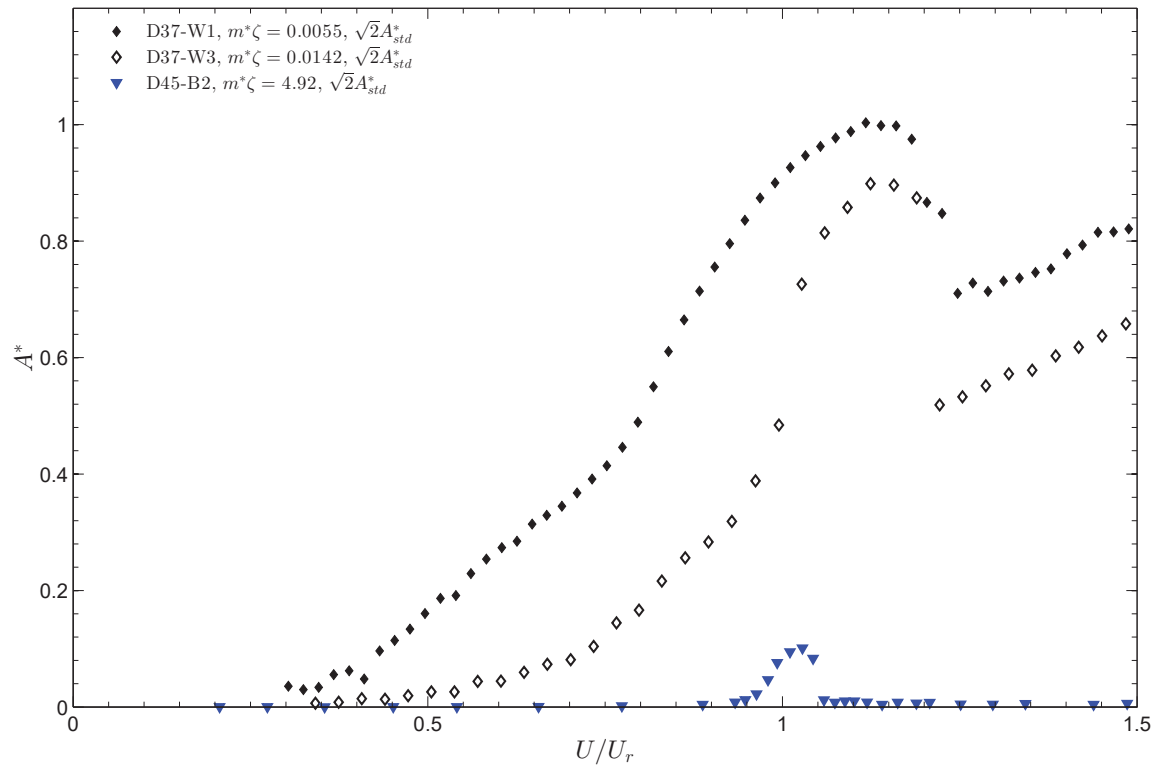


Fig. 6.1 Experimental results in air and water for rectangular cylinder with $SR = 0.67$.

6.2.1 Results for each SR

$SR = 0.67$ in air and water

In Fig. 6.1 the results obtained for the $SR = 0.67$ rectangular section, entirely during the experimental campaigns documented in the present work, are reported for both air and water flow case. It was mentioned that D45 section (air flow) manifested itself as a hard-type oscillator in the *WT*, while it demonstrated its proneness to an instability when mounted in the *WC*, either from static or hydrodynamic tests. In the same figure is also evident the different magnitude between water and air flow responses, the latter case only showing a low peak resonance at critical velocity ($St = 0.125$); differently a $St = 0.137$ was detected for D37 case, hence the curves reported relatively to the lowest and highest m^* , show unrestricted oscillations starting practically from a near-zero reduced velocity and developing with a comparable unstable branch slope. Around the resonance there's a magnification of the response given by the interaction with the vortex shedding, as already reported in Ch. 4. It is quite interesting to note the similar shape which both the resonance bell types, in air and water, assume, with a drop down in amplitude after having reached the relative maximum; the reprise of a galloping branch is present in D37 case, more or less following the same trend showed before the resonance. It is also interesting to put the attention on the extension of the lock-in range, which is much wider in water flow case:

¹as from the definition of the standard deviation of a sine wave: $y = A \cdot \sin(\omega t)$, $\frac{A}{\sqrt{2}} = y'$

²Air-bearings are employed in the present water flow measurements, and in turn for data taken from Zhao *et al.* (2014), as well as in the contributions coming from water flume of the Hydraulic (nowadays Hydrotechnical Engineering) Laboratory of Civil Engineering Department (Bouclin, 1977) and *AEROLAB* (Feng, 1968, Santosham, 1966, Smith, 1962), both at University of British Columbia, or at Cornell-ONR Water Channel (Khalak and Williamson, 1997).

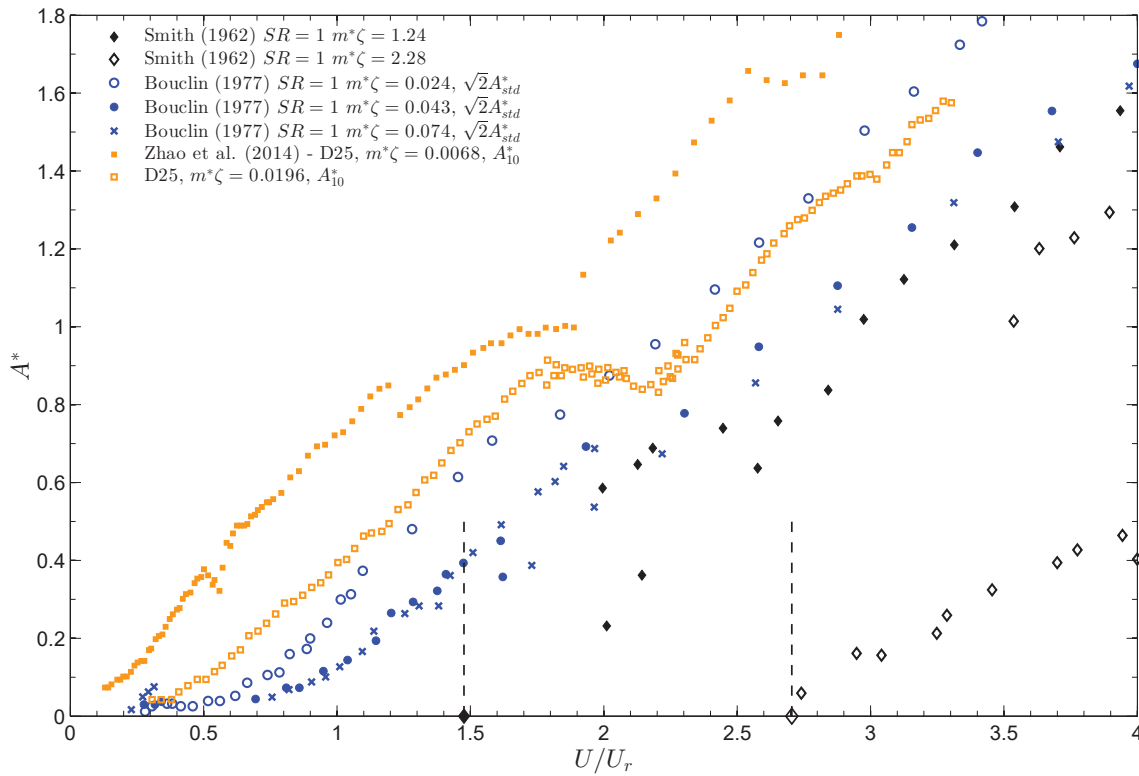


Fig. 6.2 Experimental results reported in the reference literature, in air and water, for the square section. *Air flow*: Smith (1962) results are relative to a $m^* = 1163$ and damping ratios respectively [\blacklozenge] 1.07 and [\diamond] 1.96, whose relative QS -galloping theoretical velocity is indicated with markers and dashed lines [- -]. *Water flow*: Bouclin (1977) results are relative to [\circ] $m^* = 5.38$ with $\zeta = 0.0044$, [\bullet] $m^* = 9.69$ with $\zeta = 0.0044$ and [\times] $m^* = 15.24$ with $\zeta = 0.00489$; Zhao *et al.* (2014) reported a square cylinder having $m^* = 2.64$ with $\zeta = 0.00258$ [\blacksquare], while D25 case is relative to $m^* = 15.00$ with $\zeta = 0.00131$ [\square]. D25 square data (unpublished) are available by courtesy of Dr. Jisheng Zhao.

this constitutes a parallel between air and water response type that will be discussed again in the following about the comparison with the circular cylinder case.

$SR = 1$ in air and water

Literature results for the square section are proposed in Fig. 6.2 as a valuable term of comparison for more or less elongated bodies. Concerning the slope of the post-critical branch the whole set of data in air and water seems to be consistent. Smith's air flow data, already reported in Fig. 2.16, show different proneness to the interaction with VIV as indicated by the reported theoretical QS -galloping velocities from which the response branches depart: for $m^*\zeta = 2.28$ there's no interaction and in addition an hysteresis cycle is also evident, while for $m^*\zeta = 1.24$ case an uncertain situation is shown, given that a clear onset identified by very low stable oscillation amplitude is not present neither around $U/U_r \simeq 1$ nor in correspondence of U_g/U_r .

In water flow cases unrestricted oscillations starting right after $U/U_r = 0$ are evident: in this flow regime the phenomenon referred as asynchronous quenching cannot manifests itself in the way it does in air flow, in fact also Bouclin (1977) aimed to investigate a possibility of oscillation reduction (or quenching) for $U > U_r$ but he never obtained oscillations starting at $U/U_r \simeq 1$. On the other hand the super-harmonic resonance at $U_r/3$ were present in his

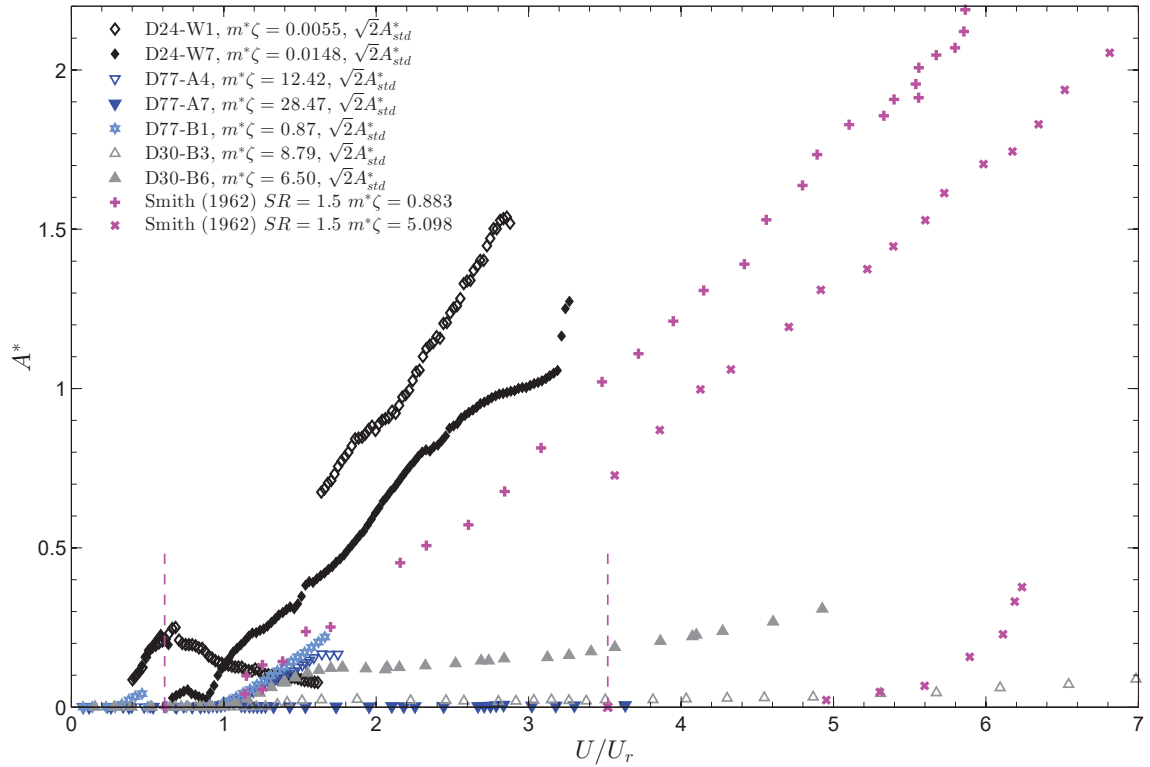


Fig. 6.3 Experimental present and literature results in air and water for rectangular cylinder with $SR = 1.5$. *Air flow*: Smith (1962) results are relative to a $m^* = 857$ and damping ratios respectively [+] 1.03 and [×] $5.94 \cdot 10^{-3}$, for which galloping instability onset velocity is indicated with markers at zero-amplitude and dashed vertical lines [- -]. *Water flow*: dynamical characteristics of the present tests sectional models are the same already mentioned.

results on three different square models, and indeed more evident for $SR = 2$ as it will be shown later; after the super-harmonic lock the galloping instability was denounced by a sudden drop down in the reduced frequency domain to quickly recover a f^* value around $0.7 \div 0.8$ according with the trend showed in present results (Fig. 4.17 or 4.18). Generally speaking, while the response shows the presence of an instability branch starting from zero a proper galloping instability is detectable only looking at reduced frequency domain, as discussed for D24 and D37 results in Ch. 4. The same behaviour is reported in Zhao *et al.* (2014)³ for a square having $m^* = 2.64$: a central wider reduced velocity region exhibiting lock-in in frequency domain shows the amplitude branch to keep the same slope, apparently without interaction with the vortex structure, although a super-harmonic narrow velocity region is present around $U_r/2$ showing a slight effect in the amplitude response as showed in Fig. 6.2 for $m^*\zeta = 0.0068$. It has to be noted that the range showing a decreasing in slope followed by a recovering of the initial slope for D25 section correspond to the end of lock-in region which begins around the critical velocity ($U/U_r = 1$).

Another general effect of the mass ratio increasing is the shift of the response branch towards higher velocities, as it's been shown for D37 passing from W1 to W3 case: curiously the same does not occur in air flow by increasing the mass ratio but a similar feature has been shown the increasing of turbulence intensity.

³see Fig. 5 in the original paper

$SR = 1.5$ in air and water

Let us move to the most investigated case of this dissertation, for which the majority of response curves come from present results. The test case selection reported in Fig. 6.3 is aimed at proposing representative examples from the campaigns conducted. For water flow the lowest and highest mass ratios for D24 were selected, while five different situations from *WT* experiments are shown, namely two fully interacting cases, though different in response branch shape (D77-A4 and D30-B6), a full interaction case showing super-harmonic resonance (D77-B1), two not interacting examples for different sectional models (D77-A7 and D30-B3). In addition, well known literature data given by Smith (1962) related to interacting phenomena ($m^*\zeta = 0.883$) or not ($m^*\zeta = 5.098$) are also reported, indicating the relative *QS*-galloping critical velocities, which allow to appreciate the hysteresis showed by the second one. It is interesting the overlapping of the initial instability branches departing from $U/U_r = 1$ with practically the same slope of D77-A4, D77-B1, D30-B6 (this one for the first portion before the decreasing of slope followed by a gradual recovery) and Smith's data for $m^*\zeta = 0.883$; in particular the best matching pair is represented by D77-B1 and Smith's results, characterized by an almost equal $m^*\zeta$ value.

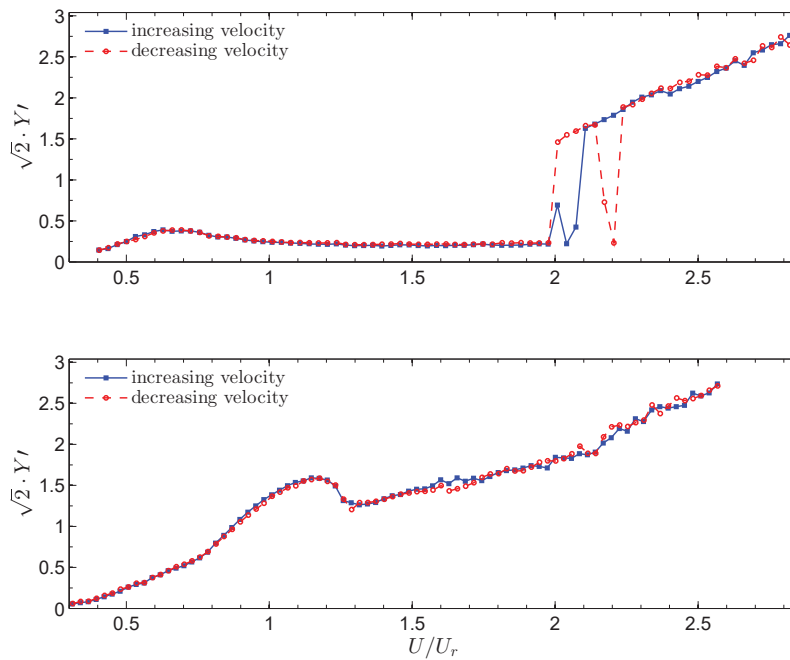


Fig. 6.4 (*top*) Competition zone found during hysteresis tests for D24-W1; (*bottom*) hysteresis test for D37-W1 section.

It is also worth reporting in this paragraph how some additional tests, namely repeatability measurements on the principal test cases (D24/D37-W1), demonstrated that the jump in amplitude suddenly occurred in a variable range of reduced velocities. In practice, once the body overcame the resonance region, the flow may supply a quantum of energy necessary to trigger the instability. From there on, the response shifts to a divergent nature. Moreover, during some tests conducted to verify the presence of an hysteresis in amplitude a , so to say, ‘competition zone’ was found in which the instability occurred for higher velocities with respect to what firstly reported for the same test case. The plot reported in Fig. 6.4.*top* is not relative to hysteresis but those points in the range $2.0 < U/U_r < 2.1$ are falling on two

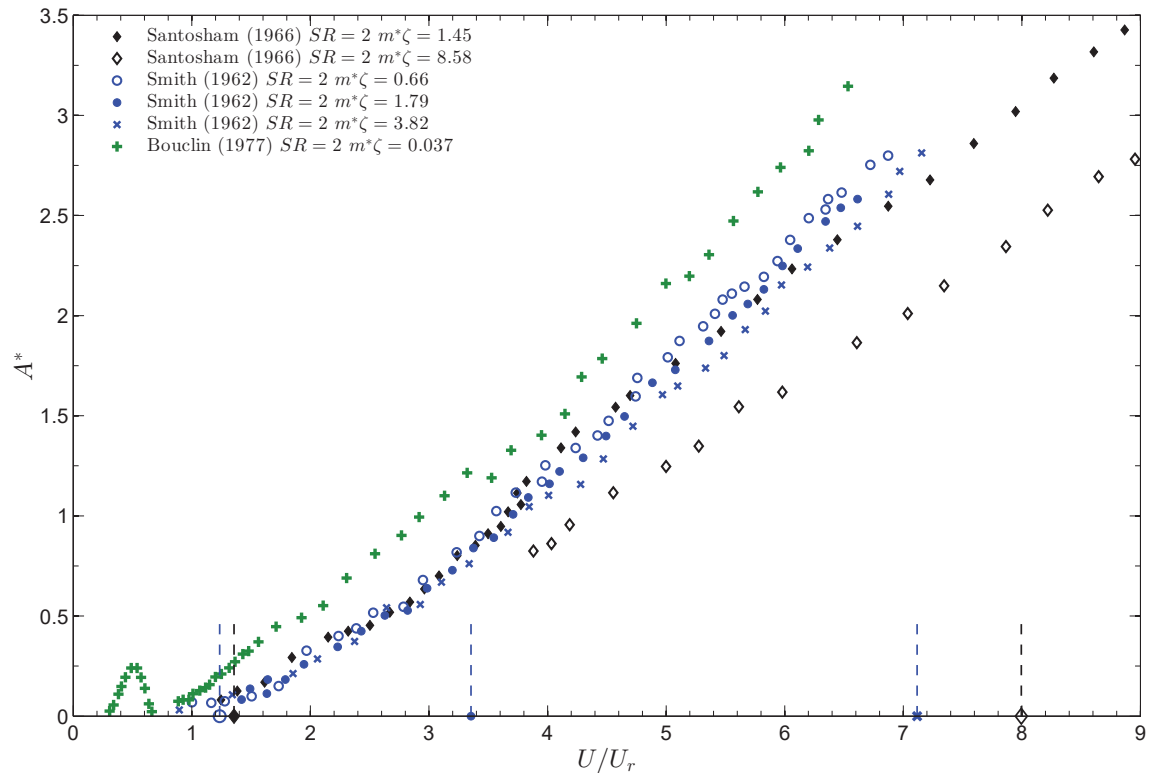


Fig. 6.5 Experimental results from literature in air and water for rectangular cylinder with $SR = 2$. *Air flow*: Santosham (1966) reported $m^* = 2093$ for ζ respectively [\blacklozenge] 0.695 and [\diamond] $4.1 \cdot 10^{-3}$; Smith (1962) gave results for a $m^* = 643$ with ζ respectively [\circ] 1.03 , [\bullet] 2.80 and [\times] $5.94 \cdot 10^{-3}$. With markers and dashed lines [- -] is indicated the relative *QS*-galloping theoretical velocity. *Water flow*: Bouclin (1977) proposed a rectangle having [+] $m^* = 11.52$ with $\zeta = 3.26 \cdot 10^{-3}$.

stable limit cycles, an upper one identified by the main instability branch, and a lower one which is an ideal continuation of the desynchronization branch. Such a behaviour was not observed for D37 section (Fig. 6.4.*bottom*).

The transition from D24-W1 to D24-W7 have already been described in Sec. 4.2.4.3, but it is here interesting to remark the similarity in shape of both the initial unstable branches, starting for the former right after the jump upwards ($0.9 < U/U_r < 1.6$) while just before $U/U_r = 1$ for the latter ($1.65 < U/U_r < 2.2$), which exhibits also a slope approximating the air flow cases.

$SR = 2$ in air and water

The last rectangular cross-section examined in this paragraph is the $SR = 2$. Only literature results can be proposed here as no experimental campaign was performed for such a section in the present work (Fig. 6.5). Santosham's results show the proneness to the instability, as assessed via force measures in his work, and to the interaction VIV-galloping too. Such a behaviour was expected for the $m^*\zeta = 1.45$ case, correspondent to a $\Lambda \simeq 1.35$; on the other hand the apparent proneness to the interaction for the high velocity ratio $\Lambda \simeq 8$ characterizing the $m^*\zeta = 8.58$ case whose response curve presents a minor slope with respect to the the previous test case; however, although the author didn't plot any point for $U/U_r < 4$, so that the instability onset at U_r is only reasonably presumed from the branch slope.

Smith's results are all related to interacting test cases, whose response branches slopes are in good agreement with that of Santosham's $m^*\zeta = 1.45$ test case; note that in calculating the theoretical galloping onset velocity the value given by Santosham $A_1 = 2.239$ was assumed for Smith's rectangle too.

Bouclin's results are reported in the same figure, showing a remarkably similar behaviour to that of D24 model: although the local maximum of super-harmonic resonance is placed at $U/U_r \simeq 0.5$, instead of 0.67 as in both D24-W1 and W7 cases, the modality in which an instability starts just before U_r and after the end of the super-harmonic bell resembles the D24-W7 case, representing in turn the outcome of the mass ratio increasing from D24-W1 situation. Considering also that Bouclin's $SR = 2$ rectangle present a $m^* = 11.52$, and that the previously reported square model cases, Fig. 6.2, whose m^* range from 5.38 to 15.24, it is an author's belief that the link among all these test cases constitutes the missing part in the evolution of the response connected necessarily to mass parameter, in addition to the system damping which is more or less negligible in water flow case. This helps in fully describing the transitions in amplitude response expressible by in stability-prone sections, representing one of the most important achievement in the present dissertation at least from the experimental point of view.

6.2.2 Comprehensive results

Aiming to give an as wider as possible overview it seemed interesting to compare experimental data sets, separately for $SR = 1.5$ and 0.67, with the circular cylinder, plotting together air and water flow measurements proposed in the present work and available in literature. This is interesting for understanding the differences in nondimensional amplitudes reachable in both the flow conditions. The results are reported respectively in Fig. 6.6 and Fig. 6.7; in each figure circular cylinder data, obviously only subject to classical VIV response, are taken from the main reference papers in air flow (Feng, 1968) and water flow (Khalak and Williamson, 1997). In addition, the previously reported data for a square section in water flow are also reported in both figures, while the $SR = 2$ Bouclin's rectangle ($m^* = 11.52$) is only present in Fig. 6.6, practically overlapped to D24-W7 case ($m^* = 9.76$). These data might constitute the elements of what has been indicated, in the present work introduction, as a complete framework.

A couple of remarks can be made by watching the circular cylinder in air and water. Feng's cylinder experiences the onset of the lock-in bell in correspondence of the critical velocity, which is quite steep and narrow by approaching its maximum. On the other hand, it drops down more softly afterwards on the desynchronization branch, giving place to a narrower bell than in water flow case. Khalak's cylinder presents an anticipated onset velocity (around $U/U_r = 0.65$), presenting a local maximum (the so-called *higher branch*) in correspondence of $U/U_r = 1$, and developing a wider response bell represented by the presence of to the *middle branch*. One can attempt to make a parallel with the rectangles situation that could constitute a possible justification for two facts. First, for the onset of the instability of D24-W7 a bit before $U_r = 1$ (Fig. 6.6), as from what would be expected, secondly, for the location of the resonance occurring in D37-W1 and W3 cases (Fig. 6.7), whose onset can be placed in proximity of $U/U_r = 0.5$ to die-out around the critical velocity. In other words, it seems that everything is slightly anticipated in the water flow case. On the

contrary, in air flow, what is supposed to happen at resonance is verified, rather precisely, either for what concern lock-in or in its interaction with galloping.

6.3 Framework for low side ratio rectangular cylinder

It can be said that dealing with the types of interactions treated in the present thesis, it is quite hard to categorize somehow a framework in a fixed scheme, because the uncertainties due to dynamical systems variables often make even the experimental evidences conflicting each other. Ranging from Kármán-vortex shedding and synchronization to galloping, the involved bodies skip through different kind of interactions between these two forms of instability, the former relative to the shear layer the latter of aerodynamic nature and connected to the loss of aerodynamic damping.

It is puzzling indeed to face the problem from different starting points and come to variable conclusions. Let us make an example taking into consideration the velocity ratio as the variable which define the boundary for the interaction occurrence. It has already mentioned in Ch. 2 that *EC 1* (2010) stated that when Λ is either lower than 0.7 or larger than 1.5 the two phenomena can be considered separately. This has been already demonstrated to be dramatically incorrect, nevertheless, as also shown *e.g.* in the results of D30-B1 case or the test case by Smith relative to $m^*\zeta = 1.24$ shown in Fig. 6.2, respectively $\Lambda \simeq 1.24$ and 1.47, for some reasons the interaction may not occurs even if expected as in those cases. Anyway, these observations are relative to the square section, which demonstrated to be generally prone to the interaction (Bearman *et al.*, 1987, Sullivan, 1977, Wawzonek, 1979). However, widening the sight to higher *SR* it can be derived the square section, in particular experimental conditions, to be less prone to the interaction, or even not, particularly by comparing its behaviour with *SR* rectangles such as those reported by Smith (1962) (*SR* = 1, 1.5, 2, 2.5, 3) or Santosham (1966) (*SR* = 2).

Alternatively the mass damping parameter, either $m^*\zeta$ or Sc , could be assumed as the discriminating factor, although it is also linearly dependent on Λ as from Eq. (2.32). Concerning *SR* = 1.5 (Fig. 6.3), present results on D77 indicate that interacting phenomena occur as long as $m^*\zeta \leq 12.42$, while phenomena are separated for $m^*\zeta = 28.47$. Then, values corresponding to the separation of VIV and galloping are respectively 6.5 and 5.1 for D30 and Smith's *SR* = 1.5 rectangle. Conversely, according to Smith's square section results reported in Fig. 6.2, even for relatively low values of $m^*\zeta$ there was no interaction. Instead, for what concerns *SR* = 2 the experimental sets given by Smith and Santosham showed interaction up to a maximum value of the mass-damping parameter of $m^*\zeta = 8.58$.

By considering all the observations above reported, together with the partially satisfying results of the semi-empirical predictive model implemented in Ch. 5, the different nature of the two phenomena does not allow to find a general set of rule to definitively characterize the occurrence and properties, either qualitative and quantitative, of the combined instability treated in the dissertation. It is believed by the author that this is the main reason for the failure of any semi-empirical model for the interaction, that is the intrinsically different physics of the two phenomena. Therefore, further investigations on the vortex structure in the near wake are needed in order to deeper understand its interaction with the shedding pattern when the instability occurs. To this aim flow visualizations or PIV measurements could constitute the appropriate kind of laboratory testing.

6.4 Chapter summary

In the present chapter it has been proposed an as wide as possible overview on the aspects involving low SR rectangular cylinders for which both literature and present experimental evidences demonstrated the possible existence of an articulated system of phenomena, ranging from separated VIV and galloping to their interaction. Different kind of instabilities have been showed to occurs, with different scenarios depending on the fluid density, and not only. The experimental and numerical comparison resulted affected by the partial effectiveness of the latter ones, so that laboratory tests still remain the best way to prevent and preventively assess the response exerted the section investigated.

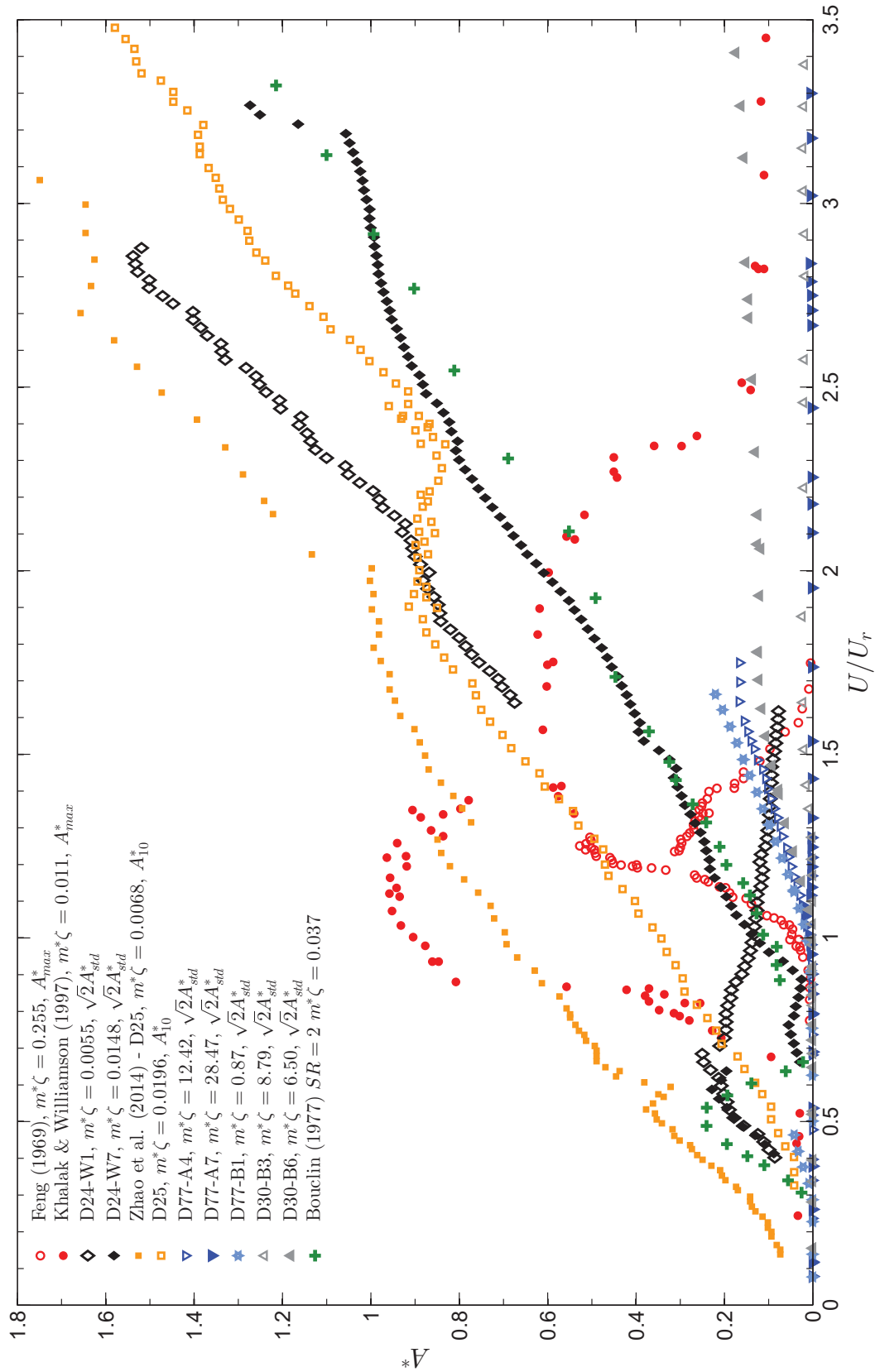


Fig. 6.6 Comprehensive overview of air and water experimental results on rectangular cylinder with $SR = 1.5$. Air flow (Feng (1968) [\bullet] $m^* = 248$ and $\zeta = 0.00103$) and water flow (Khalak and Williamson (1997) [\circ] $m^* = 2.4$ and $\zeta = 0.011$) data on the circular cylinder are superimposed together with Bouclin (1977) $SR = 2$ rectangle of $m^* = 11.52$ [$+$]. For square data the reader can refer to the caption of Fig. 6.2.

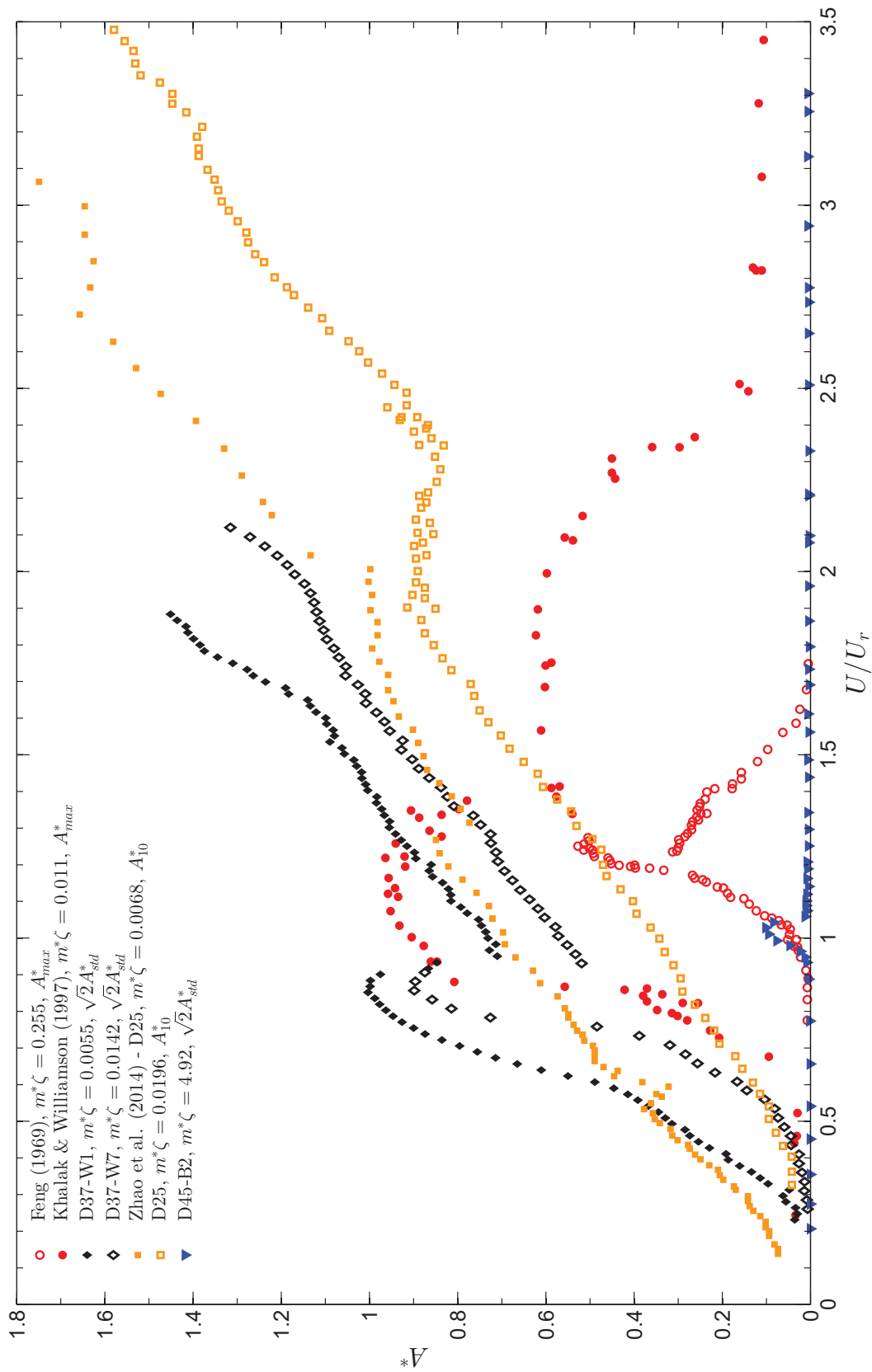


Fig. 6.7 Comprehensive overview of air and water experimental results on rectangular cylinder with $SR = 0.67$. Air flow (Feng (1968) [\bullet] $m^* = 248$ and $\zeta = 0.00103$) and water flow (Khalak and Williamson (1997) [\square] $m^* = 2.4$ and $\zeta = 0.011$) data on the circular cylinder are superimposed. For square data the reader can refer to the caption of Fig. 6.2.

Chapter 7

Conclusions

In the present work the aerodynamics and flow-induced vibrations features of low side ratio rectangular cylinders have been investigated, taking into account air- and water flow regimes, a variety of dynamical configurations in different laboratories and on several sectional models. It will hopefully constitutes a useful dataset in this research field for the scientific community, collocating itself in good agreement with the relative literature and adding some original contributions. Attention has been extensively paid to the mechanism of the interaction between vortex-induced vibrations and galloping, which takes place in particular conditions addressed since the beginning of the work and finally characterized after the evaluation of present results. Although the investigation is unbalanced on the experimental side, the capabilities of numerical predictive models for the interaction have been checked.

7.1 Main contributions of the present work

Original contributions might be summarized as follows.

- i.* **Experimental data set** The investigation of a large variety of sectional models employing several experimental rigs was conducted for different Re conditions and mass/damping factors, allowing to describe the responses of dynamically different structures. Aeroelastic and static tests were conducted on $SR = 1.5, 1$ and 0.67 sections; smooth and turbulent flow regimes were tested in the wind tunnel for two different sectional models.
Concerning water flow measurements, it is worth stressing that such a campaign on these SR has never been conducted, especially for the low mass ratio(s) obtained, whose results integrated previous investigations reported in literature.
- ii.a.* **Peculiar responses (*Air flow*)** In smooth flow different sectional models with equal SR gave different responses: the wooden model (D77) presented a marked proneness to the interaction with unrestrictedly growing amplitudes departing at resonance velocity, and overlapping as long as the two phenomena do not separate each other by increasing a lot the Sc value. It also showed a super-harmonic resonance, already observed in some literature results, only by using a recently designed aeroelastic test rig (F_{d2}), while, unexpectedly, the aluminium model (D30) experienced several forms

of instability, switching from QS ‘classical’ galloping to interaction in a less clear manner, whose causes are still to be understood and currently under investigation.

- ii.b. Peculiar responses (Water flow)* After present water flow experiments the response of a $SR = 1.5$ rectangular cylinder with $m^* = 2.24$, never investigated so far, has been described showing a peculiar transition from VIV to galloping. The peculiar features of its response put in light similarities and differences observed with previous literature results. The mass ratio study conducted on the $SR = 1.5$ underlined the transition of the response from the lower to higher value, being this last one perfectly in line with that one related to a $SR = 2$ rectangle reported in literature (Bouclin, 1977), constituting one of the most interesting findings to the author opinion.
- iii.a. Contrasts with literature (Air flow)* Concerning turbulence flow measurements, it has to be remarked that they put in light an apparent contrast with literature findings (*e.g.* reporting the effect of turbulence integral length scale to be small with respect to a considerable effect of I_u). Present tests showed the dominant effect to be more the integral length scale effect than the turbulence intensity one.
- iii.b. Contrasts with literature (Air- vs. Water flow)* Another interesting achievement arising by comparing air- and water flow results, is the proneness to the instability of $SR = 0.67$ section in water (D37) with respect to the same case in air (D45). Wind tunnel static tests, consistently with aeroelastic ones, asserted it to be a hard-type oscillator, according to quasi-steady theory, meaning the instability needs a very high initial amplitude to be triggered for this section type. Nevertheless, in the water channel experiments static and hydroelastic tests showed D37 model to be unstable already at very low reduced velocities.
- iv. Uncommon tests* Although their general validity and theoretical treatment has still to be addressed, forced rotation experiments on rectangular sections having $SR = 1.5$ and 1 were conducted. The motivation for these tests was the determination of the Magnus-effect parameter involved in Tamura & Shimada model for the interaction. To the author’s knowledge, apart from circular cylinders, such experiment has never been conducted before. As expected, the linear dependency parameter linking Magnus-induced lift and the angular velocity ratio is remarkably higher in the square section, and much more in $SR = 1.5$ one, compared to circular cylinder. Therefore, the mechanism generating the additional lift force is different in sharp-edged bodies, so that one has to be careful in making comparisons.
- v. Unsatisfying results (Numerics)* The probable physical inconsistency in coupling two predictive models for phenomena which are so different in their intrinsic nature has been hypothesized. The numerical integration of Tamura & Shimada model for the interaction is able to predict the onset of the instability and some qualitative features such as the slope of post-critical branch in case the polynomial coefficients, fitting the lateral force coefficient experimental curve, were carefully identified. Nevertheless, it seems to be unable to give a reliable amplitude response prediction, always overestimating the system response at resonance. Concerning simulations performed with water density, numerical problems occurred, whose solution is still under investigation.

7.2 Recommendations for future work and outlooks

In the work lots of efforts were put in providing some more elements for a deeper understanding of the phenomena object of the thesis; nevertheless, some questions still need to be answered and some extra ideas occurred during the research period for which there was no time or the adequate instruments to developed.

- The peculiar behaviour of D30 model needs to be further investigated to fully understand the factors causing such a different response characteristics with respect to D77 model, from the moment that, so far, only a *Re*-effect was hypothesized to be responsible for it.
- A specular campaign, with respect to the mass ratio study in water, employing variable (increasing) damping ratio, that means in turn the *Sc*, *e.g.* by using an eddy currents damper, might be carried out in the wind tunnel; such campaigns were already performed by distinguished authors (Bearman *et al.*, 1987, Smith, 1962).
- In the thesis reference was made to the kink observed in amplitude responses, whose characteristics and effective existence should be assessed relying on force measurements during cylinder motion, or alternatively the sectional model have to be equipped with pressure taps for deriving the aerodynamic forces by integrating surface pressures.
- After the proposed results Tamura & Shimada model implementation, the elaboration of a more reliable model should be undertaken, considering that the coupling of different models demonstrated to be unsatisfying, and always keeping in mind that lots of efforts were already spent form renowned specialists in nonlinear dynamics, meaning that the task will be quite hard to be performed.
- The results of forced-rotation test has to be further understood and developed, formulating also an as adequate as possible theoretical background to support experimental findings.

Appendix A

Aerodynamics characteristics for rectangular sharp edged cross-sections of low side ratio

Here below three different tables reporting the principal aerodynamic features of $SR = 1.5, 1, 2$ reproduced by courtesy of the authors (Mannini *et al.*, 2014b), then, some data has been integrated.

Tab. A.1 Aerodynamic parameters and relative test conditions for the rectangular cylinder with side ratio 3:2. The aspect ratio in case of confined 2D test cases is indicated as ∞ ; in case of 3D prisms I_u and L_u are meant to be measured at the top of tower models; the asterisk * indicates that the numerical value was inferred by the Writers from a published figure; the apex + identifies the results of numerical CFD simulations.

Reference	AR	block.	I_u	L_u/D	$Re \times 10^{-3}$	St	C_D	A_1
	[-]	[%]	[%]	[-]	[-]	[-]	[-]	[-]
Smith (1962)	∞	2.8	< 0.5	-	20.496	0.108	-	2.47 ^a
Nakaguchi <i>et al.</i> (1968)	∞	-	smooth	-	20.0-60.0	0.108	1.65-1.73 ^b	-
Novak and Tanaka (1974)	∞	-	< 1	-	89.0	-	-	1.91
	∞	-	11	1.19	89.0	-	-	1.83
	6.25	-	< 1	-	89.0	-	-	2.6*
	6.25	-	11	1.19	89.0	-	-	stable ^c
Otsuki <i>et al.</i> (1974)	∞	-	< 1	-	20-330.0	0.100	-	-
Washizu <i>et al.</i> (1978)	∞	5.5	0.3	-	-	0.100	-	-
Courchesne and Laneville (1979)	∞	-	smooth	-	-	-	1.8	-
Bokaian and Geoola (1983)	∞	3.2	6.5	1.6	3.3	0.105	-	3.09*
	∞	3.1	11.9	0.8	3.3	0.105	-	stable
Okajima <i>et al.</i> (1982)	∞	-	<0.5	-	6.0	0.109	-	-
ECCS (1987)	∞	-	smooth	-	-	0.102	-	1.91
	∞	-	10	-	-	-	-	1.8 3
	∞	-	20	-	-	-	-	stable
Norberg (1993)	∞	< 5.0	< 0.06	-	1.0	0.105	1.70 ^d	-
	∞	< 5.0	< 0.06	-	5.0	0.115	-	-
Haaker and vanOudheusden (1997)	∞	-	-	-	-	-	-	5.37 ^b
Robertson <i>et al.</i> (2003) ⁺	∞	-	smooth	-	0.250	0.158	-	5.44
EC 1 (2010)	∞	-	-	-	-	0.09	-	1.7
Borri <i>et al.</i> (2012)	∞	-	smooth	-	-	0.110/0.100 ^e	1.18/1.35 ^e	1.26/1.99 ^e
Mannini <i>et al.</i> (2014b)	∞	4.8	~1	-	64.0	0.106	1.73	4.9
	∞	4.8	~1	-	90.0	0.106	1.76	5.7

^a deduced from the value of Λ reported in Parkinson and Wawzonek (1981).

^b value corresponding to a section with $B/D = 1.60$.

^c turbulence generated by mesh grid.

^d value corresponding to a section with $B/D = 1.62$ for a $Re = 1300$.

^e values corresponding respectively to sections with $B/D = 1.25$ and 1.31 .

Tab. A.2 Aerodynamic parameters and relative test conditions for the square cylinder.
See also caption of Tab. A.1

Reference	L/D	block.	I_u	L_u/D	$Re \times 10^{-3}$	St	C_D	A_1
	[-]	[%]	[%]	[-]	[-]	[-]	[-]	[-]
Brooks (1960)	∞	5.5	< 0.5	-	66.0 ^a	0.130	2.29	3.11 ^a (3.0 ^b)
	∞	2.8	< 0.5	-	22.3	0.135	-	2.69 ^c
Smith (1962)	∞	2.8	< 0.5	-	22.3	-	-	2.54 [*] (2.72 ^b)
	∞	2.8	< 0.5	-	27.3	-	-	2.60 [*]
	∞	2.8	< 0.5	-	33.1	-	-	2.40 [*]
	∞	2.8	< 0.5	-	36.0	-	-	2.26 [*]
Heine (1964)	∞	-	smooth	-	20.0-100.0	0.12	-	-
	∞	5.4	6.7	1.34	31-33.0 ^d	-	1.81 ^e	3.30 [*] (3.19 ^b)
Laneville (1973)	∞	5.4	9.1	1.25	31-33.0 ^d	-	1.59 ^e	3.01 [*] (3.19 ^b)
	∞	5.4	12.5	1.08	31-33.0 ^d	-	1.35 ^e	3.72 [*] (3.49 ^b)
	∞	5.4	12.7	2.15	31-33.0 ^d	-	1.50 ^e	2.44 [*] (2.62 ^b)
Nakamura and Mizota (1975a;b)	∞	-	smooth	-	70-100.0	0.125	2.27	3.82 [*]
Mukhopadhyay and Dugundji (1976)	123	-	smooth	-	1.8	-	-	0.65 [*]
	123	-	smooth	-	3.1	-	-	0.89 [*]
	100	-	smooth	-	3.0	-	-	1.51 [*]
Nakamura and Tamonari (1977)	∞	2.5	0.1	-	-	-	-	3.98 [*]
	∞	2.5	0.1	-	70.0	-	-	4.01 ^{*f}
	∞	2.5	0.1	-	100.0	-	-	4.29 ^{*f}
	∞	2.5	12	-	70.0	-	-	4.23 ^{*f}
	∞	2.5	12	-	100.0	-	-	3.61 ^{*f}
	6	2.0	smooth	-	35.0	-	-	0.63 [*]
Sullivan (1977)	12	2.0	smooth	-	35.0	-	-	stable
	13	2.0	smooth	-	35.0	-	-	0.39 [*]
	6	2.0	13 ^g	5.7-6.1 ^h	40.0	-	-	1.65 [*]
	8	2.0	10.5 ^g	5.7-6.1 ^h	40.0	-	-	2.05 [*]
	10	2.0	9 ^g	5.7-6.1 ^h	40.0	-	-	1.65 [*]
	14	2.0	5 ^g	5.7-6.1 ^h	40.0	-	-	1.29 [*]
	∞	3.6	< 0.1	-	8.8	-	-	3.85
Wawzonek (1979)	∞	3.6	< 0.1	-	12.4	-	-	3.70
	∞	3.6	< 0.1	-	28.8	-	-	2.88
	18	1.5	1	-	-	-	-	1.03 [*]
Kwok and Melbourne (1980)	18	1.5	7 ^{g,l}	9	-	-	-	1.51 [*]
	18	1.5	9 ^{g,l}	0.53	-	-	-	3.85 [*]
	∞	-	-	-	-	0.125	-	-
Miyata <i>et al.</i> (1983)	∞	3.3	6.5	1.6	8.0	0.125	-	2.50 [*]
Bokaian and Geoola (1983)	∞	6.9	< 0.5	-	650.0	0.121	2.15	2.20
Schewe (1984)	∞	6.9	< 0.5	-	2700.0	0.121	2.16	1.97
Bearman <i>et al.</i> (1987)	∞	4.2	< 0.5	-	140.0	0.133	-	5.4 (4.3 ⁱ)
	∞	4.2	6.5	1.3	140.0	-	-	3.9 (4.0 ⁱ)
	∞	4.2	10.5	1.3	140.0	-	-	3.4 (2.9 ⁱ)
ECCS (1987)	∞	-	smooth	-	-	0.120	-	2.7
	∞	-	10	-	-	-	-	2.6
	∞	-	20	-	-	-	-	1.5
Luo and Bearman (1990)	∞	5.5	0.05	-	22.6	-	-	3.52 [*] (3.86 ^m)
	∞	5.5	0.05	-	46.0	-	-	4.14 [*]
	∞	5.5	0.05	-	66.0	-	-	3.69 [*]
Knisely (1990)	∞	7.5	< 0.5	-	22-62.0	0.129	2.02	3.97 [*]
Norberg (1993)	∞	< 5.0	< 0.06	-	5.0	0.129	2.21	3.73 (3.62 [*])
	∞	< 5.0	< 0.06	-	13.0	0.132	2.16	4.68 (4.44 [*])
Luo <i>et al.</i> (1994)	∞	5.0	< 0.5	-	34.0	0.130	2.2	2.05
Ruscheweyh <i>et al.</i> (1996)	∞	-	2	-	-	-	-	1.28 [*]
Robertson <i>et al.</i> (2003) ⁺	∞	-	smooth	-	0.250	-	-	2.69
EC 1 (2010)	∞	-	-	-	-	0.12	-	1.2
Borri <i>et al.</i> (2012)	∞	-	smooth	-	-	0.120	1.38	1.128
Joly <i>et al.</i> (2012) ⁺	∞	-	smooth	-	0.200	0.151	1.44	1.78

^a reported in Parkinson and Brooks (1961)

^b value also estimated by Wawzonek (1979) from the graph

^c reported in Parkinson and Smith (1964)

^d reported in Laneville and Parkinson (1971)

^e $Re \approx 70,000$

^f based on free vibrations

^g at the top of the model

^h at 6.7D and 8.3D, respectively, over the test section floor

ⁱ by using the method proposed by Nakamura and Tamonari (1977)

^l turbulence generated by a rod placed upstream of the model

^m value assumed in their calculations

Tab. A.3 Aerodynamic parameters and relative test conditions for the rectangular cylinder with side ratio 2:1. See also caption of Tab. A.1

Reference	L/D [-]	block. [%]	I_u [%]	L_u/D [-]	$Re \times 10^{-3}$ [-]	St [-]	C_D [-]	A_1 [-]
Brooks (1960)	∞	2.8	<0.5	-	33.0 ^a	0.079 ^b	1.53	3.23*
Santosham (1966)	∞	2.6	<0.1	-	20.4	-	1.53	2.33
	∞	2.6	<0.1	-	20.4	0.083 ^c	1.53	3.85* (4 ^c)
	∞	2.6	<0.1	-	32.5	0.083 ^c	1.52	3.2 ^c
	∞	2.6	<0.1	-	38.0	0.083 ^c	1.49	2.94* (2.95 ^c)
Heine (1964)	∞	-	smooth	-	13.0-80.0	0.081	-	-
Nakaguchi <i>et al.</i> (1968)	∞	-	smooth	-	20.0-60.0	0.085	1.46-1.54	-
Novak (1972)	6.9	-	smooth	-	47.3	0.081 ^d	-	3.78*
	6.9	-	5	-	47.3	-	-	2.96*
	6.9	-	8.5	-	47.3	-	-	stable
	6.9	-	11	-	47.3	-	-	stable
Laneville (1973)	∞	2.6	6.7	2.78	15-16.0	-	1.21 ^c	6.27*
	∞	2.6	9.1	2.59	15-16.0	-	1.08	4.42*
	∞	2.6	12.5	2.23	15-16.0	-	0.98	stable
	∞	2.6	12.7	4.46	15-16.0	-	1.11	stable
Nakamura and Mizota (1975b)	∞	-	smooth	-	-	0.083	1.69	6.1*
Washizu <i>et al.</i> (1978)	∞	5.5	0.3	-	-	0.077	1.48	4.71
	∞	5.5	0.3	-	-	0.077	1.48	3.86*
Bokaian and Geoola (1983)	∞	3.1	6.5	1.6	5.0	-	-	stable
Miyata <i>et al.</i> (1983)	∞	-	-	-	-	0.083	-	-
Okajima <i>et al.</i> (1982)	∞	-	<0.5	-	20.0	0.076-0.079	-	-
Bokaian and Geoola (1985)	∞	6.5	6.5	0.82	5-9.0	-	-	stable
	∞	6.5	11.9	0.41	5-9.0	-	-	0.679
ECCS (1987)	∞	-	smooth	-	-	0.085	-	2.8
	∞	-	10	-	-	-	-	stable
	∞	-	20	-	-	-	-	stable
Ruscheweyh <i>et al.</i> (1996)	∞	-	2	-	-	-	-	4.31*
Deniz and Staubli (1997)	∞	-	smooth	-	32.0	0.087	1.40	7.19
	∞	-	smooth	-	48.0	0.089	1.38	7.82
	∞	-	smooth	-	80.0	0.088	1.26	5.92
Itoh and Tamura (2002)	∞	5	<0.5	-	3.7-37	0.078	-	-
Robertson <i>et al.</i> (2003) ⁺	∞	-	smooth	-	0.250	-	-	1.60
EC 1 (2010)	∞	-	-	-	-	0.06	-	2.0
Hansen (2013)	∞	-	2	-	-	0.066	1.4	8.6

^a reported in Parkinson and Brooks (1961)^b for a Re of 19,000^c reported in Wawzonek (1979)^d reported in Novak (1971) for Re of 31,500 and 63,000^e Detected from graphical results

Appendix B

Instrumentation technical characteristics

Property	involved force component	spec
Sensor type	-	Axial force (tens./compr.) sensor
Model	-	S2M
Mass (with cable)	m	500 [g]
Accuracy		
Repeatability error	b_{rg}	0.02 [%]
Relative reversibility error	v	0.02 [%]
Nonlinearity	d_{lin}	0.02 [%]
Relative creep over 30 min.	$d_{cr, F+E}$	0.02 [%]
Relative reversibility error	v	0.02 [%]
Effect of temp. on sensitivity	TK_C	0.02 [%/10K]
Effect of temp. on zero-signal	TK_0	0.02 [%/10K]
Electrical characteristic values		
Nominal (rated) sensitivity	C_{norm}	2 [mV/V]
Relative zero-signal error	$d_{S,0}$	5 [%]
Relative sensitivity error	d_c	0.25 [%]
Rel. tens./compr. sensitivity variation	d_{ZD}	0.1 [%]
Input resistance	R_i	> 345 [Ω]
Output resistance	R_o	350 \pm 50 [Ω]
Insulation resistance	R_{is}	> 2 [G Ω]
Operating range of excit. voltage	B_{UG}	0.5 ... 12 [V]
Reference excitation voltage	U_{ref}	5 [V]
Connection	-	six-wire circuit
Temperature		
Nominal (rated) temperature range	$B_{(T,norm)}$	-10° \div +45° [$^{\circ}C$]
Operating temperature range	$B_{(T,G)}$	-10° \div +70° [$^{\circ}C$]
Storage temperature range	$B_{(T,S)}$	-10° \div +85° [$^{\circ}C$]
Mechanical characteristic quantities		
Max. operating force	F_G	150% FS [N]
Limit force	F_L	1000% FS [N]
Breaking force	F_B	1000% FS [N]
Limit torque	M_L	28 [Nm]
Limit bending moment	$M_{b, perm}$	50 [Nm]
Static lateral limit force	F_Q	100 [% of F_{norm}]
Nominal (rated) displacement	s_{norm}	0.15 [mm]
Fundamental resonance frequency	f_G	358 [Hz]
Relative permissible oscillatory stress	F_{rb}	140 [% of F_{norm}]

Tab. B.1 Technical specifications of the HBM S2M load cell employed in B_s static tests

Property	involved force component	spec
Sensor type	-	Axial force (tens./compr.) sensor
Model	-	535 QD
Width	-	76 [mm]
Height	-	56 [mm]
Thickness	-	29 [mm]
Measuring range	-	$\pm 0 \div 6 - 12 - 25$ FS [kg]
Maximum error (non-linearity + hysteresis + + temperature effect on sensitivity)	d_{lin}	C3 = 3000 intervals: $< \pm 0.023\%$ FS [kg]
Safe load limit	$F_{o,x}$	$\pm 50\%$ FS [kg]
Ultimate load limit	$F_{U,x}$	≈ 3 times FS [kg]
Repeatability error	e_r	$< \pm 0.033\%$ FS [kg]
Sensitivity	S_F	2 [mV/V]
Zero unbalance	F_Z	$< \pm 2\%$ FS [kg]
Bridge impedance	I_{br}	350, typical [Ω]
Insulation resistance	R_{iS}	> 5000 [M Ω]
Temperature limit (compensated)	T_c	$-10^\circ \div +40^\circ$ [$^\circ C$]
Temperature limit (operating)	T_o	$-15^\circ \div +75^\circ$ [$^\circ C$]

Tab. B.2 Technical specifications of the ES Europe 535 QD load cell employed in F_{s1} static tests



Fig. B.1 Picture of the HBM S2M force sensor.



Fig. B.2 Picture of the ES Europe 535 QD force sensor.

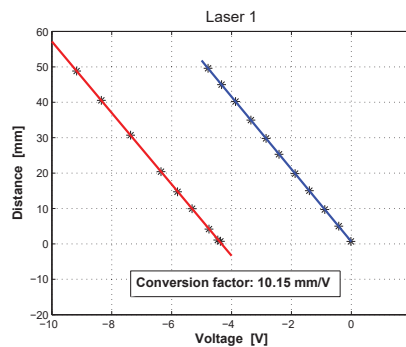


Fig. B.3 (left) View of a laser triangulator device for displacement measurement; (right) Relationship between laser output voltage and actual object distance. [reproduced from Mannini (2006)]

Property	involved force component	spec
Sensor type	-	Force sensor
Model	-	FT-Delta
Mass	-	913 [g]
Diameter	-	94.5 [mm]
Height	-	33.3 [mm]
Measuring range	F_x, F_y	± 165 [N]
"	F_z	± 495 [N]
"	M_x, M_y, M_z	± 15 [Nm]
Resolution	F_x, F_y	$\pm 1/128$ [N]
"	F_z	$\pm 1/64$ [N]
"	M_x, M_y, M_z	$\pm 1/2112$ [Nm]
Overload	F_{xy}	± 13500 [N]
"	F_z	± 11900 [N]
"	T_{xy}	± 230 [Nm]
"	T_z	± 420 [Nm]
Rigidity	KF_x, KF_y	$37 \cdot 10^6$ [N]
"	KF_z	$61 \cdot 10^6$ [N]
"	KM_x, KM_y	$52 \cdot 10^6$ [Nm]
"	KM_z	$94 \cdot 10^6$ [Nm]
Resonance frequency	F_x, F_y, M_z	1.5 [kHz]
"	M_x, M_y, F_z	1.7 [kHz]
Max load	F_{xy}	± 660 [N]
Max bending moment	M_{xy}	± 60 [Nm]

Tab. B.3 Technical specifications of the ATI Model FT-Delta force balance employed in F_{s2} static tests

Property	spec
Sensor type	Laser-sensor
Model	LD 1605
Type	200
Measuring range	± 100 [mm]
Stand-off midrange	340 [mm]
Non-linearity $\leq \pm 0.3$ % d.M.	600 [μ m]
Resolution (noise) static	60 [mm]
Measuring spot dia. midrange	2 [mm]
Light source (laser)	1 [mW]
Wavelength	red 675 [nm]
Sampling frequency	600 40 [kHz]
Laser class	2
Analogical Input	
Displacement	± 10 [V]
Output impedance	≈ 0 [Ω] (10 [mA] max.)
Angle dependence	≈ 0.5 % when turning $\pm 30^\circ$ about long.axis
Rise time	0.1/0.2/2 or 20 [ms] selectable
Frequency response	10 [kHz] , 3 [kHz] , 250 [Hz] or 25 [Hz]
Temperature stability	0.03 [% / $^\circ$ K]
Intensity of reflecting light	1 to 10 [V/max]; 0 to +13 [V]
Permissible ambient light	20000 [Lux]
Life time	50000 [h] for laser-diode
Insulation	200 [VDC, 0 [V] against housing
Max. vibration	10 [g] to 1 [kHz]
Operation temperature	0 to 50 [$^\circ$ C]

Tab. B.4 Technical specifications of the Micro-epsilon Model OptoNCDT-1605/200 laser employed in F_{d1} and F_{d2} dynamic test rig

Appendix C

Hydroelastic tests' extensive results

Angle of attack study results

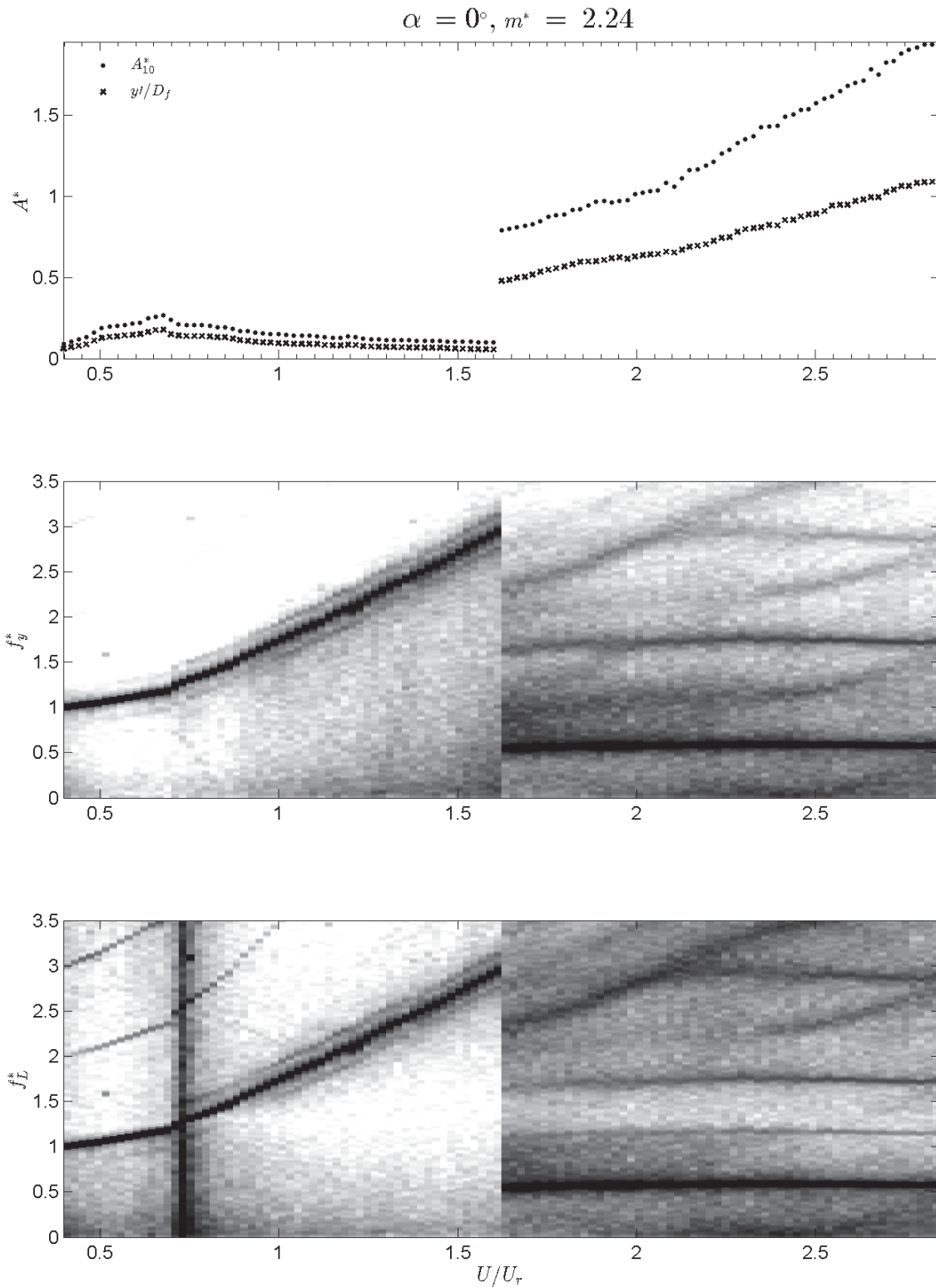


Fig. C.1 Angle of attack's study for $m^* = 2.24$: nondimensional amplitude, oscillation and lift frequencies vs. reduced velocity with respect to resonance one, for $\alpha = 0^\circ$ ($SR = 1.5$).

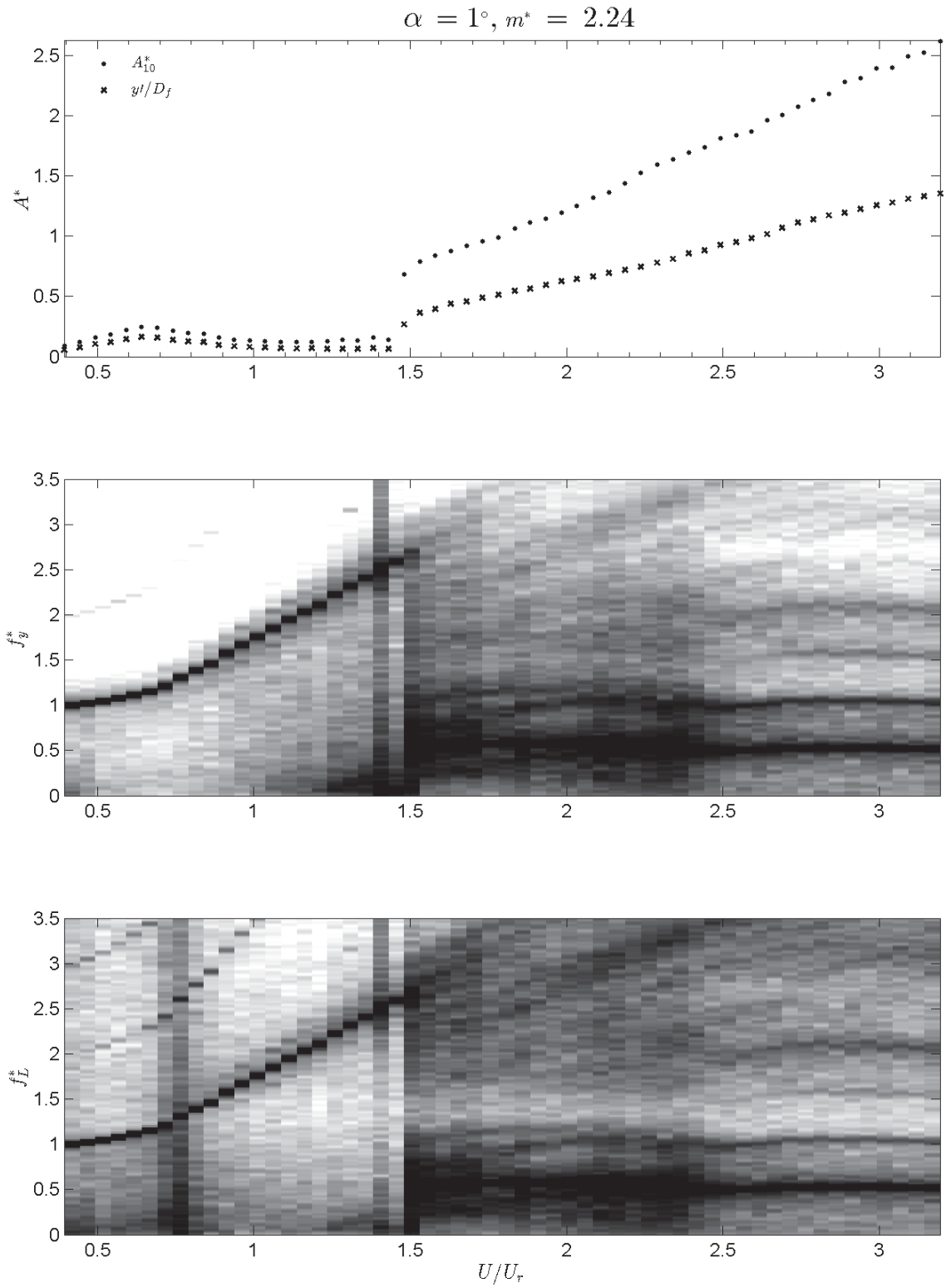


Fig. C.2 Angle of attack's study for $m^* = 2.24$: nondimensional amplitude, oscillation and lift frequencies vs. reduced velocity with respect to resonance one, for $\alpha = 1^\circ$.

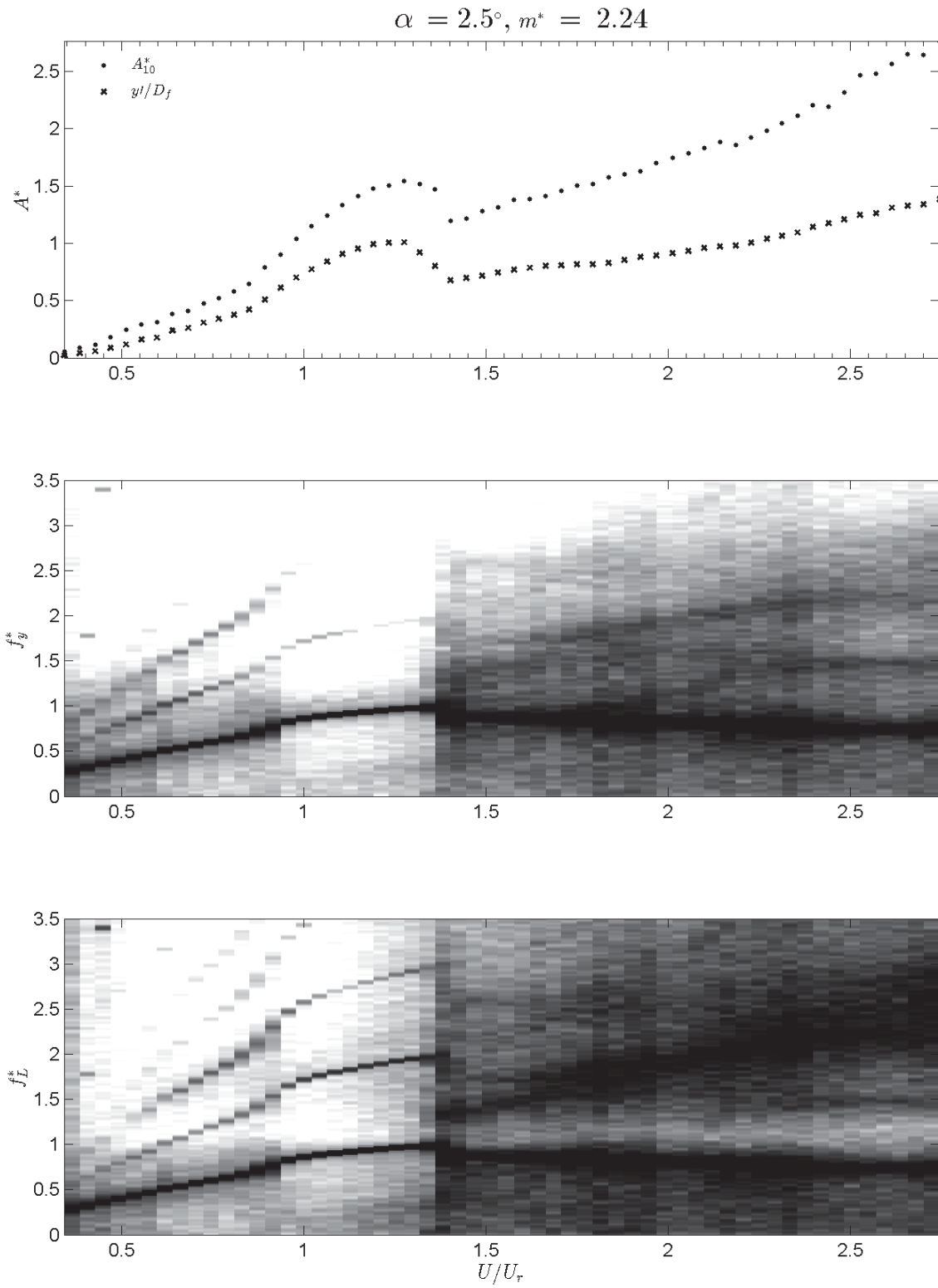


Fig. C.3 Angle of attack's study for $m^* = 2.24$: nondimensional amplitude, oscillation and lift frequencies vs. reduced velocity with respect to resonance one, for $\alpha = 2.5^\circ$.

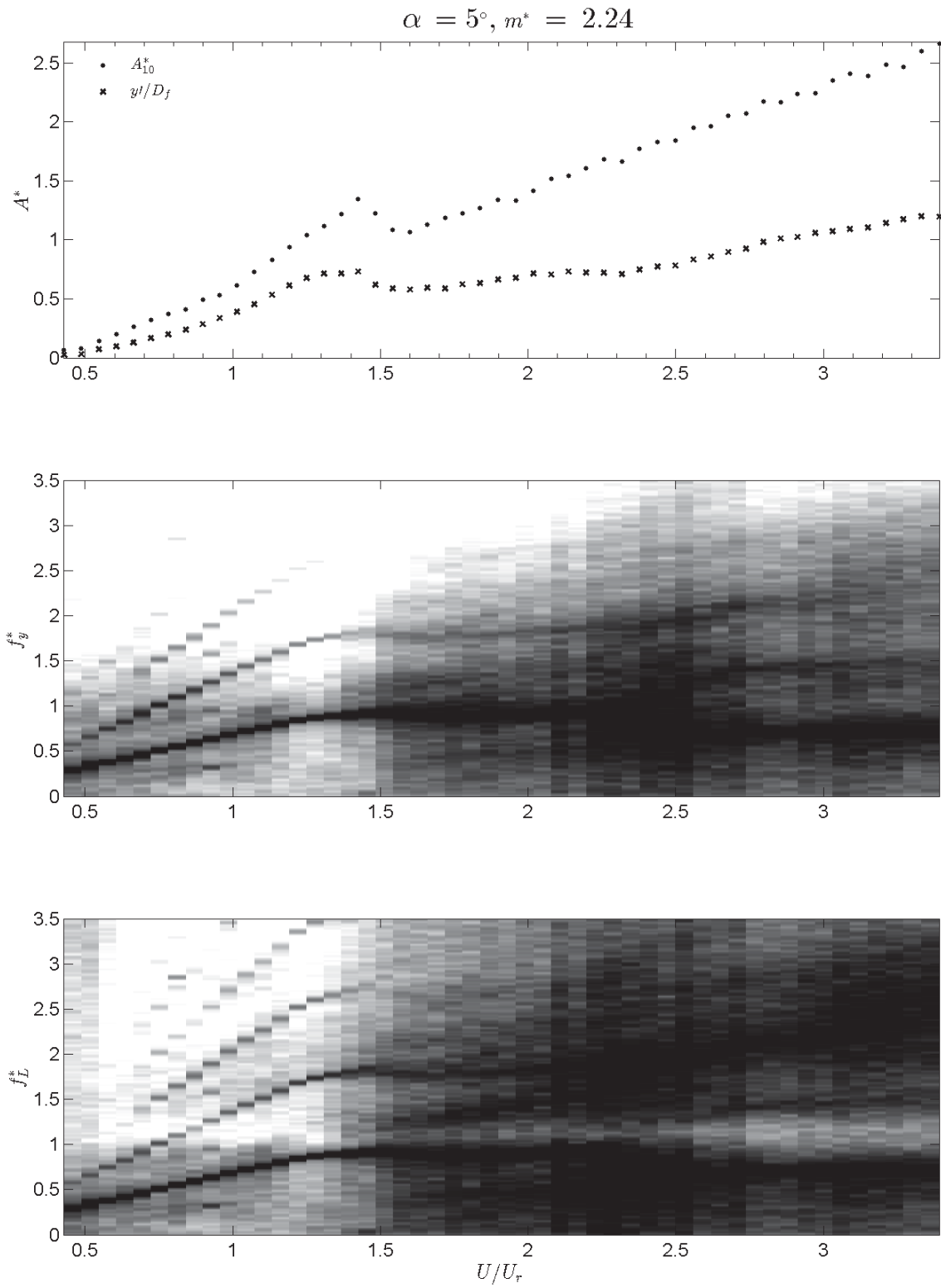


Fig. C.4 Angle of attack's study for $m^* = 2.24$: nondimensional amplitude, oscillation and lift frequencies vs. reduced velocity with respect to resonance one, for $\alpha = 5^\circ$.

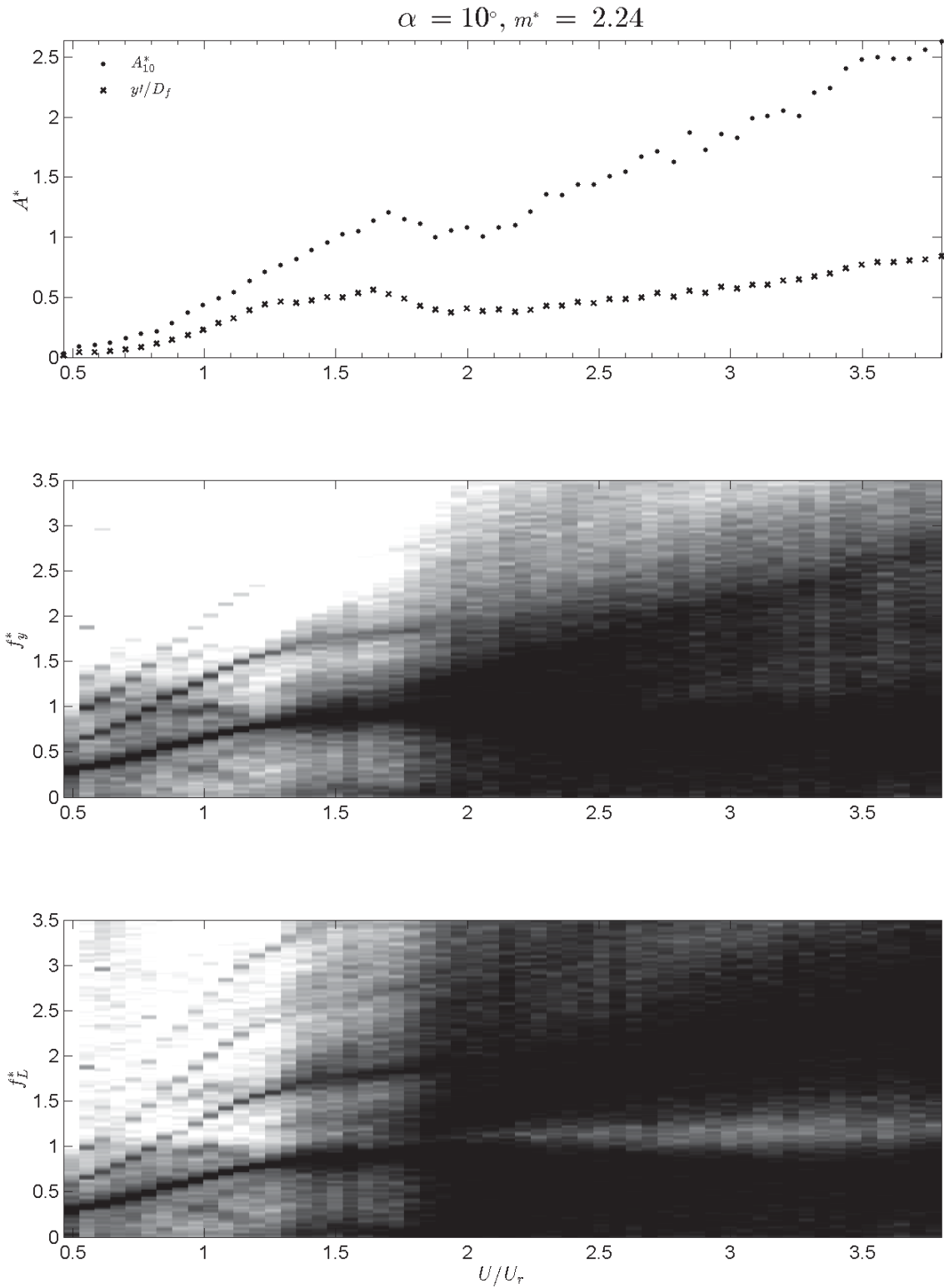


Fig. C.5 Angle of attack's study for $m^* = 2.24$: nondimensional amplitude, oscillation and lift frequencies vs. reduced velocity with respect to resonance one, for $\alpha = 10^\circ$.

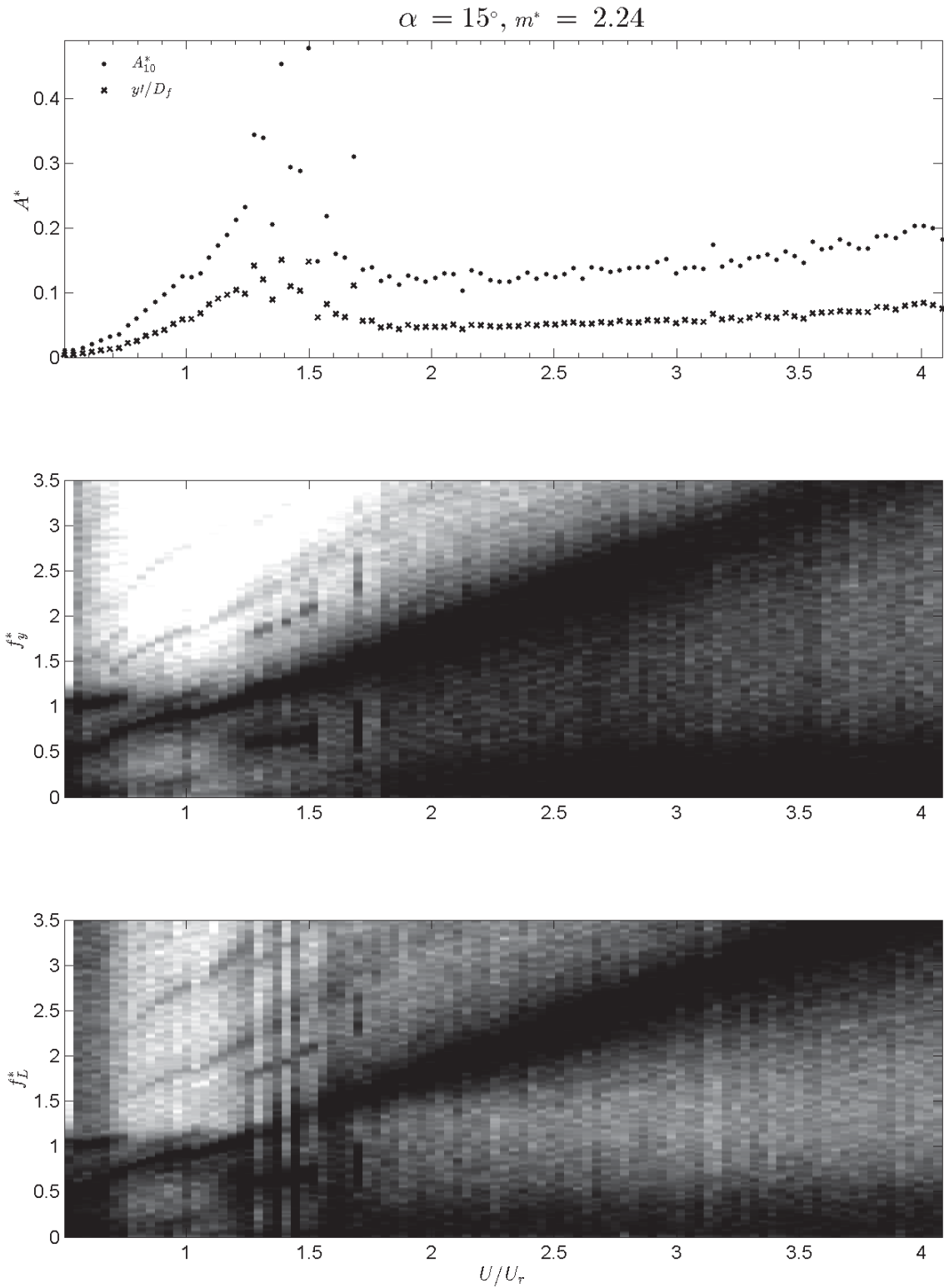


Fig. C.6 Angle of attack's study for $m^* = 2.24$: nondimensional amplitude, oscillation and lift frequencies vs. reduced velocity with respect to resonance one, for $\alpha = 15^\circ$.

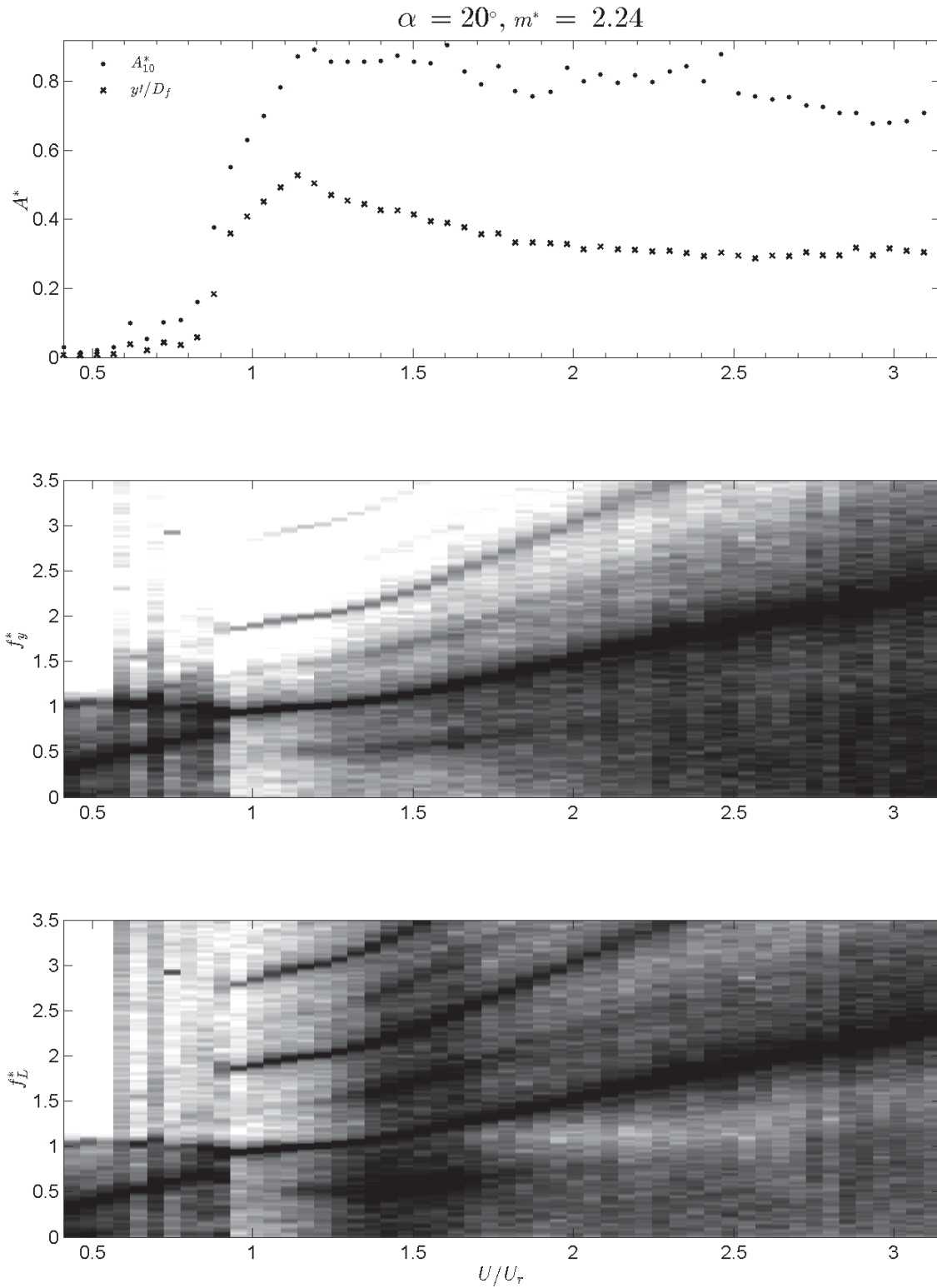


Fig. C.7 Angle of attack's study for $m^* = 2.24$: nondimensional amplitude, oscillation and lift frequencies vs. reduced velocity with respect to resonance one, for $\alpha = 20^\circ$.

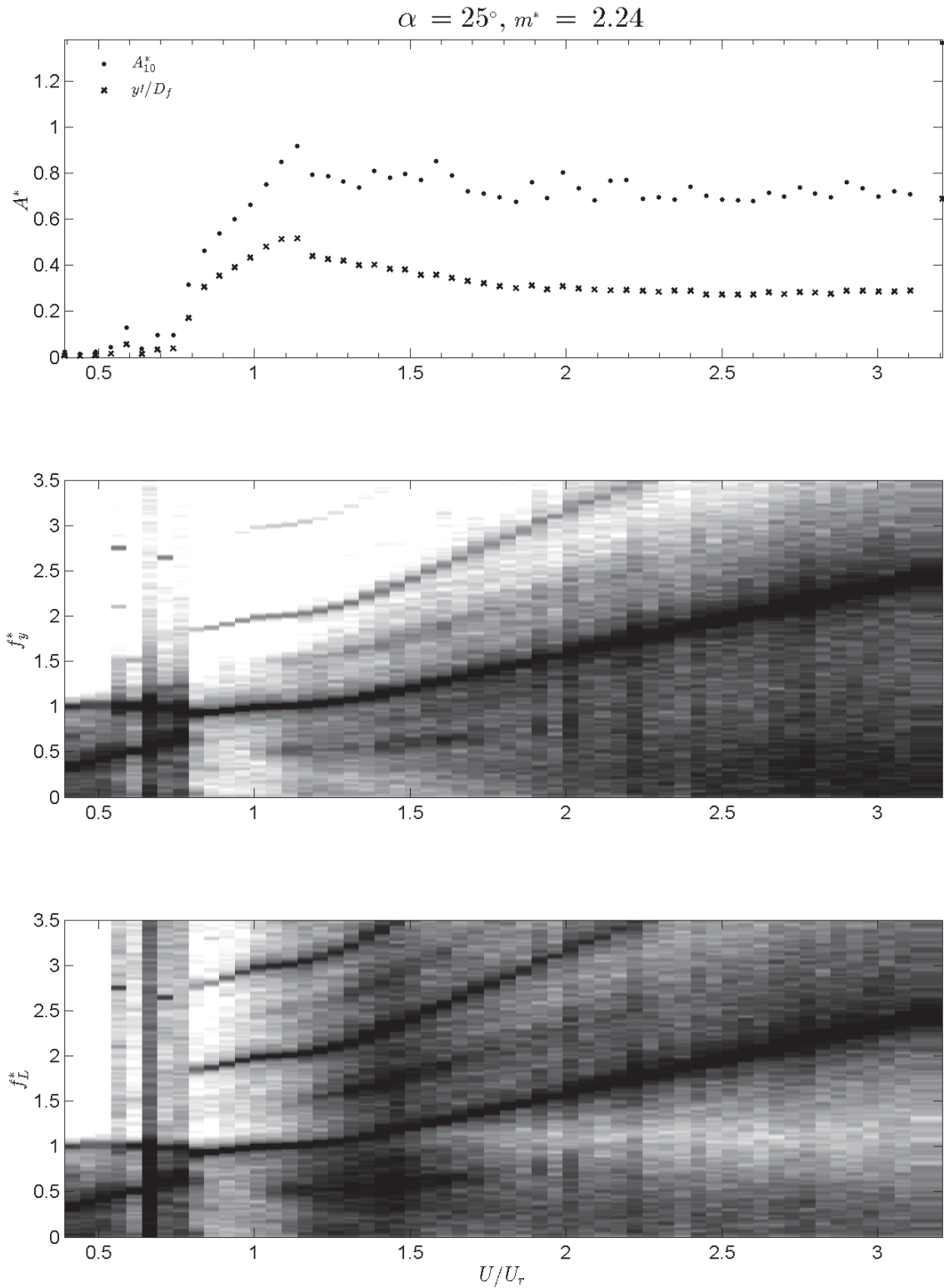


Fig. C.8 Angle of attack's study for $m^* = 2.24$: nondimensional amplitude, oscillation and lift frequencies vs. reduced velocity with respect to resonance one, for $\alpha = 25^\circ$.

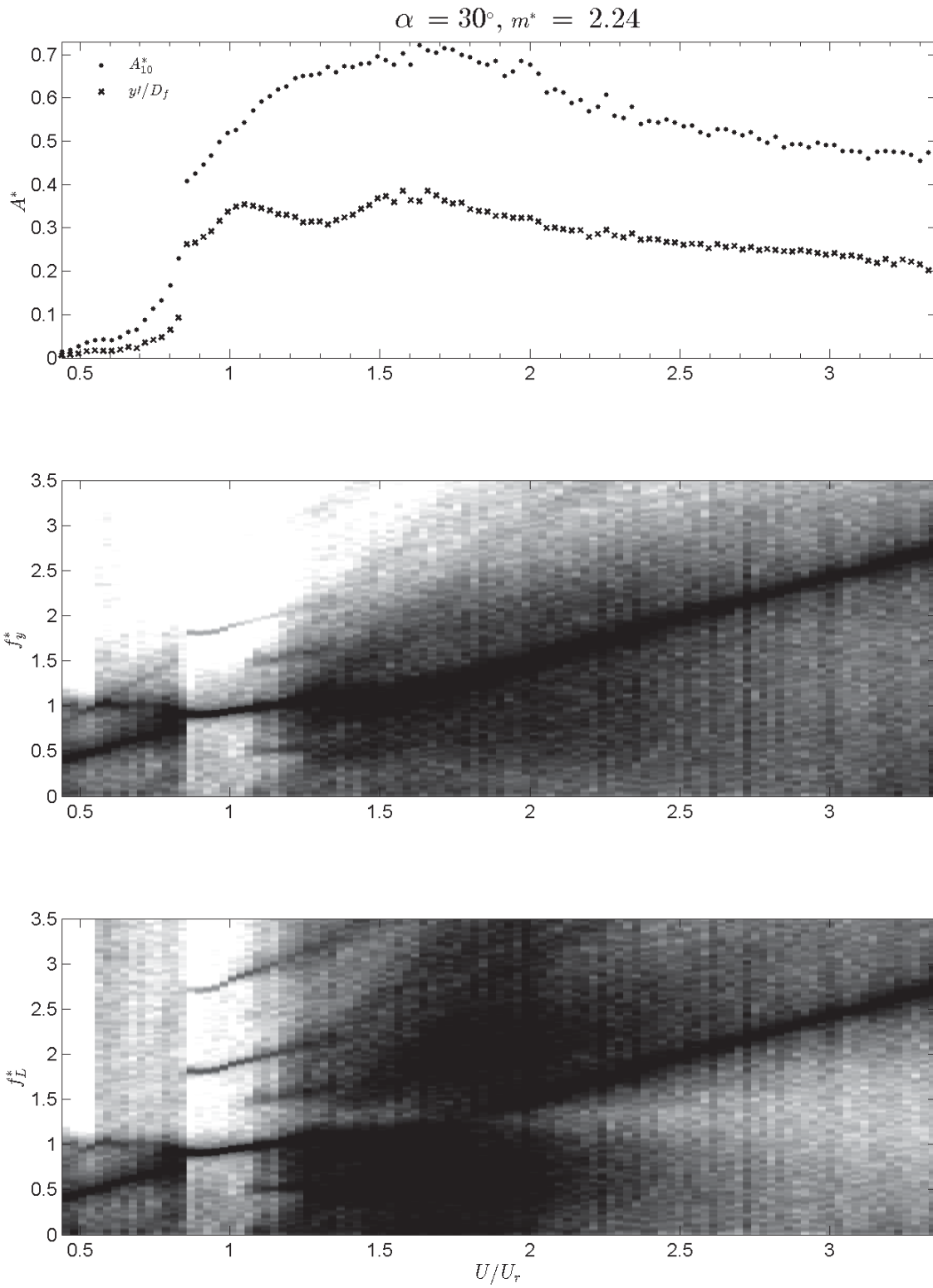


Fig. C.9 Angle of attack's study for $m^* = 2.24$: nondimensional amplitude, oscillation and lift frequencies vs. reduced velocity with respect to resonance one, for $\alpha = 30^\circ$.

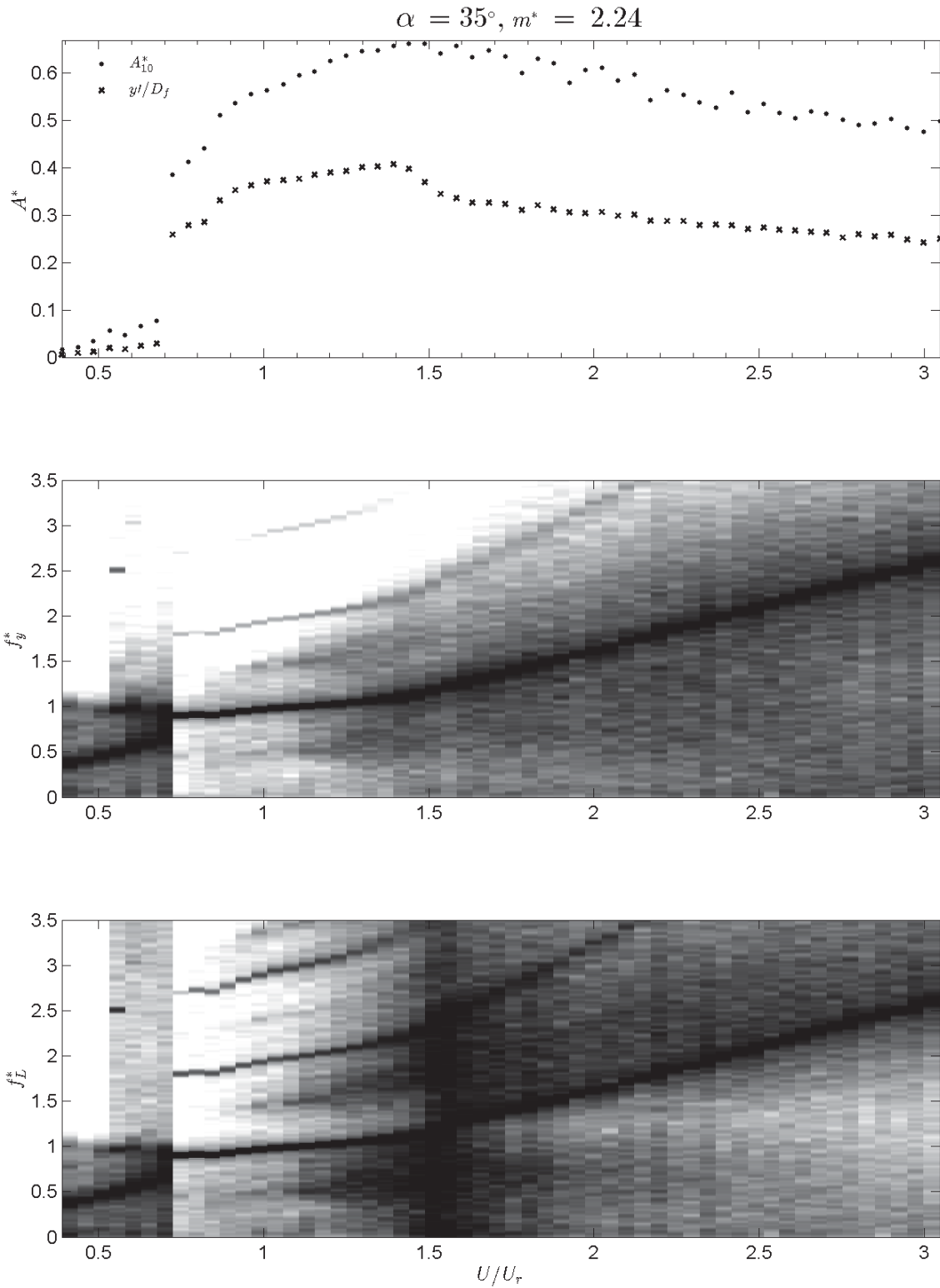


Fig. C.10 Angle of attack's study for $m^* = 2.24$: nondimensional amplitude, oscillation and lift frequencies vs. reduced velocity with respect to resonance one, for $\alpha = 35^\circ$.

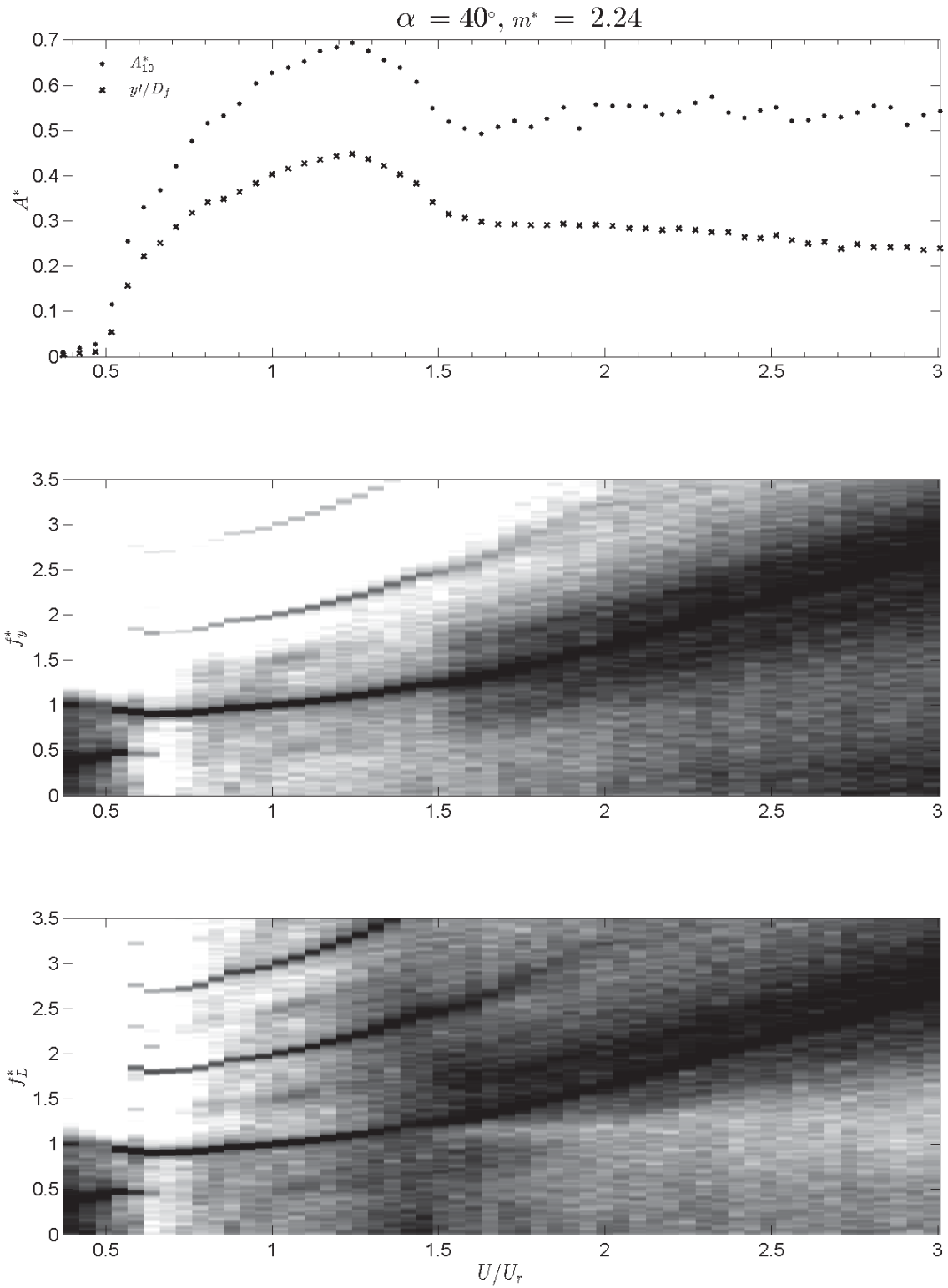


Fig. C.11 Angle of attack's study for $m^* = 2.24$: nondimensional amplitude, oscillation and lift frequencies vs. reduced velocity with respect to resonance one, for $\alpha = 40^\circ$.

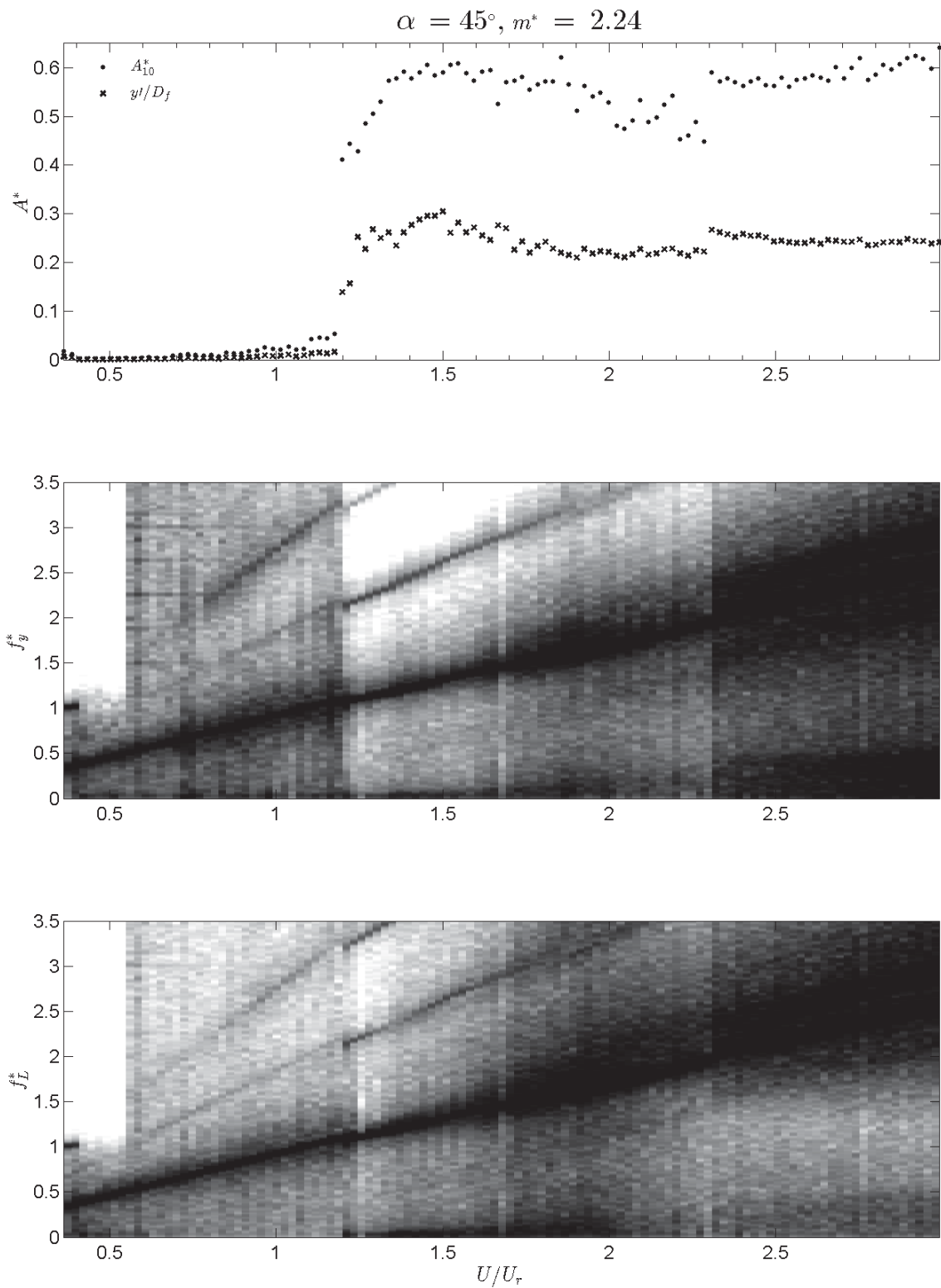


Fig. C.12 Angle of attack's study for $m^* = 2.24$: nondimensional amplitude, oscillation and lift frequencies vs. reduced velocity with respect to resonance one, for $\alpha = 45^\circ$.

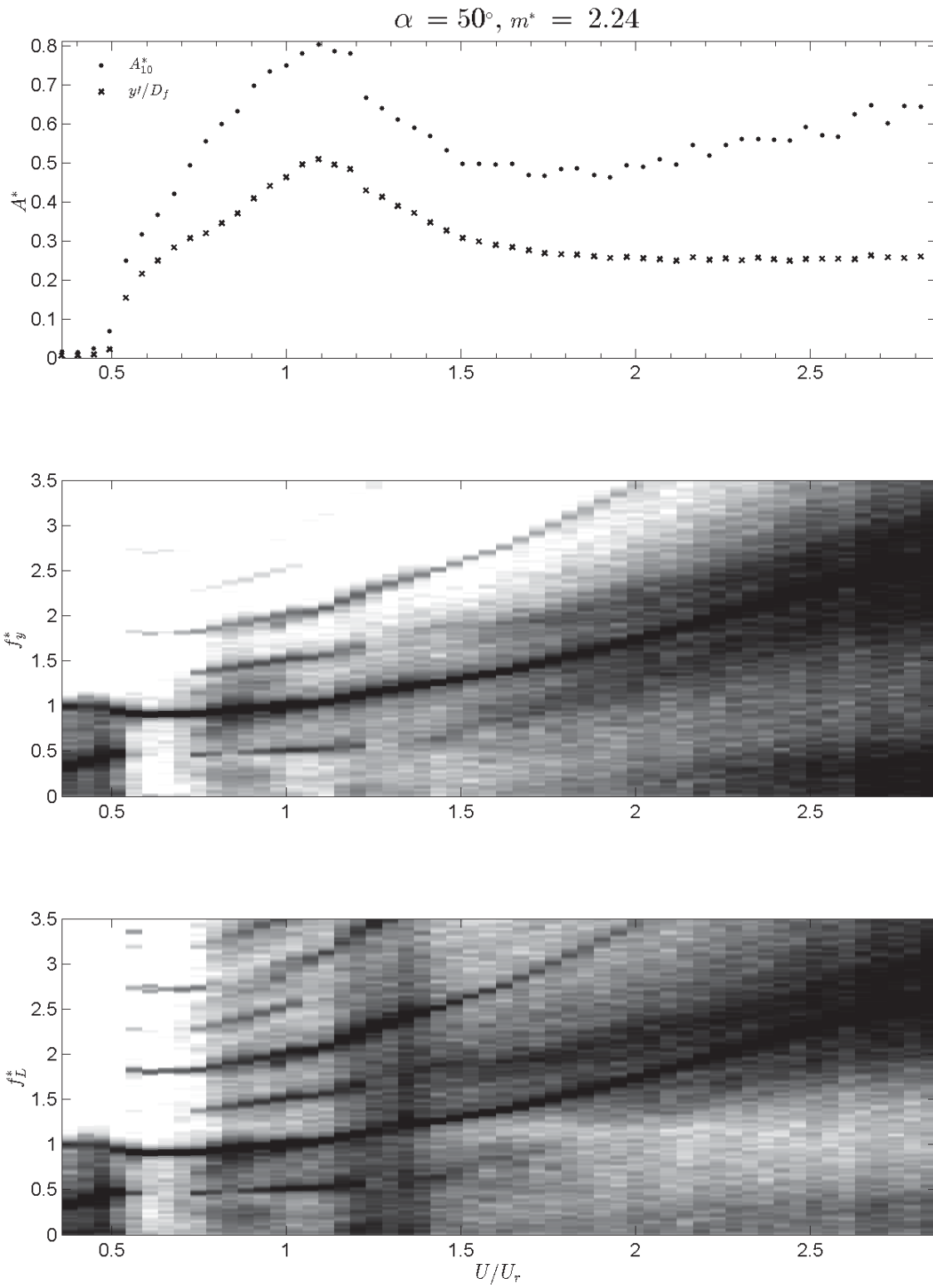


Fig. C.13 Angle of attack's study for $m^* = 2.24$: nondimensional amplitude, oscillation and lift frequencies vs. reduced velocity with respect to resonance one, for $\alpha = 5^\circ$.

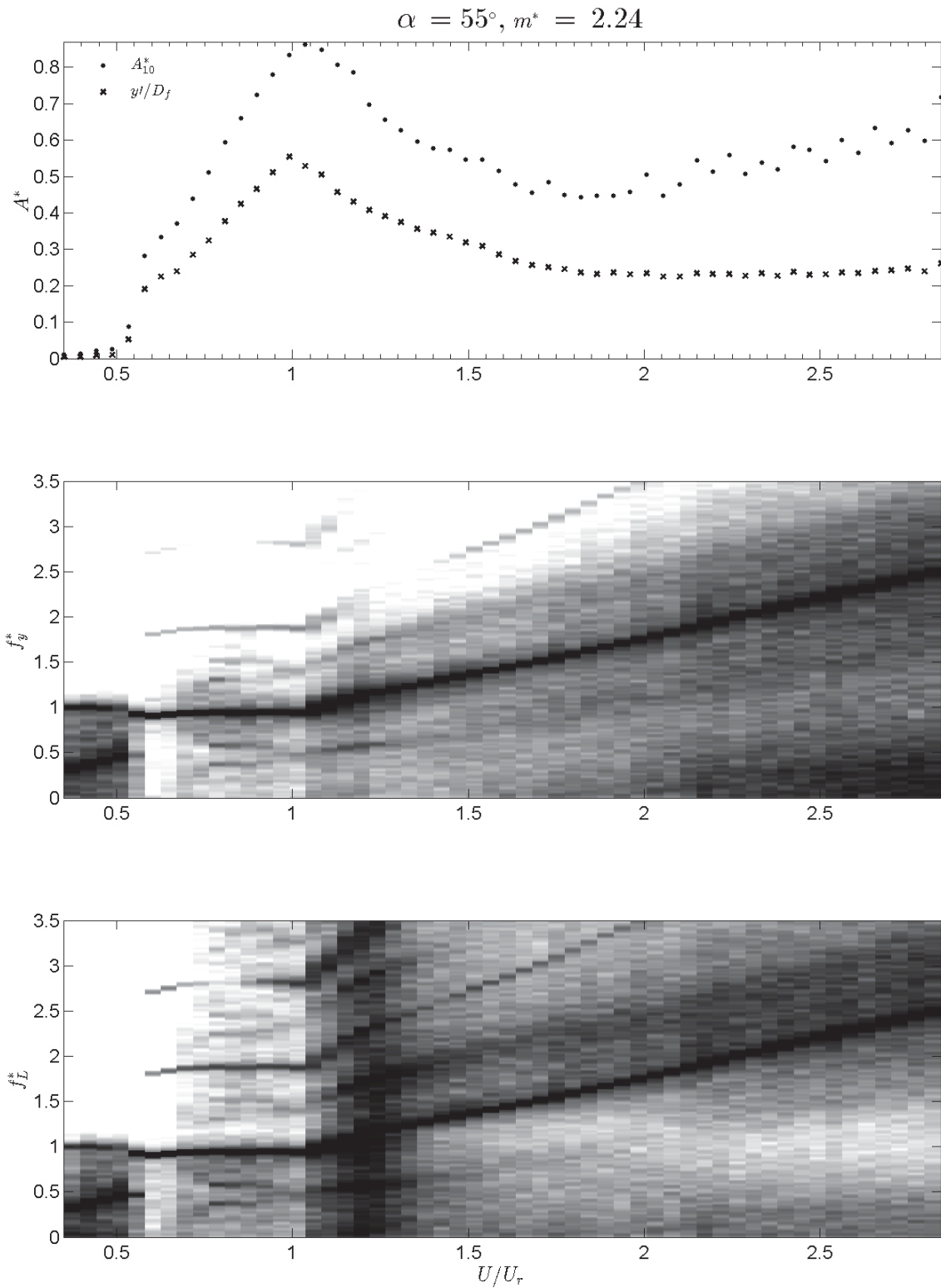


Fig. C.14 Angle of attack's study for $m^* = 2.24$: nondimensional amplitude, oscillation and lift frequencies vs. reduced velocity with respect to resonance one, for $\alpha = 55^\circ$.

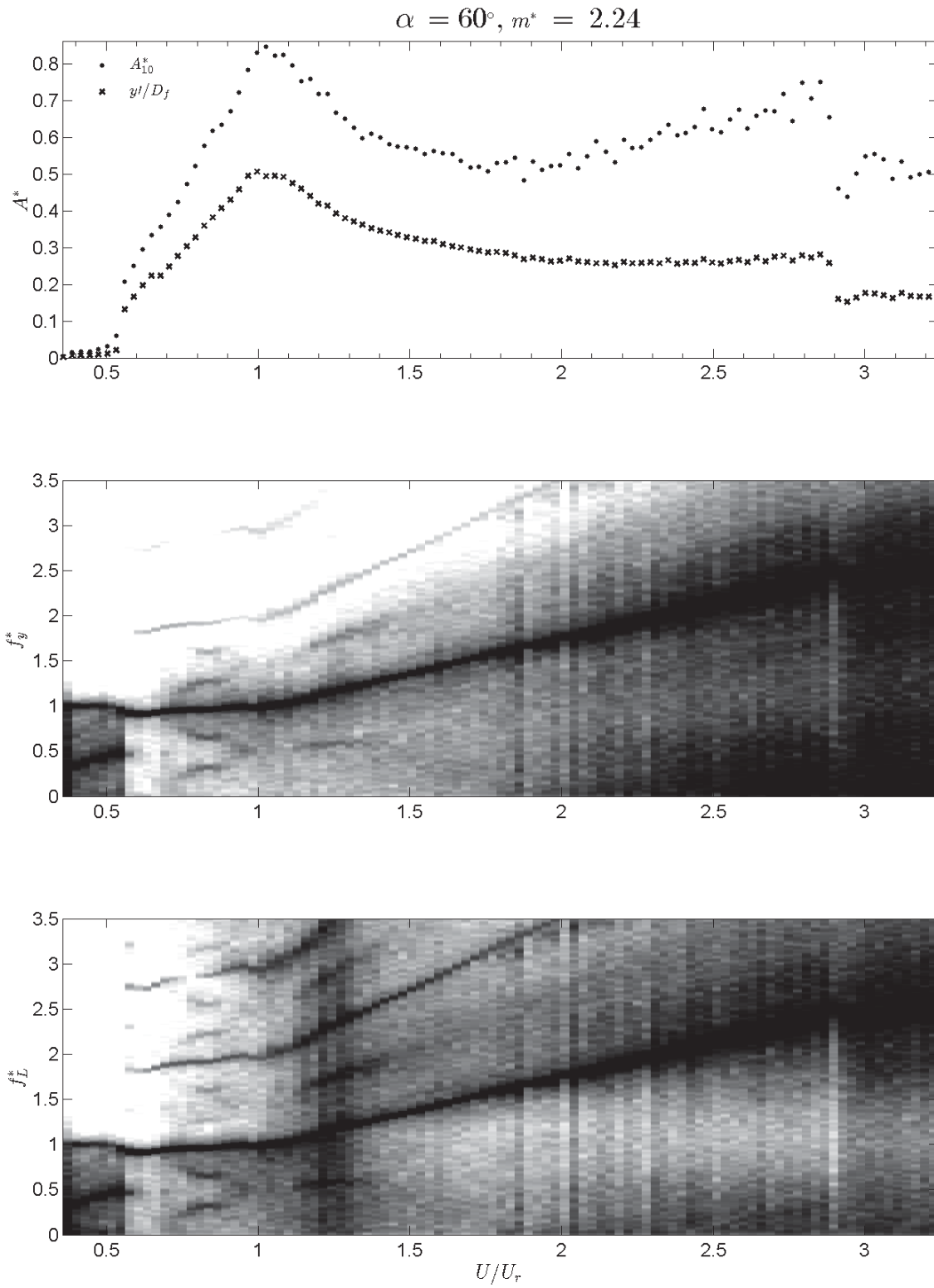


Fig. C.15 Angle of attack's study for $m^* = 2.24$: nondimensional amplitude, oscillation and lift frequencies vs. reduced velocity with respect to resonance one, for $\alpha = 60^\circ$.

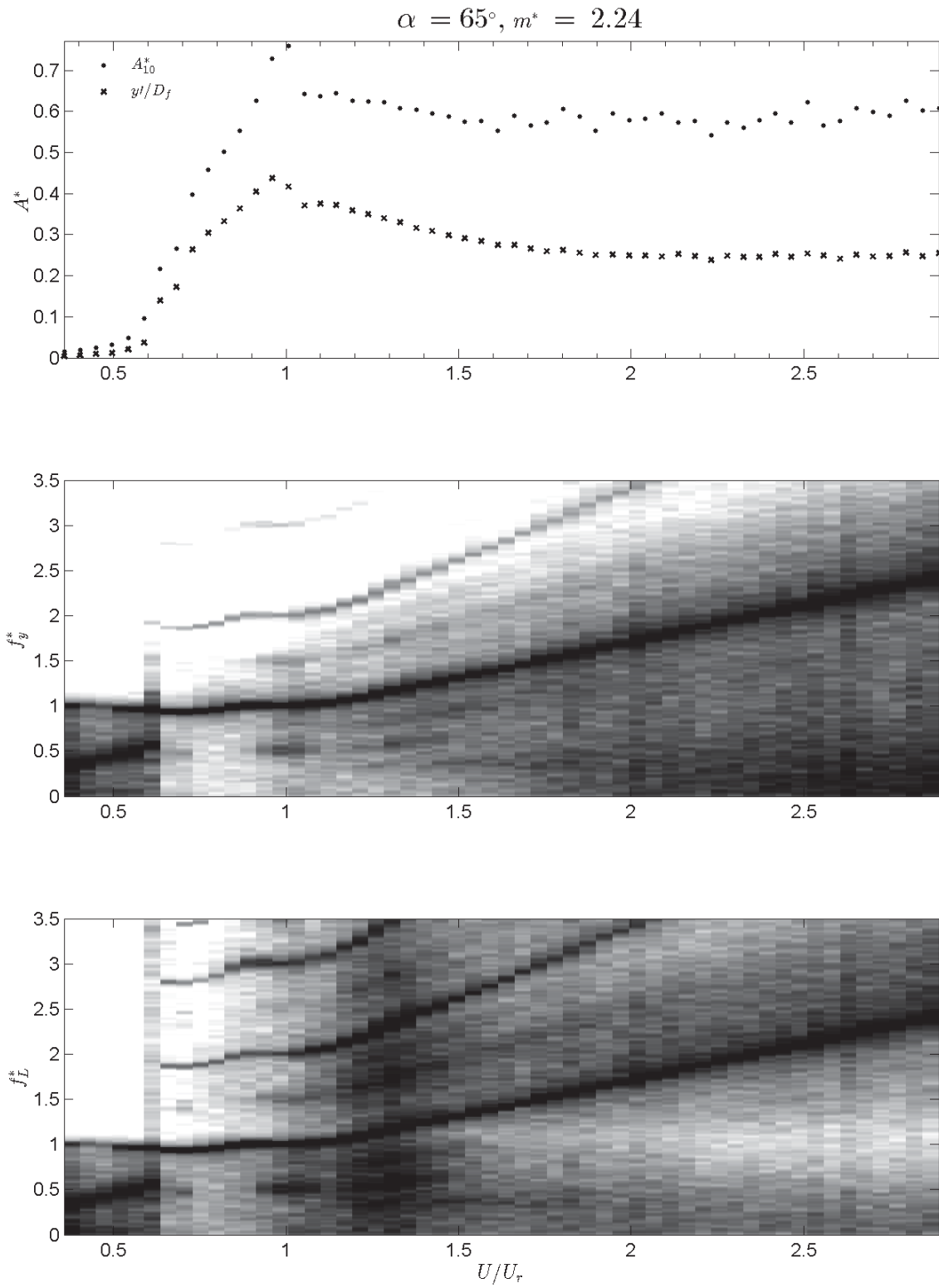


Fig. C.16 Angle of attack's study for $m^* = 2.24$: nondimensional amplitude, oscillation and lift frequencies vs. reduced velocity with respect to resonance one, for $\alpha = 65^\circ$.

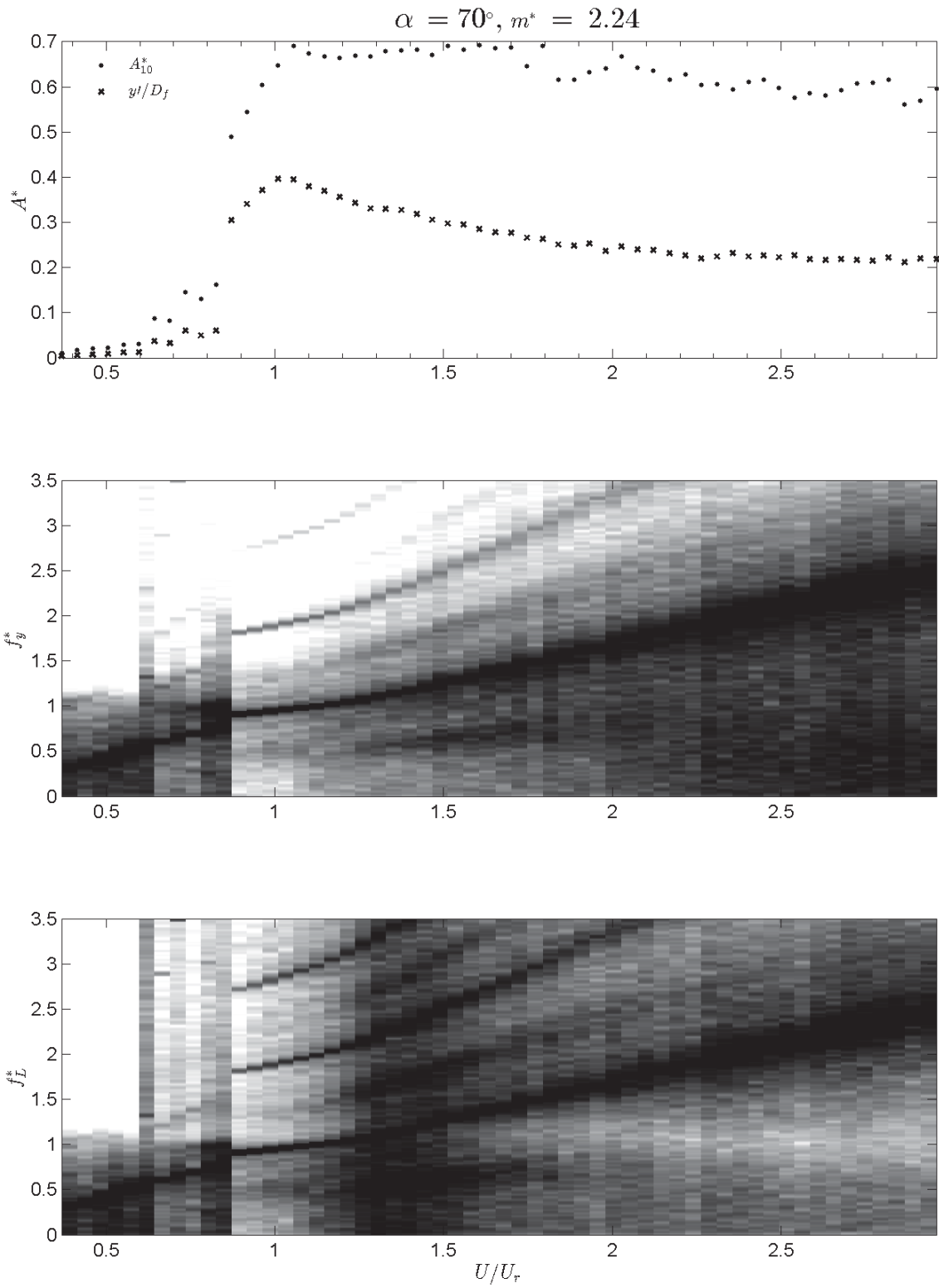


Fig. C.17 Angle of attack's study for $m^* = 2.24$: nondimensional amplitude, oscillation and lift frequencies vs. reduced velocity with respect to resonance one, for $\alpha = 70^\circ$.

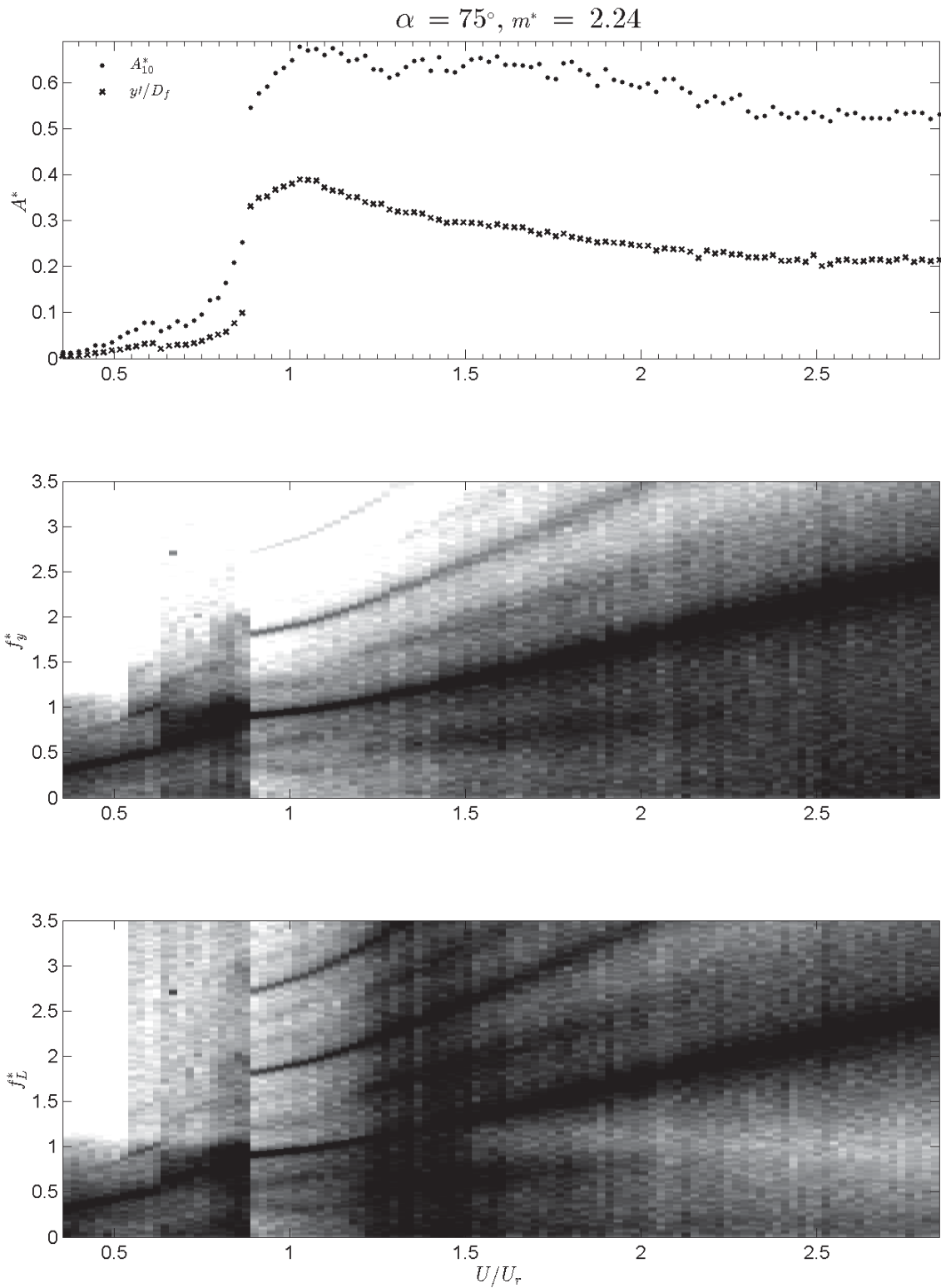


Fig. C.18 Angle of attack's study for $m^* = 2.24$: nondimensional amplitude, oscillation and lift frequencies vs. reduced velocity with respect to resonance one, for $\alpha = 75^\circ$.

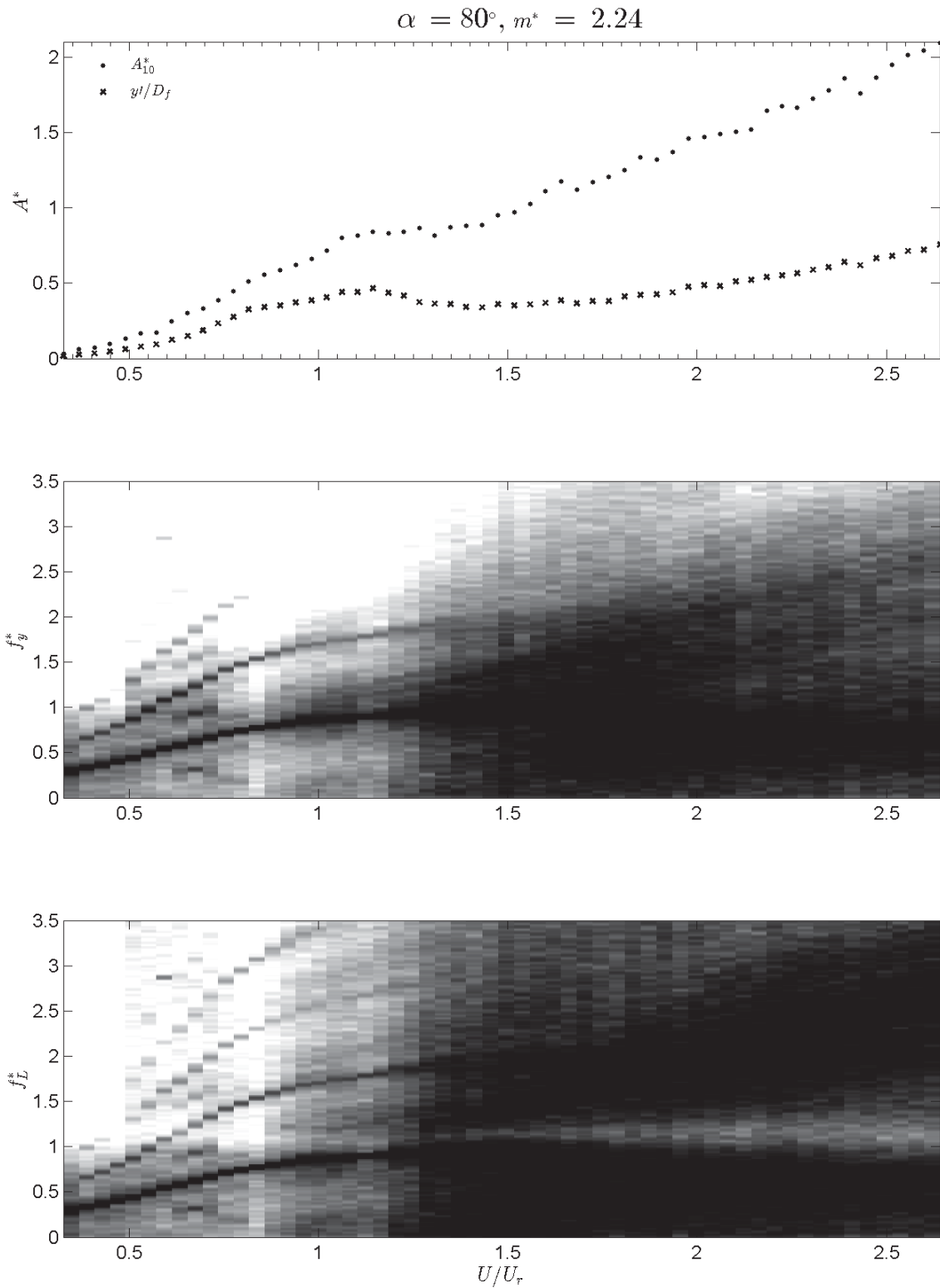


Fig. C.19 Angle of attack's study for $m^* = 2.24$: nondimensional amplitude, oscillation and lift frequencies vs. reduced velocity with respect to resonance one, for $\alpha = 80^\circ$.

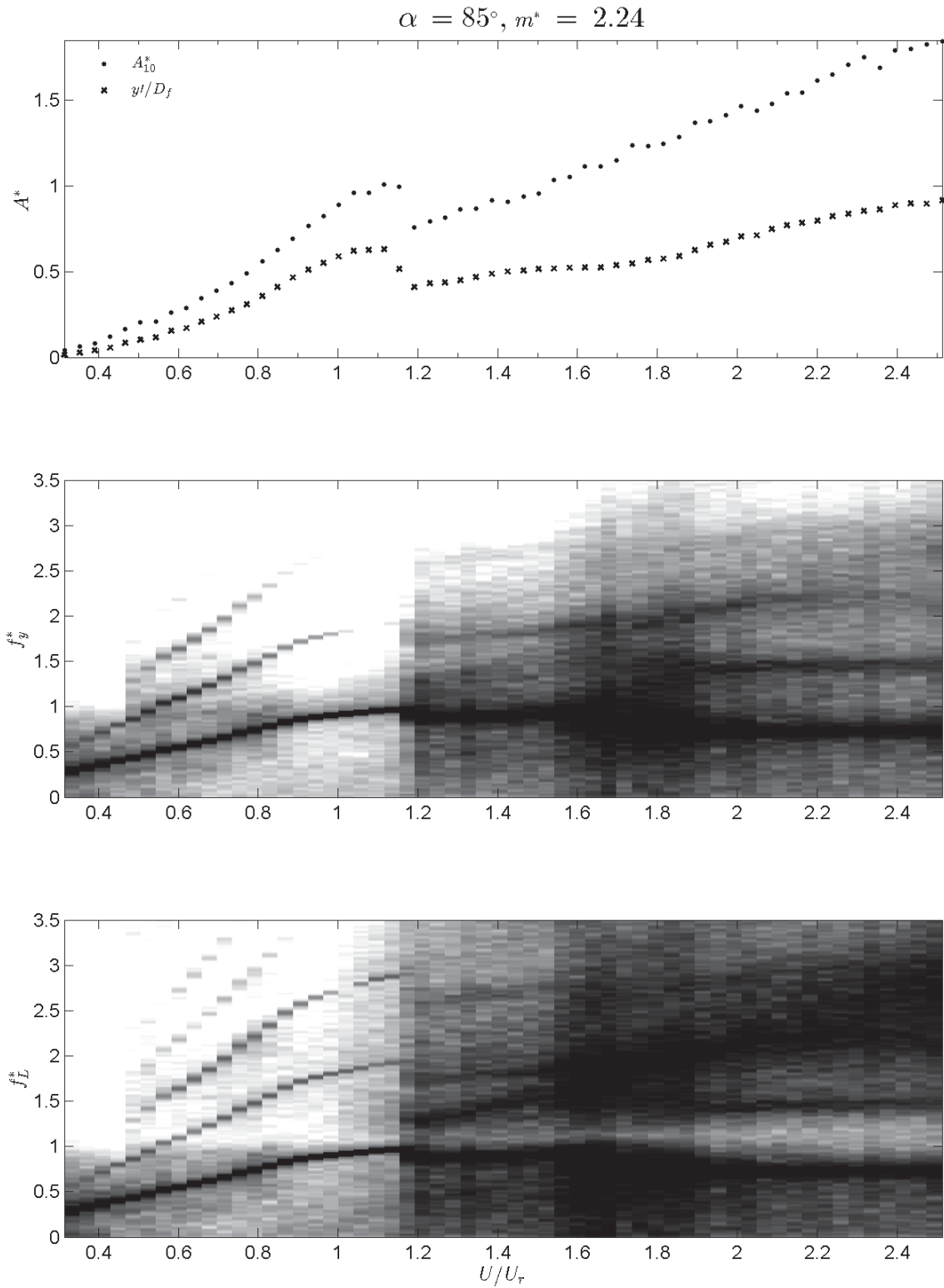


Fig. C.20 Angle of attack's study for $m^* = 2.24$: nondimensional amplitude, oscillation and lift frequencies vs. reduced velocity with respect to resonance one, for $\alpha = 85^\circ$.

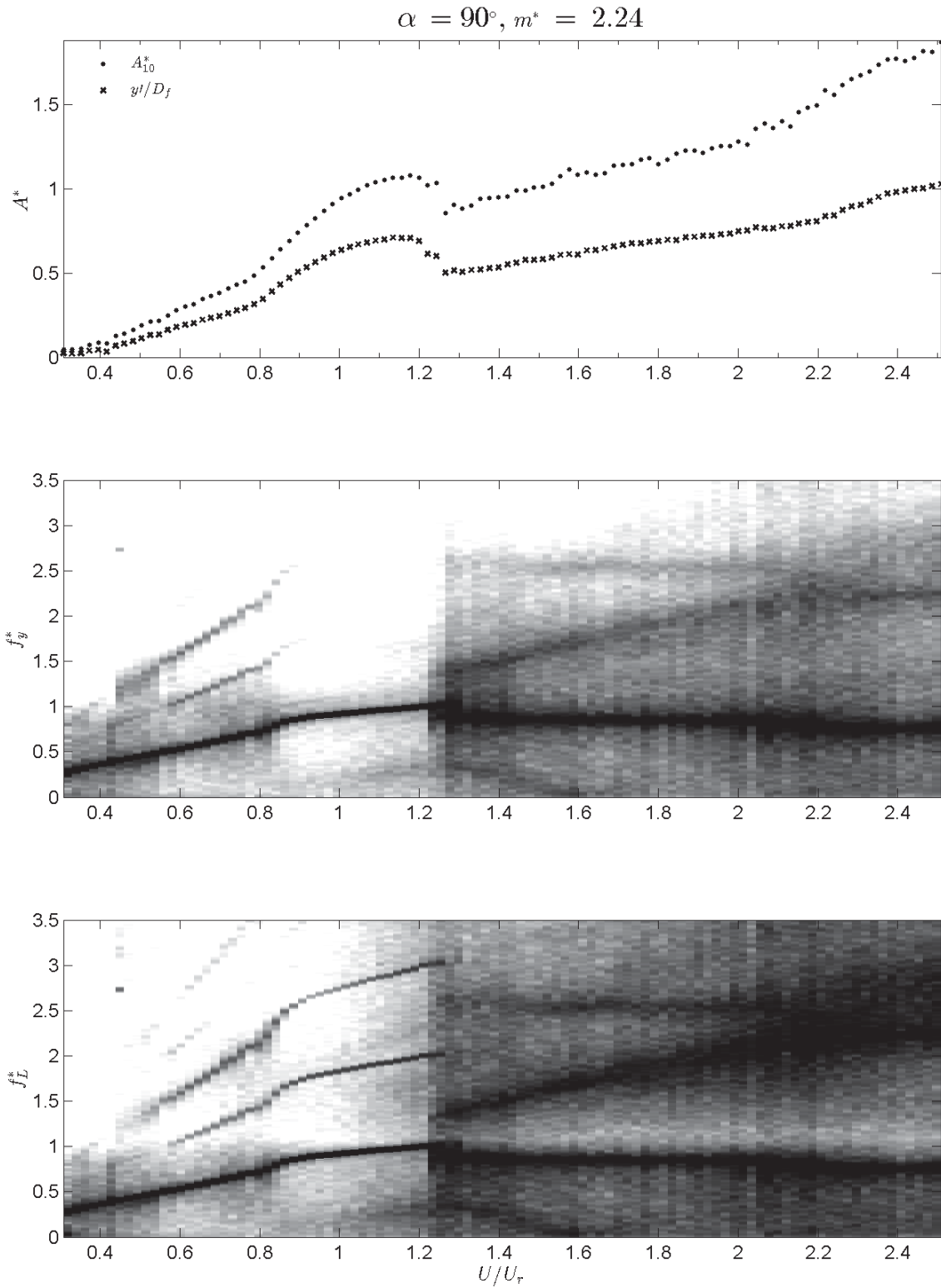


Fig. C.21 Angle of attack's study for $m^* = 2.24$: nondimensional amplitude, oscillation and lift frequencies vs. reduced velocity with respect to resonance one, for $\alpha = 90^\circ$ ($SR = 0.67$).

Mass ratio variation study results

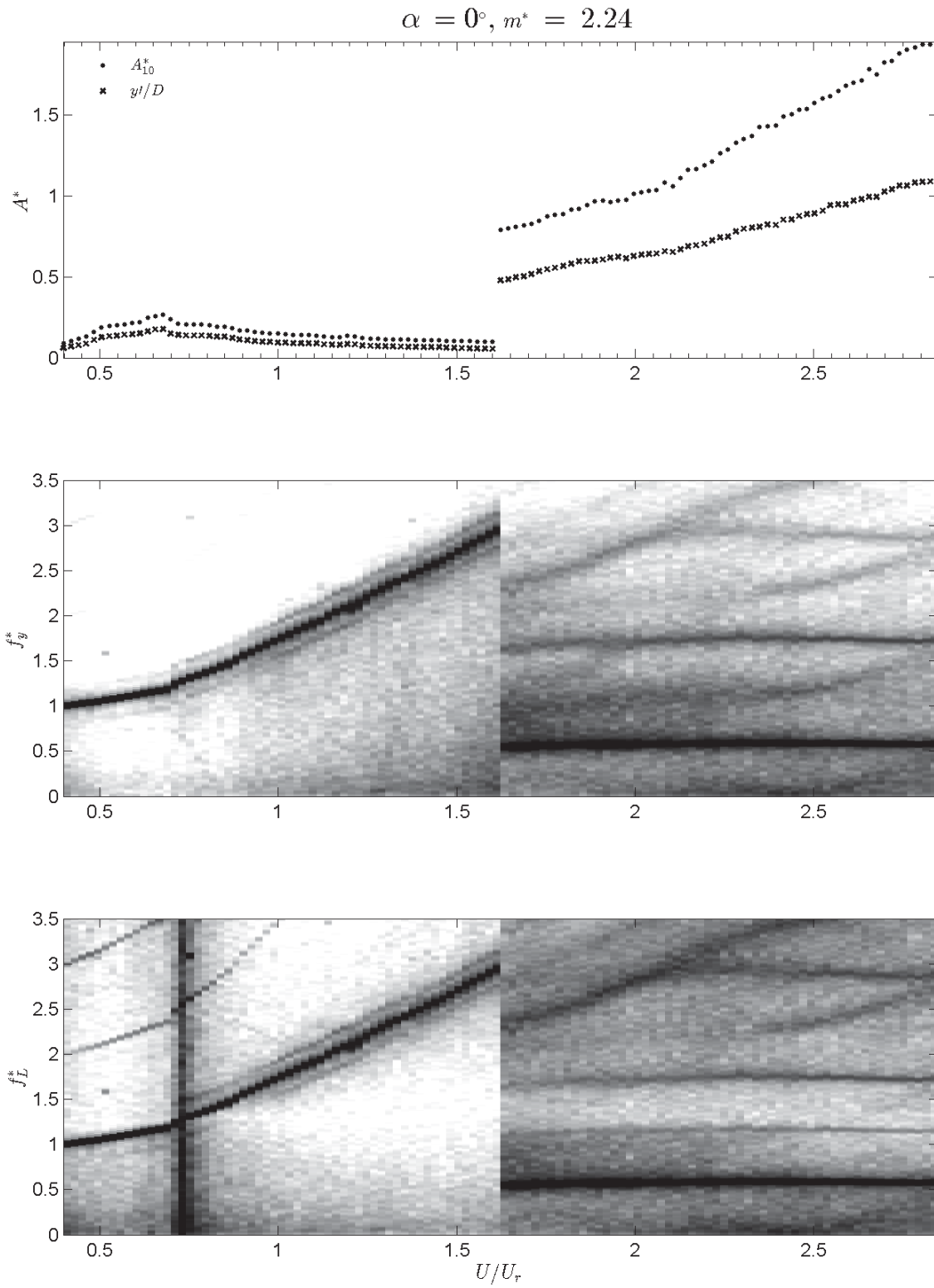


Fig. C.22 Mass ratio's study for $SR = 1.5$: nondimensional amplitude, oscillation and lift frequencies vs. reduced velocity with respect to resonance one, for $m^* = 2.24$.

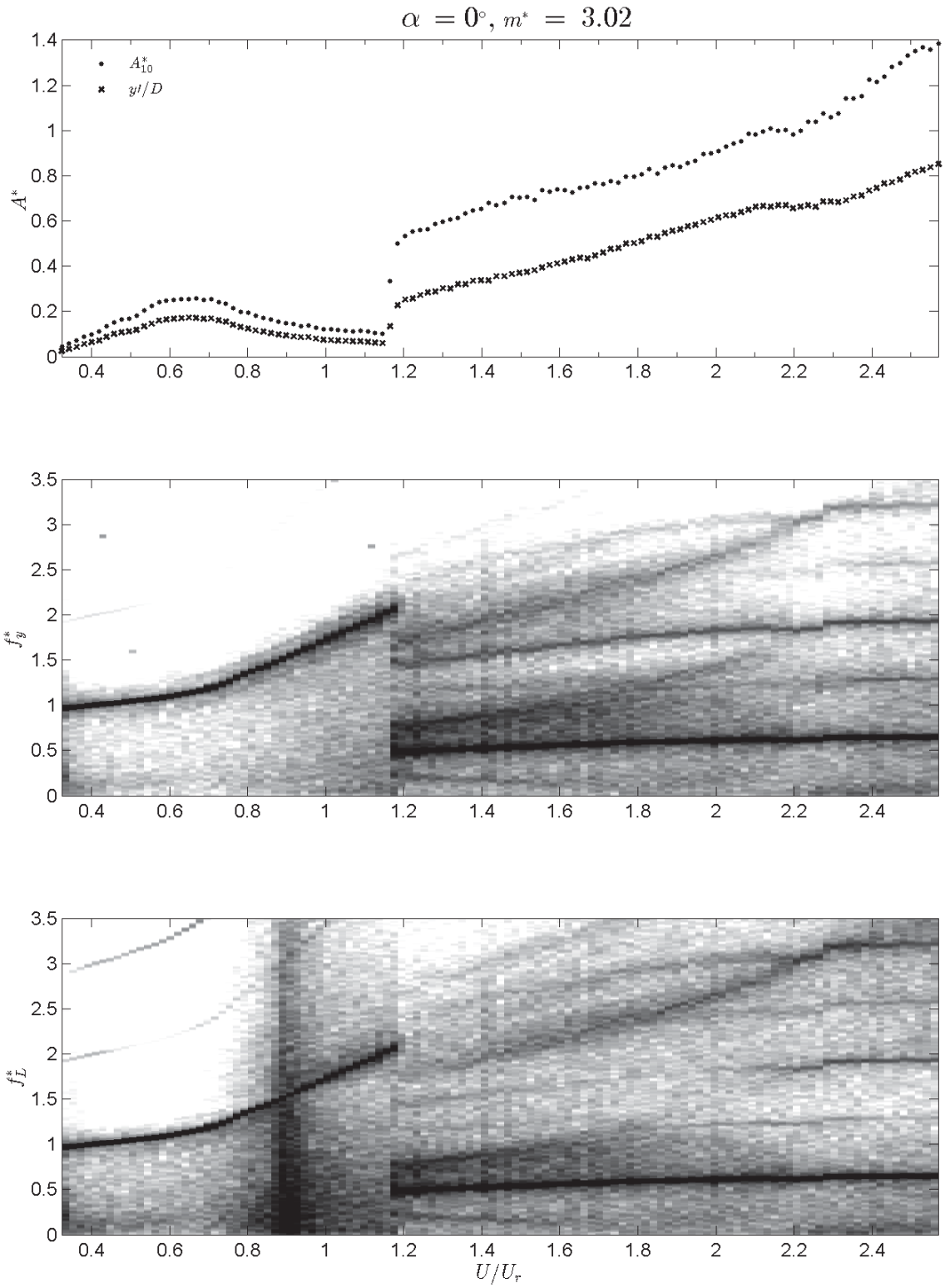


Fig. C.23 Mass ratio's study for $SR = 1.5$: nondimensional amplitude, oscillation and lift frequencies vs. reduced velocity with respect to resonance one, for $m^* = 3.02$.

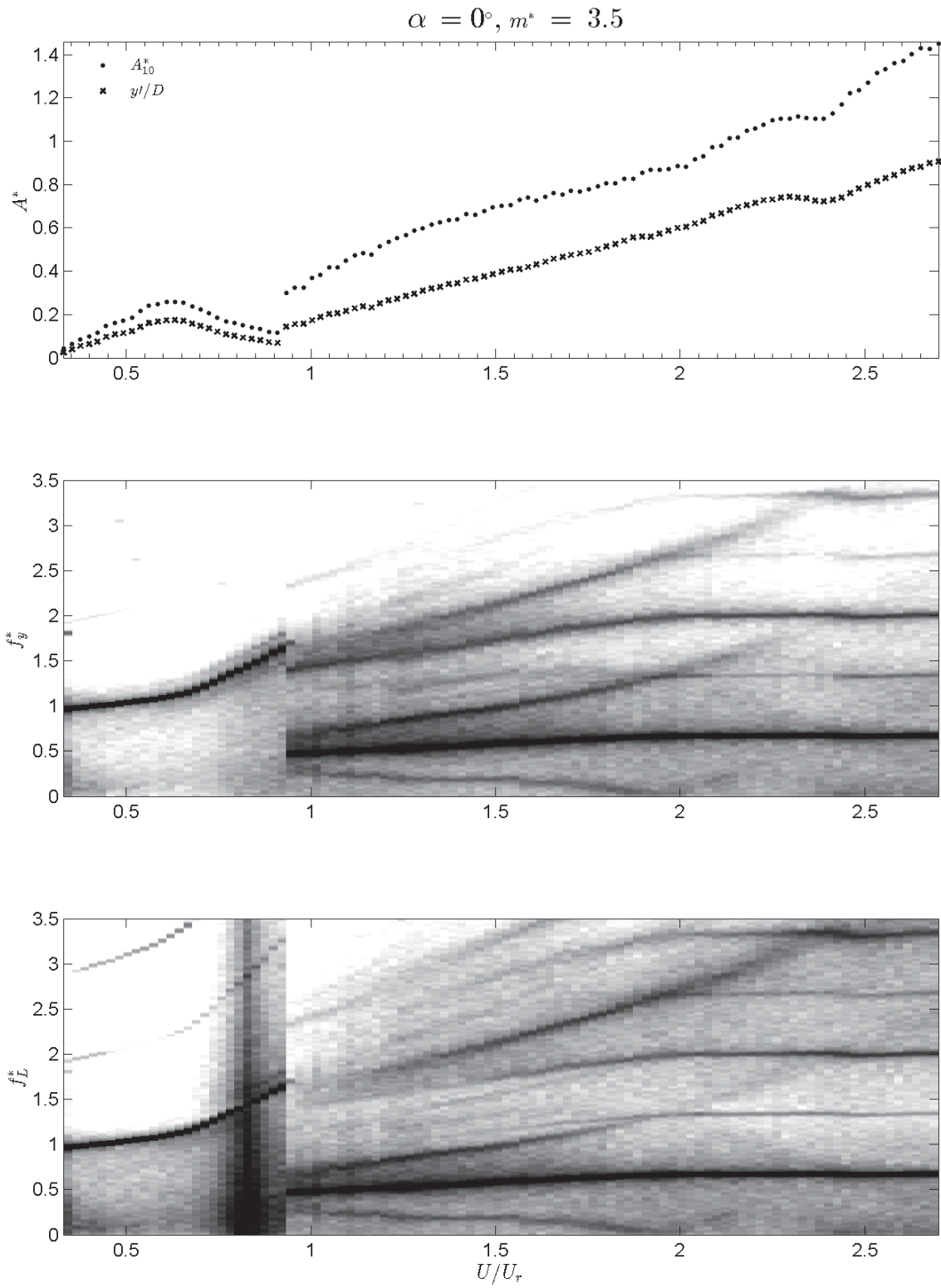


Fig. C.24 Mass ratio's study for $SR = 1.5$: nondimensional amplitude, oscillation and lift frequencies vs. reduced velocity with respect to resonance one, for $m^* = 3.50$.

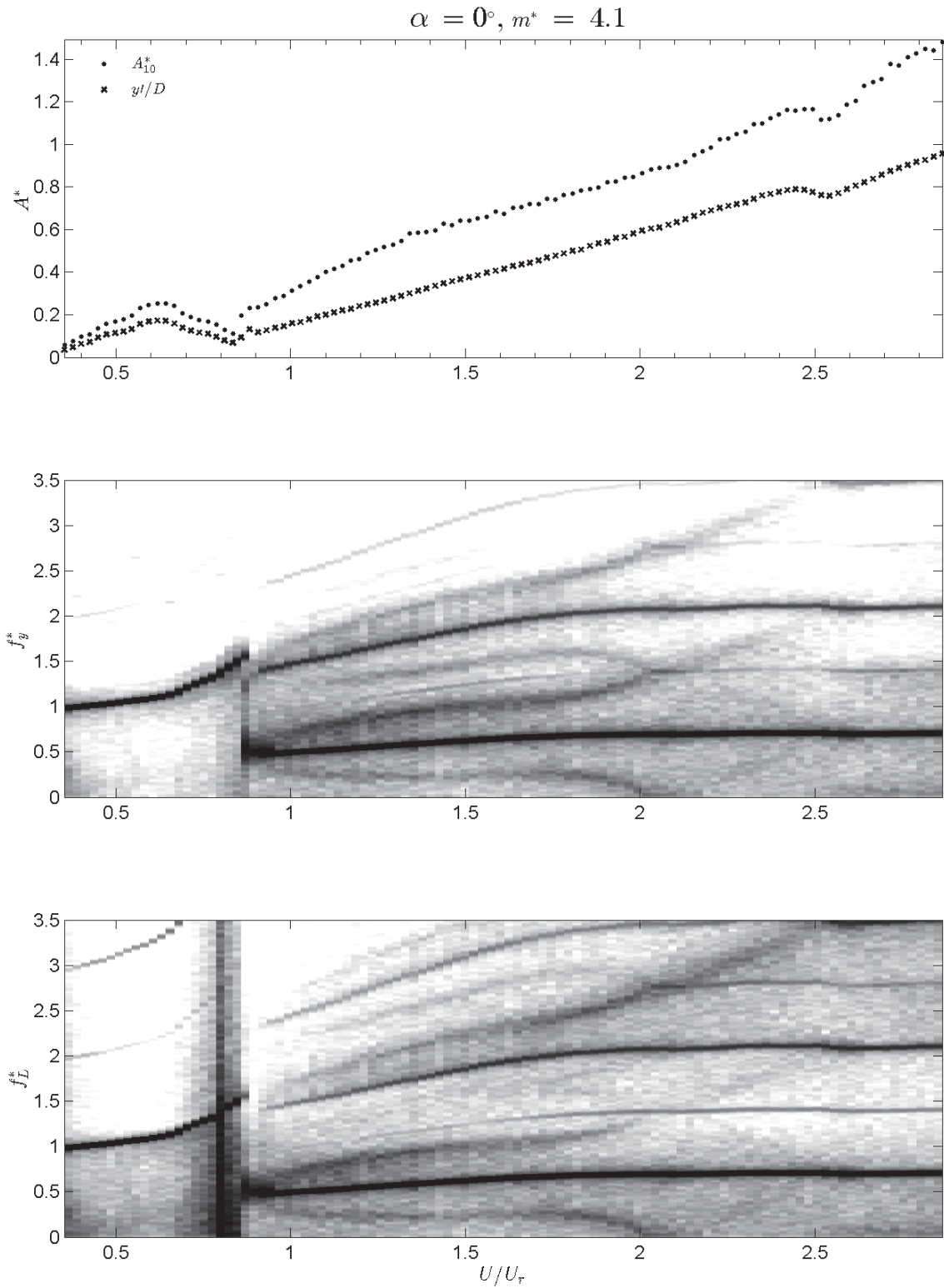


Fig. C.25 Mass ratio's study for $SR = 1.5$: nondimensional amplitude, oscillation and lift frequencies vs. reduced velocity with respect to resonance one, for $m^* = 4.10$.

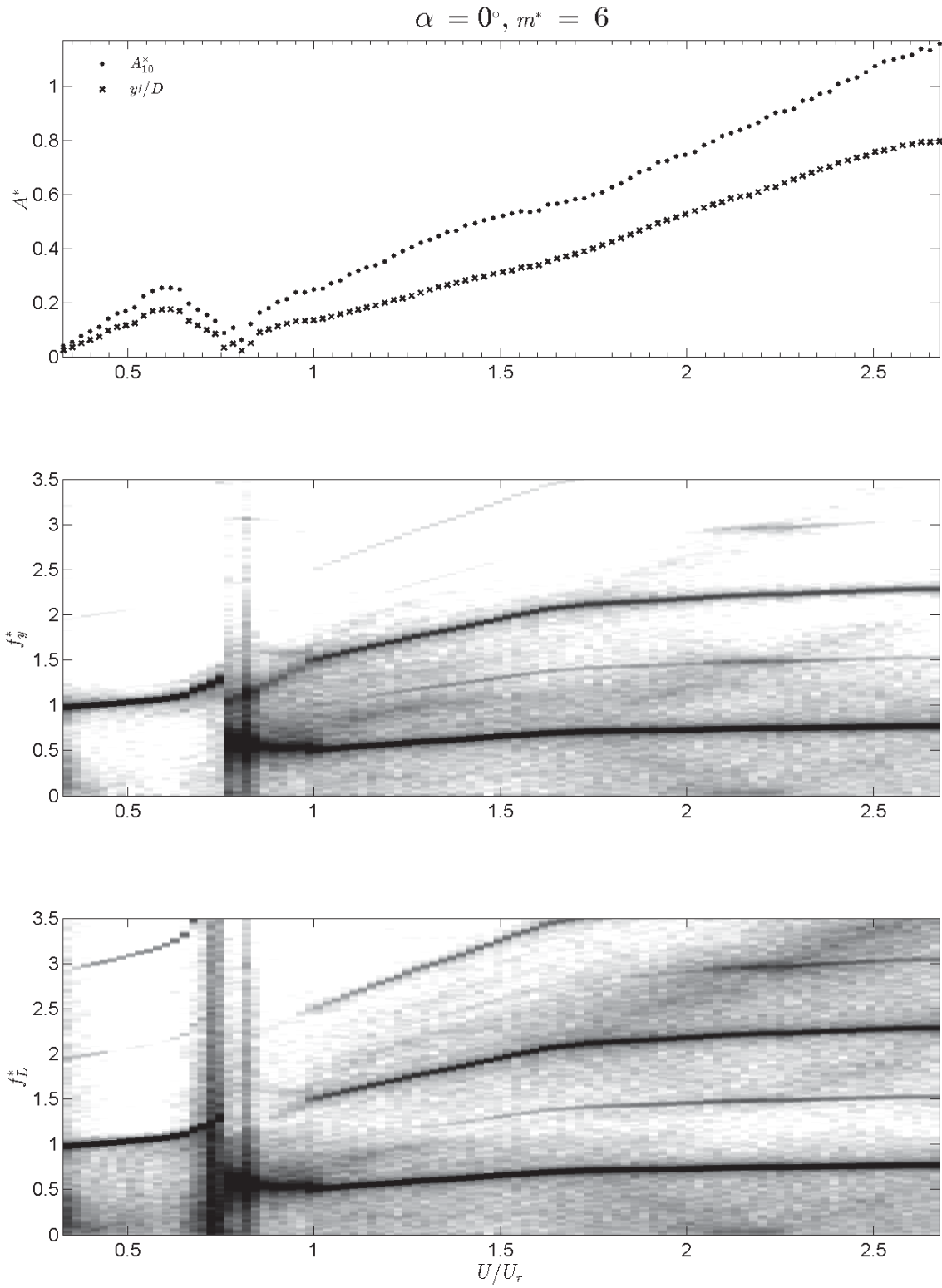


Fig. C.26 Mass ratio's study for $SR = 1.5$: nondimensional amplitude, oscillation and lift frequencies vs. reduced velocity with respect to resonance one, for $m^* = 6.00$.

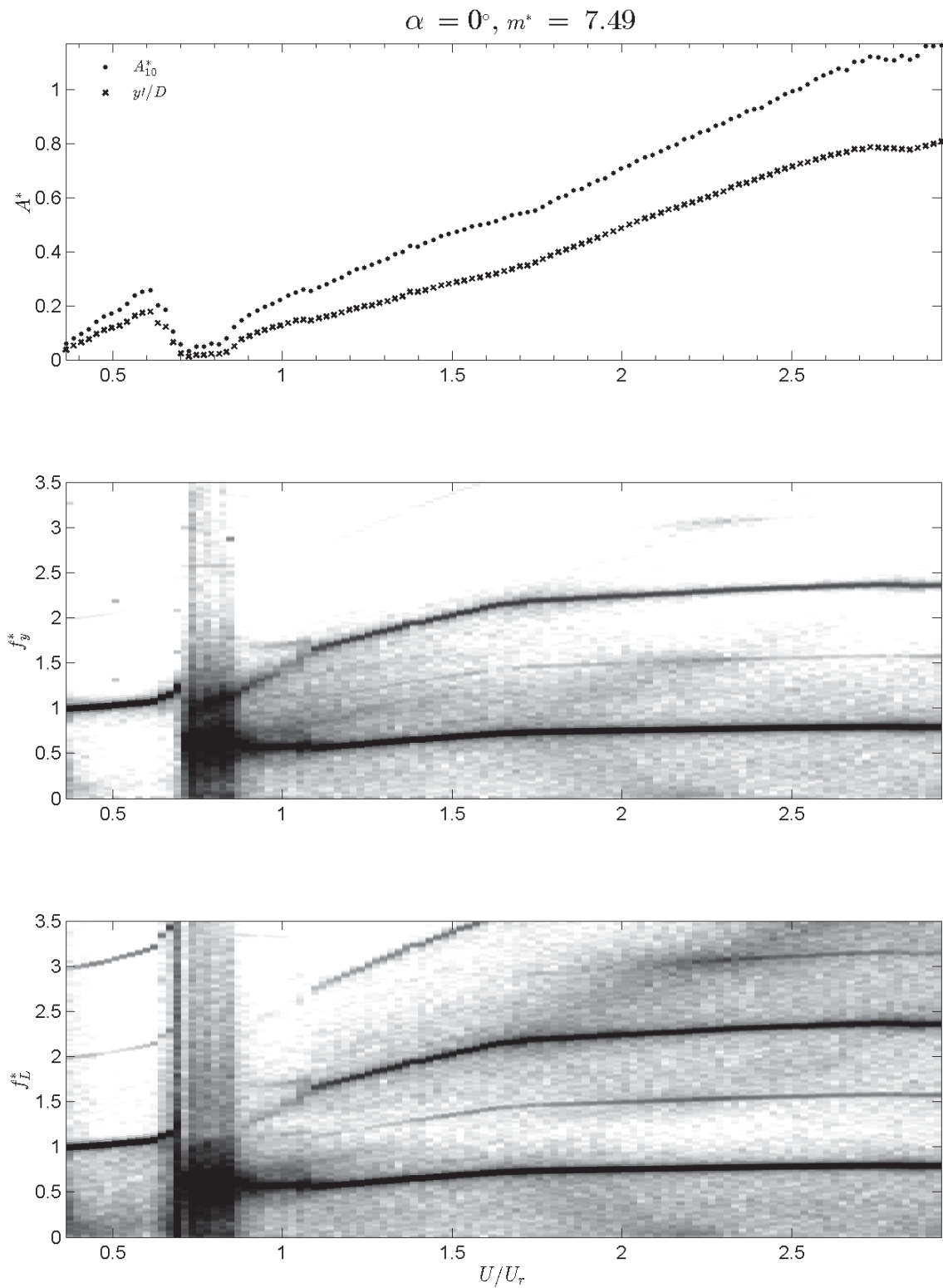


Fig. C.27 Mass ratio's study for $SR = 1.5$: nondimensional amplitude, oscillation and lift frequencies vs. reduced velocity with respect to resonance one, for $m^* = 7.49$.

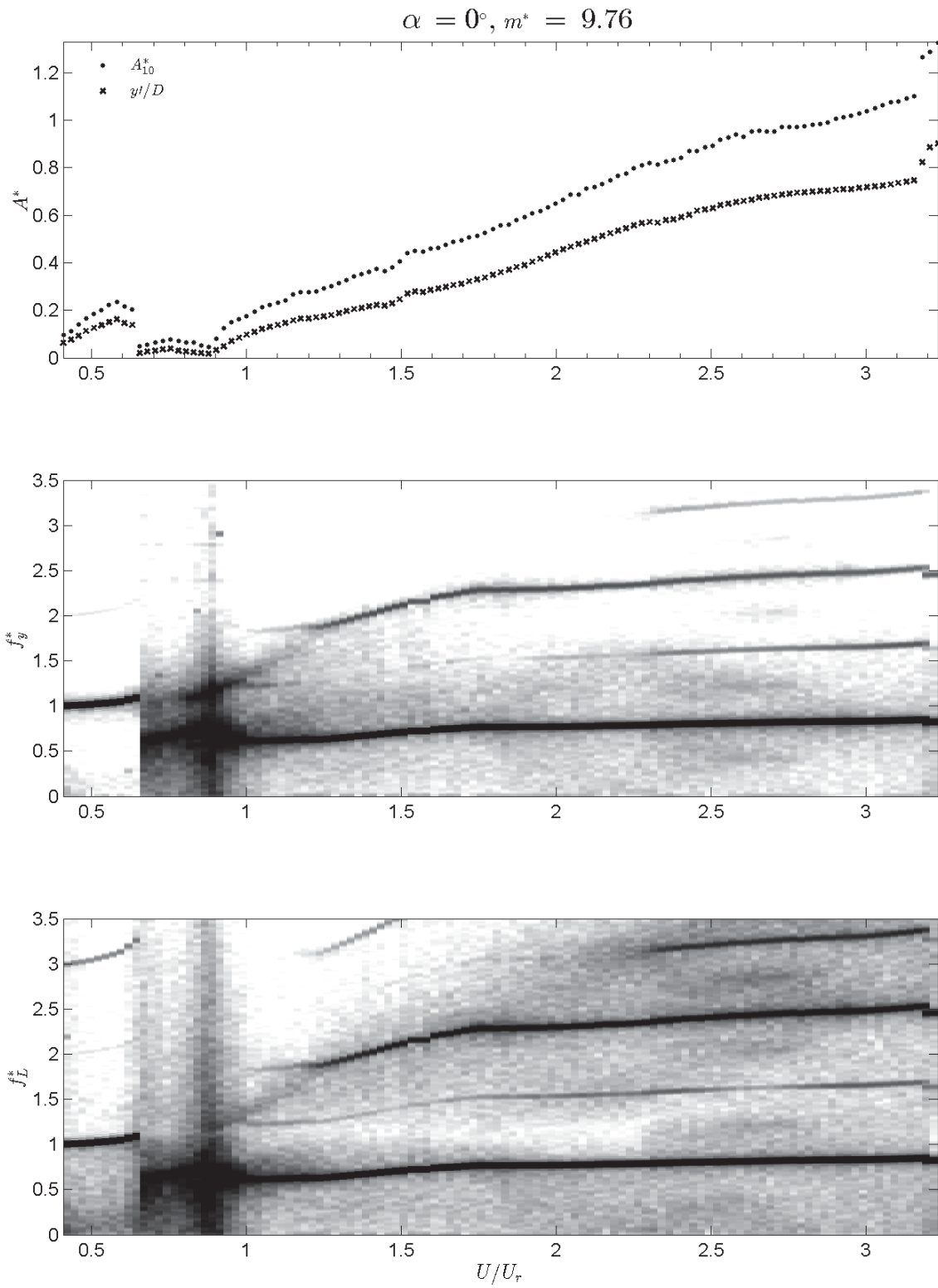


Fig. C.28 Mass ratio's study for $SR = 1.5$: nondimensional amplitude, oscillation and lift frequencies vs. reduced velocity with respect to resonance one, for $m^* = 9.76$.

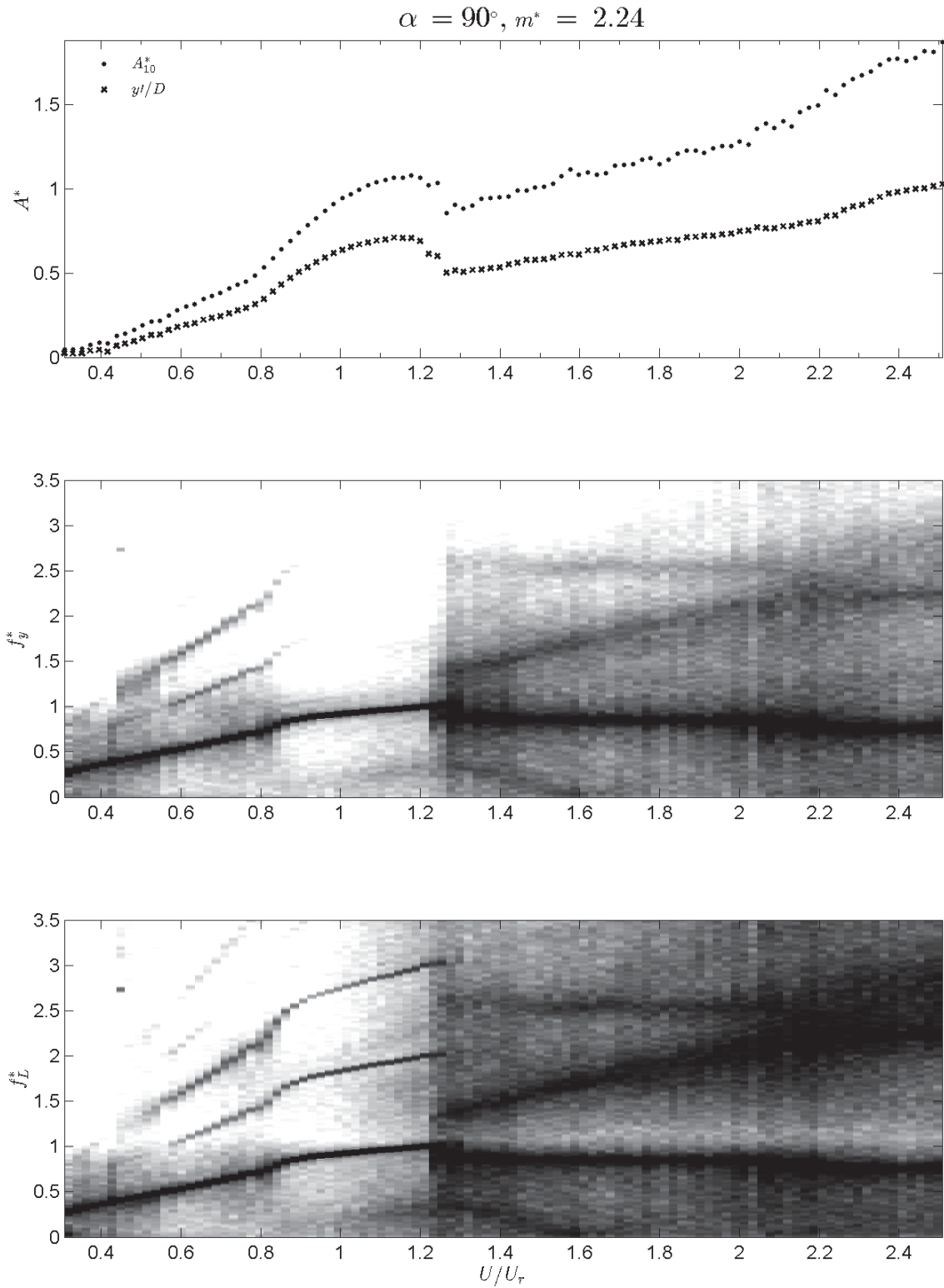


Fig. C.29 Mass ratio's study for $SR = 0.67$: nondimensional amplitude, oscillation and lift frequencies vs. reduced velocity with respect to resonance one, for $m^* = 2.24$.

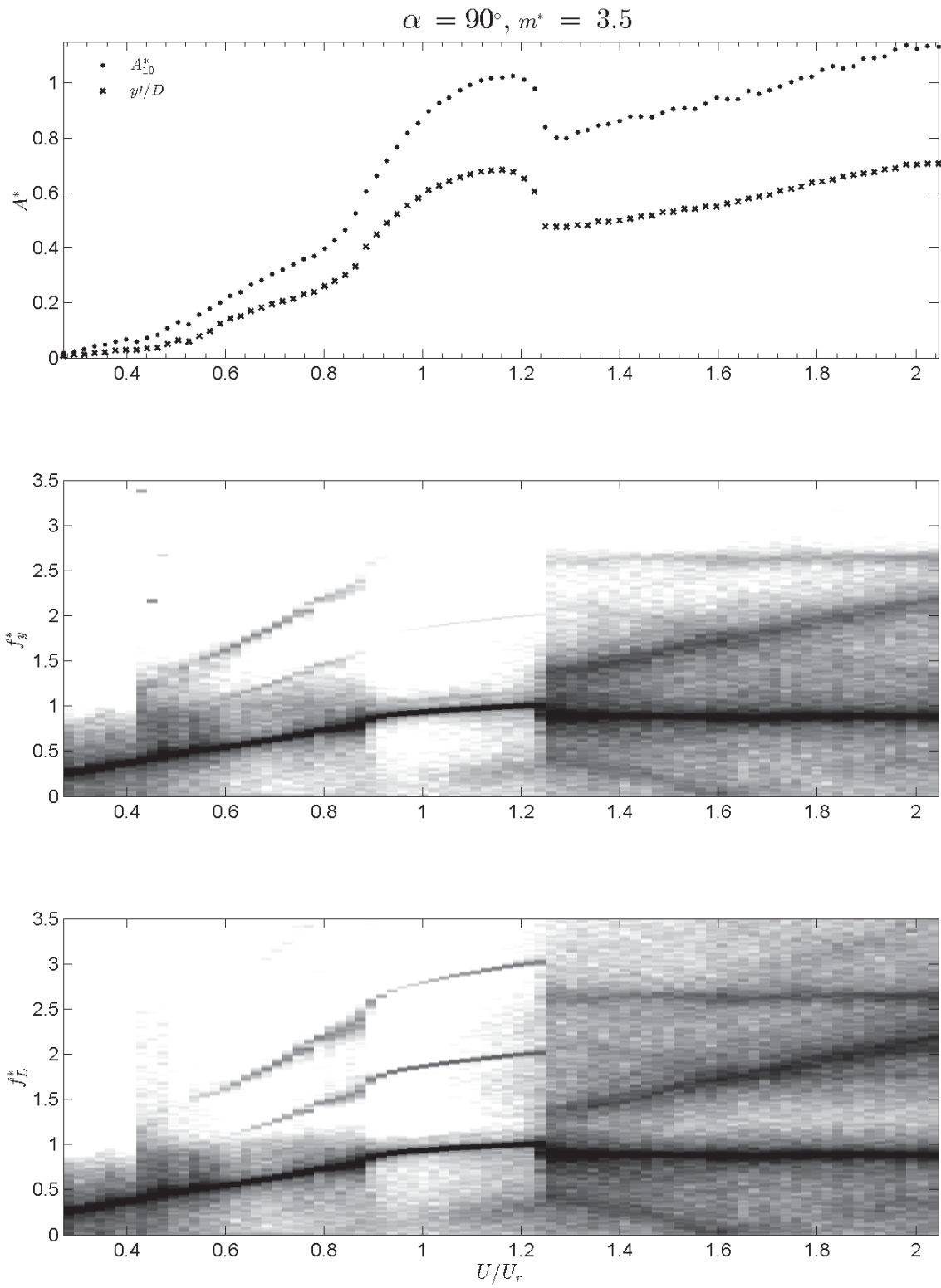


Fig. C.30 Mass ratio's study for $SR = 0.67$: nondimensional amplitude, oscillation and lift frequencies vs. reduced velocity with respect to resonance one, for $m^* = 3.5$.

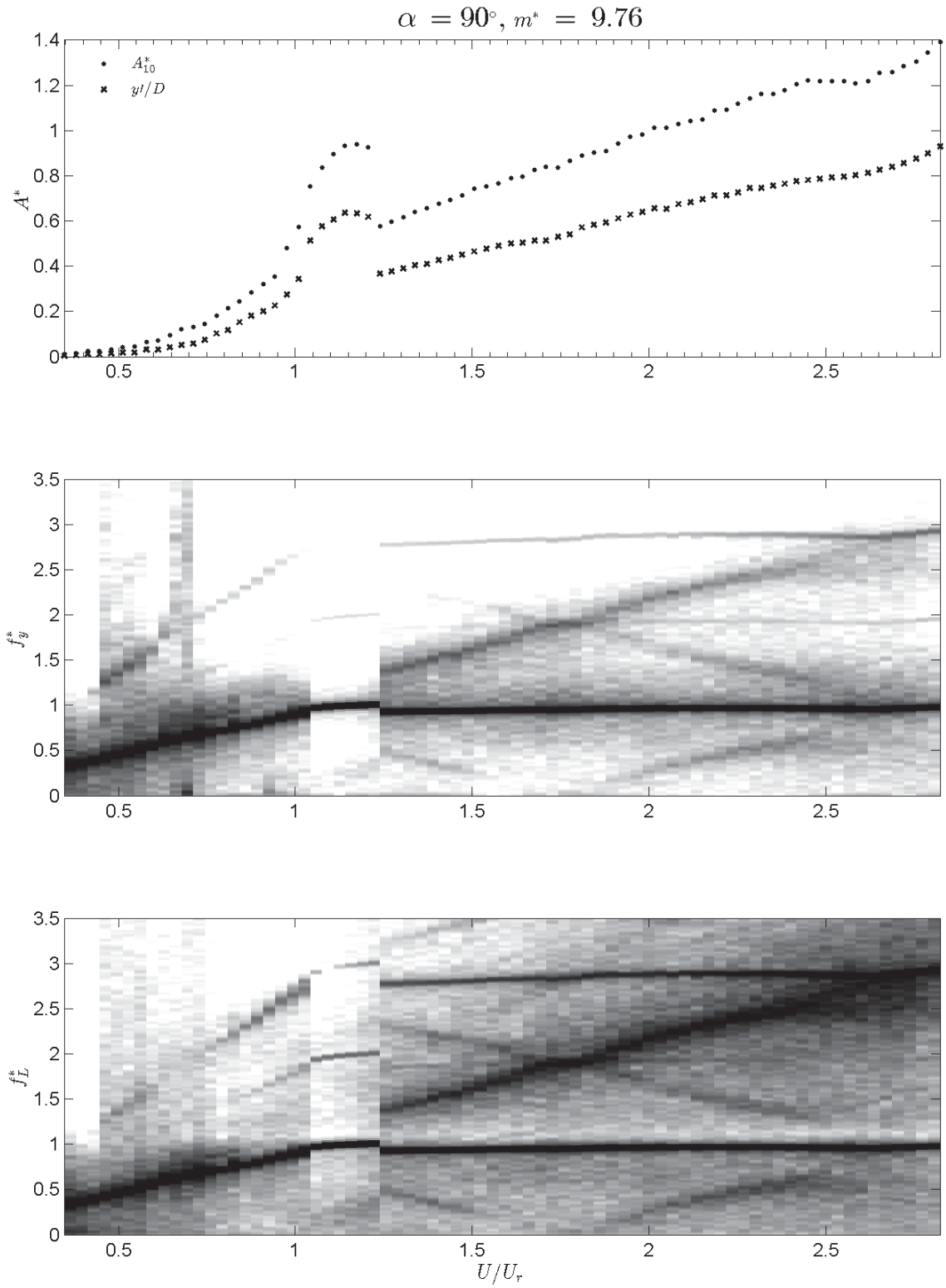


Fig. C.31 Mass ratio's study for $SR = 0.67$: nondimensional amplitude, oscillation and lift frequencies vs. reduced velocity with respect to resonance one, for $m^* = 9.76$.

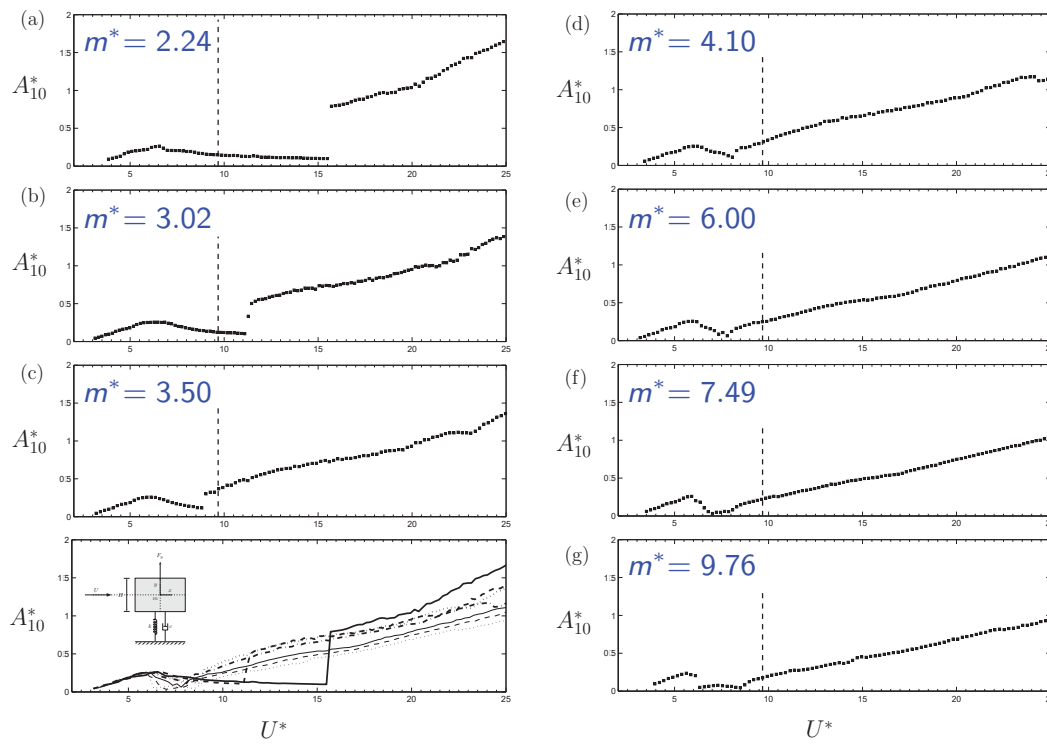


Fig. C.32 Mass ratio variation study (general overview) for D24-W1-7; note that the dashed line indicates the critical velocity.

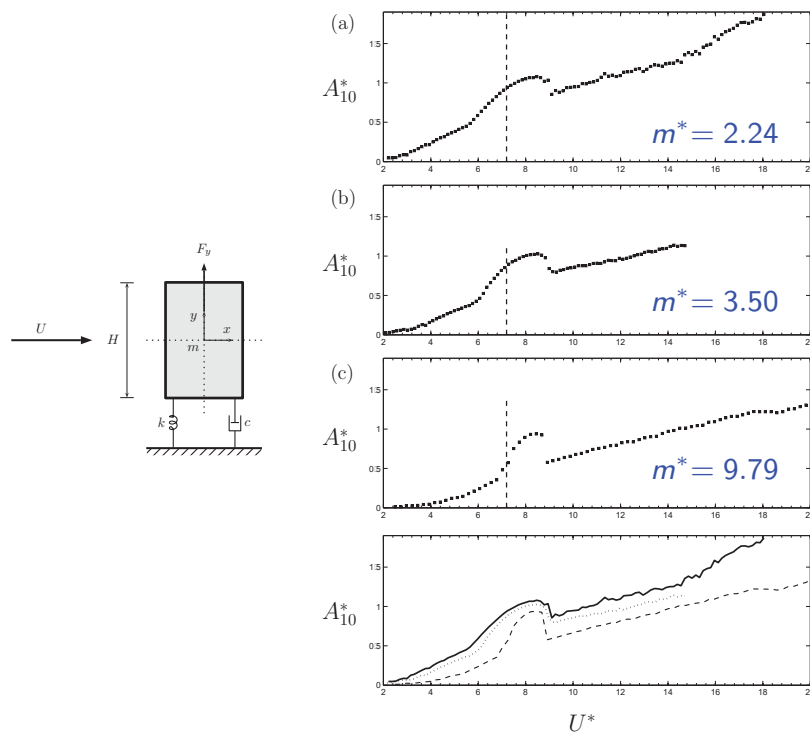


Fig. C.33 Mass ratio variation study (general overview) for D37-W1-3; note that the dashed line indicates the critical velocity.

Bibliography

- Augusti, G., Spinelli, P., Borri, C., Bartoli, G., Giachi, M., , and Giordano, S. (1995). The C.R.I.A.C.I.V. atmospheric boundary layer wind tunnel. In *Proceedings of the 9th International Conference on Wind Engineering, New Delhi*.
- Bartoli, G., Contri, S., Mannini, C., and Righi, M. (2009). Toward an improvement in the identification of bridge deck flutter derivatives. *Journal of Engineering Mechanics*, **135**(8), 771–785.
- Bearman, P. (1967). On vortex street wakes. *Journal of Fluid Mechanics*, **28**(4), 625–641.
- Bearman, P. (1984). Vortex shedding from oscillating bluff bodies. *Annual Review of Fluid Mechanics*, **16**, 195–222.
- Bearman, P. and Obasaju, E. (1982). An experimental study of pressure fluctuations on fixed and oscillating square-section cylinders. *Journal of Fluid Mechanics*, **119**, 297–321.
- Bearman, P. and Trueman, D. (1972). An investigation of the flow around rectangular cylinders. *The Aeronautical Quarterly*, **23**, 229–237.
- Bearman, P., Gartshore, I., Maull, D., and Parkinson, G. (1987). Experiments on flow-induced vibration of a square-section cylinder. *Journal of Fluids and Structures*, **1**(1), 19–34.
- Bearman, P. W. (1965). Investigation of the flow behind a two-dimensional model with a blunt trailing edge and fitted with splitter plates. *Journal of Fluid Mechanics*, **21**(2), 241–255.
- Bénard, H. (1908). Formation de centres de giration a l’arriere d’un obstacle en mouvement. *C.R. Acad. Sci. Paris*, **147**, 839.
- Benaroya, H. and Lepore, J. (1983). Statistical flow-oscillator modeling of vortexshedding. *Journal of Sound and Vibration*, **86**(2), 159–179.
- Bennett, M., Schatz, M. F., Rockwood, H., and Wiesenfeld, K. (2002). Huygens’s clocks. *Proceedings: Mathematical, Physical and Engineering Sciences, The Royal Society*, **458**(2019), 563–579.
- Berger, E. (1978). Some new aspects in fluid oscillaoor model theory. In *Proceedings of the 3rd Colloquium on Industrial Aerodynamics, Aachen*, volume 2.
- Berger, E. (1987). On a mechanism of vortex-excited oscillations of a cylinder. In *Proceedings of the 7th International Conference on Wind Engineering, Aachen*.

- Berger, E. and Wille, R. (1972). Periodic flow phenomena. *Annual Review of Fluid Mechanics*, **4**, 313–340.
- Billah, K. (1989). *A study of Vortex Induced Vibration*. Ph.D. thesis, Princeton University, New Jersey.
- Birkhoff, G. (1953). Formation of vortex streets. *Journal of Applied Physics*.
- Bishop, R. and Hassan, A. (1964). The lift and drag forces on a circular cylinder oscillating in a flowing fluid. *Proceedings of the Royal Society of London, series A*, **277**(1368), 51–75.
- Blevins, R. (1977). *Flow-Induced Vibrations*. Van Nostrand Reinhold Co.
- Blevins, R. (1990). *Flow-Induced Vibration, 2nd Ed.* Krieger Publishing Co., Florida.
- Bokaian, A. and Geoola, F. (1983). On the cross flow response of cylindrical structures. *ICE Proceedings*, **75**, 397–418.
- Bokaian, A. and Geoola, F. (1984). On the cross flow response of cylindrical structures (discussion). *ICE Proceedings*, **77**, 99–101. Discussion by Obasaju, E.D.
- Bokaian, A. and Geoola, F. (1985). Effects of vortex resonance on nearby galloping instability. *Journal of Engineering Mechanics*, **111**(5), 591–609.
- Borg, J. (1986). Magnus effect. an overview of its past and future practical applications. Technical Report AD-A165 902, VAVSEA - Department of the Navy - Washington, DC.
- Borri, C., Zhou, S., and Chen, Z. (2012). Coupling investigation on vortex-induced vibration and galloping of rectangular cylinders. In *Proceedings of the tth International Colloquium on Bluff Body Aerodynamics and Applications, Shanghai (China)*.
- Bouclin, D. (1977). *Hydroelastic oscillations of square cylinders*. Master's thesis, the University of British Columbia.
- Branković, M. (2004). *Vortex-induced vibration attenuation of circular cylinders with low mass and damping*. Ph.D. thesis, Imperial College London.
- Brika, D. and Laneville, A. (1993). Vortex-induced vibrations of a long flexible circular cylinder. *Journal of Fluid Mechanics*, **250**, 481–508.
- Brooks, P. (1960). *Experimental investigation of the aeroelastic instability of bluff two-dimensional cylinders*. Master's thesis, the University of British Columbia.
- Bruno, L. and Khris, S. (2003). The validity of 2d numerical simulations of vortical structures around a bridge deck. *Mathematical and Computer Modelling*, **37**, 795–828.
- Buresti, G. (1998). *Vortex shedding from bluff-bodies*, chapter 4, pages 61–96. Taylor & Francis.
- Chaplin, J. and Shaw, T. (1971). Flow-induced dynamic ppressure on square section cylinders. In *Proceedings of the International Association for Hydro-Environment Engineering and Research (IAHR) Conference, Paris*, volume 2.

- Corless, R. (1986). *Mathematical modelling of the combined effects of Vortex-Induced Vibration and Galloping*. Ph.D. thesis, the University of British Columbia.
- Corless, R. and Parkinson, G. (1988). A model of the combined effects of vortex-induced oscillation and galloping. *Journal of Fluids and Structures*, **2**(3), 203–220.
- Corless, R. and Parkinson, G. (1993). Mathematical modelling of the combined effects of vortex-induced vibration and galloping. part {II}. *Journal of Fluids and Structures*, **7**(8), 825–848.
- Courchesne, J. and Laneville, A. (1979). A comparison of correction methods used in the evaluation of drag coefficient measurements for two-dimensional rectangular cylinders. *Journal of Fluids Engineering*, **101**(4), 506–510.
- Courchesne, J. and Laneville, A. (1982). An experimental evaluation of drag coefficient for rectangular cylinders exposed to grid turbulence. *Journal of Fluids Engineering*, **104**, 523–527.
- Cowdrey, C. (1963). A note on the use of end plates to prevent three-dimensional flow at the ends of bluff cylinders. C.P. 683, Ministry of Aviation, Aeronautical Research Council.
- Currie, I. G., Hartlen, R., and W.W., M. (1972). The response of circular cylinders to vortex shedding. In *In. Symposium on Flow-Induced Structural Vibrations, Karlsruhe*, pages 128–142.
- Da Vinci, L. (1828). *Del moto e misura dell'acqua*. Published by Francesco Cardinali (Bologna, Italy).
- D'Asdia, P. and Noé, S. (1998). Vortex induced vibration of reinforced concrete chimneys: in situ experimentation and numerical previsions. *Journal of Wind Engineering and Industrial Aerodynamics*, **74-76**, 765–776.
- D'Asdia, P., Sepe, V., Caracoglia, L., and Noé, S. (2003). A model for vortex-shedding induced oscillations of long-span bridges. In *Proceedings of the 2nd International Structural Engineering and Construction Conference (ISEC-02), University of Rome (Italy)*, volume 3, pages 2331–2336.
- den Hartog, J. (1930). *Transmission Line Vibration Due to Sleet*, volume 49, page 444.
- den Hartog, J. (1932). Transmission line vibration due to slit. *Transaction of EE*, **51**(4), 1074–1086.
- Deniz, S. and Staubli, T. (1997). Oscillating rectangular and octagonal profiles: interaction of leading and trailing-edge vortex formation. *Journal of Fluids and Structures*, **11**(1), 3–31.
- Diana, G., Resta, F., Belloli, M., and Rocchi, D. (2006). On the vortex shedding forcing on suspension bridge deck. *Journal of Wind Engineering and Industrial Aerodynamics*, **94**(5), 341–363.
- Dowell, E. (1981). Non-linear oscillator models in bluff body aero-elasticity. *Journal of Sound and Vibration*, **75**(2), 251–264.

- Ehsan, F. and Scanlan, R. (1990). Vortex-induced vibrations of flexible bridges. *Journal of Engineering Mechanics*, **116**(6), 1392–1411.
- EC 1 (2010). EN 1991 - parts 1-4: Wind actions.
- ECCS (1987). Recommandations pour le calcul des effets du vent sur les constructions, deuxième édition.
- Fage, A. and Johansen, F. C. (1927). On the flow of air behind an inclined flat plate of infinite span. In *Proceedings of the Royal Society of London. Series A, Containing Papers of a Mathematical and Physical Character*, volume 116, pages 170–197.
- Feng, C. (1968). *The measurement of vortex induced effects in flow past stationary and oscillating circular and D-section cylinders*. Master's thesis, the University of British Columbia.
- Ferguson, N. (1965). *The measurement of wake and surface effects in the subcritical flow past a circular cylinder at rest and in vortex-excited oscillation*. Master's thesis, the University of British Columbia.
- Funakawa, M. (1969). Excitation mechanism of an elastically supported circular cylinder in a flowing fluid. *Bulletin of JSME (in Japanese)*, **35**(270), 303–312.
- Gerrard, J. H. (1966). The mechanics of the formation region of vortices behind bluff bodies. *Journal of Fluid Mechanics*, **25**(02), 401–413.
- Glauert, H. (1919). The rotation of an aerofoil about a fixed axis. Technical Report 595, Advisory Committee for Aeronautics.
- Goswami, I. (1991). *Vortex-Induced vibration of circular cylinders*. Ph.D. thesis, Johns Hopkins University, Baltimore, Maryland.
- Goswami, I., Scanlan, R. H., and Jones, N. P. (1992). Vortex shedding from circular cylinders: Experimental data and a new model. *Journal of Wind Engineering and Industrial Aerodynamics*, **41**(1-3), 763–774.
- Goswami, I., Scanlan, R., and Jones, N. (1993). Vortex-induced vibration of circular cylinders. ii: New model. *Journal of Engineering Mechanics*, **119**(11), 2288–2302.
- Govardhan, R. and Williamson, C. (2000). Modes of vortex formation and frequency response of a freely vibrating cylinder. *Journal of Fluid Mechanics*, **420**, 85–130.
- Greenwell, D. and Garcia, M. (2014). Autorotation dynamics of a low aspect-ratio rectangular prism. *Journal of Fluids and Structures*.
- Haaker, T. and vanOudheusden, B. (1997). One-degree-of-freedom rotational galloping under strong wind conditions. *International Journal of Non-Linear Mechanics*, **32**(5), 803–814.
- Hansen, S. (2013). Wind loading design codes. In *In: 50 Years of Wind Engineering - Prestige Lectures from the 6th European and African Conference on Wind Engineering*. University of Birmingham, pages 35–68.

- Hartlen, R. and Currie, I. G. (1970). Lift-oscillator model of vortex-induced vibration. *Journal of the Engineering Mechanics Division - Proceedings of the ASCE*, **EM5**, 577–591.
- Heine, W. (1964). *On the experimental investigation of vortex excited pressure fluctuations*. Ph.D. thesis, the University of British Columbia.
- Higgins, C., Froidevaux, M., Simeonov, V., Vercauteren, N., Barry, C., and Parlange, M. (2012). The effect of scale on the applicability of Taylor's frozen turbulence hypothesis in the atmospheric boundary layer. *Boundary-Layer Meteorology*, **143**(2), 379–391.
- Hover, F., Techet, A., and Triantafyllou, M. (1998). Forces on oscillating uniform and tapered cylinders in cross flow. *Journal of Fluid Mechanics*, **363**, 97–114.
- Itoh, Y. and Tamura, T. (2002). The role of separated shear layers in unstable oscillations of a rectangular cylinder around a resonant velocity. *Journal of Wind Engineering and Industrial Aerodynamics*, **90**, 377–394.
- Iwan, W. and Blevins, R. (1974). A model for vortex induced oscillation of structures. *Journal of Applied Mechanics*, **41**(3), 581–586.
- Iwan, W. and Botelho, D. (1985). Vortex-induced oscillation of structures in water. *Journal Waterway, Port, Coastal & Ocean Engineering. ASCE*, **111**, 289–303.
- Joly, A., Etienne, S., and Pelletier, D. (2012). Galloping of square cylinders in cross-flow at low Reynolds numbers. *Journal of Fluids and Structures*, **28**, 232–243.
- Khalak, A. and Williamson, C. (1996). Dynamics of a hydroelastic cylinder with very low mass and damping. *Journal of Fluids and Structures*, **10**(5), 455–472.
- Khalak, A. and Williamson, C. (1997). Fluid forces and dynamics of a hydroelastic structure with very low mass and damping. *Journal of Fluids and Structures*, **11**, 973–982.
- Knisely, C. (1990). Strouhal numbers of rectangular cylinders at incidence: A review and new data. *Journal of Fluids and Structures*, **4**(4), 371–393.
- Krenk, S. and Nielsen, S. (1999). Energy balanced double oscillator model for vortex-induced vibrations. *Journal of Engineering Mechanics*, **125**, 263–271.
- Kwok, K. and Melbourne, W. (1980). Free stream turbulence effects on galloping. *Journal of the Engineering Mechanics Division - Proceedings of the ASCE*, **106**(2), 273–278.
- Lanchester, F. (1907). *Aerodynamics*. Archibald Constable & Co. Ltd.
- Landl, R. (1975). A mathematical model for vortex-excited vibrations of bluff bodies. *Journal of Sound and Vibration*, **42**(2), 219–234.
- Laneville, A. (1973). *Effects of turbulence on wind induced vibrations of bluff cylinders*. Ph.D. thesis, the University of British Columbia.
- Laneville, A. and Parkinson, G. (1971). Effects of turbulence on galloping of bluff cylinders. In *Proceedings 3rd International Conference on Wind Effects on Buildings and Structures (Tokyo, Japan)*.

- Laneville, A. and Yong, L. (1983). Mean flow patterns around two-dimensional rectangular cylinders and their interpretation. *Journal of Wind Engineering and Industrial Aerodynamics*, **14**, 387–398.
- Larsen, A. (1995). A generalized model for assessment of vortex-induced vibrations of flexible structures. *Journal of Wind Engineering and Industrial Aerodynamics*, **57**(2-3), 281–294.
- Leweke, T. (2002). Flair water channel - characterisation of flow quality. Technical report, Monash University, Melbourne, Australia.
- Lienhard, J. (1966). Synopsis of lift, drag, and vortex frequency data for rigid circular cylinders. Technical extension service, Washington State University.
- Luo, S. and Bearman, P. (1990). Predictions of fluctuating lift on a transversely oscillating square-section cylinder. *Journal of Fluids and Structures*, **4**(2), 219–228.
- Luo, S., Yazdani, M., Chew, Y., and Lee, T. (1994). Effects of incidence and afterbody shape on flow past bluff cylinders. *Journal of Wind Engineering and Industrial Aerodynamics*, **53**(3), 375–399.
- Luo, S., Chew, Y., and Ng, Y. (2003). Hysteresis phenomenon in the galloping oscillation of a square cylinder. *Journal of Fluids and Structures*, **18**(1), 103–118.
- Magnus, H. (1853). 'Über die abweichung der geschosse. *Poggendorffs Annalen der Physik und Chemie*, **88**(1), 1–14.
- Mannini, C. (2006). *Flutter Vulnerability Assessment of Flexible Bridges*. Ph.D. thesis, University of Florence - Technical University of Braunschweig.
- Mannini, C., Marra, A., Massai, T., and Bartoli, G. (2013). Viv and galloping interaction for a 3:2 rectangular cylinder. In *Proceedings of the 6th European and African Wind Engineering Conference - EACWE 6*. IAWE.
- Mannini, C., Marra, A., and Bartoli, G. (2014a). Experimental investigation on viv-galloping interaction of a rectangular 3:2 cylinder. *Meccanica*, pages 1–13.
- Mannini, C., Marra, A., and Bartoli, G. (2014b). Viv-galloping instability of rectangular cylinders: Review and new experiments. *Journal of Wind Engineering and Industrial Aerodynamics*, **132**, 109–124.
- Marra, A., Mannini, C., and Bartoli, G. (2011). Van der pol-type equation for modeling vortex-induced oscillations of bridge decks. *Journal of Wind Engineering and Industrial Aerodynamics*, **99**, 776–785.
- Matsumoto, M. (1996). Aerodynamic damping of prisms. *Journal of Wind Engineering and Industrial Aerodynamics*, **59**(2-3), 159–175.
- Minorsky, N. (1960). Theoretical aspects of nonlinear oscillations. In *IRE Transactions on Circuit Theory*, volume 7, pages 368–381.
- Minorsky, N. (1962). *Nonlinear oscillations*. D.Van Nostrand Inc.

- Miyata, T., Miyazaki, M., and Yamada, H. (1983). Pressure distribution measurements for wind induced vibrations of box girder bridges. *Journal of Wind Engineering and Industrial Aerodynamics*, **14**(1-3), 223–234.
- Mizota, T. and Okajima, A. (1981). Experimental studies of unsteady flows around rectangular prisms. *Proceedings of the JSCE E (in Japanese)*, **213**, 49–57.
- Morse, T., Govardhan, R., and Williamson, C. (2008). The effect of end conditions on the vortex-induced vibration of cylinders. *Journal of Fluids and Structures*, **24**(8), 1227–1239.
- Mukhopadhyay, V. and Dugundji, J. (1976). Wind excited vibration of a square section cantilever beam in smooth flow. *Journal of Sound and Vibration*, **45**(3), 329–339.
- Nakaguchi, H., Hashimoto, K., and Muto, S. (1968). An experimental study of aerodynamic drag of rectangular cylinders. *Journal of the Japan Soc. Aerospace Sci.*, **16**(168), 1–5.
- Nakamura, Y. (1969). Vortex excitation of a circular cylinder treated as a binary flutter. *Reports of Research Institute of Applied Mechanics*, **XVII**(59), 217–234. Research Institute of Applied Mechanics, Kyushu University, Fukuoka, Japan.
- Nakamura, Y. and Hirata, K. (1991). Pressure fluctuations on oscillating rectangular cylinders with the long side normal to the flow. *Journal of Fluids and Structures*, **5**(2), 165–183.
- Nakamura, Y. and Matsukawa, T. (1987). Vortex excitation of rectangular cylinders with a long side normal to the flow. *Journal of Fluid Mechanics*, **180**, 171–191.
- Nakamura, Y. and Mizota, T. (1975a). Torsional flutter of rectangular prisms. *Journal of the Engineering Mechanics Division - Proceedings of the ASCE*, **101**(2), 125–142.
- Nakamura, Y. and Mizota, T. (1975b). Unsteady lifts and wakes of oscillating rectangular prisms. *Journal of the Engineering Mechanics Division - Proceedings of the ASCE*, **101**(6), 855–871.
- Nakamura, Y. and Ohya, Y. (1984). The effects of turbulence on the mean flow past two-dimensional rectangular cylinders. *Journal of Fluid Mechanics*, **149**, 255–273.
- Nakamura, Y. and Tamonari, Y. (1977). Galloping of rectangular prisms in a smooth and in a turbulent flow. *Journal of Sound and Vibration*, **52**(2), 233–241.
- Naudascher, E. and Rockwell, D. (1993). *Flow induced vibration: an engineering guide*. Balkema, Rotterdam.
- Nemes, A., Zhao, J., Lo Jacono, D., and Sheridan, J. (2012). The interaction between flow-induced vibration mechanisms of a square cylinder with varying angles of attack. *Journal of Fluid Mechanics*, **710**, 102–130.
- Norberg, C. (1993). Flow around rectangular cylinders: Pressure forces and wake frequencies. *Journal of Wind Engineering and Industrial Aerodynamics*, **49**(1–3), 187–196.
- Norberg, C. (2001). Flow around a circular cylinder: aspects of fluctuating. *Journal of Fluids and Structures*, **15**, 459–469.

- Novak, M. (1969). Aeroelastic galloping of prismatic bodies. *Journal of the Engineering Mechanics Division - Proceedings of the ASCE*, **EM1**, 115–142.
- Novak, M. (1971). Galloping and vortex-induced oscillations of structures. In *Proceedings of the 3rd International Conference on Wind Effects on Buildings and Structures, Tokyo (Japan)*, pages 799–809.
- Novak, M. (1972). Galloping oscillations of prismatic structures. *Journal of the Engineering Mechanics Division - Proceedings of the ASCE*, **98**(EM1), 27–46.
- Novak, M. and Davenport, A. G. (1970). Aeroelastic instability of prisms in turbulent flow. *Journal of the Engineering Mechanics Division - Proceedings of the ASCE*, **EM1**, 17–26.
- Novak, M. and Tanaka, H. (1972). Pressure correlations on vertical cylinder. In *Proceedings of the 4th International Conference on Wind Effects on Structures*, pages 227–232. Cambridge University Press.
- Novak, M. and Tanaka, H. (1974). Effect of turbulence on galloping instability. *Journal of the Engineering Mechanics Division - Proceedings of the ASCE*, **100**(EM1), 27–47.
- Obasaju, E. (1979). On the effects of end plates on the mean forces on square sectioned cylinders. *Journal of Industrial Aerodynamic*, **5**(12), 189–190.
- Obasaju, E. (1983). Forced-vibration study of the aeroelastic instability of a square-section cylinder near vortex resonance. *Journal of Wind Engineering and Industrial Aerodynamics*, **12**(3), 313–327.
- Okajima, A. (1976). Flow around an oscillating circular cylinder. In *Proceedings of the 4th Symposium on Wind Effects on Structures, Japan*, pages 147–154.
- Okajima, A., Mizota, T., and Tanida, Y. (1982). Observation of flow around rectangular cylinders. In *Flow visualization III; Proceedings of the Third International Symposium*, volume 123, pages 379–398, Washington, DC. Hemisphere Publishing Corp.
- Otsuki, Y., Washizu, K., Tomizawa, H., Ohya, A., and Fujii, K. (1971). Experiments on the aeroelastic instability of prismatic bars with rectangular sections. In *Proceedings of the Third International Conference on Wind Effects on Buildings and Structures, Tokyo (Japan)*, page 891898.
- Otsuki, Y., Washizu, K., Tomizawa, H., and Ohya, A. (1974). A note on the aeroelastic instability of a prismatic bar with square section. *Journal of Sound and Vibration*, **34**(2), 233–248.
- Parkinson, G. (1963). Aeroelastic galloping in one degree of freedom. In *1st Symposium on Wind effects on Building and Structures - Teddington, UK*, volume 1, page 582. Her Majesty's Stationery Office, London.
- Parkinson, G. (1989). Phenomena and modelling of flow-induced vibrations of bluff bodies. *Progress in Aerospace Sciences*, **26**(2), 169–224.
- Parkinson, G. and Brooks, P. (1961). On the aeroelastic instability of bluff cylinders. *Transaction of ASME*, pages 252–258.

- Parkinson, G. and Modi, J. (1967). Recent research on wind effects on bluff two-dimensional bodies. In *Proceedings of the International Research Seminar on Wind Effects on Buildings and Structures, Ottawa, Canada*, pages 485–513. University of Toronto Press.
- Parkinson, G. and Smith, J. (1964). The square prism as an aeroelastic non-linear oscillator. *The Quarterly Journal of Mechanics and Applied Mathematics*, **17**(2), 225–239.
- Parkinson, G. and Sullivan, P. (1979). Galloping response of towers. *Journal of Wind Engineering and Industrial Aerodynamics*, **4**, 253–260.
- Parkinson, G. and Wawzonek, M. (1981). Some considerations of combined effects of galloping and vortex resonance. *Journal of Wind Engineering and Industrial Aerodynamics*, **8**(1–2), 135–143.
- Perry, A. E., Chong, M. S., and Lim, T. T. (1982). The vortex-shedding process behind two-dimensional bluff bodies. *Journal of Fluid Mechanics*, **116**, 77–90.
- Prandtl, L. and Tietjens, O. (1934). *Applied Hydro and Aeromechanics*. McGraw-Hill.
- Prandtl, L. and Tietjens, O. (1957). *Applied Hydro and Aeromechanics*. Dover Pubns.
- Reid, E. (1924). Tests of rotating cylinders. TN 209, NACA.
- Robertson, I., Li, L., Sherwin, S. J., and Bearman, P. W. (2003). A numerical study of rotational and transverse galloping rectangular bodies. *Journal of Fluids and Structures*, **17**(5), 681–699.
- Robinson, A. and Saffman, P. (1982). Three-dimensional stability of vortex arrays. *Journal of Fluid Mechanics*, **125**, 411–427.
- Ruscheweyh, H., Hortmanns, M., and Schnakenberg, C. (1996). Vortex-excited vibrations and galloping of slender elements. *Journal of Wind Engineering and Industrial Aerodynamics*, **65**(1-3), 347–352.
- Santosham, T. (1966). *Force measurements on Bluff Cylinders and Aeroelastic Galloping of a rectangular Cylinder*. Master’s thesis, the University of British Columbia.
- Sarpkaya, T. (1978). Fluid forces on oscillating cylinders. *Journal Waterway, Port, Coastal & Ocean Engineering. ASCE*, **104**, 275–290.
- Sarpkaya, T. (1979). Vortex-induced oscillations: A selective review. *Journal of Applied Mechanics*, **46**, 241–258.
- Sarpkaya, T. (2004). A critical review of the intrinsic nature of vortex-induced vibrations. *Journal of Fluids and Structures*, **19**(4), 389–447.
- Scanlan, R. (1981). On the state-of-the-art methods for calculations of flutter, vortex-induced and buffeting response of bridge structures. Technical report, FHWA/RD-80/050, Nat. Tech. Information Service, Springfield (VA).
- Scanlan, R. (1998). Bridge flutter derivatives at vortex lock-in. *Journal of Structural Engineering*, **124**(4), 450–458.

- Schewe, G. (1984). Untersuchung der aerodynamischen kräfte, die auf stumpfe profile bei großen reynoldszahlen wirken. Technical Report Dfvlr-mitt.84-19, Deutsche Forschungs- und Versuchsanstalt für Luft- und Raumfahrt.
- Schewe, G. (1989). Nonlinear flow-induced resonances of an h-shaped section. *Journal of Fluids and Structures*, **3**, 327–348.
- Scruton, C. (1963). The wind-excited oscillations of stacks, towers and mast. In *Proceedings of 16th N.P.L. Symp. on Wind effects on building and structures, Teddington, Middlesex*, volume 16, pages 798–837.
- Shapiro, A. and Bergman, R. (1962). Experiments performed under the direction of L. Prandtl (Göttingen). Fm-11 film loop, National Committee for Fluid Mechanics.
- Silvio, G. (1969). Self-controlled vibration of cylinder in fluid stream. *Journal of the Engineering Mechanics Division - Proceedings of the ASCE*, **95**(2), 347–352.
- Simiu, E. and Scanlan, R. (1996). *Wind effects on structures*. John Wiley & Sons, Inc., New York.
- Sisto, F. (1953). Stall-flutter in cascades. *Journal of the Aeronautical Sciences (Institute of the Aeronautical Sciences)*, **20**(9), 598–604.
- Skop, R. A. and Griffin, O. M. (1973). A model for the vortex-excited resonant response of bluff cylinders. *Journal of Sound and Vibration*, **27**(2), 225–233.
- Smith, J. D. (1962). *An experimental study of the aeroelastic instability of rectangular cylinders*. Master's thesis, the University of British Columbia.
- Staubli, T. (1983). Calculation of the vibration of an elastically mounted cylinder using experimental data from forced oscillation. *Journal of Fluids Engineering*, **105**, 225–229.
- Sullivan, P. P. (1977). *Aeroelastic galloping of tall structures in simulated winds*. Master's thesis, the University of British Columbia.
- Sumer, B. and Fredsøe, J. (1997). Hydrodynamics around cylindrical structures. In *Advanced Series on Ocean Engineering*, volume 12. World Scientific, 1st edition.
- Swanson, W. (1961). The magnus effect: A summary of investigations to date. *Journal of Basic Engineering*, **WA150**(60), 461–470.
- Takeuchi, T. and Matsumoto, M. (1992). Aerodynamic response characteristics of rectangular cylinders in tandem arrangement. *Journal of Wind Engineering and Industrial Aerodynamics*, **41**(1-3), 565–575.
- Tamura, Y. and Matsui, G. (1979). Wake oscillator model of vortex-induced oscillation of circular cylinder. In *Proceedings of the Fifth International Conference on Wind Engineering*, volume 2, pages 1085–1094.
- Tamura, Y. and Shimada, Y. (1987). A mathematical model for transverse oscillations of square cylinders. In *Proceedings of the International Conference on Flow-Induced Vibrations*, pages 267–275.

- Taneda, S. (1956). Experimental investigation of the wakes behind cylinders and plates at low reynolds numbers. *Journal of the Physical Society of Japan*, **11**(3), 302–307.
- Taylor, G. (1938). The spectrum of turbulence. *Proceedings of the Royal Society of London*, **164**, 476–490.
- Thom, A. (1925). Experiements on the air forces on rotating cylinders. ARC/R&M 1018, NACA - ARC Reports & Memoranda.
- Thom, A. (1934). Effects of discs on the air forces on a rotating cylinder. ARC/R&M 1623, NACA - ARC Reports & Memoranda.
- Thom, A. and Sengupta, S. (1932). Acylinder on a cylinder rotating in an air stream. ARC/R&M 1520, NACA - ARC Reports & Memoranda.
- Thompson, M., Leweke, T., and Williamson, C. (2001). The physical mechanism of transition in bluff-body wakes. *Journal of Fluids and Structures*, **15**(3-4), 607–616.
- Van der Pol, B. (1927). Forced oscillations in a circuit with non-linear resistance. (reception with reactive triode). *Philosophical Magazine, Series 7*, **3**(13).
- Vickery, B. (1966). Fluctuating lift and drag on a long cylinder of square cross-section in a smooth and in a turbulent stream. *Journal of Fluid Mechanics*, **25**, 481–494.
- Vickery, B. (1969). Load fluctuations in turbulent flow. *Journal of Engineering Mechanics Division (ASCE)*, **94**(EM1).
- Vickery, B. and Basu, R. (1983). Across-wind vibrations of structures of circular cross-section. part i: development of a mathematical model for two-dimensional conditions. *Journal of Wind Engineering and Industrial Aerodynamics*, **12**(1), 49–73.
- von Kármán, T. (1911). Über den mechanismus des widerstands, den ein bewegter bewegter körper in einer flüssigkeit erfahrt. *Göttingen Nach. Math. Phys. Kl.*, pages 509–519.
- Washizu, K., Ohya, A., Otsuki, Y., and Fujii, K. (1978). Aeroelastic instability of rectangular cylinders in a heaving mode. *Journal of Sound and Vibration*, **59**(2), 195–210.
- Wawzonek, M. A. (1979). *Aeroelastic behavior of square section prisms in uniform flow*. Master's thesis, the University of British Columbia.
- Williamson, C. (1996). Vortex dynamics in the cylinder wake. *Annual Review of Fluid Mechanics*, **28**, 477–539.
- Williamson, C. and Roshko, A. (1988). Vortex formation in the wake of an oscillating cylinder. *Journal of Fluids and Structures*, **2**(4), 355–381.
- Williamson, C. H. K. (1989). Oblique and parallel modes of vortex shedding in the wake of a circular cylinder at low reynolds numbers. *Journal of Fluid Mechanics*, **206**, 579–627.
- Wong, K., Lo Jacono, D., and Sheridan, J. (2014). Flow-induced vibration of an elastically-mounted cylinder under forced rotation. In *Proceedings of the ASME 2014 International Design Engineering Technical Conference and Pressure Vessels & Piping Division Conference (IDETC/PVP)*, Anaheim, USA, number 28814 in PVP2014.

- Wood, K. (1976). *Coupled-oscillator models for vortex-induced oscillation of a circular cylinder*. Master's thesis, the University of British Columbia.
- Wooton, L. (1969). The oscillations of large circular stacks in wind. In *Proc. Inst. Civ. Eng.*, volume 43, pages 573–598.
- Wyatt, T. A. and Scruton, C. (1981). *A brief survey of the aerodynamic stability problems of bridges*. TTL, London, pp. 21-31.
- Yamaguchi, T., Shiraki, K., Umemura, S., and Matsui, Y. (1970). On the vibration of cylinder by karman vortex. Technical Report 7(4), pp. 451-457, Mitsubishi Tech. Rev.
- Zdravkovich, M. M. (1997). *Flow Around Circular Cylinders, Vol 1: Fundamentals*, volume 1. Oxford University Press.
- Zhao, J. (2012). *Flow-Induced Vibration of Circular and Square Cylinders with Low Mass and Damping*. Ph.D. thesis, Monash University.
- Zhao, J., Leontini, J., Lo Jacono, D., and Sheridan, J. (2014). Fluid-structure interaction of a square cylinder at different angles of attack. *Journal of Fluid Mechanics*, **747**, 688–721.